OPTICAL PROPERTIES OF FLY ASH

Contract No. DE-AC22-87PC 79903

FINAL REPORT

Prepared for Pittsburgh Energy Technology Center

Principal Investigator: Professor S. A. Self

December 1994

HIGH TEMPERATURE GASDYNAMICS LABORATORY
Mechanical Engineering Department
Stanford University

DISCLAIMER

PREFACE

Research performed under this contract was divided into four tasks under the following headings:

Task I	Characterization of Fly Ash
Task II	Measurements of the Optical Constants of Slags
Task III	Calculations of the Radiant Properties of Fly Ash Dispersions
Task IV	Measurements of the Radiant Properties of Fly Ash Dispersions

Tasks I and IV constituted the Ph.D. research topic of Sarbajit Ghosal, while Tasks II and III constituted the Ph.D. research topic of Jon Ebert. Together their doctoral dissertations give a complete account of the work performed.

This final report, issued in two volumes consists of an Executive Summary of the whole program followed by the dissertation of Ghosal (Vol. I) and Ebert (Vol. II). Each volume includes a list of publications and conference presentations resulting from the work.

Sidney A. Self

Stanford December 1994

ACKNOWLEDGEMENTS

It is a pleasure to record my personal satisfaction in advising Drs. Ebert and Ghosal in their graduate studies; their insights, energies and good humor made the direction of this work a rewarding experience.

Together, we should like to thank Mr. James D. Hickerson, PETC program manager, for his support and encouragement. We must also acknowledge the many practical contributions of Mr. Rodman Leach, Research Engineer on this project.

Finally we wish to record our debt to Dr. D. G. Goodwin, who was co-advised by Professors M. Mitchner and S. A. Self, for his pioneering work in this field under an earlier program support by the National Science Foundation.

EXECUTIVE SUMMARY

The overall goal of this project was to provide a fundamental scientific basis for understanding and calculating radiative heat transfer in coal combustion systems, particularly as influenced by the presence of inorganic constituents deriving from the mineral matter in coal.

The calculation of radiative heat transfer requires specification of the spectral absorption and scattering coefficients (a_λ and s_λ) and the scattering phase function (Φ_λ) of the medium. While the contributions to these properties by the infrared-active gases (CO_2 and H_2O) are well-documented, the contribution by the dispersed particulate phase (fly ash) may be large and hitherto was poorly understood. In general, the particulates produce two opposing tendencies on radiation transfer. Scattering impedes the transfer of gas radiation, while particle emission enhances the overall radiation transfer. In addition slag layers on combustor walls, deposited from entrained fly ash, provide a significant barrier to heat transfer.

Calculation of the optical properties of a particulate dispersion rests on the Mie theory for a single particle. This theory is readily available only for a homogeneous, isotropic sphere and requires specification of the size parameter $x \equiv (\pi d/\lambda)$ and the complex refractive index $m \equiv (n+ik)$ of the particle material, a function of composition, wavelength and temperature. The optical properties of the dispersion is then obtained by convolving the Mie theory for a single sphere with the size and refractive index distributions of the polydispersion.

In practice, it is not possible to invert measurements of the optical properties of a particulate dispersion to infer the size and refractive index distributions of the particulates. Even if one knows the size distribution from independent measurements, one can infer, at best, only some effective average refractive index. Because of the impracticality of obtaining fundamental data on the complex refractive index of particulates from measurements on a polydispersion, and in view of the heterogeneity of composition of fly ash, an alternative strategy was adopted.

The basic approach was to measure the optical constants (i.e. the components, n, k of the complex refractive index) on bulk samples of synthetic slags, for which reliable techniques are available. Such measurements were made over relevant ranges of wavelength, composition and temperature, and constitute the fundamental data base for computing radiation transfer in fly ash laden combustion gases. To utilize such data on the optical constants of slag in calculations of radiation transfer in ash dispersions, it is also

necessary that the ash be characterized with respect to its size and composition distributions. Characterization of a range of representative ashes constituted a second component of the work. It should be recognized that this basic approach rests on the fortunate fact that the vast majority of fly ash particles are closely spherical, optically isotropic (because they are vitreous) and homogeneous, although the composition varies significantly from particle to particle.

The research program consisted of four tasks, as outlined below.

TASK 1 - CHARACTERIZATION OF FLY ASH

Representative samples of fly ashes were characterized with respect to their size and composition distributions, including correlation of composition with size over ranges of interest for radiation transfer. Ashes from six coals selected for study under the concurrent PETC program on "Transformation of Inorganic Coal Constituents in Combustion Systems" were obtained from electric power plants or from samples produced earlier in the 10^6BTU/hr pilot combustor at Foster-Wheeler.

Size distributions were determined by Coulter counter, while size-composition distributions were obtained from computer-controlled SEM-EDX microprobe analyses.

In addition, techniques were developed for ash separation by both size and density by combined wet sieving and centrifuging in liquids of various specific gravity, as well as separation of the magnetic component (magnetite from the combustion of pyrite). Analysis of the separated fractions yielded further information on the size-composition distributions as well as information on the fraction of cenospheric ash (i.e. particles containing gas bubbles).

TASK II - MEASUREMENTS OF THE OPTICAL CONSTANTS OF SLAGS

Coal slags and fly ash are basically impure calcium-aluminosilicate glasses. The host glass is essentially transparent ($k \leq 10^{-4}$) in the visible and near infrared, with a very strong absorption band ($k \sim 1$) in the range 8-12 μm due to vibration of the Si-O bond. The principal infrared-active impurity is iron (as the ferrous ion) which produces significant absorption ($k \sim 10^{-4}$–10^{-3}) in the range 0.5–5 μm, important for radiation transfer at combustion temperatures.

Synthetic slags of controlled composition were produced by melting appropriate mineral oxides in a furnace at ~1560°C and cooled slowly to produce homogeneous bulk samples. For measurements at low temperatures (to ~800°C) thin wafers (50–500 μm) were cut and optically polished. The optical constants over the wavelength range 0.5–8 μm were

determined by measuring the absorption and surface reflectance and use of the Fresnel relations. For the range 8–13 μm where the absorption is too strong ($k > 10^{-2}$) to allow direct measurements of absorption on thin wafers, n and k were obtained from surface reflectance measurements at normal incidence using the Kramers-Kronig relations.

At high temperatures (≥1600°C) when the slag is liquid, an alternative technique was devised for measuring the absorption of thin liquid layers, by a double pass using reflection from a submerged platinum mirror. The absorption coefficient (and hence k) was determined from the change in signal when the liquid film depth was changed a known amount by raising or lowering the mirror by a micrometer-controlled increment.

For the longer wavelengths ($\lambda \geq 8$ μm), where the absorption is too strong ($k \geq 10^{-2}$) to allow direct absorption measurements on a thin film, n and k were determined solely from surface reflectance measurements on the liquid slag using the Kramers-Kronig technique.

The final outcome of Task II is a set of correlation formulae for the complex refractive index of synthetic slags as a function of composition, wavelength and temperature. These formulae constitute a fundamental data base for the calculation of radiation transfer in ash-laden combustion gases.

TASK III - CALCULATION OF THE RADIANT PROPERTIES OF FLY ASH DISPERSIONS

Sample calculations were made for typical ash loadings, size distributions and compositions for simple geometries, with two main purposes: first, to provide insight and physical understanding of the role of fly ash in radiative heat transfer in combustion systems; second, to indicate the sensitivity of the results to the characteristics of the input data. Such calculations were also used to determine appropriate conditions and to predict the expected measured radiative properties for the experiment of Task IV.

TASK IV - MEASUREMENTS OF THE RADIANT PROPERTIES OF FLY ASH DISPERSIONS

This experiment was intended to validate the overall approach by critically testing our ability to predict the measured spectral absorption and scattering coefficient of hot, gaseous fly ash dispersions under well-controlled laboratory conditions utilizing the ash characteristics and the optical property data developed in Tasks I and II. However, in the event, it proved impossible to generate well-deagglomerated aerosols from ash powder samples, so we settled for a somewhat less stringent but much easier-to-accomplish test using room-temperature dispersions of ash in several infrared transmitting liquids covering the wavelength range 1-

13 μm. Measurements of spectral extinction (by scattering and absorption) showed good agreement with predictions for four ashes when account was taken of the presence of cenospheres in the ash. The effect of cenospheres is greatly enhanced in liquid dispersions compared with gaseous dispersions, for which it is essentially negligible.

In summary, the overall goal of the research was accomplished; a new, general method for realistically incorporating the effects of fly ash in radiative transfer computations in coal combustion systems has been established. With the use of the correlation formulae for the dependence of the complex refractive index of fly ash on composition, wavelength and temperature, resulting from this work, all that is required to calculate heat transfer in the radiant section of a particular coal combustor is specification of the geometry and boundary conditions, plus data from standard microanalytical techniques of the size and composition distributions of a sample of ash from the particular coal of interest. The correlation formulae are also directly applicable for calculating radiation transfer through slag deposits on combustor walls.

PUBLICATIONS AND CONFERENCE PRESENTATIONS

1. D. G. Goodwin and J. L. Ebert, "Rigorous Bounds on the Radiative Interaction between Real Gases and Scattering Particles," Journal of Quantitative Spectroscopy and Radiative Transfer 37, no. 5, pp. 501-508, 1987.

2. Sidney A. Self, Comment on "Rigorous Bounds on the Radiative Interaction between Real Gases and Scattering Particles," by D. G. Goodwin and J. L. Ebert, Journal of Quantitative Spectroscopy and Radiative Transfer 37, no. 5, pp. 513-514, 1987.

3. J. L. Ebert and S. A. Self, "Radiation Heat Transfer in a Dispersion of Flyash," in R. W. Bryers and K. S. Vorres (eds), Engineering Foundation Conference on Mineral Matter and Ash Deposition from Coal, Santa Barbara, CA, Feb. 22-26, pp. 599-611, 1988.

4. J. L. Ebert and S. A. Self, "The Optical Properties of Molten Coal Slag," Proc. 26th National Heat Transfer Conference, Philadelphia, PA, August 1989.

5. S. Ghosal and S. A. Self, "Optical Characterization of Coal Fly Ash," *Radiative Transfer - Theory and Applications*, Ed. A. M. Smith and S. H. Chan, American Society of Mechanical Engineerings, HTD-Vol. 244, pp. 105-115, 1993.

6. S. Ghosal, J. L. Ebert and S. A. Self, "Size Distributions of Fly Ashes by Coulter Multisizer: Use of Multiple Orifices and Fitting to Truncated Lognormal Function," Particle and Particle Systems Characterization, Vol. 10, pp. 11-18, 1993.

7. S. Ghosal and S. A. Self, "Infrared Extinction Measurements on Fly Ash Dispersions," *General Papers in Radiative Transfer*, Ed. M. F. Modest, I. S. Habib, and M. Sohal, American Society of Mechanical Engineers, HTD-Vol. 257, pp. 51-61, 1993.

8. S. Ghosal, J. L. Ebert and S. A. Self, "The Infrared Refractive Indices of $CHBr_3$, CCl_4, and CS_2," Infrared Physics, Vol. 34, No. 6, pp. 621-628, 1993.

9. S. Ghosal, J. L. Ebert and S. A. Self, "Chemical Composition and Size Distributions for Fly Ashes," Fuel Processing Technology, in press.

10. S. Ghosal and S. A. Self, "Particle Size-Density Relationship and Cenospheric Content of Coal Fly Ashes," Fuel, in press.

OPTICAL CHARACTERIZATION OF COAL FLY ASHES AND INFRARED EXTINCTION MEASUREMENTS ON ASH SUSPENSIONS

A DISSERTATION
SUBMITTED TO THE DEPARTMENT OF MECHANICAL ENGINEERING
AND THE COMMITTEE ON GRADUATE STUDIES
OF STANFORD UNIVERSITY
IN PARTIAL FULFILLMENT OF THE REQUIREMENTS
FOR THE DEGREE OF
DOCTOR OF PHILOSOPHY

By
Sarbajit Ghosal
November 1993

Abstract

Fly ash is generated from the non-volatile inorganic constituents of coal during combustion in pulverized coal-fired combustors. As the char fragments and burns out, these micron-size molten droplets (mixtures of clayey minerals composed primarily of alumina and silica, with small amounts of iron oxide, calcia, etc.) are entrained, and swept out of the combustor with the flue gas. In the process, they are rapidly cooled into glassy, predominantly spherical, ash particles. The ash droplets influence the radiative heat transfer from the flame to the combustor wall in two ways — by absorbing/emitting, and by scattering radiation. Accurate prediction of combustor wall temperatures and flue gas exit temperatures are important for combustor design.

Although absorption/emission by the gas bands of CO_2 and water vapor is well documented, the role of the fly ash in radiative transfer has hitherto been poorly understood. For improving understanding, knowledge of the optical properties of fly ash is needed in the form of the distribution of the complex refractive index of the ash, $m{=}n + \mathrm{i}\,k$. These optical properties depend on the radiation wavelength, λ, chemical composition, and temperature. Although a single ash particle is generally quite homogeneous, the chemical composition varies significantly from particle to particle. Silica and iron oxides are the primary determinants of the absorption index, k and thus contribute to emission/absorption, but all constituents influence scattering through n, the real part of the refractive index.

The two aims of this research are (1) to document the data on particle size and composition distributions that will allow reliable calculations of radiative heat transfer in fly ash laden combustion gases when the size and composition distributions of the ash are specified, and (2) to conduct a bench-scale experiment to determine whether extinction by a slab of optically characterized ash can be accurately predicted using Mie theory. To this end, six ashes, representative of coals burnt in the U.S., were obtained for study.

As a part of physical characterization of the ashes, their size distributions, in the diameter range of 1–200 μm, were determined using the Coulter

Multisizer. Lognormal functions, truncated outside the measurements limits, were found to fit the size distribution data for all the ashes quite well. The mass median diameter and the geometric standard deviation of most of the ashes are in the ranges 10–15 μm and 2.0–3.0, respectively. Density classification was performed by centrifugal separation to determine the fraction of hollow particles in the ashes. Computer controlled scanning electron microscopy and associated energy dispersive x-ray spectroscopy (CCSEM) were carried out on large numbers of particles of each ash to obtain statistically accurate chemical composition distributions. For each ash, this data was used to create classes based on the complex refractive index.

A bench-scale experiment was carried out to measure extinction by fly ashes at ambient temperature. The ash was dispersed in CCl_4, $CHBr_3$, and CS_2, and the extinction measured over separate wavelength ranges where these liquids are transparent. Because of a lack of accurate spectral data for $n(\lambda)$ of $CHBr_3$, and CS_2, measurements were made using the near-normal reflectance method. Transmittance measurements were made on four of the six characterized ashes over the wavelength range (1–13 μm). After accounting for compositional heterogeneity and the presence of cenospheres in the ash, the results are seen to agree quite well with the predictions of Mie calculations. Comparison with calculations using room temperature and high temperature optical property data show that the optical properties of the ash is closer to that of the melt than to glass prepared through a gradual cooling process. This similarity of molecular structure (which influences the optical properties) between glassy ash and molten slag is a result of the high quench rates of the ash particles as they leave the flame region.

Nomenclature

A	area, Legendre coefficient
a, b	lower and upper limits of size measurement, Mie coefficients
a_A	radius of aperture stop
a_F	radius of field stop
C	composition, normalizing constant for matching Multisizer data
$C_o(D)$	average oxide content (element o) of particles with diameter $\leq D$
c	phase velocity
c_o	velocity of light in vacuum
D	particle diameter
$\bar{D}_j$	median diameter of the j^{th} moment of $F(D)$
D_{max}	largest particle diameter in CCSEM sample
D_{32}	Sauter mean diameter
d	optical path length difference between the two test-cell chambers
E	extinction
$\mathbf{E}$	electric field vector
e	electronic charge
$F(D)$	cumulative number distribution
f	focal length
$f(D)$	differential number distribution
$f_j(D)$, $F_j(D)$	j^{th} moment distribution of $f(D)$, $F(D)$
$f_j^{(a,b)}(D)$, $F_j^{(a,b)}(D)$	$f_j(D)$, $F_j(D)$ truncated outside $a \leq D \leq b$
$f_o(x)$	ash volume fraction with $< x$ (mass) percent of oxide o
F/#	F number, acceptance (solid) angle of optical component/system
$\mathbf{H}$	magnetic field vector
h	monochromator slit height
I	radiance
K	extinction coefficient
$\mathbf{K}$	complex wave vector
k	absorption index, imaginary part of m
L	thickness of slab of ash suspension
M	optical magnification
m	complex refractive index relative to vacuum
$\bar{m}$	complex refractive index relative to surrounding medium

m_r	complex refractive index of ash particle relative to suspending liquid
m_p	ionic mass
n	refractivity, real part of m
N	ash particles per unit volume
N_p	ions per unit volume
P	Legendre function, Cauchy principal value of integral, perimeter, radiant power
p	mean electrical polarizability per molecule
p, q	coefficients of polynomial used to match Multisizer size data
$Q_{a,\lambda}$	spectral absorption efficiency
$Q_{s,\lambda}$	spectral scattering efficiency
$\bar{Q}_{a,\lambda}$, $\bar{Q}_{a,\lambda}$	size averaged values of above efficiencies
R	reflectance
R_c	ratio of inner to outer diameter of cenosphere
r	reflection coefficient
S	shape factor
s	path length, monochromator slit width, object/image distance
s_o	standard deviation of oxide o in ash
T	transmittance, temperature
t	time
V_a	ash volume loading
X_o	mass fraction (of oxide o)
$\bar{X}_o$	average oxide mass fraction in ash
X_s	average oxide mass fraction in slag
x	size parameter, $\pi D/\lambda$
$\mathbf{x}$	position vector
α_λ	spectral absorption coefficient
γ	damping coefficient
$\delta_o(d)$	oxide distribution function (see Section 4.3)
ϵ	permittivity
μ	permeability
λ	wavelength
Φ_λ	spectral scattering phase function
η	truncation error in lognormal functions
θ	angle
θ_R	phase shift on reflection
ρ	density, normal reflectivity
ρ_{ash}	measured average ash density
ρ_c	calculated density for slags or ash composition class
$\bar{\rho}_c$	calculated average ash density
ρ_e	effective density of oxide
ρ_m	experimentally measured slag density
Ψ	Ricatti-Bessel function

ξ	Ricatti-Bessel function
$\xi_o(x, D)$	oxide distribution function (see Section 4.3)
σ_λ	spectral scattering coefficient
σ	electrical conductivity, statistical standard deviation
σ_g	geometric standard deviation
τ	optical thickness
τ_w	window transmittance
χ	susceptibility
ω	angular frequency
Ω	albedo, solid angle
$\zeta_o(x)$	oxide distribution function (see Section 4.3)
ε	etendue
ϑ_o	average (bulk) mass fraction of oxide of element o

Subscripts

$a, 2$	area basis
b	property of bubbles
c	cenospheres, complex electric/magnetic field
l	property of liquid medium
n	number/count basis
o	property related to oxide of element o
r	property relative to medium
$v, 3$	volume basis
w	property relative to that of cell window
$x\%$	x percent undersize
< 2.2	density less than 2.2 g/cc
> 2.2	density greater than 2.2 g/cc

Superscripts

(a, b)	$f_j(D), F(D)_j$ truncated outside $a < D < b$

Contents

Chapter 1

Introduction

1.1 Background and Motivation

Fly ash is generated from the non-combustible inorganic constituents (mostly clays such as illite, kaolinite, etc.) of coal during combustion, e.g., in pulverized coal-fired combustors. Following devolatilazation, as the char fragments and burns, micron-sized molten droplets (mixtures of mainly silica and alumina, with small amounts of iron oxide, calcia, etc.) are entrained, and swept out of the combustor with the combustion (or flue) gases, being rapidly cooled in the process to form glassy spherical ash particles. They are later removed by collection devices (such as electrostatic precipitators, or baghouses) located downstream.

U. S. coals contain between 5–25% by weight of inorganic mineral matter, commonly called ash. In pulverized coal-fired combustors (also referred to as burners or furnaces), 50% to 80% of the ash is emitted as fly ash, the remainder being deposited on the walls and the bottom of the radiant section as slag. Typically, a steam generator of 1000 MW capacity produces over a thousand tonnes of fly ash per day.

The major consideration is designing combustor equipment is usually heat transfer rather than combustion characteristics. An accurate prediction of combustor wall temperatures and flue gas exit temperatures are of paramount importance for combustor design. To reduce expenses, it is important to keep the size of the burner as small as possible. A smaller combustor implies higher operating temperatures, the limits on which are set by the wall materials. On the other hand, the temperature of the ash particles leaving the radiant section should be below the softening temperature (1100–1300°C range) to prevent fouling

of the heat exchangers in the downstream convective section.

While the desired peak flame temperature determines the furnace plan area in design considerations, the ash and gas exit temperatures determine the furnace height. There still remains considerable uncertainty in predicting the exit temperature under various operating conditions (Sarofim, 1978). Radiative transfer is the dominant heat transfer mode in the combustor and radiant section*. In recent years, complex two or three-dimensional computer models have been developed to simulate radiative transfer in furnaces (e.g., Gupta *et al*, 1983). The models, however, are still not reliable due, primarily, to insufficient data on the optical properties of the ash particles.

Both particulates and the combustion gases contribute to the radiative transfer process. The role of carbon dioxide and water vapor has been studied extensively (e.g., Edwards, 1976). In the absence of particles, the spectral band models of the infrared radiative properties of these gases can predict fluxes and temperature distributions under typical combustor operating conditions within uncertainties of 5–10%. Carbonaceous particles, i.e., soot and char, are present in significant quantities in the flame region of the combustor. Due to their high emissivities in the wavelength range of interest, they contribute significantly to the radiative transfer process in this zone. Results of optical characterization of char and soot are available from previous studies (Brewster and Kunitomo, 1984; Lee and Tien, 1981). However, accurate predictions of soot loadings are still not possible because of insufficient understanding of the mechanisms of soot formation and burnout under various operating conditions.

The flame region occupies a relatively small fraction of the combustor volume. Downstream of the flame where burnout is complete, and in the radiant section, the fly ash contributes strongly to the radiative transfer process to the wall in two ways — by absorbing/emitting, and by scattering gas band radiation. This property of fly ash to markedly affect radiative transfer has been noted from experience for many years (e.g., Field *et al*, 1967; Wall, 1979; Macek, 1979).

Because of the nature of their formation process (i.e., quenching of liquid droplets), the ash particles are predominantly glassy, spherical, reasonably homogeneous and isotropic†, although there is strong inter-particle variation in chemical composition. Hence, straightforward Mie theory can be employed to calculate the absorption and scattering efficiencies for

*Typically, 90% of the total heat transfer occurs in the radiant section.

†From the viewpoint of infrared optical properties.

an ash particle as a function of the complex refractive index, $m(=n+\mathrm{i}\,k)$, and the size parameter, $x(\equiv \pi D/\lambda)$, where D is the particle diameter. These efficiencies can be calculated for various composition classes for a given ash, and convolved with the size distribution and loading to obtain overall absorption and scattering coefficients for the ash dispersion. These coefficients can then be used in the equation for radiative transfer.

Several numerical studies (e.g., Wall *et al*, 1981; Viskanta *et al*, 1981; Gupta *et al* 1983; Boothroyd and Jones, 1983) predict a significant role for fly ash in radiative heat transfer in coal combustion products. However, due to the absence of an experimental database, these studies made grey-body assumptions about the absorption and scattering coefficients. As a result, some of the conclusions, e.g., on the temperature dependence of the Planck mean absorption efficiency, were contradicted when the spectral features were properly taken into account (Goodwin, 1986).

To determine the absorption and scattering coefficients of an ash dispersion, accurate knowledge of the optical properties and ash size distribution are necessary. By optical properties we mean the complex refractive index, $m(=n+\mathrm{i}\,k)$, and its dependence on wavelength, temperature, and chemical composition of the ash. The real part of m, n, is called the refractive index, and controls scattering by the ash. The imaginary part, k, referred to as the absorption index, determines the absorption and emission of radiation by the ash. Since blackbody emission corresponding to typical coal combustor temperatures (1500–2000 K) peaks in the range 1.5–2.0 μm, the wavelength range of interest is the near-infrared, $\approx$1–10 μm[‖].

Several investigators have attempted to determine the optical properties of individual ash particles (e.g., Wyatt, 1980; Marx, 1983) or of ash in powder form (e.g., Volz, 1973). For various reasons, explained in detail by Goodwin (1986), the data reported in these studies are either flawed, or are limited to a few ash particles with insufficient linkage to the chemical composition. Consequently, no general conclusions about ash radiative properties can be drawn from these studies. Bohren and Hoffman (1983) explain very clearly the near-impossibility of measuring the optical properties of particulate samples, even when all the particles have the same composition. In the case of fly ashes, the composition, and hence the optical properties, vary significantly from particle to particle, making it necessary to adopt a different approach to the problem.

[‖]The long wavelength limit of interest stretches farther on the long wavelength side compared to the short wavelength side because the blackbody curve has a lower slope at this end.

1.2 Present Approach

To account for the effects of fly ash on radiative heat transfer requires a knowledge of the contributions of the ash to the spectral absorption (α_λ) and scattering (σ_λ) coefficients of the particulate dispersion, together with the phase function Φ_λ describing the anisotropy of the scattering. These quantities depend on the particulate loading as well as the distributions of the size and optical properties of the particles.

For a spherical, dielectric particle of homogeneous, optically isotropic material, characterized by the complex refractive index, m, Mie theory allows one to compute the spectral absorption ($Q_{a,\lambda}$) and scattering ($Q_{s,\lambda}$) efficiencies of the particle, as well as the phase function Φ_λ. For randomly polarized radiation, these quantities are a function of the particle size parameter, x, and $m(C, \lambda, T)$, a function of composition, wavelength and temperature. The fact that the bulk of the ash consists of reasonably spherical, compositionally homogeneous, and vitreous (and therefore optically isotropic) particles is very fortunate, since these conditions satisfy the assumptions of Mie theory remarkably well.

For a monodispersion of identical spherical particles of specified loading (i.e., number density), N, the particulate's contribution to the radiative properties (α_λ, σ_λ, and Φ_λ) of the medium are simply related to the spectral properties ($Q_{a,\lambda}$, $Q_{s,\lambda}$, Φ_λ) of a single particle (see Siegel and Howell, 1992). It is also straightforward to compute the spectral radiative properties for a polydispersion of spheres of identical composition, by convolving the results of Mie calculations for spheres of varying diameter (i.e. x) for fixed wavelength (and hence fixed m), with the particle size distribution, $f(D)$. For example,

$$\sigma_\lambda = N \int_0^\infty \left(\frac{\pi}{4} D^2\right) Q_s \, f(D) \, \mathrm{d}D$$

Here, $\int_0^\infty f(D) \, \mathrm{d}D = 1$. The scattering coefficient can be expressed as

$$\sigma_\lambda = \frac{3}{2} \frac{V_a}{D_{32}} \bar{Q}_{s,\lambda}$$

Here, D_{32} is the Sauter mean diameter, $\bar{Q}_{s,\lambda}$ is the size-integrated scattering efficiency, and V_a is the ash volume loading given by

$$V_a = N \int_0^\infty \left(\frac{\pi}{6} D^3\right) f(D) \, \mathrm{d}D$$

In the case of fly ash whose composition, although reasonably uniform within a particle, shows strong inter-particle variation, it is still possible to compute the spectral characteristics of the dispersion by dividing the particles into an appropriate number of classes of

varying composition (and hence m), each having a specified size distribution, and summing over all p composition classes

$$\sigma_\lambda = \sum_{i=1}^{p} \sigma_{\lambda,i} = \frac{3}{2} \sum_{i=1}^{p} \frac{V_{A,i}}{D_{32,i}} \bar{Q}_{s,\lambda,i}$$

Similarly, expressions can be obtained for α_λ and Φ_λ. A more detailed explanation is given in Chapter 2.

In radiative heat transfer calculations, the contribution of the gas to the spectral absorption coefficient is added to that of the particles to obtain the combined absorption coefficient of the medium on a spectral basis. The latter, together with the scattering coefficients due to particles, are then used as input for a radiation transfer code to calculate spectral radiative fluxes for a particular combustor geometry and boundary conditions. Finally, to obtain total heat transfer quantities such as the overall radiant heat flux, integrations must be made over wavelength.

The procedure outlined above represents the only logical approach to the computation of radiative heat transfer in fly ash laden combustion gases. To implement this procedure requires, as input, a detailed characterization of the ash with respect to its size and (complex) refractive index distributions on a spectral basis.

While techniques are available for determining the size distribution of powder samples, such as fly ash, there are no practical means available for reliably determining the complex refractive index distribution of a complex material such as fly ash either on a single particle basis, as a powder or as a dispersed aerosol. Bohren and Hoffman (1983) clearly explain the near-impossibility of measuring the optical constants (n, k) of particulate samples, even when all the particles have the same composition. On the other hand, there are well-established techniques for measuring the refractivity and absorption index for bulk samples. Using classical solid state physics, the sample compositions can be related to the complex refractive index of their material.

Although n and k of a heterogeneous powder cannot be measured directly, it is possible, using computer-automated SEM/EDX (energy dispersive X-ray spectroscopy associated with scanning electron microscopy) analysis, to determine its size and chemical composition on a particle-by-particle basis for a statistically large sample. Thus, the key requirements for this approach are twofold:

- Obtain data on the optical constants (i.e., the components n, k of the complex refractive index) of a bulk slag[‡] as a function of composition, wavelength and temperature (covering the range of compositions found in representative ashes).

- Comprehensively characterize a particular ash in terms of its size and composition distributions.

Because the optical constants are material properties, the best approach, in this situation, is to measure the bulk optical properties of synthetic slags of known composition at specific temperatures on a spectral basis. The complex refractive index of a slag at a specified wavelength and temperature are functions only of the composition. Once these properties of various slags having representative compositions are determined as functions of temperature and wavelength, the optical properties of a fly ash of known chemical composition and size distribution can be obtained relatively easily from calculations based on Mie theory.

The first detailed study of the optical properties of coal slags was made at Stanford with NSF support by Goodwin (1986), who focused attention on the fundamental absorption mechanisms that control the optical properties in the wavelength range relevant to coal combustion. The absorption index, k, in the range 1–4 μm is controlled by the intervalence charge transfer mechanism between Fe^{3+} and Fe^{2+}, and the ligand absorption band of Fe^{2+}. Beyond 4 μm, the optical properties are dominated by the broad *Reststrahlen* absorption band of SiO_2, associated with the stretch vibrations of the Si–O–Si and $Si–O^-$ bonds. (These mechanisms are discussed in greater detail in the next chapter.) The study confirmed that the emission/absorption by fly ash is determined almost entirely by its silica and iron oxides content. On the other hand, all constituent oxides contribute to n; oxides of higher molecular weight producing a proportionately larger value of n.

Goodwin (1986) measured the complex refractive index, m, in the wavelength range 1—13 μm, of bulk synthetic slags prepared by melting mixtures of silica (SiO_2), alumina (Al_2O_3), calcia (CaO), and iron oxide (Fe_2O_3). The iron oxide content was varied from slag to slag in the range ≈0–20%, while keeping the SiO_2/Al_2O_3 ratio approximately constant. Transmittance measurements through thin slag wafers were used to measure k, while the

[‡]The definitions of the terms 'ash' and 'slag' are the same as in Goodwin (1986). While 'slag' denotes a bulk, macroscopic sample prepared by cooling melts, 'ash' is generally used to refer to any mineral matter, regardless of physical state. However, in this study, the term ash is mostly used as an abbreviation of 'fly ash'.

near-normal reflectance technique was used to determine n. In the wavelength range 8–13 μm, where absorption is too strong to allow transmittance measurements on wafers, the Kramers-Kronig relations were used to obtain both n and k solely from reflectance data. The composition dependence of m was presented as 'mixture rules', i.e., as a function of the weight percentage composition of the constituent oxides in the slag using literature values of the optical constants for the individual oxides.

Goodwin's measurements were restricted to solid slags. Ebert (1993) has extended the measurements to higher temperatures ($\approx$1900 K, comparable to those in actual combustors) on molten synthetic and natural slags. His choice of synthetic slags spans a greater range of silica and calcia levels than do Goodwin's. Because the temperature of the ash droplets decreases sharply as they leave the flame region, they are quenched into a glassy state with a molecular structure similar to that of the melt. Hence, the optical properties determined by Ebert can be expected to represent those of ash particles more accurately than those of Goodwin's slags which were cooled relatively slowly.

Ebert (1993) has presented comprehensive correlations for the magnitude of the absorption index in the range λ=4–13 μm as a function of SiO_2 content. The location of the broad absorption peak is also correlated with the silica content, shifting to shorter wavelengths as the silica level increases. In summary, it can be said that the results presented by Goodwin and Ebert provide the necessary database for predicting the spectral optical constants for slags (and, thus, ash particles) of a specified composition. In order to predict the radiative properties of fly ash dispersions, the remaining data needed are the size and composition distributions of the ashes. However, until now, no systematic effort has been made to determine the optical characteristics of ashes, which vary significantly depending on the rank of the coal, and the particular mine.

Detailed characterization of fly ash morphology has been carried out by several investigators in the areas of environmental, combustion, and fly ash utilization technologies (e.g., Fisher *et al*, 1978; Ramsden and Shibaoka, 1982; Hemmings and Berry, 1986). However, most of these provide little quantitative data. They tend to focus undue attention on unusual and 'interesting' components of the ash, many of which are often present in small proportions and may not affect bulk properties. For example, ashes contain small amounts of unburnt char particles as well as some irregular mineral particles with rounded edges (henceforth referred to as adventitious rock). The former, with its porous network structure, occurs as a result of incomplete combustion. Density separation shows that the char

content of the ashes studied here is negligible. In pulverized coal combustors where temperatures are very high (≈2000K), most adventitious rock particles melt to form spheres. Only a few large ones resist melting; their edges being rounded by partial melting. However, because of their unique structures and relatively large sizes (>50 μm), both char and adventitious rock are extensively documented in optical and scanning electron microscopy (SEM) studies. Similarly, the majority of published studies on the chemical composition of single ash particles (or bulk ashes) fail to present a unified picture through comprehensive characterization. A more detailed survey of existing literature on ash characterization is included in Chapter 3 and 4.

By contrast, an effort has been made in this study to obtain detailed physical and chemical data on a quantitative or, at least, semi-quantitative basis, followed by suitable simplifications to create plausible optical property models, i.e., size, density, and refractive index distributions.

Although much of the ash is glassy, there commonly are inhomogeneities in the glass in the form of micro-bubbles, phase separation, and cenospheres. Additionally, there is usually a small fraction of irregular particles which, as mentioned above, consist of mineral matter that has not undergone complete melting. However, to render the problem tractable, it is essential to make the simplifying assumptions that ash particles are spherical, glassy, and homogeneous. These are not unreasonable assumptions since the optical properties of a suspension of randomly oriented crystalline somewhat non-spherical (say, ellipsoidal) particles are not very different from their glassy spherical counterpart (Bohren and Huffman, 1983). Whether Mie calculations can be used to predict heat transfer quantities (such as temperature distributions and heat flux at combustor walls) can only be ascertained by designing and carrying out controlled experiments using well-characterized ashes. There do not appear to be any reports of such experiments in the literature.

Lowe *et al* (1979) made emission measurements in the range λ=1–5 μm, in a large utility boiler using four different coals. However, the interpretation of the data is not easy since emission by the combustion gases, soot, char, and the hot walls are not taken into account, resulting in overestimation of the absorption coefficient. They also fail to account for in-scatter into the optical measurement path. These problems are unavoidable in making measurements on uncharacterized ashes, and in hot, emitting media. However, the authors do recognize the importance of ash composition and size distribution to the radiative transfer process.

1.3 Objectives and Scope of Present Study

The broad aim of this experimental study is to determine the actual optical-radiative properties of representative fly ashes (produced from coals typically burnt in U.S. power plants) using the available data on the fundamental optical properties of coal slags (Goodwin, 1986; Ebert, 1993). To this end, the work can be viewed as consisting of two distinct, yet related, parts.

1. The first objective is to characterize six representative ashes for their optical properties using standard microanalytical techniques. Such characterization may be broadly divided into two categories, physical and chemical. The former includes measurement of ash size and density distributions, and estimation of the fraction of ash containing trapped gas 'bubbles'. Chemical characterization involves not only the determination of the bulk composition of ashes in terms of the major component oxides, but also developing semi-quantitative methods to express the strong inter-particle variation in composition.

2. The second objective is to design and carry out an experimental test of the basic thesis that one can calculate the optical-radiative properties of an adequately characterized ash from Mie theory and knowledge of $m(\lambda, T, C)$. Although a test would be made most realistically on a hot gaseous dispersion, it would be extremely difficult in practice to obtain meaningful data. There are several problems, such as those related to gaseous emission, the near-impossibility of deagglomerating fly ash into a gaseous dispersion, and scattering of radiation emitted by particles into the detection path. Instead, extinction measurements (in the wavelength range 1–13 μm*) are made on the same ash samples dispersed in liquids§ at ambient temperature, and compared with predictions from the Mie calculations. The liquid medium facilitates proper ash deagglomeration, and a static cell is used to achieve a steady signal (i.e., the ash loading changes by only a very small amount over the time period taken to scan the full wavelength range).

*This wavelength range covers over 92% of the radiant energy emitted by a blackbody at 2000 K.

§Since no single liquid is transparent over such a wide spectral span, three different liquids are used over separate ranges.

This dissertation is organized into several chapters as outlined below.

- **Chapter 2:** A brief background to electromagnetic theory, including the classical oscillator model for optical constants, is presented. The results of Mie theory, and its application to polydispersions, are discussed. Since fly ash is mostly glassy, a brief outline of the structure of glass is included.

- **Chapter 3:** This chapter details the methods and results of physical characterization of the ashes, including optical and scanning electron microscopic studies, size distribution measurements, and density classification.

- **Chapter 4:** The chemical composition of individual ash particles were determined using computer controlled scanning electron microscopy, and associated energy dispersive X-ray spectroscopy (CCSEM/EDS). Bulk composition of the ashes were obtained by electron microprobe analysis of slag samples prepared by melting the ashes. These results are used to construct composition classes that allow for ash heterogeneity, and to determine the distribution of iron in the ash.

- **Chapter 5:** This chapter details a number of preliminary studies related to the extinction measurements. The spectral refractive indices of $CHBr_3$ and CS_2, used to disperse the ash, were measured using the near-normal reflectance method. Sensitivity analyses for the measured extinction are also presented in this chapter.

- **Chapter 6:** The results of extinction measurements on four ashes are presented. Comparisons are made with Mie scattering calculations based on the characterization information, and the correlations of Goodwin (1986) and Ebert (1993) of $m(\lambda, T, C)$ of slags — taking account of the presence of bubbles in ash particles and ash heterogeneity.

- **Chapter 7:** This final chapter summarizes the conclusions resulting from this research, and makes some recommendations for future investigations in this area.

The appendices detail several topics relevant to the main text. Parts of this dissertation have already been published (Ghosal and Self, 1993a, 1993b, 1993c; Ghosal, Ebert, and Self, 1993a, 1993b).

1.4 Ashes Acquired for Study

Taken together, the samples of six fly ashes obtained represent the range of coals typically burnt in U.S. pulverized coal-fired power plants. These coals are Illinois #6, Kentucky #9, Upper Freeport, PA, (all three bituminous), Beulah, ND, and San Miguel, TX (both lignites), and Eagle Butte, WY (sub-bituminous). They were among a group of seven coals chosen by Foster Wheeler, Inc. as part of a larger project to study the transformation of mineral matter in coal combustion systems. Ash from the seventh coal, Kentucky #11, was not available. The coals were selected to provide the following mineral properties (PSI, 1990).

- A range of pyrite size distribution, as well as occurrence in association with carbonaceous and mineral components.
- A range of calcium levels, present as carbonates, and in an organically bound state.
- Very high or very low levels of illite.
- Sodium present in different mineral forms and in different concentrations.
- Moderate to high levels of quartz.
- Varying slagging and fouling characteristics.

Since ash formation from these coals was extensively studied in the above project, they were a logical choice for our study.

The three bituminous ashes, and the Beulah ash, were generated in Foster-Wheeler's pilot-scale combustor, fitted with a cyclone collector followed by a baghouse. The ashes could not be reconstituted due to unavailability of information on the relative proportions of the baghouse and cyclone ashes. While only the baghouse ashes have been fully characterized, information on the size and density distribution were also obtained for the cyclone ashes.

The San Miguel ash was obtained from a full-scale power plant's electrostatic precipitator. The Eagle Butte ash was collected in the baghouse of a power plant. In the summary of Table 1.1, the listed power plants are examples of those plants that primarily fire each of the coal types separately. In many power plants, mixtures of pulverized coals from different mines are burnt, and it is not so easy to extract useful information from the resulting ash.

Table 1.1: Summary of information on the fly ashes obtained for study.

Fly ash	Coal type	Obtained from	Fired at	Collection
Kentucky #9	Bituminous	Retiki Mine Henderson County Waverly, Kentucky	Big Rivers Rue 2 Electric Coop. K. C. Coleman Plant Hawesville, Kentucky	Cyclone, Baghouse
Illinois #6	Bituminous	Freedman United Crown Mine 2 Veriden, Illinois	Labadie Station	Cyclone, Baghouse
Upper Freeport	Bituminous	Helena Mine Penn. Elec. Power Homer City, PA.	Homer City Power Stn. Penn. Elec. Power Homer City, PA.	Baghouse
Eagle Butte	Sub-bituminous	AMAX Coal Co. Wyoming	Pawnee Station Colorado Public Service Brush, Colorado	Baghouse
Beulah	Lignite	Knife River Coal Co. Bismarck, ND	Basin Electric	Cyclone, Baghouse
San Miguel	Lignite	San Miguel Texas	San Miguel Elec. Coop. Jourdanton, Texas	Electrostatic Precipitator

Analyses of four of the six coals were provided by Foster Wheeler and AMAX. Data for the remaining two (Beulah and San Miguel), obtained from Bryers's report in PSI (1990), may be less accurate since the coal may have been obtained from a different mine[¶]. The composition of the coals are given in Table 1.2.

The large variation in the ash content of the coals, (from <5% to an unusually high of 40% in the Texas lignite coal, by mass) will clearly be the single most important factor in determining the role of the ash, from a given coal, in radiative transfer. The ash content, together with combustor temperature and pressure, is used to determine the volumetric ash loading needed for radiative transfer calculations. The results of ash analyses, made available by PSI, Inc. and AMAX Co., are used later for comparison with our data.

[¶]Fuel analyses of coals obtained from different seams of the same mine may show differences. Bryers presents comparison of the analyses of seven coals by five different research groups which show some compositional variations from group to group (PSI, 1990). Since all five samples for each coal was prepared from the same shipment (blended and pulverized at Foster Wheeler), the difference probably indicates sampling limitations, and the precision limits of the standard ASTM analysis technique.

Table 1.2: Summary of fuel analyses of coals corresponding to fly ashes obtained for study. All percentages are in terms of weight (Bryers, 1987).

Description	KY #9	IL #6	UF	EB	Beulah	SM
Proximate Analysis						
Fixed Carbon	38.99	41.54	52.58	31.16	30.91	14.01
Volatile Matter	29.93	36.93	20.64	32.78	29.28	25.34
Ash	18.41	9.36	23.58	4.89	9.65	40.40
Moisture	12.67	12.17	3.20	31.17	30.16	20.25
Ultimate Analysis						
Carbon	58.21	61.36	62.54	47.29	41.30	23.15
Hydrogen	3.83	4.32	4.22	3.66	2.92	2.84
Oxygen	1.55	7.83	2.80	12.02	13.84	11.84
Nitrogen	1.04	1.17	0.70	0.61	0.82	0.44
Sulfur	4.24	3.79	2.96	0.36	1.31	1.34
Ash	18.41	9.36	23.58	4.89	9.65	40.40
Moisture	12.67	12.17	3.20	31.17	30.16	20.25
Higher Heating	9,883	10,927	11,080	8,205	6,942	4,060
Value (Btu/lb)						
Forms of Sulfur						
Sulfitic	0.0	0.0	0.0	–	0.0	0.00
Pyritic	2.28	1.15	1.97	–	1.07	0.27
Organic	1.96	2.64	0.99	–	0.24	1.07

Chapter 2

Theoretical Background

2.1 Introduction

This Chapter summarizes the theory related to this dissertation as stated in Chapter 1. The basic treatment of electromagnetic wave propagation can be found in any standard text (e.g., Jackson, 1975). While there are many hundreds of papers and several books on the problem of light scattering and absorption by small particles, we follow the treatment of Bohren and Huffman (1983). Further discussion of the application of Mie theory to absorption and scattering by fly ash can be found in Ebert (1993) and Goodwin (1986).

The Chapter includes an overview of Maxwell's equations, Mie solutions, the oscillator model for optical constants, and the equation of radiative transfer. Additionally, there is a discussion of light extinction by polydispersions suspended either in vacuum (air) or in a liquid. A description of the near-normal reflectance measurement technique, used to determine the refractive indices of $CHBr_3$ and CS_2 liquids, is included, together with a summary of the Kramers-Kronig technique employed in reducing the reflectance data. Since fly ash is predominantly glassy, a brief introduction to the structure of glass is also included.

2.2 Electromagnetic Theory and Maxwell's Equations

For linear, time-harmonic ($\propto \exp i\omega t$) electrical and magnetic fields, Maxwell's equations for propagation of radiation through matter containing no net charge take the following

form.

$$\nabla \cdot (\epsilon \mathbf{E_c}) = 0$$

$$\nabla \times \mathbf{E_c} = \mathrm{i}\omega\mu \mathbf{H_c}$$

$$\nabla \cdot (\mu \mathbf{H_c}) = 0$$

$$\nabla \times \mathbf{H_c} = -\mathrm{i}\omega\epsilon \mathbf{E_c}$$

Here, $\mathbf{E}_c$ and $\mathbf{H}_c$ are complex representation of the real electric and magnetic field vectors $\mathbf{E}$ and $\mathbf{H}$. The permeability, $\mu(\omega)$, and the permittivity, $\epsilon(\omega)$, completely characterize the electromagnetic properties of the medium at angular frequency, ω.

For non-magnetic substances, $\mu(\omega) = \mu_o$, the permeability of free space. The permittivity is determined by the bound charges through the susceptibility, $\chi(\omega)$, and by the free charges through the conductivity, $\sigma(\omega)$.

$$\epsilon(\omega) = \epsilon_o(1 + \chi(\omega)) + \mathrm{i}\,\frac{\sigma(\omega)}{\omega}$$

However, the individual contributions by the bound and free charges cannot be distinguished, and is not relevant since only ϵ appears in Maxwell's equations. For good dielectrics (insulators) such as fly ash, the contribution by free charges is negligible.

Maxwell's equations for waves propagating in an infinite, homogeneous, and isotropic medium have a solution in the form of transverse plane waves, where the electric and magnetic fields are respectively given by

$$\mathbf{E_c}(\mathbf{x},\omega) = \mathbf{E_o} \exp(\mathrm{i}\,\mathbf{K}\cdot\mathbf{x} - \mathrm{i}\,\omega t)$$

$$\mathbf{H_c}(\mathbf{x},\omega) = \mathbf{H_o} \exp(\mathrm{i}\,\mathbf{K}\cdot\mathbf{x} - \mathrm{i}\,\omega t)$$

The wave vector, $\mathbf{K}$, must satisfy the dispersion relation

$$\mathbf{K}\cdot\mathbf{K} = \omega^2\epsilon\mu = \left(\frac{\omega m}{c_o}\right)^2$$

Here, c_o is the speed of light in vacuum and m is the complex refractive index of the medium given by

$$m = n + \mathrm{i}\,k = c_o\sqrt{\epsilon\mu}$$

The real part, n, is the ratio of the phase velocity of the wave in vacuum to that in the medium, i.e., $n = c_o/c$. The imaginary part, k, is responsible for attenuation of the wave

as it propagates through the medium, and is related to the absorption coefficient, α, at wavelength λ, as shown below.

$$\alpha = \frac{4\pi k}{\lambda}$$

It is stressed here that m and λ are determined *relative* to the medium, e.g., for an ash particle suspended in a liquid, the relevant quantities are: $n_r = n/n_l$, $k_r = k/n_l$, and $\lambda_r = \lambda/n_l$. Here, n, k, and λ are quantities measured in vacuum, and n_l is the refractive index of the liquid. While the discussion in this section is restricted to measurements in vacuum, the importance of relative properties is described in a later section.

For a non-magnetic medium, $m(\omega)$ completely characterizes its interaction with radiation, and its components, $n(\omega)$ and $k(\omega)$, are known as its optical 'constants' (although they maybe strong functions of the frequency, ω). The optical properties are material properties (i.e., independent of geometry of the medium) and depend only on the composition of the medium and its temperature.

2.3 The Oscillator Model and Correlation Formulae for Optical Constants

In this section we briefly discuss the dispersion relations used to express the visible and near-infrared optical constants of dielectric materials. The following presentation should be supplemented by more detailed treatments given by Goodwin (1986), and Ebert (1993), especially for the temperature dependence; this discussion is restricted to room temperature optical properties. For convenience, the spectral dependence of most terms are not shown explicitly.

The behaviour of n and k of a dielectric over wavelength ranges that include strong absorption bands can be modeled accurately using the analogy between the complex permittivity of the material and the response of a damped harmonic oscillator (Born and Wolf, 1980), giving rise to the classic dispersion profile shown in Figure 2.1. If there are more than one active absorption mechanism (e.g., electronic or vibrational) in the wavelength range of interest, then the spectral permittivity, $\epsilon(\omega)$, can be expressed as a sum of the independent oscillators.

$$\epsilon(\omega) = \epsilon_o[1 + \chi(\omega)] = \epsilon_o \left[1 + \sum_j \frac{\omega_{pj}^2}{\omega_{oj}^2 - \omega^2 - \mathrm{i}\,\gamma_j\,\omega}\right] \tag{2.1}$$

Here, γ is the damping coefficient, ω_o is the resonance frequency, and ω_p, the plasma

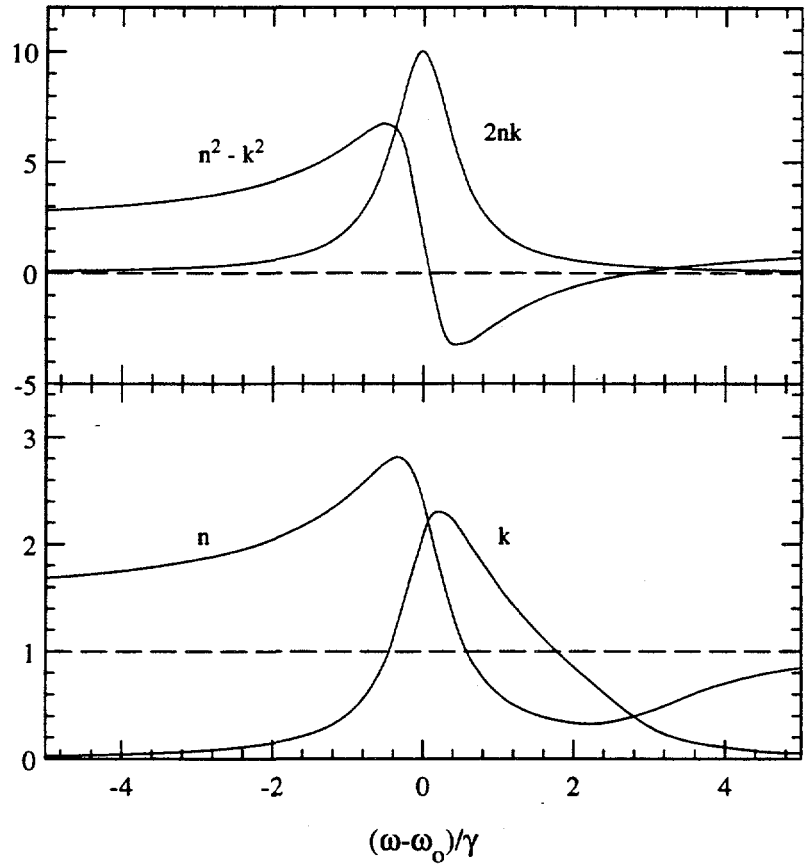

Figure 2.1: The real and imaginary parts of m^2 and m, computed using the damped harmonic oscillator model. The values of the parameters are $n_\infty = 1.5, \omega_p/\omega_o = 1.0$, and $\gamma/\omega_o = 0.1$.

frequency, related to the ionic mass, m_p, and the ion number density, N_p, as

$$\omega_p^2 = \frac{N_p e^2}{m_p \epsilon_o}$$

By substituting $m^2 = c_o^2 \epsilon \mu$, and using a real constant term, n_∞^2, to account for the polarization due to all high-frequency electronic resonances (i.e., in the ultraviolet, for which $\omega_o \gg \omega$), Equation 2.1 takes the following form

$$m^2 = n_\infty^2 + \sum_j \frac{\omega_{pj}^2}{\omega_{oj}^2 - \omega^2 - \mathrm{i}\,\gamma_j\,\omega} \tag{2.2}$$

The oscillators in Equation 2.2 now represent only vibrational resonances. The real and imaginary parts of m^2, i.e., $n^2 - k^2$ and $2nk$ respectively, can be added for multiple resonances, although n and k individually are not additive. If the parameters of the oscillators

are available, then Equation 2.2 can be solved for n and k.

It is noted in Figure 2.1 that n and k are distinctly asymmetrical about $\omega=\omega_o$, with n peaking just before, and k just following, ω_o. The values of the parameters in Figure 2.1) are consistent with the presence of a strong resonance accompanied by appreciable damping. Additionally, it is seen that there is a wavelength range over which the value of n is less than unity. Due to the strong anomalous absorption, n passes through unity twice (the second intersection occurs beyond the upper limit of the abscissa shown in Figure 2.1). At these wavelengths, referred to as Christiansen wavelengths, the reflectance at a dielectric-vacuum interface is minimized.

This simple oscillator model is sufficient for radiative transfer considerations. More accurate quantum mechanical models show the damping coefficient to be a function of frequency (Bendow, 1978). As a result, the classical model, although accurate in the region of the absorption band where n and k are large, overpredicts k in the 'wings', far from the band center.

Three sets of correlations are used to describe the optical constants (n, k) of the ash particle (or slag) in terms of the properties of each of its component oxides over the wavelength range 1–13 μm. Although the correlations are not totally independent of each other (a strong absorption band will affect n at shorter wavelengths), the separate models are adequate for engineering purposes.

1. In the range $1 \leq \lambda < 8$ μm, n is modeled using a single harmonic oscillator.
2. For $\lambda < 4$ μm, the imaginary part (or the absorption index) is correlated to the iron content.
3. In the wavelength range $8 \leq \lambda \leq 13$ μm, where the vibrational absorption bands of SiO_2 dominate, three-oscillator models are used to correlate the complex relative permittivity, $\epsilon = m^2$ to the wavelength and composition.

The actual correlations used are described in the following sections.

2.3.1 Expression for $n(\lambda)$ for $\lambda < 8$ μm

The real part of the refractive index in this range can be modeled using a single oscillator. After separating the real and imaginary parts of m in Equation 2.2, and replacing the

frequency with the free-space wavelength, one can obtain the following form (Born and Wolf, 1980).

$$n^2 - 1 = C + \frac{B\lambda^2}{\lambda^2 - \lambda_o^2} \tag{2.3}$$

B and C are constant terms representing respectively the longer wavelength absorption band strength and an adjustment for shorter wavelength absorption in the ultra-violet. The term λ_o represents the resonance wavelength. Goodwin (1986) obtained sets values for B, C, and λ_o by least-square fitting Equation 2.3 to his data, $n(\lambda)$ for various slag compositions. The value of λ_o is in the range 9.8–10.3 μm, illustrating the influence of the vibrational absorption bands of SiO_2 in the range 9–11 μm. The value of C is correlated to iron content but not to its valence state*.

In the wavelength range $1 \leq \lambda < 8$ μm, the value of n is much larger than k. For this reason, k is neglected in developing a mixture rule for n. The basis of the mixture rule is the assumption that the polarizabilities of individual molecules are not significantly altered when present in a mixture where the bond structure *within* the molecule is not changed (as in the case of glass). The Lorentz–Lorenz formula shown below which relates the refractive index, a material quantity, to the atomic (or molecular) density, N_p, is used in developing the mixture rule (see Born and Wolf, 1980).

$$p = \frac{3}{4\pi N_p} \frac{n^2 - 1}{n^2 + 2}$$

Here p is the mean polarizability per molecule, i.e., the mean polarization induced by an electric field of unit strength, averaged over all directions. Approximating the average polarizability of a mixture by the sum of the polarizabilities of L individual constituents, one obtains

$$\frac{n^2 - 1}{n^2 + 2} \simeq \rho \sum_{i=1}^{L} \left[\left(\frac{X_{m,i}}{\rho_i} \right) \frac{n_i^2 - 1}{n_i^2 + 2} \right] \tag{2.4}$$

Here, ρ is the mixture density, while $\rho_i, X_{m,i}$, and n_i are the density, mass fraction, and the refractive index of each component, respectively.

Equations 2.3 and 2.4 are used to obtain a final mixture rule of the following form for L different oxides

$$\frac{n^2 - 1}{n^2 + 2} \simeq \rho \sum_{i=1}^{L} \left(\frac{\text{wt.\% of } i}{100} \right) F_i(\lambda)$$

*Iron absorbs strongly in the ultraviolet and at visible wavelengths. For this reason, slag wafers that are one mm thick and contain as little 1–2% Fe_2O_3 are virtually opaque to the eye.

Table 2.1: Mixture rule parameters for six oxides present in fly ashes.

Oxide	a	b	c	d
SiO_2	0.9389	53.00	5.001	420.0
Al_2O_3	1.914	174.0	10.36	1633.8
Fe_2O_3	1.647	0.00	11.36	0.00
CaO	4.250	827.7	16.63	6102.3
MgO	1.278	136.9	7.433	1200.9
TiO_2	2.720	260.0	15.80	1954.4

where ρ is the density in g/cc and $F_i(\lambda)$ has the following functional form (λ in μm)

$$F_i(\lambda) = \frac{a_i\lambda^2 - b_i}{c_i\lambda^2 - d_i}$$

Goodwin (1986) obtained values for the parameters a_i, b_i, c_i, and d_i for six oxides[†] (see Table 2.1) by fitting his data measured at room temperature on synthetic slags. For refractive indices of pure oxides, he used literature values. Ebert (1993) has presented values of the parameters at temperatures relevant to combustor conditions.

For his synthetic slags (composed of the four abundant oxides, SiO_2, Al_2O_3, Fe_2O_3 and CaO, with an approximately constant SiO_2/Al_2O_3 mass ratio of 2:1), Goodwin (1986) correlated the densities with Fe_2O_3 content. However, that correlation does not predict the densities of 'natural' slags (made by melting fly ash) because of significant changes in the glass structure caused by large variations in Si/Al and Si/Ca ratios, and by the presence of several other oxides. Empirical methods for determining the densities of slags (of stated compositions) with considerable accuracy are given in Chapter 4.

Finally, Figure 2.2 shows a range of values of $n(\lambda)$ measured by Goodwin (1986), and the corresponding least-square fits. The refractive index increases with iron oxide content (from $\approx$0% Fe_2O_3 in SA00 to $\approx$20% Fe_2O_3 in SB20) because of the high density of Fe_2O_3(5.24 g/cc).

[†]Four of the six oxides, SiO_2, Al_2O_3, Fe_2O_3, and CaO, are the most abundant in slags. The other two oxides TiO_2 and MgO are present in relatively smaller quantities. Infrared optical constants of three other oxides typically present in fly ash, Na_2O, K_2O, and BaO were not available.

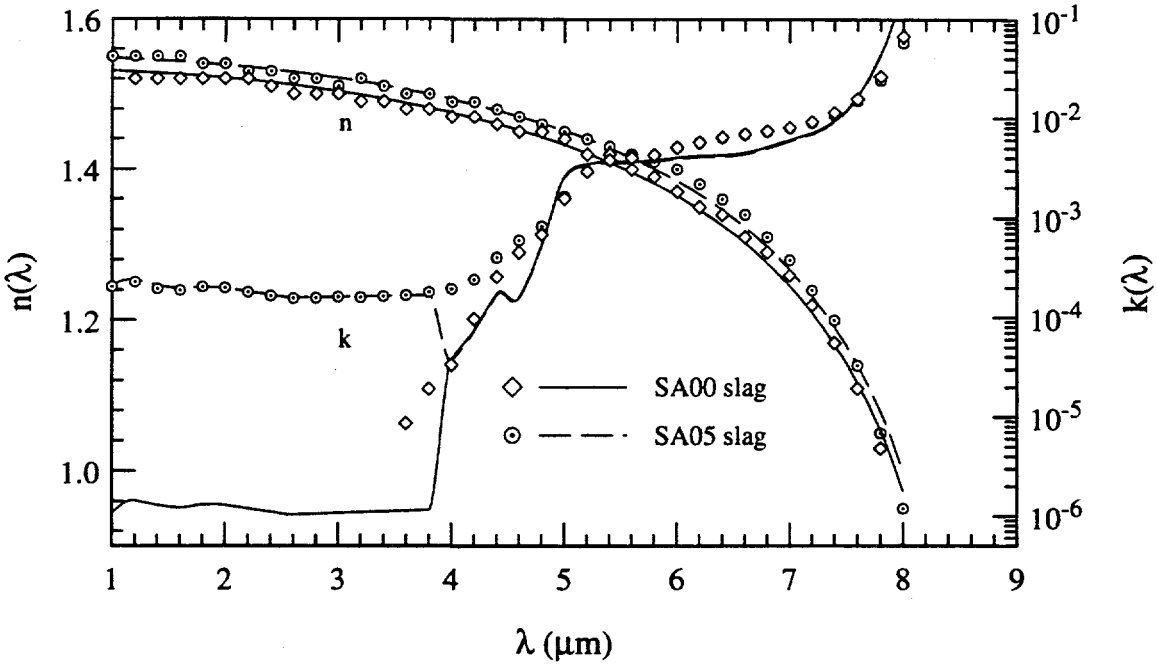

Figure 2.2: Near-infrared wavelength dependence of n and k of synthetic slags SA00 (no Fe_2O_3) and SA05 ($\approx$5% Fe_2O_3) showing the measured data and correlation fits (Goodwin, 1986).

2.3.2 Expression for $k(\lambda)$ for $\lambda < 4\ \mu m$

The major absorber in this range is iron, the two absorption mechanisms being the ligand absorption bands of Fe^{2+} with the primary peak at 1.1 μm, and the strong band, centered in the visible, which results from intervalence charge transfer (ICT) between Fe^{2+} and Fe^{3+} when the two ions are sufficiently close that their electronic wavefunctions overlap (see Bates, 1962, and Goodwin, 1986). Figure 2.2 shows that k increases by orders of magnitude as the Fe_2O_3 content is increased. Any absorption in this wavelength range in the iron-free slag (SA00) is due to minute amounts of impurities of transitional elements.

Goodwin (1986) presented correlations that accurately predict $k(\lambda)$ at room temperature. However, in order to use them, it necessary to know the Fe^{2+}/Fe^{3+} ratio in addition to the Fe_2O_3 content. Goodwin's (1986) Mossbaüer measurements on synthetic slags prepared in environments of varying oxidizing/reducing conditions, showed a ferrous/ferric range of $0.58 \leq (Fe^{2+}/Fe^{3+}) \leq 1.0$. Vorres (1979) suggested a representative value of 0.8. In principle, one can use Mossbaüer analysis of small samples of ash to determine an average value of

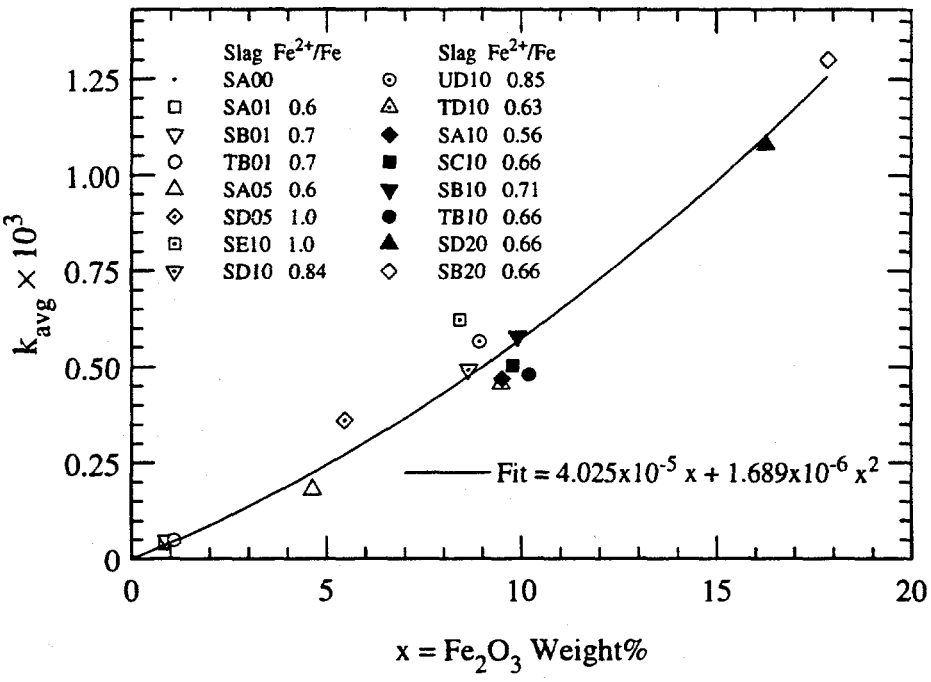

Figure 2.3: Average value of the absorption index, k_{avg}, plotted as a function of Fe_2O_3 mass percentage for several slags at room temperature (Ebert, 1993).

the ratio, since the latter probably varies from particle-to-particle. In fact, Ramsden and Shibaoka (1982), in their optical microscopic study of individual fly ash particles, observed that the ferrous and ferric oxides tend to intimately intergrow in the same particle. It is possible that some of the ferrous iron is oxidized to ferric under cooler and/or oxidizing conditions. It appears that the Fe^{2+}/Fe^{3+} ratio of an ash particle depends on combustor operating conditions (i.e., oxidizing or reducing atmosphere) and the time-temperature history of the ash.

Because of these uncertainties and the fact that fly ash is a relatively poor emitter in this wavelength range (compared to water vapor, carbon dioxide, char and soot) Ebert (1993) has proposed two simplifications to the model. First, it is sufficient to use a fixed Fe^{2+}/Fe^{3+} ratio (e.g., 0.8). Second, he recommends the use of a single wavelength-independent value of k that is correlated with the Fe_2O_3 content (Figure 2.3). The following quadratic function correlates the average value of k to the mass percentage of Fe_2O_3, $x\%$, quite well.

$$k_{avg} = 4.025 \times 10^{-5}\, x + 1.689 \times 10^{-6}\, x^2$$

2.3.3 Absorption Index, $k(\lambda)$, for 5 $\mu m < \lambda <$ 8 μm

In this wavelength range, the k spectrum exhibits a broad plateau independent of the iron content with $k \simeq 10^{-2}$. The positive slope of $k(\lambda)$ increases with SiO_2 content, and its behaviour in this wavelength range is described well by the two–phonon model (Ebert, 1993; Goodwin, 1986).

2.3.4 Optical Constants for 8 $\mu m < \lambda <$ 13 μm

The dominant vibrational absorption band in this range is the broad *Reststrahlen* region of SiO_2 with three absorption peaks[‡]. The first peak at $\approx$9.4 μm represents the stretching vibration[§] of Si–O in the Si–O–Si bond. The oxygen atom is said to 'bridge' the Si atoms in two separate tetrahedra. The second peak at $\approx$10.4 μm increases in strength with increasing Fe_2O_3 content and is associated with the vibration of the $Si–O^-$ bond involving the non-bridging oxygen. The final peak at 13 μm may be due to the occurrence of ring groups and is considerably weaker than the first two (Simon, 1960). Only the first and third bands are seen in fused silica due to the absence of non-bridging oxygen[¶]. The location and strength of these bands are further discussed in Section 2.8 on the structure of glassy fly ash.

Goodwin fitted a three-oscillator model (corresponding to the three absorption peaks) to the experimental data for n and k in the wavelength range 8 $\mu m \leq \lambda <$13 μm (see Equation 2.1). Sets of parameter values for various slags are available in Goodwin (1986) and are not reproduced here. Figure 2.4 shows the refractive and absorption indices, of SA05 slag (SiO_2=53.53%, Al_2O_3=26.32%, Fe_2O_3=4.65%, and CaO=15.5%) obtained by Goodwin (1986). Both the experimental data and the fit are shown.

Since optical properties of molten slags are given separately by Ebert in the concurrent study (Ebert, 1993), the high temperature data (including comparisons with room temperature properties) are not repeated here. However, they are used in predicting extinctions by dispersed ashes in Chapter 6. In summary, we note that given the composition distribution and temperature of an ash, it is possible to obtain the distributions of $n(\lambda)$ and $k(\lambda)$ using the data base made available from the work of Goodwin (1986) and Ebert (1993).

[‡]The absorption bands of the other predominant oxides are located well away from the wavelength range of interest. The peaks are centered at $\approx$15.7 μm (Al_2O_3), 33.9 μm (CaO), and 24.9 μm (MgO) (Goodwin, 1986).

[§]The vibrational bands of interest here are the bond 'stretching' modes; the 'bending' modes being weak and located farther in the infrared.

[¶]In Section 2.8, it is explained how CaO in the synthetic slags produces non-bridging oxygen atoms.

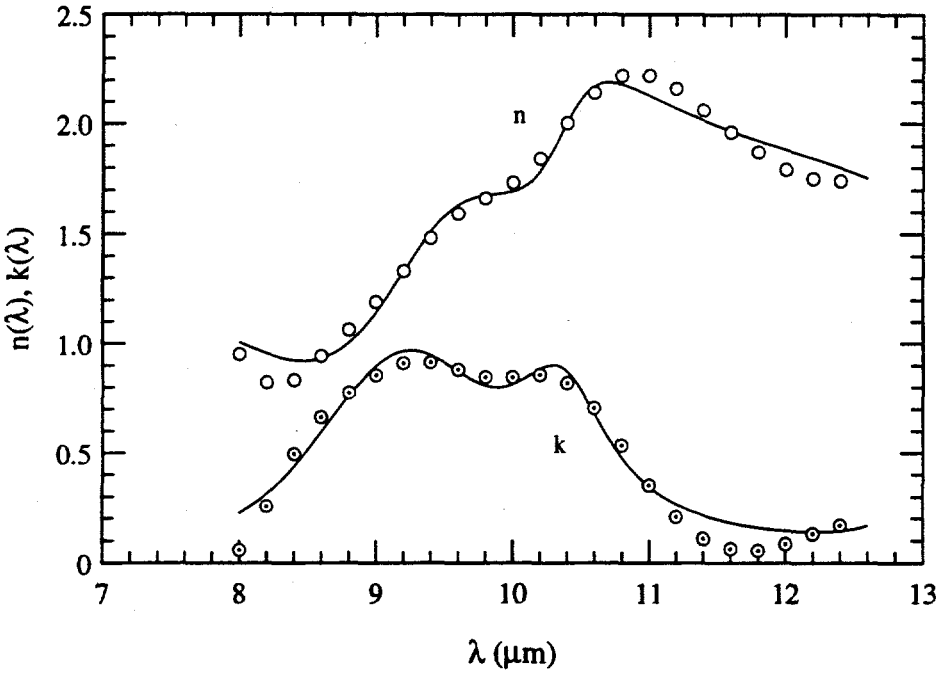

Figure 2.4: The real and imaginary parts of the refractive index of SA05 slag at room temperature (Goodwin, 1986). The solid lines represent the three-oscillator fit.

2.4 Mie Solution to Maxwell's Equations

As stated earlier, because ash particles are formed by the rapid cooling of molten mineral matter, they are predominantly spherical and homogeneous. Additionally, because of their glassy nature, they are isotropic and insulating (dielectric).

While the solution of Maxwell's equations for an infinite medium is straightforward, the solution for a sphere is mathematically complex. In 1908, Mie and Lorenz independently solved the problem of the interaction of a plane-polarized, monochromatic wave with a homogeneous, isotropic, dielectric sphere as a boundary value problem. The absorption and scattering characteristics are expressed in terms of cross-sections that can be computed given the complex refractive index of the particle[‖] and the size parameter, $x(\equiv \pi D/\lambda)$. The absorption efficiency, $Q_{a,\lambda}$, and the scattering efficiency, $Q_{s,\lambda}$, of a single particle are defined as the ratio of the power that is absorbed or scattered, respectively, to the power

[‖]As stated earlier, the refractive index, in general must be specified *relative* to the surrounding medium, $\bar{m}(= m/n_{medium})$ (which is taken as vacuum in this discussion). The case of ash suspended in a liquid is dealt with in Section 2.6. It is also clear that the solutions are dependent on the temperature through m, the latter being a function of wavelength, chemical composition *and* temperature.

incident on the cross-sectional area of the particle**. The extinction efficiency, $Q_{e,\lambda}$, is the sum of $Q_{a,\lambda}$ and $Q_{s,\lambda}$.

$$Q_{e,\lambda} = Q_{a,\lambda} + Q_{s,\lambda}$$

The extinction and scattering efficiencies are expressed in terms of the following infinite series (Bohren and Huffman, 1983).

$$Q_{e,\lambda} = \frac{2}{x^2}\sum_{n=1}^{\infty}(2n+1)\,\mathrm{Re}(a_n + b_n)$$

$$Q_{s,\lambda} = \frac{2}{x^2}\sum_{n=1}^{\infty}(2n+1)(|\,a_n\,|^2 + |\,b_n\,|^2)$$

The complex Mie coefficients (or amplitudes) a_n and b_n are functions of (x, m) and are expressed in terms of the Ricatti-Bessel functions $\Psi_n(x)$ and $\xi_n(x)$

$$a_n = \frac{\{d_n(mx)/m + n/x\}\Psi_n(x) - \Psi_{n-1}(x)}{\{d_n(mx)/m + n/x\}\xi_n(x) - \xi_{n-1}(x)}$$

$$b_n = \frac{\{m d_n(mx) + n/x\}\Psi_n(x) - \Psi_{n-1}(x)}{\{m d_n(mx) + n/x\}\xi_n(x) - \xi_{n-1}(x)}$$

where the function $d_n(y)$ satisfies the following downward recurrence relations.

$$d_{n-1}(y) = \frac{n}{y} - \frac{1}{d_n(y) + n/y}$$

Both Ricatti-Bessel functions can be computed by the following upward recurrence relation

$$\Psi_{n+1}(x) = \frac{2n+1}{x}\,\Psi_n(x) \;-\; \Psi_{n-1}(x) \tag{2.5}$$

$$\xi_n(x) = \Psi_n(x) - \mathrm{i}\,\chi_n(x) \tag{2.6}$$

The term, $\chi_n(x)$, appearing in the above equation, can also be obtained using the recurrence relation in 2.5. The starting conditions for upward recurrence are given as

$$\Psi_{-1}(x) = \cos x, \qquad \Psi_0(x) = \sin x$$

$$\chi_{-1}(x) = -\sin x, \qquad \chi_0(x) = \cos x$$

The computation of the series has to be terminated after a finite number of terms. Bohren and Huffman (1983) indicate that approximately $x + 4x^{1/3} + 2$ (rounded off to the nearest

**For large size parameters, scattering can be considered as the combined effect of reflection, refraction, and diffraction.

integer) terms are needed for accurate determination of $Q_{e,\lambda}$ and $Q_{s,\lambda}$. A more detailed treatment of the computational procedures (used later for sensitivity analyses in Chapter 5, and comparison with experimental data in Chapter 6) can be found in Ebert (1993).

The phase function, Φ_λ, which describes the angular distribution of the scattered radiation, is expanded in terms of Legendre polynomials.

$$\Phi_\lambda(\mu) = \sum_{k=0}^{\infty} A_k \, P_k(\mu)$$

Here, $\mu \equiv \cos(\theta), \theta$ being the polar angle. Dave (1970) presents a procedure for computing the Legendre coefficients, A_k.

In the last decade, the availability of high-speed computers has made routine Mie scattering calculations practicable. However, the physical interpretations of the results often present greater challenges. Bohren and Huffman (1983) present excellent discussions of several aspects of absorption and scattering problems, stressing the physical/practical implications of the results. Finally, it is noted that efficiencies computed using Mie theory are henceforth simply referred to as Mie calculations.

2.5 Extinction of Electromagnetic Radiation by Polydispersions

As Chapters 3 and 4 will show, fly ash has a broad size distribution, and the composition (and hence, optical properties) varies significantly from particle to particle. Consequently, the Mie calculations must be integrated over the size and refractive index distributions.

For a monodisperse aerosol, scattering can be considered to be independent if the mean separation of the centers of two particles is greater than four times the particle diameter, i.e.,

$$\frac{1}{N^{1/3}} \gtrsim 4D$$

where N=number of particles per unit volume and D=particle diameter. This condition is almost always satisfied, except in certain cases such as fluidized beds and pneumatic conveyance of powders. The scattered waves from adjacent particles then have random phases, and the total scattering from an elementary volume can be obtained by adding the intensities scattered by each particle in the volume. Consider the attenuation of a plane, monochromatic electromagnetic wave of wavelength λ (in vacuum) by a monodisperse

aerosol of particle diameter D and concentration N. The change in intensity (units: W/m^2) of the beam due to extinction (i.e., scattering and absorption) between s and $s + \mathrm{d}s$ is given by

$$\mathrm{d}I_\lambda(s) = -I_\lambda(s)\, K_\lambda\, \mathrm{d}s \tag{2.7}$$

where K_λ, the spectral extinction coefficient (units: m^{-1}), is the sum of the spectral scattering and absorption coefficients of the medium.

$$K_\lambda = \sigma_\lambda + \alpha_\lambda \tag{2.8}$$

Since the particles are spherical, the scattering and absorption coefficients are given by

$$\alpha_\lambda = Q_{a,\lambda}(x, m)\, \pi\, \frac{D^2}{4}\, N \tag{2.9}$$

$$\sigma_\lambda = Q_{s,\lambda}(x, m)\, \pi\, \frac{D^2}{4}\, N \tag{2.10}$$

Here $Q_{a,\lambda}$ and $Q_{s,\lambda}$ are the absorption and scattering efficiencies per particle computed from Mie theory as a function of the size parameter, $x \equiv \pi\, D/\lambda$, and the complex refractive index, $\bar{m} = m/n_{medium}$, of the particle material *relative* to that of the medium (assumed real). The complex refractive index of the material is generally a function of its composition, temperature and the wavelength, i.e., $m \equiv m(C, \lambda, T)$. On integrating Equation 2.7 over the path $s = 0$ to $s = L$, one obtains Bouguer's (or Beer–Lambert's) law:

$$I_\lambda(L) = I_\lambda(0) \exp(-K_\lambda\, L) \tag{2.11}$$

The optical depth or optical thickness, τ_λ, is defined as

$$\tau_\lambda = K_\lambda\, L$$

If $\tau_\lambda \ll 1$, the medium is said to be optically thin or transparent at wavelength λ. Conversely, if $\tau_\lambda \gg 1$, the medium is optically thick or opaque. Bouguer's law is valid for single scattering when $\tau \lesssim 0.2$. When the optical depth is larger, as in atmospheric clouds at visible wavelengths, there is multiple scattering by more than one droplet or particle. In such cases, one must use the equation of radiation transfer (see Section 2.7), and the calculation of extinction is much more complicated.

The spectral transmittance, T_λ, of the monodispersion is defined as

$$T_\lambda = \frac{I_\lambda(L)}{I_\lambda(0)} = \exp(-K_\lambda\, L) = \exp(-\tau_\lambda)$$

and decreases exponentially with increase in the optical depth. The spectral extinction, E_λ, is defined as $E_\lambda = 1 - T_\lambda = 1 - \exp(-K_\lambda L)$.

The foregoing discussion is restricted to monodisperse aerosols of uniform composition. For a heterogeneous polydisperse material such as fly ash, we subdivide it into a number of composition classes (within which the composition, and hence, the complex refractive index of all particles is identical), the properties of the i^{th} class being denoted in subscript. The particle size distribution of the i^{th} class is $f_i(D)$, so that there are $f_i(D)\,\mathrm{d}D$ particles per unit volume with diameters between D and $D + \mathrm{d}D$. The size distribution is normalized so that $\int_0^\infty f_i(D)\,\mathrm{d}D = 1$

In dealing with polydispersions, it is noted that for a fixed value of N, the aerosol loading increases as D^3. Hence, it is meaningful to consider a fixed volumetric loading of aerosol, V_a (or $V_{a,i}$ for the i^{th} composition class), defined as

$$V_{a,i} = \frac{\text{volume of aerosol particles}}{\text{volume of dispersing medium}} = N_i \int_0^\infty \frac{\pi}{6} D^3 f_i(D)\,\mathrm{d}D = \frac{\pi N_i}{6} \langle D^3 \rangle$$

where $\langle D^3 \rangle$ is the third moment of $f_i(D)$ about the diameter, D, over all diameters. For a polydispersion of composition class i, one can obtain, using Equations 2.8, 2.9 and 2.10, a size-integrated extinction coefficient

$$K_{\lambda,i} = N_i \int_0^\infty \frac{\pi}{4} D^2 f_i(D)\, Q_{e,\lambda,i}\,\mathrm{d}D$$

$$= \frac{\pi N_i}{4} \langle D^2 Q_{e,\lambda,i} \rangle$$

Here $\langle D^2 Q_{e,\lambda,i} \rangle$ is the extinction coefficient weighted by particle area:

$$\langle D^2 Q_{e,\lambda,i} \rangle = \int_0^\infty D^2 f_i(D)\, Q_{e,\lambda,i}\,\mathrm{d}D$$

In terms of $V_{a,i}$

$$K_{\lambda,i} = \frac{3}{2} \frac{V_{a,i} \langle D^2 Q_{e,\lambda,i} \rangle}{\langle D^3 \rangle}$$

By defining a mean extinction efficiency for the i^{th} composition class

$$\bar{Q}_{e,\lambda,i} = \frac{\langle D^2 Q_{e,\lambda,i} \rangle}{\langle D^2 \rangle}$$

the final form of the extinction coefficient is obtained as

$$K_{\lambda,i} = \frac{3}{2} \frac{V_{a,i}}{D_{32,i}} \bar{Q}_{e,\lambda,i} \tag{2.12}$$

where $D_{32,i} = \langle D^3 \rangle / \langle D^2 \rangle$ is the Sauter mean diameter*, of the polydispersion of the i^{th} composition class. This $K_{\lambda,i}$ used in Bouguer's law yields the extinction of radiation of a single wavelength, λ, by all particles in a specified composition class.

Similarly, the two components of the extinction coefficient are given by

$$\alpha_{\lambda,i} = \frac{3}{2} \frac{V_{a,i}}{D_{32,i}} \bar{Q}_{a,\lambda,i} \qquad \sigma_{\lambda,i} = \frac{3}{2} \frac{V_{a,i}}{D_{32,i}} \bar{Q}_{s,\lambda,i}$$

The phase function of a polydispersion, averaged over polarizations, is given by

$$\bar{\Phi} = \frac{1}{\bar{Q}_{s,\lambda,i}} \frac{\langle D^2 Q_{s,\lambda,i} \Phi_{\lambda,i}(D) \rangle}{\langle D^2 \rangle}$$

Finally, the extinction coefficient of the heterogeneous polydispersion is calculated by summing over all p composition classes

$$K_\lambda = \sum_{i=1}^{p} K_{\lambda,i} = \frac{3}{2} \sum_{i=1}^{p} \frac{V_{a,i}}{D_{32,i}} \bar{Q}_{e,\lambda,i}$$

2.6 Extinction by a Particle Suspended in a Liquid

For an electromagnetic wave propagating in a lossless medium of refractive index n with velocity c

$$n = \frac{c_o}{c} = \sqrt{\frac{\epsilon \mu}{\epsilon_o \mu_o}} = \frac{\lambda_o}{\lambda} \; (> 1, \text{ for ordinary materials})$$

where the subscript o is used in this section to refer to vacuum (and is not to be confused with resonant absorption described in Section 2.3). For an aerosol the relevant wavelength is λ_{air}. However, at STP, $n_{air} \simeq 1.0003$ in the visible and near-infrared, and so $\lambda_{air} \simeq \lambda_o$. In Mie theory for a general liquid (of complex refractive index $m_l(\lambda_o) = n_l(\lambda_o) + \mathrm{i}\, k_l(\lambda_o)$), the relevant wavelength in the definition of the size parameter, x_r, is $\lambda_r = \lambda_o / n_l(\lambda_o)$ (e.g., $n_l(\lambda_o) \approx 1.4$ for CCl_4). Hence

$$x_r (\equiv \frac{\pi D}{\lambda_r}) > x_o (\equiv \frac{\pi D}{\lambda_o})$$

Here the subscript r denotes a property of the material of the ash particle relative to the dispersing liquid, while the subscript l denotes a property of the liquid relative to vacuum.

*This diameter is the ratio of the third moment of the size distribution function about the diameter, to the second moment, integrated over all diameters.

For the fly ash particle dispersed in liquid, the relative complex refractive index is used in Mie theory and is given by

$$m_r(\lambda_o) = n_r(\lambda_o) + \mathrm{i}\, k_r(\lambda_o) = \frac{n_A(\lambda_o)}{n_l(\lambda_o)} + \mathrm{i}\frac{k_A(\lambda_o)}{n_l(\lambda_o)} \quad (< n_A(\lambda_o) + \mathrm{i}\, k_A(\lambda_o))$$

The subscript A refers to a property of the fly ash material relative to vacuum. Clearly, an accurate knowledge of the spectral refractive index of the liquid, n_l, is needed for extinction calculations. Another point to be noted is that at wavelengths where the ash is non-absorbing, scattering vanishes when n_r is unity (i.e., $n_A = n_l$), and any extinction is solely due to absorption.

The above results are limited to wavelengths away from strong absorption bands of the liquid. If absorption by the liquid (over a path length equal to the particle diameter) is comparable to absorption by the particle, then Mie theory is clearly not applicable. However, for size distributions and wavelengths of interest here, simple calculations show that Mie solutions are valid for weak absorption bands ($k_l \ll 10^{-2}$), (Self, 1990).

2.7 Equation of Radiation Transfer

The absorption and scattering coefficients determined using optical constants data and Mie theory, are used in the equation of radiative transfer for a participating medium. This equation represents the change in the spectral radiance, $\mathrm{d}I_\lambda(s)$, over a path length $\mathrm{d}s$ (Siegel and Howell, 1981). Such scattering is illustrated in Figure 2.5.

$$\frac{\mathrm{d}I_\lambda(s)}{\mathrm{d}s} = \underbrace{-\alpha_\lambda\, I_\lambda(s)}_{\text{Loss by absorption}} + \underbrace{\alpha_\lambda\, I_{b,\lambda}(s)}_{\text{Gain by emission}} - \underbrace{\sigma_\lambda\, I_\lambda(s)}_{\text{Loss by scattering}} + \underbrace{\frac{\sigma_\lambda}{4\pi}\int_{\omega_i=4\pi} I_\lambda(s,\omega_i)\,\Phi_\lambda(\omega,\omega_i)\,\mathrm{d}\omega_i}_{\text{Gain by scattering into s direction}}$$

Here $I_{b,\lambda}$ is the black body radiance at the same temperature and wavelength. The above integro-differential equation can be manipulated to the following integrated form

$$I_\lambda(\tau_\lambda) = \underbrace{I_\lambda(0)\exp(-\tau_\lambda)}_{\text{Bouguer's Law term}} + \underbrace{\int_0^{\tau_\lambda} S(\tau_\lambda^*,\omega)\exp\{-(\tau_\lambda - \tau_\lambda^*)\}\mathrm{d}\tau_\lambda^*}_{\text{Source term}} \qquad (2.13)$$

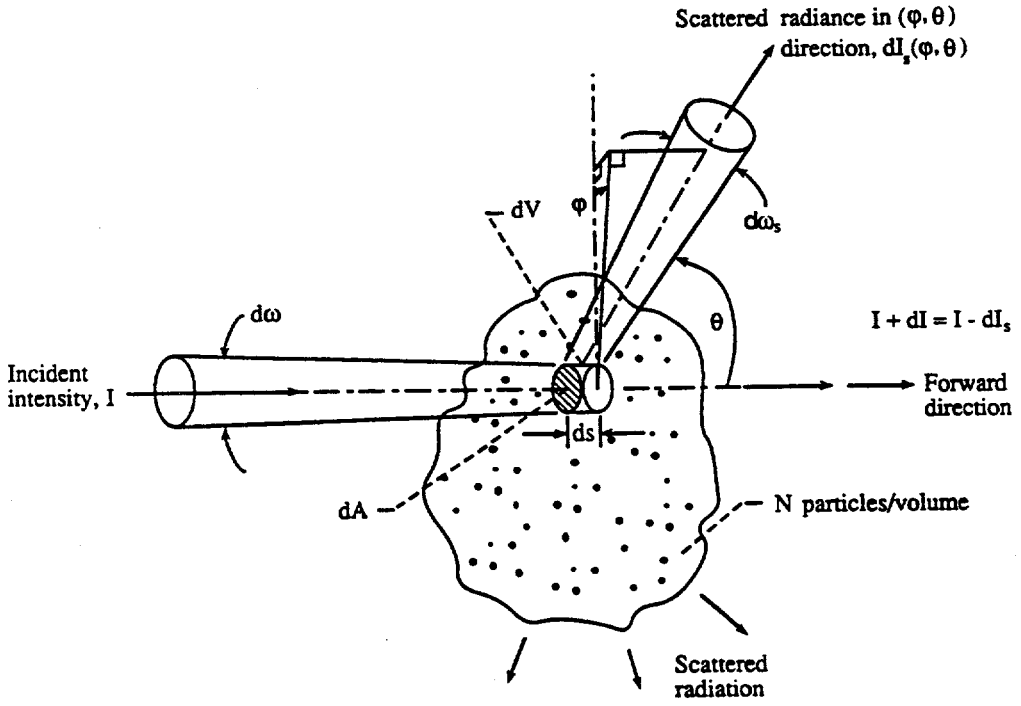

Figure 2.5: Scattering into direction (θ, φ) from incident radiation within solid angle $d\omega_i$ (Siegel and Howell, 1981).

The source term is given by

$$S(\tau_\lambda^*, \omega) = (1 - \Omega_\lambda)\, I(\tau_\lambda, \omega_i) + \frac{\Omega_\lambda}{4\pi} \int_{\omega_i = 4\pi} I(\tau_\lambda, \omega_i)\, \Phi(\lambda, \omega, \omega_i)\, d\omega_i$$

The term, $\Omega(\lambda)$, is called the albedo, and is a measure of the contribution of scattering to extinction.

$$\Omega_\lambda \equiv \frac{\sigma_\lambda}{K_\lambda} \equiv \frac{\sigma_\lambda}{\alpha_\lambda + \sigma_\lambda}$$

The change in radiance in Equation 2.13 is composed of an exponential attenuation term, and a second term which accounts for both radiation emitted by the medium along the path, and that scattered from other directions into the path (both reduced by absorption along the path). At room temperatures (i.e., negligible emission) and for small optical depths ($\tau \lesssim 0.2$), the radiative transfer equation reduces to Bouguer's law (Equation 2.11).

Except for a few simple cases Equation 2.13 has to be solved numerically. Ebert (1993) uses a finite-difference technique called the *discrete ordinates method* to obtain solutions for

simple geometries applicable to coal combustors, for various boundary conditions. Other techniques are discussed at length by Chandrasekhar (1960).

2.8 The Structure of Glassy Fly Ash

The molten minerals that coalesce on the surface of the char particle are entrained as the latter fragments and burns out. As these ash particles leave the flame region where temperatures are ≈2000K, they cool rapidly, dropping in temperature by hundreds of degrees Centigrade over a time scale of a few seconds at most. Such high rates of cooling do not permit crystallization. For comparison, it is noted that critical cooling rates required for industrial glass formation are ≈1K/s.[††] Of course, the cooling rates need to be considerably higher in the presence heterogeneities that provide nucleation sites. Even so, elementary calculations show that the interiors of ash particles with diameters below 10 μm have cooling rates that are a couple of orders above those stated above. At such high quenching rates, the vast majority of the molten ash particles form glasses.

There are many definitions of the glassy state, and at least some glasses have been formed with materials having all types of bondings — ionic, covalent, metallic, etc. Apart from cooling a material from the liquid state, glasses can be formed in other ways, *viz*, condensation from vapor state, pressure quenching, solution hydrolysis, gel formation, anodization, and by bombardment of crystals with high-energy particles (Uhlmann and Yinnon, 1983). The definition of glass adopted here is that glass is a supercooled liquid that has solidified without crystallization. While the general term *amorphous solid* applies to any solid having a non-periodic atomic/molecular array (described below), the term *glass* has conventionally been reserved for an amorphous solid prepared by melt quenching (Zallen, 1983).

The glass formation process is illustrated in Figure 2.6 as change in volume with time (reading from right to left, i.e., as the melt cools). Initially the gas, whose volume is determined by the container, cools to a liquid of fixed volume (but whose shape is determined by the container) at temperature T_b. On further cooling, the volume of the liquid decreases steadily, until the fusion temperature, T_f, is reached. At this point, provided the cooling rate is sufficiently low, the liquid volume contracts abruptly forming a crystal which exhibits long-range order in its atomic arrangement. Other physical properties (e.g., heat capacity, density, thermal and electrical conductivities, dielectric constant, and refractive index) show

[††]0.1 K/s for silica glass and 2.2 K/s for some lunar glasses (Uhlmann and Yinnon, 1983).

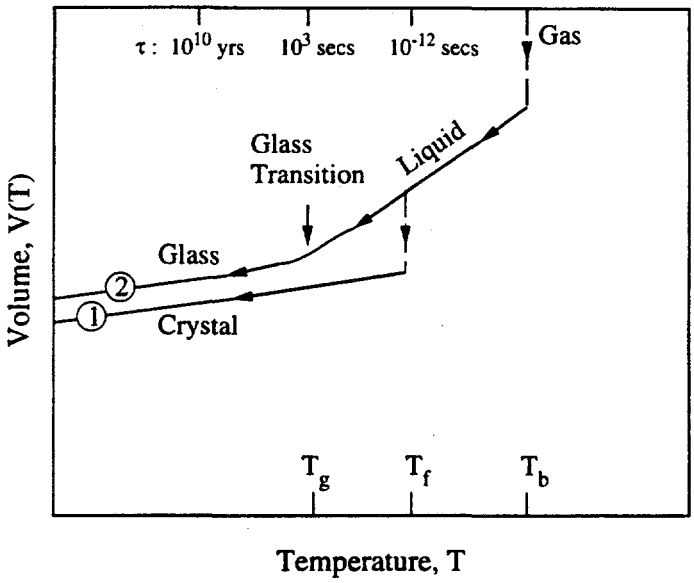

Figure 2.6: The two general cooling paths by which an assembly of atoms can condense into the solid state. Path 1 is the route to the crystalline state; path 2 is the rapid-quench path to the amorphous solid state (Zallen, 1983).

similar discontinuous changes at the point of the liquid→crystal change.

However, when the cooling rate is sufficiently high, most materials follow path 2 after bypassing T_f. The liquid phase persists till a lower, glass transition, temperature, T_g, is reached (T_g is ≈1430 K for SiO_2). The liquid→glass transformation takes place over a narrow temperature *interval* close to T_g. The change in $V(T)$ is continuous, and path 2 bends to take on a smaller slope (i.e., smaller coefficient of thermal expansion) which is characteristic of solids. The primary structural difference between the amorphous and crystalline states is that the former has no long-range order (say, $\gtrsim$ 1000 atomic diameters), the array of equilibrium atomic positions being strongly disordered. While an understanding of short-range (i.e., atomic scale) structures of single or two component glasses have improved significantly in recent years with the emergence of powerful microscopes and spectroscopic techniques, the structure of multi-component glasses such as fly ash is still not clearly understood (Hemmings and Berry, 1988).

The kinetic aspect of glass formation is illustrated by the dependence of T_g on cooling rate. The transition temperature shifts to lower temperatures when the cooling rate is decreased because of the temperature dependence of the molecular relaxation time, τ (Zallen, 1983). The quantity $1/\tau$ represents the rate at which atomic/molecular configuration of the

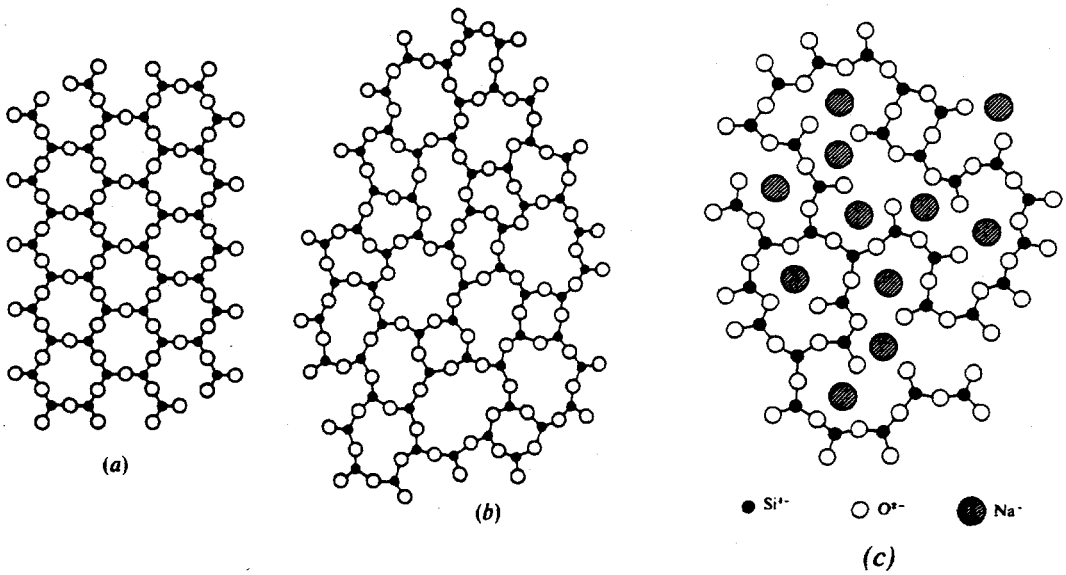

Figure 2.7: Two dimensional schematic of (a) structure of crystalline silica, (b) glassy silica, and (c) a binary (sodium) silicate glass.

condensed system responds to changes in temperature. τ is a very steep function of temperature with a minimum value (typically 10^{-12} seconds) at T_f. As $T \rightarrow T_g, \tau(T)$ becomes comparable to the time scale of measurement (10^3–10^5 seconds). At lower temperatures, τ becomes too large to measure experimentally. The atoms get 'frozen' at equilibrium positions about which they oscillate, corresponding to their configuration at T_g. Such a kinetic model implies that the properties of glass depend, to some extent, on the *rate* of cooling.

Models proposed to describe glass formation can be categorized as structural, thermodynamic, and kinetic (Uhlmann and Yinnon, 1983). These groups are not independent, each often borrowing concepts from the others. The earliest and best-known model for amorphous solids was the structural model of Zachariasen (1932), referred to as the *continuous random network (crn)* model. It is described below for the case of fused silica. More detailed discussions of this model can be found in most books on the amorphous state (e.g., Zarzycki, 1982; Zallen, 1983).

When pure SiO_2 liquid is cooled slowly, it crystallizes to form cristobalite[‡‡] that is stable at room temperatures. Its structure consists of regular repeating unit cells, each

[‡‡]The other two crystalline forms of silica are quartz and tridymite.

silicon atom being associated with four oxygen atoms in a tetrahedral SiO_4. In addition, each oxygen atom is associated with two silicon atoms to form a three dimensional network that possesses long range order. However, in fused/glassy silica formed by rapid quenching, all long range order is lost, resulting in a distorted three dimensional structure (Figure 2.7 attempts to show this disorder in two dimensions). Short range order in the form of similar Si–O relationship persists, i.e., the network is built with the same SiO_4 units joined at the corners, but the mutual orientation of consecutive tetrahedra is random. In addition, there is a spreading of the O–Si–O bond angle.

Structural perturbation or disorder can also be caused by network substitution and by cation modification. Network substitution occurs when a network former such as SiO_2 is melted with other oxides that provide elements with coordination numbers three or four. These elements, such as Al, Fe, Pb, Zn, and Ti, are called *network intermediates* and are capable of replacing Si in the polymeric network of oxygen tetrahedra in association with another cation*. For example, when trivalent Al replaces tetravalent Si in the polymeric network, the excess negative charge has to be neutralized by the inclusion of a cation, M^+.

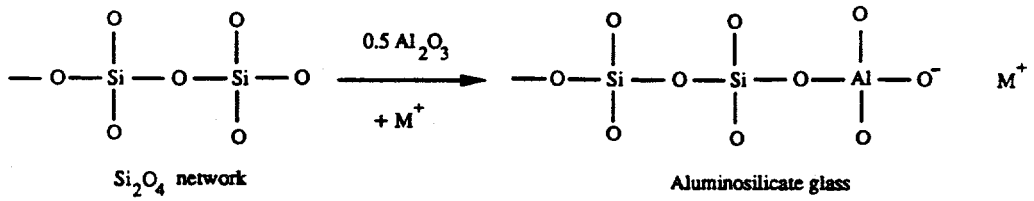

However, the fraction of intermediate cations that do not replace Si may break down the three-dimensional structure in a manner similar to the modifying cations described next. Thus, it can be said that the glass intermediates cause disorder (or entropy increase, from a thermodynamic standpoint) in two ways: by random substitution of Si in the SiO_4 tetrahedra, and by destroying the three-dimensional structure (Hemmings and Berry, 1988).

Cation modification is caused by the addition of alkali and alkaline earth metals (i.e., Na, K, Ca, Mg, Ba) with coordination number > 6. These elements, called *network modifiers*, increases the degree of disorder in the glass. To preserve charge neutrality, the Si–O–Si bond breaks, producing so-called non-bridging oxygen atoms (NBO). The ratio of non-bridging

*The group of oxides that can form glasses are called *glass-formers*, and include SiO_2, GeO_2, B_2O_3, P_2O_5, As_2O_3, etc.

oxygen atoms to glass-forming tetrahedral cations (Si in our case), referred to as NBO/T, is a measure of the degree of polymerization (three-dimensional structure) of the glass. For example, introducing Na_2O in silica glass produces the following structural change.

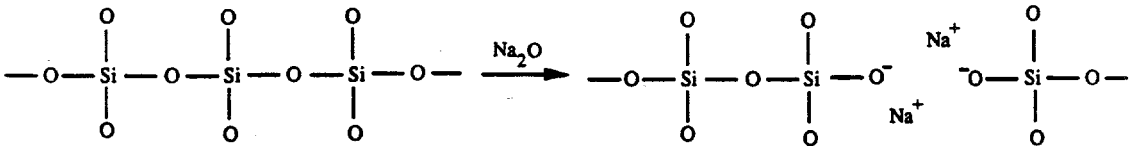

The Na^+ and O^- behave like a dipole in the otherwise predominantly covalently bonded glass (very few of the bonds are purely ionic or purely covalent). The presence of NBO atoms increases with increasing modifier content, expressed as NBO/Si ratio that spans the range zero (as in pure SiO_2 glass) to four (fully depolymerized glass).

It is noted that several glasses (e.g., metallic and chalcogenide glasses) can be made that are exceptions to the Zachariasen rules for glass formation. The model cannot describe the structure of pure aluminosilicate glasses with no cations available for charge balancing. However, the Zachariasen model is intuitive, and is still widely considered to be useful in understanding behaviour and properties of various glasses, especially those with few components. Apart from kinetic and thermodynamic models, there are other, more restrictive, structural models (Zallen, 1983).

The constituent oxides in glassy igneous rocks (e.g., basalt) are similar to those in fly ash because they both originate from mineral matter in the earth's crust. Hence, some idea of the complex multi-component glass structure in the ash can be obtained from studies of glasses of mineralogical interest e.g., Mysen *et al* (1982, 1985) and Seifert *et al* (1982). The authors summarize previous investigations, and present Raman spectra of glasses of various compositions and quenched under different pressure and initial temperature conditions, including those prepared under conditions similar to combustors (atmospheric pressure, $\approx$1900K). Their studies confirm that aluminosilicate glasses, containing Na_2O, CaO, and MgO, consist of interconnected, three-dimensional Si–, (Si, Al)–, and Al– bearing tetrahedra, their relative proportions depending on Si/Al ratio. Hence, the NBO/Si ratio takes on all possible values, although a single value predominates which depends on the composition. The authors suggest a method for calculating a bulk value of NBO/Si to characterize a melt.

The Si–O–Si bond angle distribution, unlike in SiO_2 where it is symmetric, shows a bimodal distribution. Their results appear to confirm that monovalent Na^+ charge-balances Al^{3+}, while the modifiers reduce the three-dimensional nature of the glass as explained earlier.

A relevant question is to what extent the structure of quenched slag represents the actual structure (and hence many of the properties) of high temperature (or molten) ash particles. The study by Sweet and White (1969) suggests that melts do not undergo detectable structural changes when quenched rapidly ($\gtrsim$ 100 K/s) from temperatures above the liquidus. Of course, as the melt temperature is significantly raised ($\gtrsim$ 2000K), there will be significant depolymerization of the original three-dimensional structure, with increasing fractions of sheets, chains, dimers, and monomers (in gaseous phase, all constituent atoms will exist as monomers). For this study, as in most mineralogical studies, we assume that the available information on the structures of quenched melts can be used for ash particles in the combustor.

2.8.1 Effect of Glass Structure on Optical Properties

Certain properties of glass depend mostly on the properties of each atomic species (and, thus, on the mass fractions) rather than on the nature of the bonds connecting them. Examples of such properties, called *additive properties* are density (more on this topic in Chapter 4), and refractivity (the basis of the 'mixture' rule described earlier). These properties (say, Υ) in glasses tend to be relatively close to those of the pure oxides, and can obtained by simple additive methods.

$$\Upsilon_{\mathbf{glass}} = \sum_{i=1}^{L} X_i \Upsilon_i$$

where X_i is the mole (or mass) fraction of the i^{th} of L oxides in the glass. However, for other properties, such as the 'loss' properties (dielectric loss, acoustic loss, etc.) the values are significantly different in glasses compared to those of pure oxides. Similarly, the vibrational absorption bands associated with silica are dependent on the modification of the network structure by other oxides.

The only strong stretch vibration mechanism active in pure fused silica is that of the bridging oxygen Si–O–Si centered at 9 μm. Glass intermediates like Al or Fe replace Si in the tetrahedra when added in small quantities, along with alkali or alkaline earth metal cations for charge neutralization (the latter causing silica bond rupture). However, as stated

earlier, when slags have high intermediate content (say, >20%) these elements cannot replace sufficient Si, and, consequently, act as depolymerizing agents. The formation of Si–O^- bonds is accelerated by the presence of modifier elements. Thus, the decrease of silica in the slag is accompanied by an increase in the strength of the absorption band, centered at $\approx$10.5 μm, resulting from the stretch vibration of the Si–O^- bond.

The location of the absorption peak is also dependent on the glass composition. This dependence is not unexpected, since the force constants of the bonds that determine the frequency are dependent not only on the atoms involved (e.g., the force constant of the bond Si–O–Si is different from that of Al–O–Si), but also on the presence of neighbouring ions. Ebert (1993) provides useful correlations relating peak absorption wavelength with silica percentage in the slag. Finally, it is noted that the absorption mechanisms in the near-infrared, determined by the iron content, result from electronic transitions, and are not directly controlled by the glass structure.

2.9 Measurement of $n(\lambda)$ Using the Near-normal Reflectance Technique

The near-normal reflectance measurement technique refers to the measurement of spectral reflectance of a plane solid or liquid surface using a very small angle of incidence (i.e., almost normal incidence). The measured reflectance, $R(\lambda)$, which is the ratio of the reflected to the incident intensities, is related to $n(\lambda)$ and $k(\lambda)$ of the complex refractive index by the Fresnel formula (Born and Wolf, 1980).

$$R(\lambda) = \frac{\{n(\lambda) - 1\}^2 + k^2(\lambda)}{\{n(\lambda) + 1\}^2 + k^2(\lambda)} \tag{2.14}$$

Away from absorption bands, when $k^2(\lambda) < \{n(\lambda) - 1\}^2$, the $k^2(\lambda)$ term in the above equation can be neglected, and $n(\lambda)$ can be expressed in terms of $R(\lambda)$ as

$$n(\lambda) \simeq \frac{1 + \sqrt{R(\lambda)}}{1 - \sqrt{R(\lambda)}} \tag{2.15}$$

2.9.1 The Kramers-Kronig Technique

In the vicinity of a strong absorption band where $k \geq 0.1$, Equation 2.14 cannot be used to obtain $n(\lambda)$ since $k(\lambda)$ is unknown. However, the Kramers-Kronig relations yield values of both $n(\lambda)$ and $k(\lambda)$ that are accurate, provided one has reflectance data over a

sufficiently wide range of wavelengths (Born and Wolf, 1980). In essence, these relations express the Cauchy conditions between the real and imaginary parts of analytic functions. The Kramers-Kronig integrals relating n and k are given by

$$n(\omega) - 1 = \frac{2}{\pi} P \int_0^\infty \frac{\omega' k(\omega')}{\omega'^2 - \omega^2} \, \mathrm{d}\omega' \tag{2.16}$$

$$k(\omega) = -\frac{2}{\pi} P \int_0^\infty \frac{n(\omega')}{\omega'^2 - \omega^2} \, \mathrm{d}\omega' \tag{2.17}$$

Here ω is the frequency and P denotes the Cauchy principal values of the integrals. Far from absorption bands, these relations yield incorrect values of k, although the values of n obtained are still accurate.

In these forms (Equations 2.16 and 2.17), the relationships are not very useful since neither n and k can be measured directly. Alternate forms can be derived in terms of the reflection coefficient, r, and the phase shift on reflection, θ_R, that are defined *via* $R = |r|^2$ and $r = |r| \exp(\mathrm{i}\,\theta_R)$. Using these terms, the Kramers-Kronig relations can be expressed as (see, e.g., Cardona, 1969)

$$\theta_R(\omega) - \pi = -\frac{\omega}{\pi} P \int_0^\infty \frac{\ln R(\omega')}{\omega'^2 - \omega^2} \, \mathrm{d}\omega' \tag{2.18}$$

Once θ_R is computed, n and k can be obtained using the following relations.

$$n = \frac{1 - R}{1 + R + 2\sqrt{R}\cos\theta_R} \tag{2.19}$$

$$k = \frac{-2\sqrt{R}\sin\theta_R}{1 + R + 2\sqrt{R}\cos\theta_R} \tag{2.20}$$

The integral in Equation 2.18 can be evaluated analytically outside the wavelength range for which one has data by assuming that the reflectivity is constant outside that range. In other words, assume $R(\omega) = R(\omega_a), (\omega \le \omega_a)$, and $R(\omega) = R(\omega_b), (\omega \ge \omega_b)$, where $\omega_a \le \omega \le \omega_b$ is the frequency range of the available reflectance data. By subtracting $\ln R(\omega')/(\omega'^2 - \omega^2)$ from the integrand of Equation 2.18 (which is valid, since $\int_0^\infty 1/(\omega'^2 - \omega^2)\,\mathrm{d}\omega' = 0$), the integration limits become finite, and the integral can easily be computed. The resulting expression for the phase shift is

$$\begin{aligned} \theta_R(\omega) - \pi \;=\; & \frac{\ln(R(\omega_a)/R(\omega))}{2\pi} \ln\frac{\omega + \omega_a}{\omega - \omega_a} + \\ & \frac{\ln(R(\omega)/R(\omega_b))}{2\pi} \ln\frac{\omega_b - \omega}{\omega_b + \omega} - \\ & \frac{\omega}{\pi} \int_{\omega_a}^{\omega_b} \frac{\ln R(\omega') - \ln R(\omega)}{\omega'^2 - \omega^2} \, \mathrm{d}\omega' \end{aligned} \tag{2.21}$$

It is noted that for $k \sim 0$, the phase shift is very near π, and Equation 2.19 reduces to

$$n \simeq \frac{1-R}{1+R-2\sqrt{R}} = \frac{1+\sqrt{R}}{1-\sqrt{R}}$$

which is the same as that obtained from the Fresnel relations in Equation 2.15.

The Kramers-Kronig technique was used earlier to determine the optical constants of synthetic slags (Goodwin, 1986; Ebert, 1993). Further discussion of the technique and on the numerical solution of Equation 2.21, especially refined techniques such as the 'subtractive' method used to minimize error, are available in these two references. A computer program, written by Ebert, was used to compute $n(\lambda)$ and $k(\lambda)$ of $CHBr_3$ and CS_2 from the reflectance data using the above relation (Chapter 5). These liquids were used to form suspensions of fly ash for extinction measurements.

In summary, it can be said that the main advantage of this technique is that *both* $n(\lambda)$ and $k(\lambda)$ can be determined from a quantity that is relatively simple to measure, *viz*, the reflectance, $R(\lambda)$, measured over a sufficiently wide spectral range. The main disadvantage is that measurements are often possible only over a limited wavelength range, and the presence of an absorption band just beyond a measurement limit may reduce the accuracy of the calculated constants close to that limit. Additionally, values of $k(\lambda)$ cannot be determined accurately if $k(\lambda) < 0.1$. Still, this technique is popular, and is found to yield accurate values of optical constants of water from reflectance measurements over the wavelength range 1–13 μm, as shown in Chapter 5.

Chapter 3

Physical Characterization of Fly Ashes

3.1 Introduction

This Chapter describes the characterization procedures and results with respect to size distributions and density classification of the six selected ashes. At the outset, it is stressed that our broad objective is to obtain relatively accurate bulk properties. There is a large body of publication that describes qualitatively the morphological and structural variations among ash particles. No attempt was made to systematically duplicate these studies, although several informal studies (mainly microscopic) were initially conducted to compare and contrast the present ash samples with published observations. Qualitative inferences of physical characteristics of ashes were drawn from these optical and SEM examinations. Size distributions in the diameter range 1–200 μm were determined using the Coulter Multisizer, while centrifugal separation was used for density classification. The latter results are used to estimate the cenospheric content of the ashes. The average densities of the whole ashes were also measured in order to accurately determine the ash loading in the transmittance experiments (of Chapter 6).

3.2 Background

It is important to stress that the physical characteristics of fly ash depend considerably on the rank and source of the coal, the ash composition, and how the coal is burned (i.e., combustor type and operating conditions). However, from a morphological viewpoint, there appear to be five broad types of particles listed below.

1. Glassy spheres containing SiO_2, Al_2O_3, Fe_2O_3, CaO, etc., in varying proportions.
2. Glassy cenospheres (i.e., having one or more interior gas bubbles).
3. Large, irregular, partially melted adventitious rocks present in the coal grind.
4. Black, iron-rich, magnetic spheres, a fraction of which is generated from pyrite combustion.
5. Incompletely burned char particles that are generally large ($\gtrsim$ 100 μm), black, and porous.

Though the relative proportions of these classes vary, the first two generally constitute more than 90% of the ash, by mass. In modern p.f. combustors, the char content tends to be very small. Additionally, with the use of coal cleaning technology (which settles out the dense pyrite), the proportion of Class 4 is considerably reduced.

Although the literature surveyed here deals primarily with physical characterization, some discussion of ash chemical composition is inevitable. One of the earliest detailed characterization studies was performed by Fisher *et al*, (1978) on fly ash derived from a Western U.S. power plant burning low-sulfur, high-ash coal. They presented the physical and morphological properties of fly ash collected in cyclone separators of a power plant. The ash was size separated *in situ* into four classes of volume median diameters 20 μm, 6.3 μm, 3.2 μm, and 2.2 μm. Eleven morphological particle types were identified based on optical microscopic studies of $\approx$ 3000 particle in each of the four size classes. Size distributions of the classes performed with Coulter Counter, and Zeiss particle analyzers associated with SEM, and centrifugal sedimentation techniques revealed discrepancies, especially for the coarser fractions, which the authors were not able to explain*. The morphological classification is not, *per se*, a particularly fundamental characteristic because, by the authors' admission,

*A plausible explanation is put forward at the end of the next chapter where Multisizer and SEM size data are compared.

particles with similar morphologies may have dramatically different chemical compositions. However, it was noted that the particles showing significant departure from sphericity (e.g., vesicular) and presence of crystals (non-opaque spheres with crystals) were detected in significant proportions only in the two coarser size classes. Unfortunately, no attempt was made to characterize the whole (unseparated) ash. The abundance ratios of solid spheres to cenospheres for the four size classes were estimated at 40:60, 69:31, 86:14, and 92:8 (on a number basis). Thus, cenospheres are concentrated in the larger size classes.

Ramsden and Shibaoka (1982) used optical and scanning electron microscopy, and electron microprobe analysis of ash sections to examine the size, morphology, and composition of fly ash obtained from Australian power plants burning bituminous coals. They divided the ash into seven classes based on morphology, iron content, etc. Although detailed chemical compositions of each class is presented, the sample sizes were relatively small ($\approx$30 particles), and no estimate of the relative proportions of the classes is presented. The micrographic discussions are detailed, but there is too much stress on the variety of ash particles with little attempt to show common, unifying features. However, it is clear that most of the classes (e.g., quartz, irregular 'spongy' particles, char, 'vesicular' glassy particles) consist of large particles ($\gtrsim 40\ \mu m$). Using knowledge of typical ash size distributions, one concludes that six of the classes *together* constitute a small fraction of the ash. Most of the ash is contained in the seventh class i.e., the class composed of glassy ash particles (diameters $\lesssim 20\ \mu m$) that are solid or cenospheric.

As explained earlier, an accurate knowledge of the size distribution of the ash is needed for Mie calculations. It is known that the median diameter by volume lies typically in the range 10–20 μm, whereas the median diameter by number count is typically $< 1\ \mu m$. However, there is little accurate information available in the literature on ash size distributions, especially for geometric diameters.

In several reported studies (e.g., PSI, 1990), cascade impactors are used to determine size distributions. The impactors yield aerodynamic diameter data resolved into relatively few overlapping bins (Newton *et al*, 1977). The geometrical size of a particle cannot be obtained from the aerodynamic diameter without knowledge of its density, which exhibits considerable inter-particle variation. Similarly, standard sedimentation techniques, such as the Andreasen pipette method, yield distributions based on the Stokes diameter (Allen, 1981).

Light scattering techniques are unsuitable for fly ashes because their chemical composition, and hence their optical properties, vary significantly from particle to particle. When optical sizing is performed using the geometric approximation (e.g., Diamond, 1988), a large fraction of the particles with size parameters in the Mie scattering range will be assigned incorrect sizes.

Ash collected in particulate clean-up devices occurs in a highly agglomerated state and cannot be sized in a dry state. Furuya *et al* (1987) used ultrasonic sieving in methanol for classifying the ash (generated by burning Japanese brown coal) into nine size bins. Apart from insufficient resolution, their minimum size was limited to 5 μm, when it is well known that a significant mass fraction of the ash falls below this limit. Image analysis of SEM fields has been used to determine size distributions (e.g., Casuccio *et al*, 1983; Barta *et al*, 1990). However, there are statistical artifacts associated with this technique that are discussed in Chapter 4. In these circumstances, the Coulter Multisizer was found to be the most appropriate instrument for determining the size distribution of ashes in terms of the geometric diameter.

To the author's knowledge, the only detailed study of size and density separated ash fractions (including chemical compositions) were presented by Hemmings and Berry (1986), and Hemmings *et al* (1987). They studied a composite sub-bituminuous ash collected from a four-stage ESP of a power plant, and a high-iron bituminous ash from eastern Canada, respectively. The studies showed that the larger and less dense cenospheric fraction was richer in silica and poorer in alumina, calcia, and iron oxide, compared with the non-cenospheric fraction. For the latter fraction, size classification did not reveal any chemical or morphological differences between the classes, which agrees with the observations of Fisher *et al* (1978). As can be expected, the density classification showed a continuous distribution of particle density caused by the great variation of composition from particle to particle. As the average particle size decreased, they noted a trend towards a narrower density distribution and higher median density. They concluded that broad density distributions in larger particles is caused by the presence of cenospheres rather than by compositional differences. The cenospheric ash in the lightest density class was crushed to produce samples of the 'wall' material; its density was found to be 2.6 g/cc, typical of aluminosilicate glass.

Magnetic separation of fly ash followed by SEM/EDS and X-ray diffraction studies by Norton *et al* (1986) showed that the magnetic fraction ($\approx$ 15% by mass) consisted predominantly of solid, spherical particles. The morphological diversity appeared to be comparable

to that of the unseparated ash, suggesting that iron is included in the aluminosilicate matrix. X-ray diffraction measurements showed magnetite to be the major form of the iron that is not incorporated in the glassy matrix.

As part of an initial study, separation of the magnetic ash fraction was carried out using hand-held magnets. The results showed that the measured abundance of this fraction is strongly dependent on the field strength of the magnets. Consequently, magnetic separation was not considered to be a useful quantitative characterization technique[†].

With respect to density, the greatest cause of inhomogeneity in fly ash, by far, is the presence of cenospheres. The 'bubbles'[‡] in these cenospheres may be present either in the form of multiple bubbles within a particle, or as a single (concentric or eccentric) bubble with a diameter that may nearly equal that of the particle (i.e, thin-walled cenospheres). The cenospheres can readily be detected by density separation. Their presence in fly ash was noted by Raask (1968), who assumed that only those ash particles lighter than water were cenospheric. However, from an examination of the densities of the oxides typically present in fly ash, it appears that the minimum density of a solid (non-cenospheric) ash particle is about 2.2 g/cc — the density of pure vitreous silica. As a result, ash particles with densities below 2.2 g/cc can be expected to be cenospheric. However, particles with density greater than 2.2 g/cc may also contain bubbles.

To the knowledge of the author, no method for determining the cenospheric fraction is available in the literature, nor any information available on its size distribution. However, a quantitative estimate of the cenospheric content is necessary for interpretation of the extinction measurements of Chapter 6. The relevant data is presented in Section 3.5.4.

3.3 Optical and Electron Microscope Studies of Ash Samples

Because of the presence of iron, the ash samples are black in color, except for the low-iron San Miguel and Eagle Butte ashes which are grey and light yellow, respectively. Several SEM examinations were carried out on ash samples sprinkled on double-sided sticky tape mounted on aluminium stubs (Figure 3.1). The studies confirmed that the ash particles

[†]However, the magnetic fraction of the Illinois ash on which the tests were performed, was retained for size distribution and SEM/EDS studies (Chapter 4).

[‡]Raask (1968) found that the gases trapped in these bubbles are mixtures in varying proportions of CO, CO_2, and N_2.

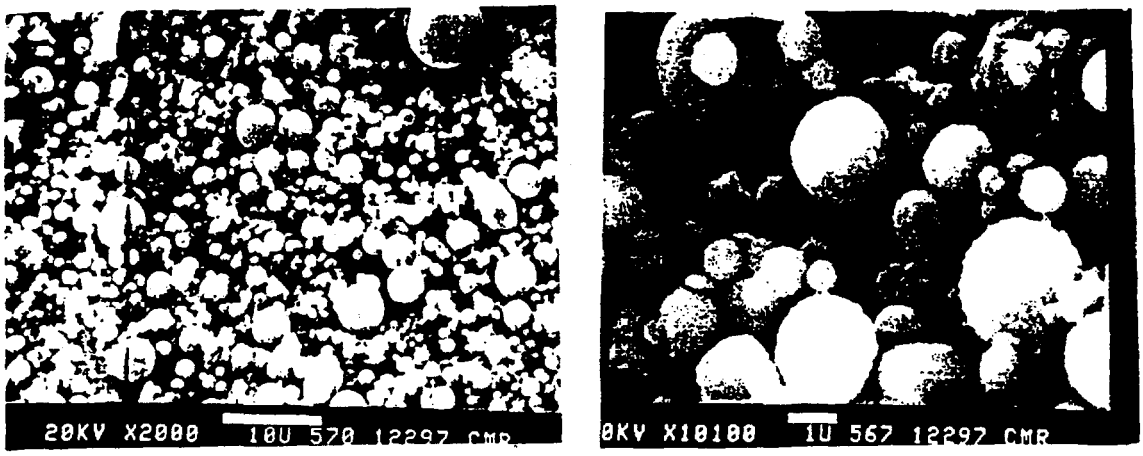

Figure 3.1: Secondary electron images of Upper Freeport fly ash sprinkled on a double-sided sticky tape. Note different magnifications.

are predominantly spherical, but exist as agglomerates on the stubs. The backscattered electron image (BEI) of many individual ash particles appeared to be of uniform intensity, indicating that the particles were reasonably homogeneous in composition.

The small non-spherical fraction consists of a variety of morphological types such as char and adventitious rocks, which is consistent with previously published studies, e.g., Fisher, *et al*, 1978, Ramsden and Shibaoka, 1982, who discussed a large number of morphological classes. The particles in most of these classes are large, irregular, and unusual, which attract the microscopist's attention. However, as size distributions measurements (Section 3.4) show, such particles comprise only a very small fraction of the ash, and can be expected to play a negligible role in radiative transfer.

The conclusions from the microscope studies is that fly ash consists overwhelmingly of closely spherical particles. The observations are confirmed by other investigators who found that spherical particles constitute >95% (by count) of the examined sample (Mamane *et al* 1986; Del Monte and Sabbioni, 1984). The smaller ash particles ($\lesssim 10\ \mu m$) are quenched most rapidly and tend to be 'glassier' than the large particles (say, $>30\ \mu m$) as noted by Hemmings and Berry, (1988), and Del Monte and Sabbioni (1984).

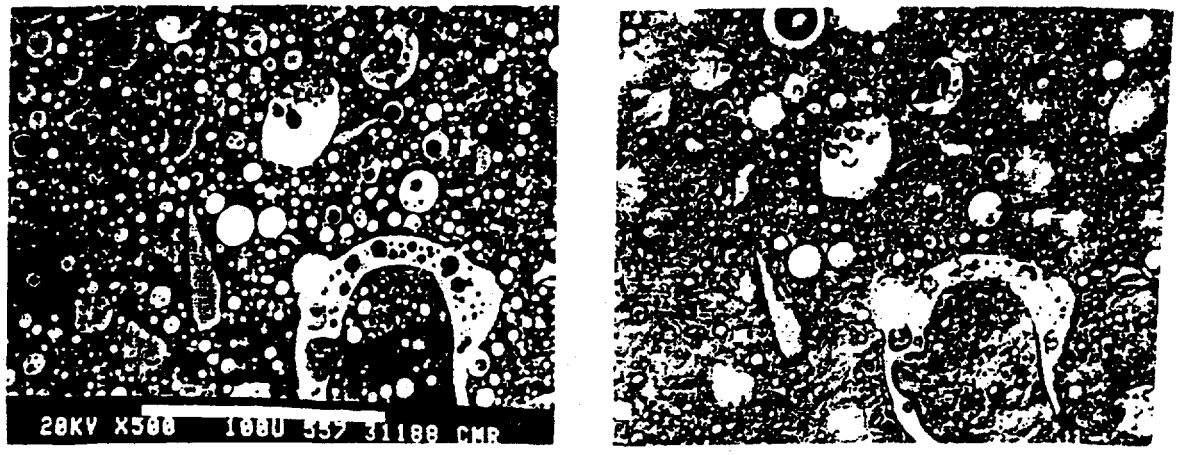

(a) (b)

Figure 3.2: Correlated (a) SEM and (b) optical microscopy of sections of Beulah ash showing two large cenospheres, and some smaller ones. Four large irregular particles (probably unmelted 'rocks', perhaps quartz) can be seen on the left of the pictures.

SEM and optical microscopic examination of a polished section of ash particles (embedded in epoxy) revealed the presence of several cenospheric particles (i.e., particles with interior voids created by trapped gas bubbles). A few large cenospheres with broken walls and containing smaller particles were seen from a carefully correlated study of the same sample area using SEM and optical microscope (Figure 3.2). All previous investigators (e.g., Fisher *et al*, 1978; Furuya *et al*, 1987) refer to such particles as pleurospheres. However, it is difficult to conceive processes that could result in their formation. A simpler and more plausible explanation is that the small particles filled the cenosphere *after* the latter's walls were ruptured during collection and/or storage. In Section 3.5, it is seen that the larger cenospheres are less dense, suggesting that their walls are thinner and relatively more fragile. The observations of Carpenter *et al* (1980) appear to support this hypothesis. They crushed large, low-density ash particles *in situ* under an optical microscope. All the particles contained voids, but *none* contained smaller particles.

The San Miguel lignite ash which has a light grey appearance was found to be primarily cenospheric. Figure 3.3 shows cross-sections of particles of this lignite ash embedded in

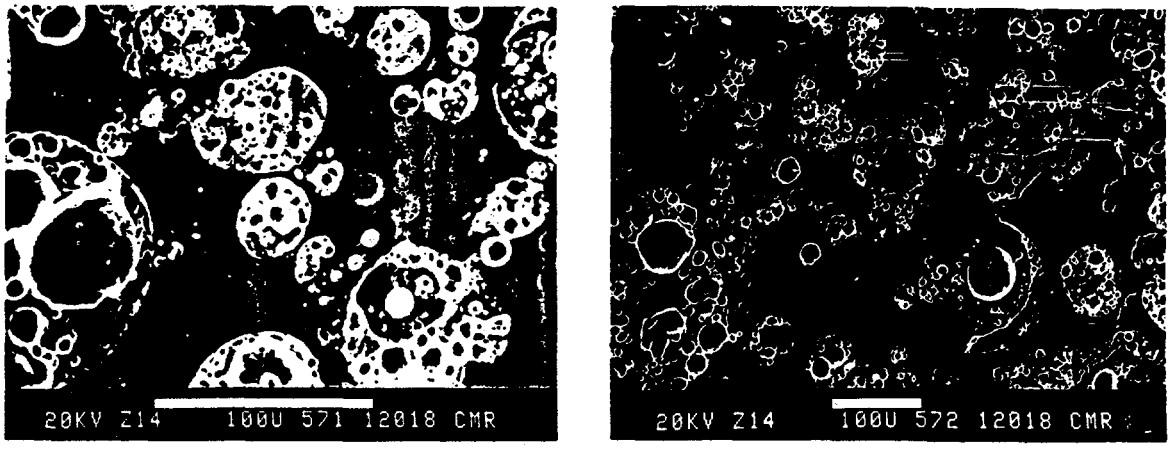

Secondary Electron Image

Backscattered Electron Image

Figure 3.3: SEM micrographs of polished sections of San Miguel ash embedded in epoxy.

epoxy.

Under the optical microscope, the black char fragments were clearly visible, as were the large, dark, iron-rich (probably magnetite) particles. In any field of view, few ash particles were seen to be colorless, suggesting that most particles contain small amounts of transition elements (primarily iron).

3.4 Measurement of Ash Size Distribution

Relatively little accurate information on ash size distribution is available in the literature. Fly ash has an unusually broad size distribution with diameters spanning more than three orders of magnitude. Hence, it is important to measure the dispersion of the size distribution (i.e., the standard deviation). In the few references giving size data (e.g., Fisher, *et al*, 1978; Wall, *et al*, 1981; Hemmings and Berry, 1986), only median diameters are discussed. Furthermore, for calculations, a suitable mathematical function is needed to describe the size distribution.

For reasons discussed in the next Section, the Coulter Multisizer was chosen as the most appropriate device for sizing collected fly ash samples for particle diameters $\gtrsim 1\ \mu m$.

The Coulter Counter, an older version of the Multisizer, has been used earlier by some investigators to size fly ash (Fisher *et al*, 1978; Hemmings and Berry, 1986; Wall *et al*, 1981). The first two studies used the instrument only to obtain median diameters without any information on the size distribution. Although Wall *et al* (1981) do not give a detailed description of the sizing method, they present the size distribution of an Australian ash resolved into nine channels spanning the range $\approx$1.5–70 μm.

The basic output of this instrument is the differential distribution by volume, from which various other representations may be computed using suitable software. However, because of limitations on the dynamic range of individual orifices, it is necessary to use more than one orifice when sizing powders like fly ash having very broad distributions. A procedure for combining data obtained using multiple orifices was developed. A wet siever was constructed to classify the ashes to prevent large particles from blocking the small orifices.

There is evidence from measurements in the submicron region that suggest fly ash is bimodal (Flagan and Friedlander, 1978). However, the contribution of the submicron particles to the higher moment distributions is very small. Moreover, submicron ash particles play a negligible role in radiation transfer in coal combustors because of their low extinction efficiencies at relevant wavelengths ($x \ll 1$). Hence, the lower limit of size measurement of 1.2 μm, set by the Multisizer's capabilities, is quite sufficient for our purposes. Size data presented in this study span the diameter range 1–200 μm.

The size distribution of fly ash is typically very broad and skewed toward small particles. For that reason, it is commonly fitted to a lognormal distribution, and the data displayed as a cumulative distribution (by number, area, volume, etc.) on a log-probability plot. However, because of the lack of size information outside the measurement limits, it was found convenient to fit the data to a truncated lognormal distribution. Data are reported for the parameters of the best-fit lognormal distribution (i.e., the various median diameters and the geometric standard deviation) for all six ashes studied.

3.4.1 The Coulter Multisizer

Figure 3.4 illustrates the working principle of the Coulter Multisizer. In essence, the instrument consists of two electrodes immersed in an electrolyte through which a constant

current (0.2–0.8 mA) flows. The two electrodes are electrically isolated from each other except for an orifice of specified diameter. The orifice diameters used here range from 30 μm to 280 μm. The powder to be sized is deagglomerated by dispersing about 2–3 mg of it in a few milliliters of distilled water or electrolyte together with a few drops of surfactant, and ultrasonically agitating the mixture. Several drops of the mixture are then added to the electrolyte of the Coulter Multisizer. The particles are kept in suspension and circulating by means of a motor-driven glass stirrer which is operated at the highest possible speed without bubble generation by cavitation. The electrolyte is drawn by low vacuum through the orifice separating the two electrodes.

When an insulating particle passes through the orifice, the electrical resistance of the aperture is momentarily increased. This increase generates a voltage pulse whose amplitude is proportional to the particle volume, within size limits expressed as fractions of the orifice diameter. The analog pulses are digitized and assigned to appropriate size bins. In this manner, tens of thousands of pulses are detected and processed, and the size distribution of the powder obtained in a few minutes. The diameter reported is actually the diameter of a sphere with the same volume as that of the particle. A detailed description of the principle and operation of the Coulter Multisizer can be found in Allen (1981), and the Coulter Handbook (1986). The results of several tests for sensitivity of the size distribution to aspects of sampling procedure and data analysis are summarized in Appendix A.

It is suggested in the literature that the lower limit of size measurement using the Multisizer is set by the signal-to-noise ratio while the upper limit is set by the departure from linearity between the voltage signal and the particle volume (Allen, 1981; Coulter, 1986). The nominal limits as stated by the manufacturer are 2% and 60% of the diameter of the orifice. However, tests described in Appendix A showed that the lower size limit is set by instrument sensitivity rather than by s/n ratio, and is closer to 4% of the orifice diameter.

The electronic unit of the Multisizer[§] displays the size distribution on a video screen on the basis of number, volume or area, in either differential or cumulative form. The display may be chosen such that the diameters corresponding to adjacent channels have either a constant difference or a constant ratio[¶]. The number of channels in each setting was found to be slightly less than that specified, e.g., the first channel in the 256 channel mode is numbered 9. Hence, the maximum of channels available is 247. In this mode,

[§]Multisizer Model 0646 was used for all measurements.

[¶]Because of the wide dynamic range, the latter option is used for all the results reported here.

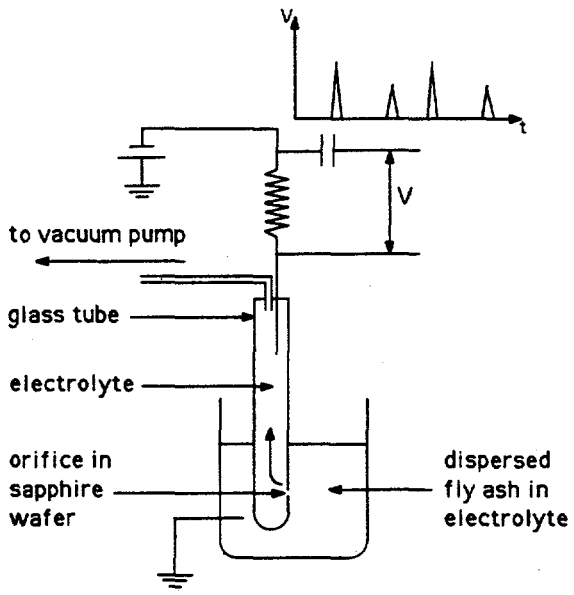

Figure 3.4: A schematic of the operating principle of Coulter Multisizer

the logarithmic spacing is such that the diameter doubles every fifty channels. Hence, the constant ratio of one channel diameter to the adjacent smaller one (also called the log-step ratio) is $2^{1/50} \approx 1.01396$.

The electronic unit outputs, via a RS232 serial port, the size data as the number count of particles in each size channel, and miscellaneous information about the sizing conditions. Although commercial data processing software is available from the manufacturer, we found it convenient to develop flexible, interactive, PC-based software for reading and analyzing the data and performing calculations for size distributions based on number, area or volume. The distributions can be displayed on the computer screen and also plotted on paper using linear, log, or log-probability scales, on the basis of any of the options available to the Multisizer electronic unit. Additionally, the software can collapse adjacent channels so that data measured with the maximum number of channels can be processed to obtain data with fewer channels but higher particle count per channel.

The size resolution is specified as $\pm$ 1 channel in the maximum channel mode, and the aperture current is stated to be accurate to within $\pm$ 0.4% of the setting. The instrument was calibrated for the various orifices using monodisperse latex microspheres, supplied by Coulter, and the electrolyte Isoton II (a filtered, phosphate-buffered saline solution). The

precision was estimated by comparing the diameter corresponding to 50% undersize by volume ($D_{50\%,v}$) for multiple measurements of the same ash sample, and was found to be within 0.7% for all the orifices (see Appendix A). This instrument has several advantages relative to alternative techniques for sizing collected fly ash, as listed below.

- Samples of insulating powders are usually available only in a highly agglomerated form whereas individual particles have to be separated for accurate sizing. Effective deagglomeration is not possible in a gaseous dispersion (as required by competing optical or aerodynamic techniques) but a convenient and effective method for dispersion is to agitate a liquid suspension in an ultrasonic bath. A few drops of the deagglomerated suspension is then added to the Multisizer electrolyte.

- A hundred thousand particles can be sized in a matter of minutes, ensuring good statistics.

- The Multisizer has a wide dynamic range of ≈17:1 on the basis of diameter (i.e., a dynamic range of ≈5000:1 in terms of volume) for each orifice**. Using the technique described here, this range can be increased to include the entire size range accessible by the orifices available from Coulter.

- The multi-channel analyzing feature of the instrument allows the measurement range of each orifice to be divided into a maximum of 247 size bins. Used with a large sample ($> 100,000$ particles), this high resolution permits accurate size distribution measurement.

- The measured diameter is independent of the particle density, in contrast to other instruments such as the cascade impactor which measures the aerodynamic diameter. Unlike sizing by optical methods, the measured diameter is independent of the refractive index of the particle.

- Unlike sizing by sieving or impaction, no tedious weighing of particles is involved.

- Lastly, since the fly ash particles are remarkably spherical, the diameter measured by the Multisizer is the actual geometrical diameter.

**Although the stated dynamic range is 30:1, the raising of the lower limit of measurement (see Appendix A) reduces this range.

3.4.2 The Wet Siever

A wet sieving apparatus was designed and constructed to remove the larger particles which would otherwise cause blockage of the orifice. The design is a modified version of the apparatus described by Daeschner (1968). A schematic of the siever is shown in Figure 3.5. The mesh sizes of the stack of sieves decrease from top to bottom. A dilute suspension of the fly ash, ultrasonically deagglomerated in distilled water with added surfactant, flows from the top to the bottom of the stack.

The important feature of this design, which distinguishes it from most commercially available ones, is the peristaltic pumping arrangement with adjustable backflow. The pump pulses the flow of the suspension through the sieves fifty times a minute. The constriction in the pump outlet causes a backflow which dislodges ash particles resting on the sieve screens until the next stroke of the pump when the action is repeated. This process induces particles smaller than the mesh size to pass through the sieve. Without the backflow, many of these particles remained on the screen. The backflow, which controls the upward force on the particles, can be adjusted using the clamp on the plastic tube. This mechanism for pulsation was found to be more stable and provided a higher pressure drop than that of Daeschner (1968), who used the squeezing action on a rubber bulb to actuate pulsation.

A small rubber wheel is mounted eccentrically on the shaft of a small motor running at 1200 r.p.m. to produce small amplitude vibration of the cylinder and sieve stack to agitate the particles on the sieve. This assists the pulsating action by re-entraining the particles from the sieves, and maintaining the ash in a deagglomerated state. Figure 3.6 illustrates the effect of sieve vibration. The size distribution of the sample obtained without sieve agitation has a deficit of small particles, and the median diameter by volume, $D_{50\%,v}$, is 10% higher.

There is a critical ash loading above which the sieves will become blinded. However, particles re-agglomerate on the screens at loadings well below this critical limit so that the residue contains a large fraction of ash particles with diameters smaller than the mesh size. An acceptable loading was defined such that particles with diameter below the mesh size constituted $\leq$5% of the volume of the residue (determined using the Multisizer). Because the dispersion was quite dilute ($\approx$0.5 gm/litre), most of the water in the filtrate had to be evaporated before sizing.

Compared to dry sieving, where agglomerates tend to persist on the screens, in wet

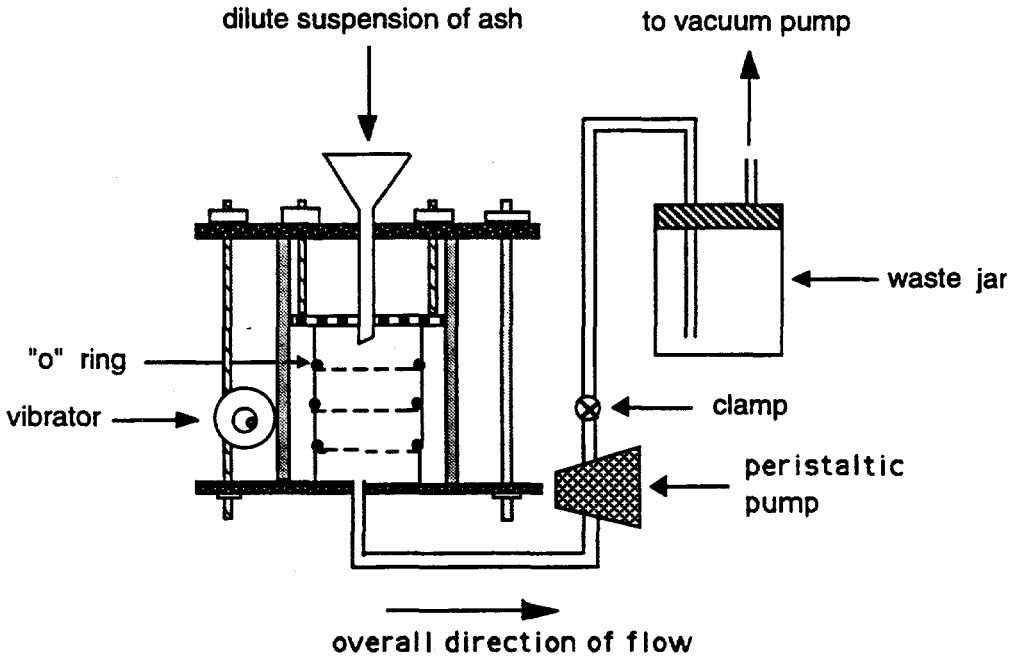

Figure 3.5: Schematic of the wet-siever designed for accurate size separation.

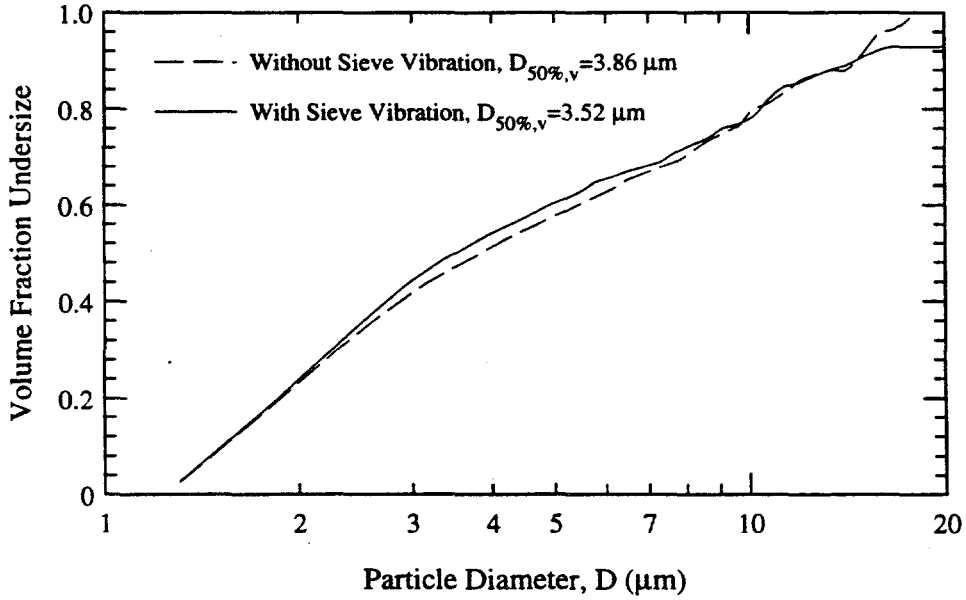

Figure 3.6: Comparison of size distribution of Illinois #6 ash sieved with 16 μm mesh with and without small-amplitude vibration of the sieve.

sieving, one is able to detach most of the small particles by ultrasonic agitation in the liquid before sieving. Daeschner (1968) recommends the use of wet-sieving for powders where particles finer than 40 μm predominate. Agglomeration is particularly acute in fly ash where the size distribution is broad, the small particles being packed in the voids between the larger ones.

For the San Miguel sample that had many large particles, a wire sieve of mesh size 53 μm was used for the size separation. The smaller fraction was sized using the Multisizer with a 100 μm diameter orifice. Next, another sample of the ash was separated with a sieve of electroformed mesh size 16 μm, and the smaller ash fraction sized using a 30 μm orifice. Finally, the size distribution of the whole (unseparated) ash was determined with a 280 μm orifice. The data obtained using the three orifices were combined in a manner described in the next section.

3.4.3 Combining Data Obtained Using Multiple Orifices

The process of combining data from different orifices is illustrated with the specific example of Illinois #6 cyclone ash. Initially, the 100 μm orifice was used for sizing the ash in the diameter range 3.5 $\mu m < D < 60$ μm. The ash was then wet sieved using a mesh size of 16 μm, and the smaller fraction sized using the 30 μm orifice to obtain the size distribution in the range 1.2 $\mu m < D < 4.0$ μm.

To match the two differential distribution functions at 4.0 μm, ten data points on each side of the matching point were curve fitted using least squares polynomial fits of the form

$$f_{30}(D) = \sum_{i=0}^{n} p_i D^i$$

$$f_{100}(D) = \sum_{i=0}^{n} q_i D^i$$

Here $f_{30}(D)$ is the least squares curve fit for the data of the ten channels below D=4.0 μm measured using the 30 μm orifice, and $f_{100}(D)$ is the fit for the ten channels above 4.0 μm measured using the 100 μm orifice. The order of the polynomial fit is n, and p_i and q_i are constant coefficients. The matching is performed close to the lower limit of the larger orifice because sufficient numbers of ash particles are present in this diameter range for both orifices.

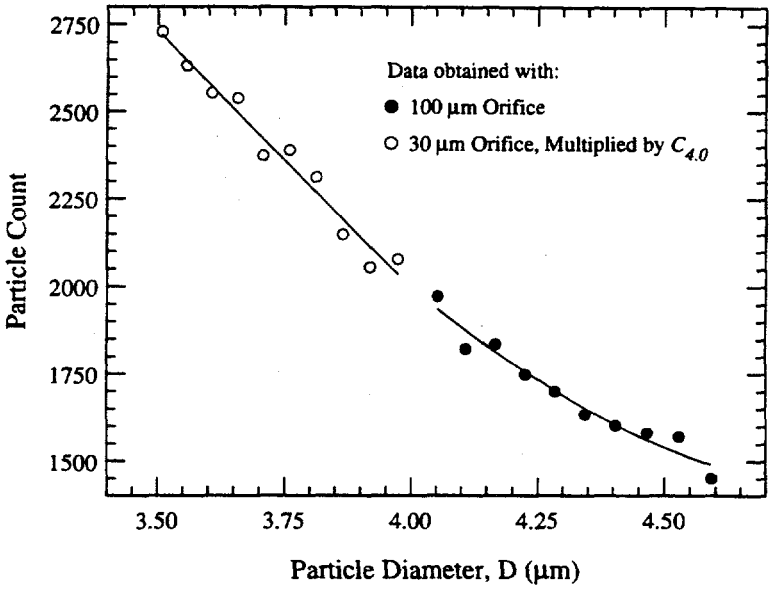

Figure 3.7: Polynomial fit for matching Illinois #6 ash size data obtained with 30 μm and 100 μm Multisizer orifices. The data were matched at 4.0 μm. The ordinate shows the number of particles sampled in each size channel.

Since the two orifices measure the same ash dispersion in the size range spanning the twenty points around 4.0 μm, the two differential distributions should bear a constant ratio to each other. The match is made by multiplying the 30 μm data by the constant $C_{4.0}$, where

$$C_{4.0} = \frac{f_{100}(D = 4.0\ \mu m)}{f_{30}(D = 4.0\ \mu m)}$$

For the Illinois #6 ash the fit was made using linear ($n = 1$), quadratic ($n = 2$) and cubic ($n = 3$) polynomials and the values of $C_{4.0}$ were 8.46, 8.99, 8.89 respectively. After noting that both cubic and quadratic fits produced the best results (differing only by about 1%), the quadratic polynomial was used. On Figure 3.7, the twenty data points are plotted along with $f_{30}(D)$ and $f_{100}(D)$, shown as solid lines. Figure 3.8 shows the two individual distributions as well as the combined one, on a volume cumulative undersize basis.

This procedure can be extended to data sets obtained with more than two orifices. However, the size ranges over which the polynomial fits are performed should contain large samples (>1000 particles per channel in the 256 channel mode), and the two distributions should have slopes of the same sign over the fitting range. If these conditions are not met, sizing with an intermediate orifice maybe necessary. In our study, data from the 30 μm, 70 μm, and 100 μm orifices were combined for the baghouse ashes. However, for the cyclone

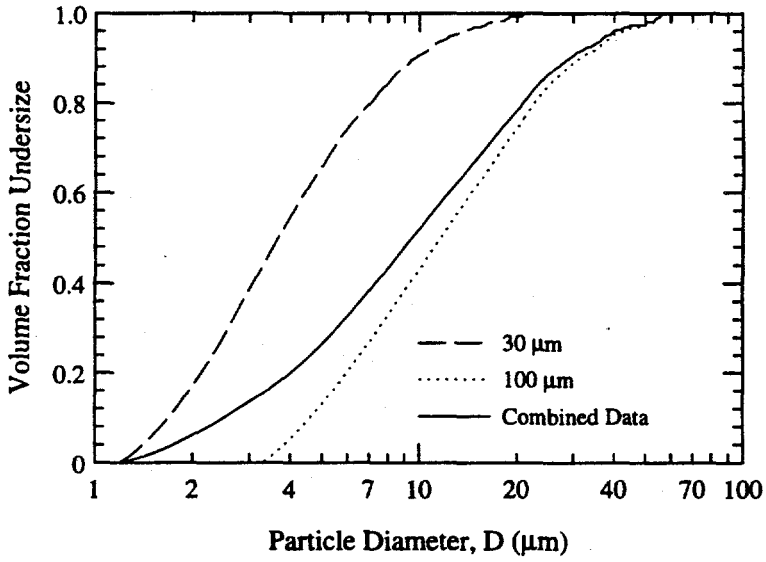

Figure 3.8: Combining size distribution data from two Multisizer orifices for Illinois #6 ash.

ashes which have narrower size distributions, the 30 μm and 100 μm orifices were found sufficient.

3.4.4 The Lognormal Distribution

The two parameter lognormal function is often used to represent the size distribution of broad particulate polydispersions. Many naturally occurring and man-made particle dispersions are found to fit the lognormal distribution rather well. A detailed description of its properties and applications can be found in Aitchison and Brown (1957) and Crow and Shimizu (1988). Specific applications in particle science are discussed in Herdan (1960), Allen (1981) and Flagan and Seinfeld (1988). In the field of particle control technology, it is conventional to fit fly ash size data to a lognormal distribution (White, 1963).

The lognormal distribution is one in which the logarithm of the variate obeys the normal law of probability.

$$f(D) = \frac{\mathrm{d}F(D)}{\mathrm{d}(\ln D)} = \frac{1}{(2\pi)^{1/2} \ln \sigma_g} \exp\left[-\frac{1}{2}\left(\frac{\ln D/D_n}{\ln \sigma_g}\right)^2\right] \tag{3.1}$$

The variate, D, in this case is the particle diameter, and $F(D)$ is the cumulative undersize distribution over all sizes up to diameter D. Hence $\frac{dF(D)}{d(\ln D)}$ is the fraction of particles with

diameters within $d(\ln D)$. Half the particles have diameters smaller than the median diameter, D_n ($=D_{50\%}$). The geometric standard deviation, σ_g, is a measure of the breadth of the distribution. Approximately 68% of the particles have diameters between $\sigma_g D_n$ and D_n/σ_g. A value of σ_g>2 implies that the powder has a very broad distribution while a closely monodisperse powder has $\sigma_g \rightarrow 1$. For powders with broad size distributions, both D_n *and* σ_g must be specified to present a complete picture. In much of the literature on fly ash (e.g., Fisher *et al*, 1978, and Hemmings and Berry (1986) both of whom used Coulter Counters for size measurements), only data on median diameters are reported.

The cumulative undersize (or oversize) form of the lognormal distribution is widely used because, whether plotted by number count, area, volume, etc., it plots as a straight line on a log-probability graph. This gives a simple method of presenting experimental data from which one can quickly determine the two parameters D_n and σ_g. While $D_n = D_{50\%}$, σ_g can be obtained from any of the following relations

$$\sigma_g = \frac{D_{84.13\%}}{D_{50\%}} = \frac{D_{50\%}}{D_{15.87\%}} = \sqrt{\frac{D_{84.13\%}}{D_{15.87\%}}}$$

As σ_g increases, the slope of the size distribution decreases. The cumulative count undersize distribution is given by:

$$F(D) = \int_{-\infty}^{\ln D} \frac{1}{(2\pi)^{1/2} \ln \sigma_g} \exp\left[-\frac{1}{2}\left(\frac{\ln x/D_n}{\ln \sigma_g}\right)^2\right] d(\ln x) \qquad (3.2)$$

$F(D)$ is linear in terms of the error function and can be expressed as

$$F(D) = \frac{1}{2}\left[1 + \text{erf}\left(-\frac{1}{2}\,\frac{\ln D/D_n}{\ln \sigma_g}\right)\right]$$

It is useful to define here the moments of the lognormal distribution because there appear to be differences in the use of the terms area and volume distributions in particle statistics and mathematical statistics (Crow and Shimuzu, 1988). Equations 3.1 and 3.2 represent the distributions by number, also referred to as the count distribution or the size-frequency distribution, in which D_n is the median diameter (sometimes referred to as the geometric mean diameter) and σ_g is the geometric standard deviation. The size distributions by surface area and volume, as defined in particle statistics, are the distributions of the second and third moments, about the diameter, of the number distribution[††]. The j^{th} moment distribution for a lognormal function, on a cumulative undersize basis, is given by

$$F_j(D) = \int_{-\infty}^{\ln D} x^j \frac{1}{\sqrt{2\pi} \ln \sigma_g} \exp\left[-\frac{1}{2}\left(\frac{\ln x/D_n}{\ln \sigma_g}\right)^2\right] \text{d}(\ln x)$$

[††]The volume distribution is *not* the distribution of the third power of D, *i.e.*, $F_j(D^3)$.

It can be shown that this distribution is also lognormal with parameters $\bar{D}_j = D_n \exp(j \ln^2 \sigma_g)$ and σ_g. Thus, $F_2(D, D_a, \sigma_g)$ and $F_3(D, D_v, \sigma_g)$ represent the area and volume distributions, respectively, where

$$D_a \equiv \bar{D}_2 = D_n \exp(2 \ln^2 \sigma_g)$$

$$D_v \equiv \bar{D}_3 = D_n \exp(3 \ln^2 \sigma_g)$$

Thus, knowledge of any one median diameter and σ_g is sufficient to calculate all the moment distributions. On log-probability axes, the moment distributions plot as parallel straight lines with the same slope. Another useful size in radiative transfer calculations is the Sauter mean diameter, D_{32}. It is the ratio of the third moment of the distribution to the second moment, each integrated over the entire diameter range.

$$D_{32} = D_n \exp(\frac{5}{2} \ln^2 \sigma_g) = D_v \exp(-\frac{1}{2} \ln^2 \sigma_g)$$

3.4.5 Fitting Cumulative Data to Truncated Lognormal Distribution

The cumulative lognormal distribution is defined for the infinite range, $D = (0, \infty)$, and is normalized on the integral of the differential distribution over this infinite range, so that $F(\infty) = 1$. Hence, in plotting experimental data one should normalize the measurements on the integral of the quantity (i.e., total number, area or volume) over the infinite range. For some particle sizing techniques, e.g., those based on sieving, settling or impaction, the integral over the infinite range is either directly measured or simply derived from the data. However, in other techniques with dynamic range limits, e.g., optical and Coulter Multisizer, there are bounds $D = (a, b)$, say, to the measurement range and one has no information on the distribution for $D < a$ and $D > b$.

If one attempts to fit the cumulative data to a lognormal distribution (e.g., by plotting $F(D)$ on log-probability axes) by normalizing on the total count in the range (a, b), then even if the distribution is truly lognormal over the whole range, the plotted data will not fall on the true straight line because the part of the distribution outside the measurement range is not included in the normalization (see Figure 3.9).

In these circumstances, a more logical procedure is to fit a truncated lognormal cumulative distribution to the experimental (truncated) cumulative distribution, since this avoids any assumptions about the form of the distribution outside the measurement range. This fit can be made using any of a number of suitable curve-fitting algorithms without introducing arbitrary assumptions.

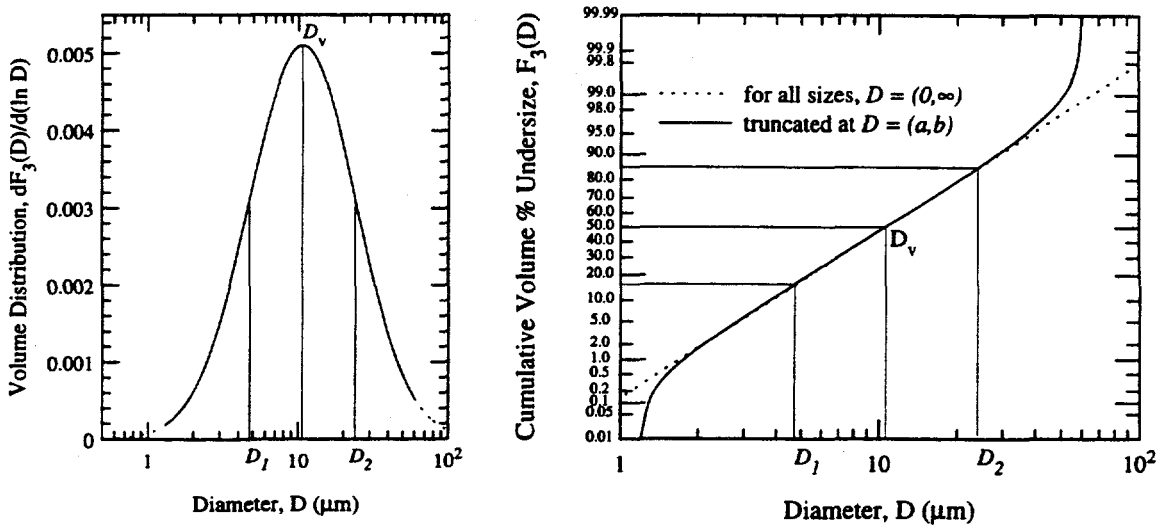

Figure 3.9: Lognormal size distribution with parameters of Kentucky #9 ash: D_v=10.64 μm, $\sigma_g = D_2/D_v = D_v/D_1$=2.23. The truncation limits are a=1.2 μm and b=60.0 μm.

The form of the lognormal distribution function, truncated outside the measurement limits a and b chosen to represent the measured fly ash size distributions is shown below:

$$f^{(a,b)}(D) = \frac{dF^{(a,b)}(D)}{d(\ln D)} = \frac{\frac{1}{(2\pi)^{1/2}\ln\sigma_g}\exp\left[-\frac{1}{2}\left(\frac{\ln D/D_n}{\ln\sigma_g}\right)^2\right]}{\int_{\ln a}^{\ln b}\frac{1}{(2\pi)^{1/2}\ln\sigma_g}\exp\left[-\frac{1}{2}\left(\frac{\ln x/D_n}{\ln\sigma_g}\right)^2\right]d(\ln x)} \qquad a \le D \le b \quad (3.3)$$

In the limit $a \to 0$ and $b \to \infty$, the denominator $\to 1$ and distribution (3.3) approaches distribution (3.1).

The cumulative undersize distribution function $F^{a,b}(D)$, obtained by integrating Equation 3.3, can be expressed in terms of the error function as

$$F^{(a,b)}(D) = \frac{\text{erf}\left(\frac{\ln D/D_v}{2^{1/2}\ln\sigma_g}\right) - \text{erf}\left(\frac{\ln a/D_v}{2^{1/2}\ln\sigma_g}\right)}{\text{erf}\left(\frac{\ln b/D_v}{2^{1/2}\ln\sigma_g}\right) - \text{erf}\left(\frac{\ln a/D_v}{2^{1/2}\ln\sigma_g}\right)} \qquad a \le D \le b \qquad (3.4)$$

It is shown in Appendix C shown that the moment distributions of the truncated lognormal distributions bear the same relationships to the number distribution as in the untruncated case described in the previous section.

The best-fit truncated lognormal function yields values of $\bar{D}_j$ and σ_g (which are the parameter values of the j^{th} moment of the untruncated distribution). This $\bar{D}_j$ is not the

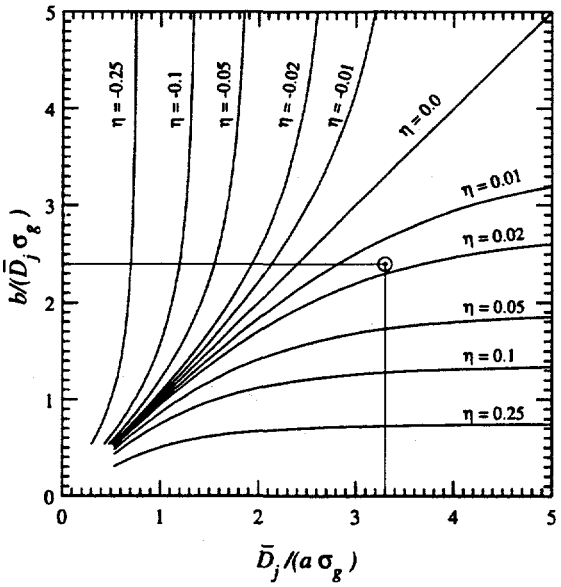

Figure 3.10: Effect of truncation on relation between D_n and $D_{50\%}$ for a lognormal function. Values of η that are too small or large suggest inappropriate choice of Multisizer orifice. The current truncation point is shown circled.

same as $D_{50\%}$ of the data. The relative difference (or 'error'), $\eta \equiv (D_{50\%} - \bar{D}_j)/\bar{D}_j$, depends on the degree of truncation, as measured by $(\frac{\bar{D}_j}{a\sigma_g})$ and $(\frac{b}{\bar{D}_j\sigma_g})$. As shown in Figure 3.10, when the latter parameters are large (slight truncation) the 'error' η is small. The circled data point represents the truncation conditions ($\eta = 2\%$) in fitting the cumulative volume distribution data for the Kentucky #9 baghouse ash using orifices of diameter 30 μm and 100 μm. At the other extreme, Figure 3.10 indicates that η is large if either $(\frac{\bar{D}_j}{a\sigma_g})$ or $(\frac{b}{\bar{D}_j\sigma_g})$ are small ($\lesssim 1$). This extreme implies that the size limits a and b are too large or too small respectively for the given size distribution, i.e., the orifice size(s) are inappropriate for the particular ash.

The function $F_3^{(a,b)}(D, D_v, \sigma_g)$ was fitted to the data obtained from the Multisizer measurement for all the ash samples. The parameters D_v and σ_g are computed by minimizing the r.m.s. error between $F_3^{(a,b)}(D, D_v, \sigma_g)$ and the data, using Nelder and Mead's multidimensional downhill simplex method for function minimization (Nelder and Mead, 1965). It is an iterative procedure which converges, in this case, in less than two minutes on an IBM PC AT. Trial values for D_v and σ_g, needed to initiate the computation, and obtained from the volume distribution data, are $D_{50\%,v}$ and $\sqrt{\frac{D_{84.13\%,v}}{D_{15.87\%,v}}}$, respectively. The final result was found to be insensitive to trial estimates, even when the latter were $> \pm 30\%$ off the final

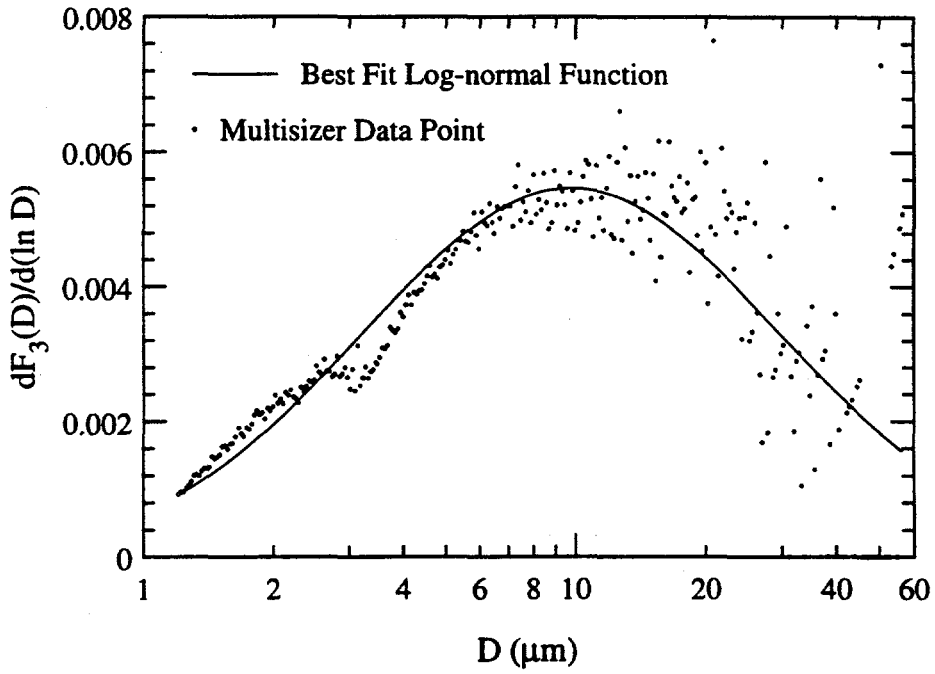

Figure 3.11: Truncated lognormal function fitted to differential volume distribution data of Illinois #6. The parameters of the best-fit function (truncated outside 1.21 μm and 55.68 μm) are D_v=10.1 μm, σ_g=2.85 μm.

converged values. This insensitivity indicates that there are no other sets of minima for (D_v, σ_g) in the vicinity of the final values.

In Figure 3.11, the best-fit truncated lognormal function is shown for the volume distribution data of Illinois #6 baghouse ash. The values of D_v and σ_g are 10.1 μm and 2.85, respectively. D_n, D_a, and D_{32} are calculated to be 0.4 μm, 3.4 μm and 5.8 μm, respectively. Because the numbers of particles corresponding to diameters over 20 μm decrease quickly, there is considerable scatter in the volume distribution in Figure 3.11 in this range. This statistical scatter can only be reduced either by increasing the sample size or by sizing with fewer channels. However, in the latter case, the resolution will then decrease and the size distribution will be less accurate over the full range of diameters. The scatter at the large diameter end is acceptable as long as the sample size is large ($> 100,000$) and the best-fit lognormal function represents the data well in the 1–10 μm range, which contains $\geq$ 99% of the detected particles (by number) for most ashes. The 'shoulder' in the distribution between 2 μm and 4 μm is a residual error arising from the data combining process. The cumulative distribution for the same ash is presented on log-probability axes in Figure 3.12,

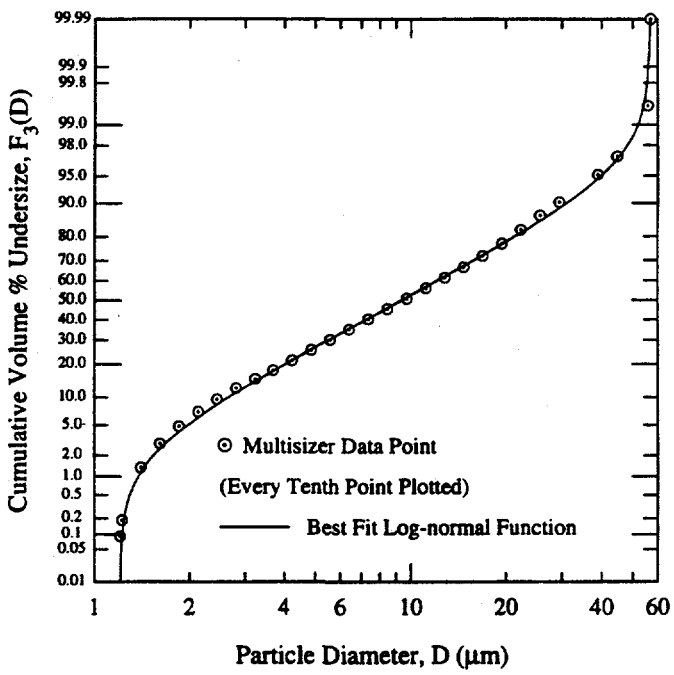

Figure 3.12: Truncated lognormal function fitted to cumulative volume distribution data for Illinois #6 ash. The function is truncated outside 1.2 μm and 55.7 μm. D_v=10.1 μm and σ_g= 2.85.

with every tenth data point plotted. The scatter seen in the differential distribution is smoothed out on the cumulative plot. The departure of the graph from a straight line at the measurement limits, similar to that in Figure 3.9, was explained earlier in the section.

Although Multisizer data were collected for the maximum number of channels (247), the software can be used to merge adjacent channels so that the resulting data appears reduced by factors that are integral exponents of two, i.e., 2, 4, 8, etc. The bargraphs in Figure 3.13 show the differential volume distribution of Upper Freeport ash after processing the original data to simulate sizing using channel numbers ranging from 282 to 36 [‡‡]. It is noted that the jaggedness at larger diameters reduces when fewer channels are used. However, D_v increases somewhat when the number of channels is reduced because the truncated lognormal function is fitted to cumulative data, and the width of each channel increases as the channel numbers are reduced. The increase in σ_g with decreasing channel number is a consequence of the increase in D_v. From this comparison, and studies of the influence of sample size on size parameters (see Appendix A), it was decided to use the maximum number of channels (for

[‡‡]The channel numbers are increased because of combining data from two Multisizer orifices.

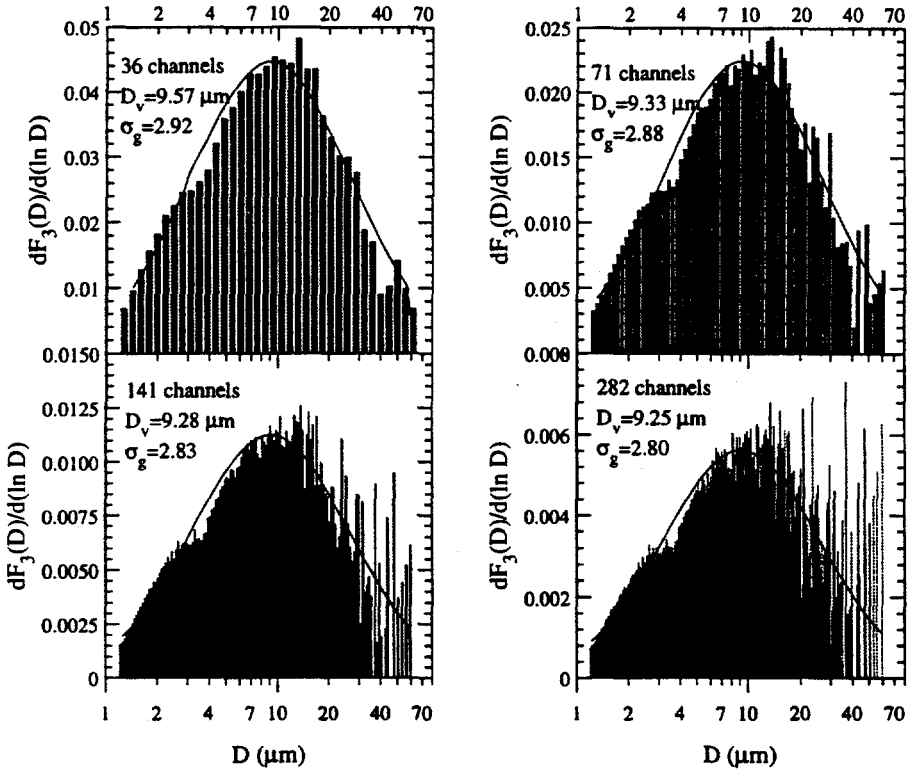

Figure 3.13: Truncated lognormal function fitted to differential volume distribution data of Upper Freeport fly ash. The original size data were collected using 30 μm and 100 μm orifices in the 256 channel mode. Adjacent channels were then merged to illustrate the effect on size distribution. The extra decimal place for D_v is used only for comparison, and does not imply increased accuracy.

sample sizes 100,000–200,000 used in this study).

Cumulative size distributions based on count, surface area and volume plotted on the same axes are shown in Figure 3.14 for San Miguel fly ash. Because the distributions have the same σ_g, they plot as parallel straight lines on log-probability axes (Aitchison and Brown, 1957), except close to the measurement limits. The sample sizes for orifices of diameters 30 μm, 100 μm, and 280 μm are 132,088, 151,495 and 194,270, respectively. However, after the 100 μm and 280 μm data are matched at 10.5 μm, the total number of particles included in the final distribution is 230,822. The parameters of the best-fit lognormal function for the volume distributions are $D_v = 32.3$ μm and $\sigma_g = 2.89$.

The size distributions of all the ashes are presented in Appendix D in cumulative and differential forms, on the bases of number, area, and volume. It is noted here that the

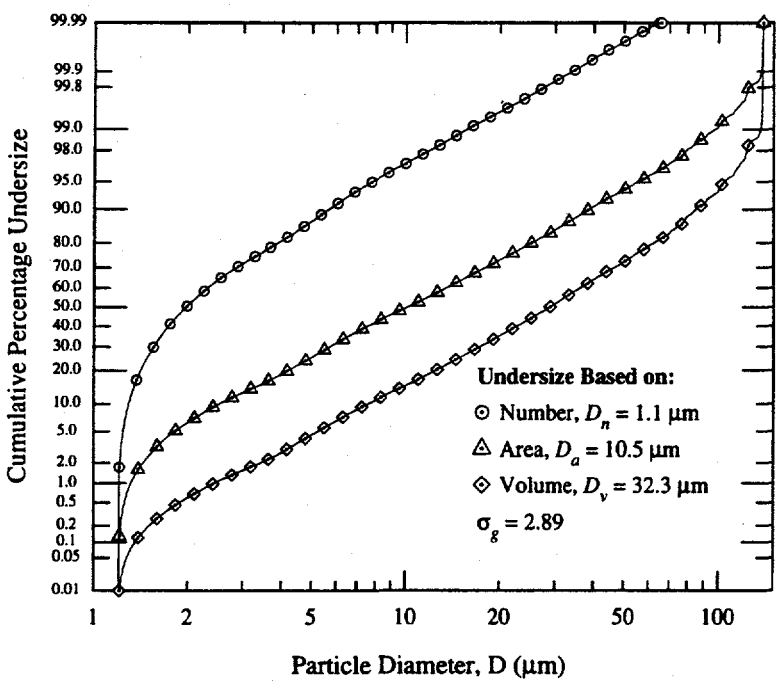

Figure 3.14: Size distributions of San Miguel ash based on number, area, and volume. Every tenth data point is plotted. Total sample size=230,822.

ash size distribution in the measured range is strictly unimodal unlike the observations of Kang *et al* (1988) who found bimodal size distributions with peaks in the ranges 1–5 μm, and also $\approx$10 μm. However, the latter measured aerodynamic diameters ($\propto D\sqrt{\rho}$) which is dependent on the particle density, ρ. The size-density relationship discussed in Section 3.5 may explain this discrepancy.

3.4.6 Size Parameters for the Fly Ashes Studied

The information on the ash size distribution is contained in the four numbers: D_v, σ_g a, and b. For all ashes except San Miguel, the size limits (a, b) can be taken as (1.2 μm,60.0 μm). The range is (1.2 μm,180.0 μm) for the San Miguel ash. Table 3.1 presents the parameters D_n, D_a, D_v, D_{32}, and σ_g, (corresponding to the best-fit truncated lognormal distributions) for the six fly ashes studied.

The values of D_v and σ_g tend to fall in the ranges of 9–15 μm and 2.0–3.0, respectively with one exception. The San Miguel lignite ash, which is almost entirely cenospheric, contains many large particles, and its D_v is two to three times larger than that of the

Table 3.1: Size parameters for best-fit lognormal functions used to represent the size distributions of the fly ashes studied. The truncation limits, (a, b), are (1.2 μm, 180.0 μm) for the San Miguel ash, and (1.2 μm, 60.0 μm) for the remaining ashes.

Fly ash	Collection	D_n	D_a	D_v	D_{32}	σ_g
Kentucky #9	Baghouse	1.2	5.1	10.4	7.3	2.33
Kentucky #9	Cyclone	3.4	9.4	15.6	12.1	2.04
Illinois #6	Baghouse	0.4	3.4	10.1	5.8	2.85
Illinois #6	Cyclone	2.3	7.9	14.6	10.7	2.19
Upper Freeport, PA	Baghouse	0.4	3.3	9.3	5.6	2.76
Eagle Butte, WY	Baghouse	0.6	5.0	14.3	8.4	2.80
Beulah, ND	Baghouse	0.4	3.9	12.7	7.0	2.98
Beulah, ND	Cyclone	1.2	5.4	11.5	7.9	2.39
San Miguel, TX	ESP	1.1	10.5	32.3	18.4	2.89

other ashes. Although only ≈50% of the Kentucky #9 cyclone ash particles have diameters greater than 3.4 μm, this fraction contributes more than 97.6% and 88.8% of the total volume and area, respectively. For many of the ashes, the values of D_n are below the lower limit of measurement. In these cases, the number of particles detected in each size channel continues to increase with decreasing diameter.

Wall *et al* (1981) do not fit their cumulative volume distribution data* to any functional form. However, a best-fit lognormal function to their data would have D_v=10.5 μm and σ_g=2.95, figures similar to those found in this study.

The particular cyclone used at Foster Wheeler does not exhibit a sharp cut-off point. However, it traps many of the larger particles before the ash is carried into the baghouse. The latter collects the remaining particles including those large particles that escaped the cyclone. Hence, the baghouse ashes have a wider size range and, as a result, larger values of σ_g. It is interesting to note that D_v for the Beulah cyclone ash is smaller than D_v of the corresponding baghouse ash. A possible explanation is that the two dominant, but opposing, forces on an ash particle in a cyclone are the centrifugal force (proportional to D^3) and the drag force (proportional to D), whose ratio is proportional to D^2. In an approximate sense, the cyclone should ideally separate particles above a critical area. Even if there is no sharp cut-off point (as in this cyclone) the cyclone ash is expected to have a larger value of the area median diameter, D_a. Table 3.1 shows that this is indeed true of

*The ash was generated from high volatile Australian bituminous coal.

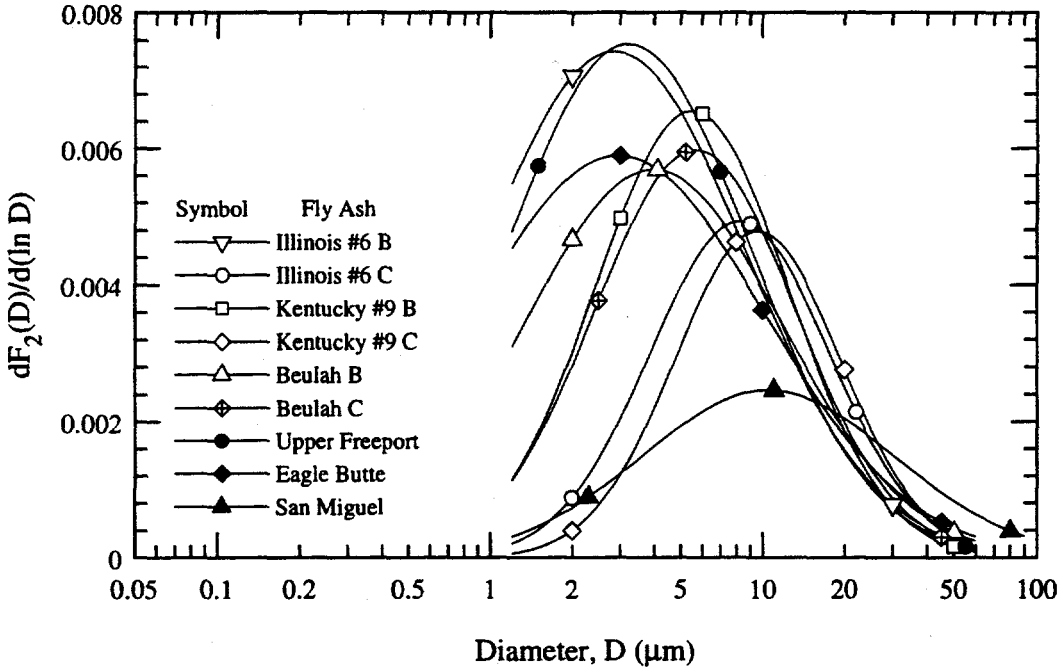

Figure 3.15: Area distributions of fly ashes. B and C refer to baghouse and cyclone ashes respectively.

all three sets of baghouse and cyclone ashes.

It is the area distribution which is most important in the context of radiative transfer. To facilitate comparison, the differential area distribution for all the fly ashes are presented in Figure 3.15. The solid symbols show data for ashes not separated by cyclone. Almost all of the total particle area is due to ash particles with diameter less than 50 μm. As explained above, the baghouse ashes have broader size distributions than the cyclone ashes.

When D_n is plotted against σ_g on log-linear scale (Figure 3.16), all the ashes with the exception of the highly-cenospheric San Miguel ash, fall close to a straight line (Ebert, 1992). While this apparent inverse relationship between D_n and σ_g is an observation that may be useful in collapsing size data, any explanation must involve ash formation mechanics and is beyond the scope of this work. However, as pointed out by Sirois (1991), the mean value and standard deviation of random variables that assume only positive values are generally not independent. He presents a similar relationship between D_n and σ_g for ionic concentration distributions in rainfall, as found here for fly ash.

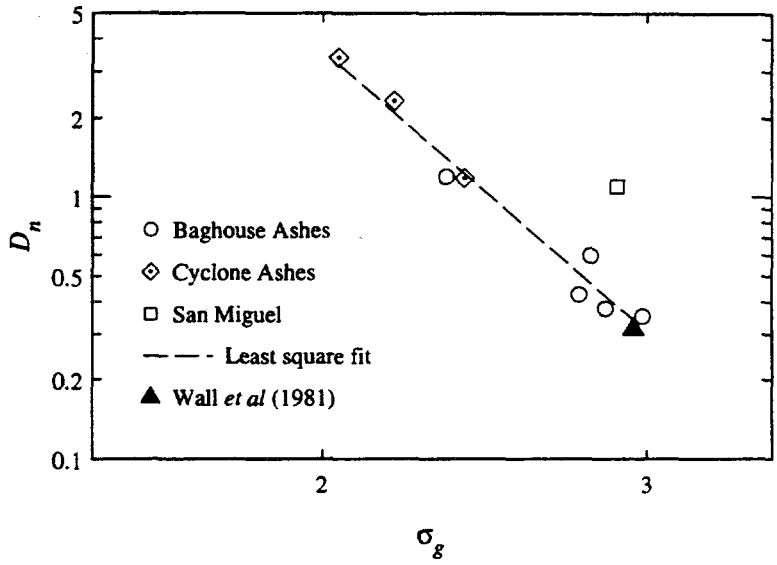

Figure 3.16: Graph of number median diameter it vs geometric standard deviation for the fly ashes. The best-fit straight line: σ_g=2.471$D_n{}^{-0.1646}$, ignores the San Miguel ash (Ebert, 1992).

3.5 Ash Density Measurements and Classification

3.5.1 Measurement of Average Densities of the Fly Ashes

For transmittance measurements, accurate determination of the ash loading, V_a (i.e., the volume of fly ash per unit volume of the dispersion) is needed. The only practical way to measure and control ash loading is by weighing. Hence, measurements of the average densities of the ashes were made.

The ash density, determined using a specific gravity bottle, involved the following four weighings: mass of specific gravity bottle (a), mass of bottle containing water and ash (b), mass of ash sample (c), and mass of the bottle filled with water (d). It can easily be shown that the ash density, ρ_{ash} is then given by

$$\rho_{ash} = \frac{c(d-a)}{V(c+d-b)} = \rho_w \left(\frac{c}{c+d-b} \right)$$

Here V is the volume of the specific gravity bottle, and ρ_w the density of water at room temperature (22°C–24°C) at which all density measurements were made.

Two possible sources of error in measuring the density of powders by this method are encountered.

Table 3.2: Average densities of fly ashes.

Fly Ash	Density (in g/cc)
Kentucky #9	2.15
Illinois #6	2.12
Upper Freeport	2.29
Eagle Butte	2.76
Beulah	2.37
San Miguel	1.73

(a) Bubbles may form in the bottle when water is added to the ash, and may remain trapped in the dispersion leading to a low estimate of the density. Bubble formation is minimized by gradually adding water to the ash in the bottle with an eye-dropper. The dispersion is then ultrasonically agitated to allow the bubbles to rise to the surface and escape.

(b) When 'topping off' the specific gravity bottle, a significant amount of ash may escape with the excess water. This loss of ash was found to result in errors $> 5\%$ of the correctly measured value. The problem is minimized by adding small drops of water one at a time when the bottle is almost full.

A number of density measurements were made for each of the six baghouse ashes. For all ashes the range of measured densities was within 1.5% of the average. The densities are shown in Table 3.2. Four of the ashes have average densities in the range 2.1–2.4 g/cc. The Eagle Butte ash has a high density due to its high calcia content (discussed in the next Chapter), while the San Miguel ash's unusually low density is due to its predominantly cenospheric nature.

3.5.2 Density Classification of Ashes

Since the optical properties (more specifically, the complex refractive index) of an ash particle depend on its composition, and since density and composition are correlated, the separation of an ash by density is a useful classification technique. In particular, one expects that char particles will be contained in the lightest fraction while iron-rich particles will be contained in the denser fractions. The cenospheric particles can be expected to occur in the lower density classes. The calcia- and alumina-rich particle should appear in the denser

Table 3.3: Composition of liquids used for density classification. All densities in g/cc.

Density	Chemicals	Volume Ratio
1.6	CCl_4	100
2.0	CCl_4 : CH_2Br_2	55:45
2.4	CCl_4 : CH_2Br_2	11:89
2.8	CH_2I_2 : CH_2Br_2	37:63
3.2	CH_2I_2 : CH_2Br_2	85:15

classes, while silica-rich particles should appear in the lower density ones.

The density classification follows the scheme of Furuya *et al*(1987). Six density classes spanning the range < 1.6 g/cc to > 3.2 g/cc were created by mixing carbon tetrachloride (CCl_4, ρ=1.594 g/cc), dibromomethane (CH_2Br_2, ρ=2.497 g/cc), and di-iodomethane (CH_2I_2, ρ=3.325 g/cc, all densities at 25°C) in proportions given in Table 3.3.

Standard centrifugal separation procedure (Browning, 1961) was employed with some modifications introduced to improve accuracy (see Appendix B). Relatively dilute ash suspensions ($\approx$ 0.3 g in 40 ml of liquid) were initially deagglomerated by ultrasonic agitation and gravitationally separated by allowing ten minutes of settling. The centrifuge speed was gradually increased to ~2000 r.p.m., which subjected the ash to an acceleration of $\sim 1000g$. These measures minimized the carryover of smaller particles into the larger sized and lighter cenospheric fraction.

Because the density of most of the ash was expected to fall between 2–3 g/cc, the liquid of density 2.4 g/cc was used for separation initially. Centrifugal separation was next performed with liquids of density 2.0 g/cc and 2.8 g/cc on the float and sink respectively. Separation was carried out in this manner for the other density classes. Repeated separation was performed until a minimum of 1 g of ash was available for the subsequent steps in the centrifugal separation process. The reproducibility of the separation process[†] was found to be ±3%.

The results of density classification are shown in Table 3.4. All but two ashes have mass fractions of 80% or more in the density range 2.0–2.8 g/cc, and average densities in the range 2.1–2.4 g/cc. Of the two prominent exceptions, the Texas lignite fly ash from San Miguel has 90% of its mass in the first two classes (<2.0 g/cc) with a negligible fraction in

[†]Reproducibility was defined as $(w_2 - w_1)/(w_2 + w_1)$, where w_1 and w_2 are the mass fractions of the float obtained from repeat measurements.

Table 3.4: Density classified fly ashes. Density classes 1–6 correspond to densities < 1.6, 1.6–2.0, 2.0–2.4, 2.4–2.8, 2.8–3.2, and > 3.2 g/cc, respectively. The figures shown are mass percentages. The last column presents the density of whole (unseparated) ash in g/cc.

Fly Ash	1	2	3	4	5	6	Ash
Kentucky #9	1.0	7.6	26.7	59.6	1.4	3.7	2.15
Illinois #6	1.2	7.2	42.8	42.0	2.8	4.0	2.12
Upper Freeport	1.3	6.7	27.0	57.0	2.4	5.6	2.29
Eagle Butte	0.5	0.2	3.5	21.4	68.5	5.9	2.76
Beulah	0.2	2.1	10.2	76.3	8.9	2.3	2.37
San Miguel	35.6	52.9	7.0	3.5	1.0	0.0	1.73

the highest density class. The low density indicates that the overwhelming fraction of the ash is cenospheric. The other exception is the Eagle Butte ash where 90% of the ash mass has a density in the range 2.4–3.2 g/cc, with more than two-thirds of the mass falling in the density class 2.8–3.2 g/cc. In Chapter 4, it is reported that electron microprobe analysis of an Eagle Butte slag sample revealed a relatively high proportion of calcia, which explains the high ash density. Figure 3.17 graphs the density distributions on a cumulative basis.

Samples of Beulah and Eagle Butte ashes from each density class, embedded in acrylic, were ground and polished to expose sections of the ash particles. Examination with the SEM shows that the first two classes (density range <1.6 g/cc to 2.0 g/cc) consist mostly of cenospheres. Small ash particles are sometimes observed inside the voids of the cenospheres. However, it is probable that the former were deposited in the voids during sample preparation. Small amounts of char are also present in Class 1. In Class 3, all the particles of diameter >15 μm are cenospheric. Very few cenospheres are seen in Classes 4, 5, and 6.

From the above observations and from Table 3.4, it appears that the cenosphere content, by mass, of the Beulah ash (<10%) and the Eagle Butte ash (<5%) are the lowest. At the other extreme, the San Miguel ash is almost entirely cenospheric. The cenospheric fraction of the other three ashes is estimated to be 15%–25%.

The ash powder in Classes 5 and 6 are visually darker than the corresponding unseparated ashes. All the ash in Class 6, and a large fraction in Class 5, is magnetic. SEM/EDS on 20–30 particles of the two classes showed that they contained high proportions of iron. A few particles composed almost solely of iron oxide were noted. These are magnetite (Fe_3O_4) particles produced from combustion of pyrite particles in the coal grind. However,

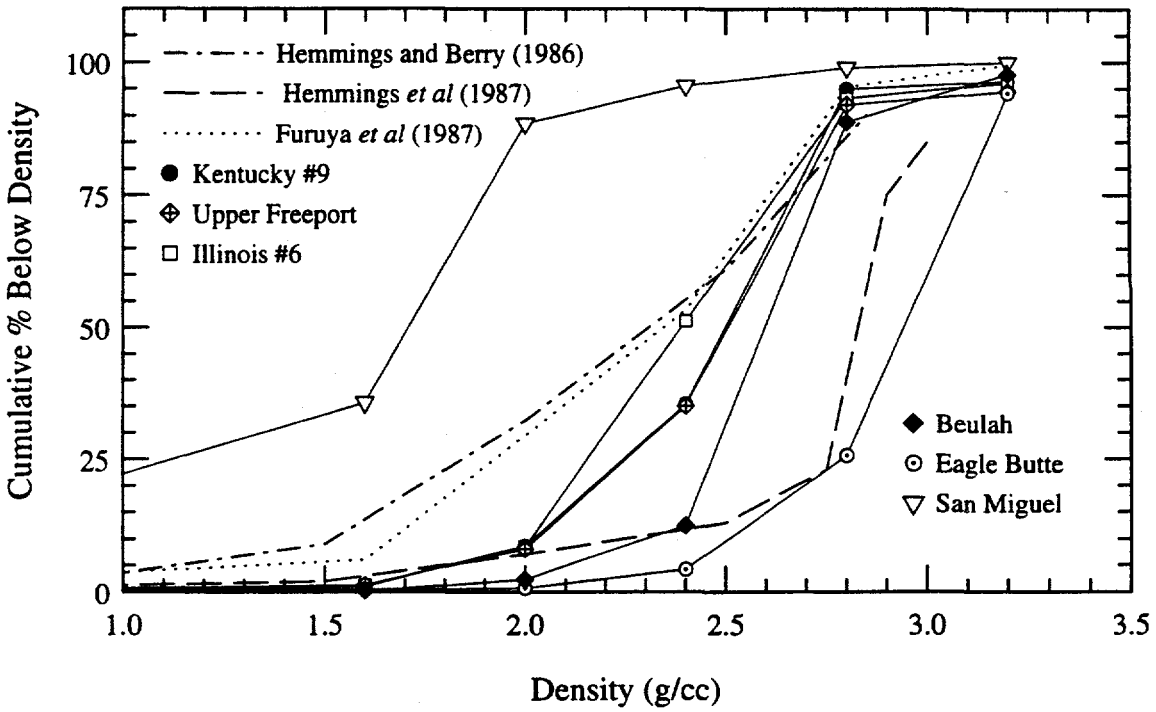

Figure 3.17: Cumulative density distributions, by mass, of the six fly ashes compared with distributions available in the literature. The coal types are sub-bituminous (Hemmings and Berry, 1986) and bituminous (Hemmings *et al*, 1987).

as discussed in Chapter 4 most of the iron in the ash is generally present in a glassy state in the aluminosilicate matrix.

3.5.3 Size Distributions of Density Classified Ashes

For each density class, the smallest possible Multisizer orifice that was not clogged by the larger ash particles in that class was used. Orifices of diameters 30 μm, 50 μm, 70 μm, 100 μm, 140 μm, and 280 μm were used, allowing measurement of particle diameters in the range 1.2 μm to 180 μm. For most classes, 100,000 to 200,000 particles were sampled by the Multisizer in three to four minutes. For a few classes the mass fraction of ash was small and the sample sizes were restricted to 70,000 to 100,000 particles by the amount of ash available.

For effective deagglomeration, the ashes in density Classes 5 and 6 were demagnetized by placing a coil carrying alternating current around a test tube of ash, and then slowly withdrawing the test tube from the coil. The ash particles were thus subjected to a rapidly

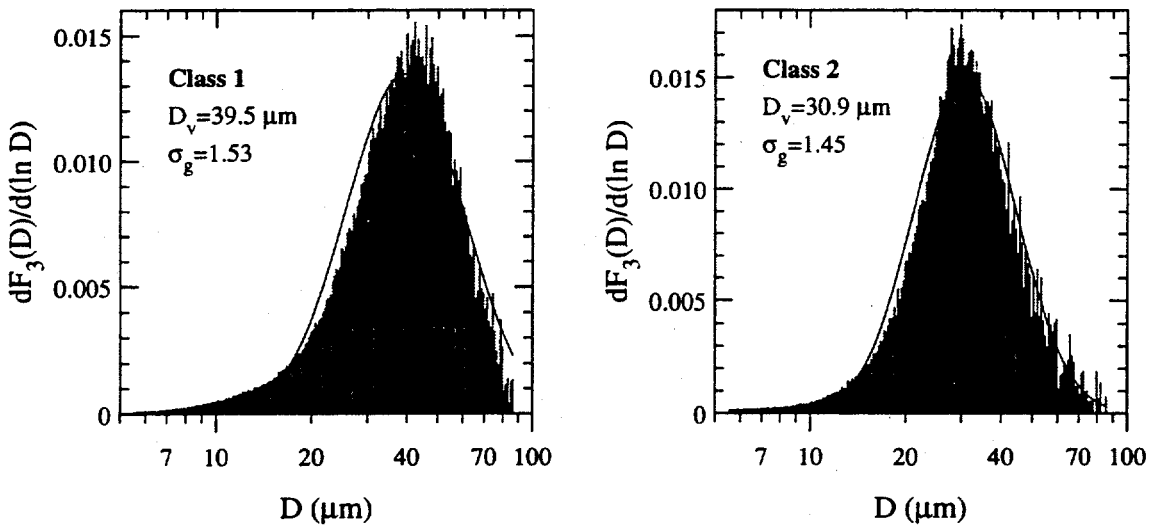

Figure 3.18: Differential size distributions of density classified Upper Freeport ash with best-fit lognormal functions. D_v for these classes are much larger than for the whole ash because they are largely cenospheric.

alternating magnetic field that gradually reduced to zero as the tube was removed a few feet from the coil. As a result the magnetic domains within the particles were randomly oriented causing the particles to be demagnetized.

To keep the particles in the density Classes 5 and 6 in suspension, small quantities of glycerol were added to the electrolyte to increase both the density and viscosity. The calibration of the Multisizer was checked using monodisperse latex particles, and it was found that the addition of glycerol to the electrolyte did not alter the calibration constant of the Multisizer.

Truncated lognormal functions were fitted to the Multisizer size data in the same way as for the unseparated ashes (Section 3.4.5). While the size parameters for the best-fit lognormal functions of all the ashes are listed in Table 3.5, detailed size distributions are given in Appendix D. The differential volume distributions of the first two classes of the Upper Freeport ash in Figure 3.18 show clearly the lognormal nature of the size distributions. The size distribution of Class 1 is less jagged at the large diameter end compared to that of Class 2 because the sample size for Class 1 is more than twice as large as that of Class 2.

As discussed earlier, the size distribution of unseparated fly ashes have been found to be closely lognormal. However, it is interesting to find that the size distributions of the density classified fractions, too, are remarkably well represented by lognormal functions.

Table 3.5: Size parameters for best-fit lognormal functions for density classified fly ashes. Classes 1–6 correspond to densities > 1.6, 1.6–2.0, 2.0–2.4, 2.4–2.8, 2.8–3.2, and > 3.2 g/cc, respectively. D_v, a, and b are in μm. The size parameters corresponding to unseparated ash are included in the last row for comparison.

Class	Kentucky #9			Upper Freeport			Beulah		
	D_v	σ_g	(a,b)	D_v	σ_g	(a,b)	D_v	σ_g	(a,b)
1	37.9	1.54	3.5,63.0	39.5	1.53	4.9,88.0	73.5	1.58	4.9,88.0
2	24.2	1.74	3.5,63.0	30.9	1.45	4.9,88.0	42.6	1.48	9.8,180.0
3	12.4	1.88	2.4,43.0	16.9	1.98	3.5,63.0	29.0	1.66	4.9,88.0
4	7.2	1.96	1.7,33.0	6.7	1.78	1.7,33.0	9.1	2.32	2.4,43.0
5	21.6	1.99	4.9,88.0	22.0	2.93	3.5,63.0	25.6	1.98	4.9,88.0
6	24.0	1.93	4.9,88.0	20.7	1.85	3.5,63.0	28.4	1.95	4.9,88.0
Ash	10.6	2.26	1.2,63.0	9.3	2.80	1.2,63.0	12.8	2.95	1.2,63.0

Class	Illinois #6			Eagle Butte			San Miguel		
	D_v	σ_g	(a,b)	D_v	σ_g	(a,b)	D_v	σ_g	(a,b)
1	63.4	1.84	9.8,180.0	47.4	1.39	9.8,180.0	94.6	2.31	9.8,180.0
2	30.8	1.65	4.9,88.0	36.9	1.56	9.8,180.0	69.8	2.60	9.8,180.0
3	13.9	2.23	3.5,63.0	33.7	1.88	9.8,180.0	30.9	2.59	9.8,180.0
4	7.5	2.23	2.4,43.0	24.7	1.88	4.9,88.0	42.4	2.56	9.8,180.0
5	14.5	2.75	2.4,43.0	8.9	2.33	2.4,43.0	73.7	2.67	9.8,180.0
6	37.0	2.12	4.9,87.0	21.0	1.80	3.5,63.0	–	–	9.8,180.0
Ash	9.7	3.02	1.2,63.0	13.7	3.45	1.2,63.0	32.2	2.89	1.2,180.0

Classes 1 and 2 have smaller values of σ_g compared to the other classes, indicating that the cenospheres have narrower size distributions than the non-cenospheric particles. The exception is the San Miguel ash, which is almost entirely cenospheric. The values of σ_g for most classes lie in the range $1.2 < \sigma_g < 2.0$, with the maximum value applying to the class with the largest mass fraction. The unseparated ash encompasses all diameter classes and has the highest σ_g (Table 3.5).

It may be noted that σ_g cannot be used to compare breadths of size distribution for two truncated lognormal distributions, one with $\eta \to 0$ and the other with η far from zero (see Section 3.4.5). Such cases occur for a few density classes where the truncated lognormal functions are not the most appropriate functions for representing size distributions, e.g., Class 5 of Upper Freeport ash, where σ_g actually exceeds that of the unseparated ash. Even in this case the function *does* represent the actual size distribution quite well. However, the function parameters may not have much physical significance.

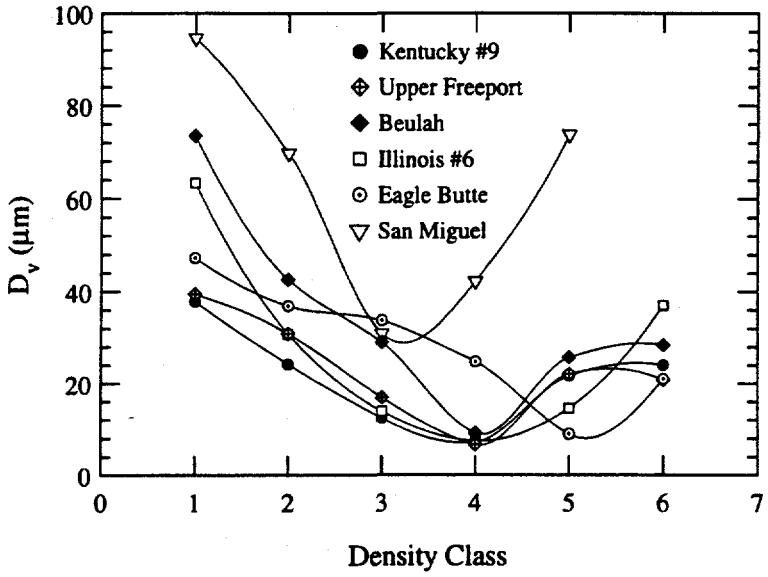

Figure 3.19: The distribution of the volume median diameter, D_v, of the density classified ashes as a function of the density class.

In Figure 3.19, it is seen that for all ashes, D_v has a V-shaped distribution when plotted as a function of density (class). The lightest class (containing thin-walled cenospheres with the outer to inner diameter ratio closest to unity) also has the largest median diameter. The median diameters decrease progressively for Classes 2 and 3. Class 4, having the smallest D_v and containing no cenospheres has the largest mass fraction for four of the ashes. (For the Illinois #6 ash, the mass fractions in Classes 3 and 4 are almost equal.) The two exceptions are Eagle Butte and San Miguel. The Eagle Butte ash, with its high calcia content, has the smallest size and largest mass fraction in Class 5. For the San Miguel ash, containing 95% cenospheres by mass, the smallest D_v is in Class 3, the maximum mass fraction is in Class 2, and the average density is in Class 1.

It is reasonable to expect that the average density of each ash, ρ_{ash}, will belong to the class containing the highest mass fraction of the ash. However, it is observed from Tables 3.2, 3.4, and 3.5 that the average density of each ash falls in the class containing the second highest mass fraction of ash, which is the class just below that containing the highest mass fraction. This skewness probably arises because the median diameters of ashes in Classes 1 and 2 are larger than those in Classes 5 and 6.

A possible formation mechanism for cenospheres is a process similar to glass blowing, when a molten ash droplet on the char particle's surface blocks a pore emitting gas under

pressure. If two molten ash particles of comparable diameters are subjected to the blowing action unequally, the particle that is 'blown' more will produce a cenosphere with a larger diameter, a thinner wall, and a lower density. This observation is borne out in the first three classes where the median diameters increase as the class number decreases from 3 to 1.

A possible explanation for the relatively large sizes of denser, iron-rich particles may lie in their formation processes. It is likely that coal particles that are high in pyrite content do not decrease in size as much as coal particles of average mineral content. A larger mass fraction (i.e., the carbon) of the latter class of coal particles convert to gaseous form during combustion. As a result, when the former burn, the ash residue is larger than for the latter class.

For all the ashes except San Miguel, the class with the largest mass fraction (Class 5 for Eagle Butte, Class 4 for the rest) also has a median diameter that is the smallest among the density classes and closest to the median diameter of the unseparated ash. The ash particles in this class contain few bubbles and are the most representative of the unseparated ash. Density Class 5 (2.8–3.2 g/cc) contains particles that are rich in iron and other relatively heavier oxides (especially calcia for the Eagle Butte ash). These oxides are present in ash particles with a broad range of diameters. Hence this class has the highest value of σ_g, with the exception of the Beulah ash.

The concentration of iron oxide in relatively large ash particles in density Classes 5 and 6 implies that such particles are few in number. A CCSEM sample size of a few thousand particles is not statistically large enough to detect sufficient numbers of such particles. This problem is discussed in Chapter 4, Section 4.6.1. The location of the iron is especially important for optical characterization because iron plays a dominant role in infrared radiation absorption mechanism in the wavelength range 1–4 μm.

3.5.4 Cenospheric Content of the Ashes

Among the major constituent oxides of essentially all ash particles, the one with the lowest density is silica (density=2.2 g/cc; see Table 4.11). Hence, it is reasonable to assume that all ash of density <2.2 g/cc is, to varying degrees, cenospheric. The cenospheric fraction is thus defined herein as the ash fraction, by mass, with density below 2.2 g/cc. Centrifugal separation was carried out with liquid of density 2.2 g/cc on the six ashes to determine

Table 3.6: Ash mass fraction with density <2.2 g/cc, and the percentage of total cenospheric mass contained in this density range.

Fly Ash	Mass %
Kentucky #9	19.3%
Illinois #6	14.6%
Upper Freeport	23.9%
Eagle Butte	3.6%
Beulah	7.7%
San Miguel	96.9%

their cenospheric content. The results are shown in Table 3.6. It is seen that the San Miguel ash is almost entirely cenospheric while the calcia rich Eagle Butte ash has very few cenospheres. The three bituminous ashes have cenospheric contents varying between 14% and 24%.

There are two sources of uncertainty in this method for determining cenospheric content. First, this method cannot detect cenospheres with particle density greater than 2.2 g/cc. However, SEM examination of sections of ash particles showed that only a small fraction of the heavier ash particles (ρ >2.2 g/cc) are cenospheric. Second, the small ash particles that cause some of the cenospheric distributions to be bimodal are probably not cenospheres. As discussed in Appendix B, some of the smaller non-cenospheric ash particles are carried over into the lighter fraction during centrifugal separation. This artifact results in an overestimation of the cenospheric content and an underestimation of D_v. However, this overestimation of the cenospheric mass fraction is compensated to some extent because it was not possible to account for a small fraction of cenospheres that have densities greater than 2.2 g/cc. A slightly more accurate estimate of D_v may be obtained by assuming that particles whose diameters are below a cut-off diameter (say 5 μm) are not cenospheric.

For comparison, it is noted that Casuccio *et al* (1983) estimated the cenospheric content of fly ash sampled from a coal-fired boiler at 32.6% by mass. Hemmings and Berry (1988) noted that at least 50% of the mass of the ashes they studied (generated from coals of different ranks) had true-particle densities (i.e., actual densities) less than that expected from solid materials of their composition.

From Tables 3.4 and 3.6, it is seen that the ash fraction with ρ <2.0 g/cc is only 8%. Thus ~16% of the ash mass (two-third of the cenospheres) have ρ between 2.0 g/cc and

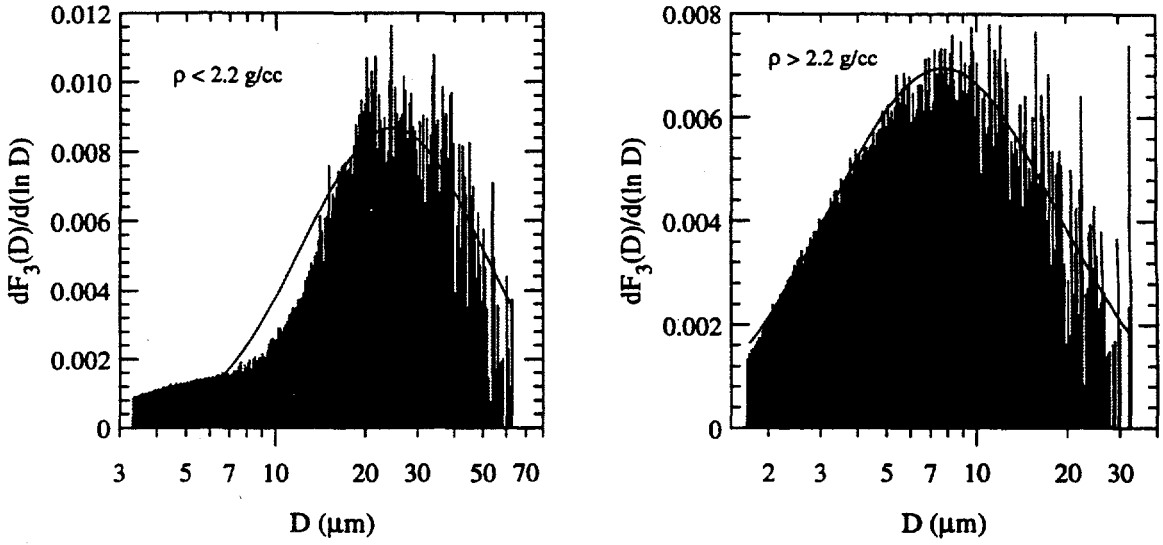

Figure 3.20: Differential size distributions of cenospheric (<2.2 g/cc) and non-cenospheric (>2.2 g/cc) Upper Freeport ash.

Table 3.7: Ash mass fraction with density 2.0< ρ <2.2 g/cc.

Fly Ash	Mass %	% of Cenospheres
Kentucky #9	10.7	55.4
Illinois #6	6.2	42.5
Upper Freeport	15.9	66.5
Eagle Butte	2.9	80.6
Beulah	5.4	70.1
San Miguel	8.4	8.7

2.2 g/cc, i.e., with $\lesssim$ 10% void. Similarly, for the other ashes, it is seen (in Table 3.7) that a large fraction of the cenospheres (~40–70%) contain such small voids. Again, the prominent exception is San Miguel, where most of the cenospheres are thin-walled. The influence of the gas bubbles on radiative transfer is further discussed in Secion 6.2.1.

The size distributions of both density fractions were measured with the Coulter Multisizer for all the ashes except the San Miguel ash, the latter being almost entirely cenospheric. Figure 3.20 shows the volume distributions for the two fractions of the Upper Freeport ash. Distributions for other ashes are given in Appendix D. Clearly, the median diameters of each fraction would decrease slightly if multiple orifices had been used, as in the case of

Table 3.8: Size parameters for best-fit lognormal functions for ash mass fractions separated using liquid of density 2.2 g/cc. D_v, a, and b are in μm. Sufficient amounts of San Miguel ash denser than 2.2 g/cc were not available.

Ash	Density <2.2 g/cc			Density >2.2 g/cc		
	D_v	σ_g	(a,b)	D_v	σ_g	(a,b)
Illinois #6	32.5	1.63	4.9,88.0	13.7	3.40	1.7,33.0
Kentucky #9	19.3	1.88	3.5,63.0	8.4	2.10	1.7,33.0
Upper Freeport	24.7	2.01	3.5,63.0	7.7	2.41	1.7,33.0
Eagle Butte	40.0	1.96	9.8,180.0	14.4	3.21	1.7,33.0
Beulah	43.3	1.61	4.9,88.0	13.4	2.17	3.5,63.0

unseparated ashes. In any case, the distributions appear to be lognormal, and the parameters for the best-fit lognormal functions for all the ashes (except San Miguel) are presented in Table 3.8. It is seen that D_v of the cenospheric fraction of an ash is two to three times larger than D_v of the fraction with ρ >2.2 g/cc.

3.6 Summary

SEM and optical microscopic examinations of ash samples confirmed that the ash particles are predominantly spherical. The non-spherical fraction consist of a variety of morphological types, which is consistent with previously published observations. Comprehensive bulk physical characterization of six fly ashes were performed with respect to the size and density distributions, and correlations between them.

The dynamic range of the Coulter Multisizer, used here for size measurement, was expanded by devising a technique for combining data obtained with multiple orifices. Truncated lognormal functions, whose properties are discussed, were fitted to the ash size data measured in the range $\approx$1–200 μm. Use of this function allows detailed information on the ash size distribution to be stored compactly using four quantities: D_v, σ_g, a, and b. The best-fit parameters, D_v and σ_g, are found to be in the range 9.0–15 μm and 2.0–3.5, respectively, for all ashes (collected in cyclone and baghouse), with the sole exception of the large censopheric San Miguel ash particles which have a large D_v of 32.2 μm.

Density classification showed that for most ashes, 80% of the mass belongs to the density range 2.0–2.8 g/cc. Of the two exceptions, the calcia-rich Eagle Butte is significantly denser

than the rest, with ≈75% of the mass having density higher than 2.8 g/cc. The San Miguel ash consists primarily of cenospheres (>95% by mass), and consequently has a low average density of 1.73 g/cc. For the remaining ashes, the cenospheric content was estimated to fall in the range 3–24%. A large fraction of the cenospheres were found to contain small voids, possessing inner to outer diameter ratio $\lesssim 0.1$.

Size measurements of the density classified ashes showed that the ashes in the extreme classes of the density scale have larger median diameters and narrower size distributions compared to the ash in classes close to the average densities. The cenospheric ash fractions have median diameters that are 2–3 times larger than that of the non-cenospheric fractions. Truncated lognormal functions were found to fit the size data very well for the majority of the density classes.

Chapter 4

Chemical Characterization of Fly Ashes

4.1 Introduction

In Chapter 2, it was explained that the optical properties of a fly ash particle (at a specified wavelength) depend on its composition. Many previous studies (e.g., Ramsden and Shibaoka, 1982) have shown that ash chemical composition tends to vary significantly from particle to particle. For this reason, knowledge of bulk composition of the ashes is insufficient for radiative heat transfer calculations, and information of compositional variation is needed from microanalytical data of individual particles.

In this Chapter, the composition variability among ash particles is described using distribution functions defined in Section 4.3. CCSEM measurements of the six ashes were made at University of North Dakota Energy and Environment Research Center (UNDEERC). The composition distribution functions were used in a search for particle size–chemical composition relationship. Additionally, bulk compositions were determined using electron microprobe analysis on slags samples prepared by melting the whole ashes. The CCSEM and slag compositions were used both for cross-checking as well as contributing to a more complete picture of composition distribution, especially for iron. A scheme for creating broad composition classes is proposed based on the microanalytical studies. Refractive index classes are then created from the composition classes, and the optical properties of melts given by Ebert (1993).

For measurements on single ash particles, it is necessary to prepare a representative distribution of ash particles on a SEM stub that are well-deagglomerated. After some experimentation and a survey of existing techniques, the freeze-drying method described below was used. The technique produced satisfactory well-deagglomerated samples on a repeatable basis.

Knowledge of the densities of ash particles are needed for determining their optical properties. Empirical 'effective' densities for the component oxides discussed in Section 4.7 allow fairly accurate estimates of slag densities. Finally, a comparison of the ash size distributions obtained with CCSEM and Coulter Multisizer data is presented*.

4.2 Background

Microanalytical techniques such as energy dispersive X-ray spectroscopy associated with scanning electron microscopy (SEM/EDS) has been used for analysis of individual ash particles for quite some time (Rothenberg *et al*, 1980). However, microanalysis of a statistically large sample (>1000 particles) has become a routine procedure only recently with the development of computer controlled SEM/EDS, henceforth referred to as CCSEM (e.g., Barta *et al*, 1990).

There have been previous studies investigating the dependence of composition on ash particle size. Kaufherr and Lichtman (1984) compared the compositions of submicron (number mean diameter 0.6 μm) ash particles with that of particles of diameter 2–7 μm. The total sample size was sixty-six. Except for an increase in the sulfur content in the submicron class, no chemical or morphological differences were detected between the two classes in an average sense. Lichtman and Mroczkowski (1985) concluded that there were no noticeable size-composition correlations for the submicron ash. However, this conclusion was based on very small sample sizes (15–20) and is statistically questionable. They also noted a bimodality in the ash size distribution centered at $\approx$0.5 μm and 5 μm for the two classes, which appears to confirm the observations of Flagan and Friedlander (1978).

Davison *et al* (1974) made careful measurements for size-composition relationship for twenty-five elements using various microanalytical techniques such as spark source mass spectroscopy, optical emission spectrography, atomic absorption spectroscopy, and X-ray

*The comparison is included in this Chapter for organizational convenience, although it is closely related to physical characterization.

fluoroscence spectroscopy. They found statistically reliable results showing that trace element concentrations increase with decreasing particle diameter.[†] While Si was seen to increase slightly with particle size, no correlation was seen for the other two major constituents, Ca and Al. Hemmings and Berry (1986), and Hemmings *et al* (1987) concluded from chemical analyses of their size-classified ashes that there were no distinguishable trends for the major constituent oxides.

A few previous investigators have used X-ray diffraction studies to quantify the amorphous (glassy) fraction of the ash. Del Monte and Sabbioni (1984) used this technique together with optical microscopy and SEM/EDS in morphological and composition studies of fly ash sampled in a power plant stack by means of an isokinetic sampler. They concluded that 90% (by mass) of the particles studied were composed of aluminosilicate glasses with variable amounts of other oxides. Other categories defined were spherical, iron-rich particles containing variable amounts of magnetite, hematite, and maghemite ($\gamma-Fe_2O_3$), spherical rutile particles, spherical lime particles, and incompletely melted mineral particles such as quartz and mullite. The last categories together constituted only 1% of the mass.

Detailed studies on individual ash particles in recent years show that there is some degree of compositional inhomogeneity within a particle, on both nanometer (nm) and micrometer (μm) length scales (Hemmings and Berry, 1988; Qian *et al*, 1989). The nm scale inhomogeneity, observed using transmission electron microscopy (TEM) and analytical electron microscopy (AEM), is apparently due to amorphous glass separation, and should not affect infrared optical properties where μm scale homogeneity is relevant. However, semiquantitative studies (EDS) that attempt to show μm scale inhomogeneity do not address the question of absorption correction for X-rays emanating from different parts of the spherical ash particle. Neither do they convince the reader that particles of diameter 1–5 μm can be adequately polished to neglect absorption errors in the case of microprobe analysis of ash sections[‡].

As discussed in Chapter 3, the primary source of density inhomogeneity in fly ash, however, is the presence of cenospheres. The detailed studies of a density and size-classified sub-bituminous and a bituminous ash by Hemmings and Berry (1986), and Hemmings *et al*

[†]The reason for this correlation is that trace elements such as Pb, Tl, Sb, Cd, Se, As, Ni, Cr, and Zn generally have high vapor pressure. Hence, they vaporize during combustion, and heterogeneously condense preferentially on the fine ash particles, or homogeneously to form fine particles.

[‡]See Appendix E for a detailed discussion of the errors associated with EDS.

(1987), respectively, were briefly described in the previous Chapter. They obtained the average chemical composition of all classes (density and size) using ICP (inductively-coupled plasma) spectroscopy. On the basis of the results, the authors proposed the existence of two primary types of glasses in the ash: Glass I — which is predominantly aluminosilicate and contains the cenospheric ash fraction, and Glass II — a calcium aluminosilicate glass that constitutes the higher density particles that are non-cenospheric. XRD analysis showed that small numbers of crystalline particles are present ($\approx$10%, by mass), consisting almost entirely of quartz and mullite, and some large iron-rich particles (discussed later in Section 4.6.1. Quartz is present mainly in the density class 2.0–2.5 g/cc, while mullite is concentrated in the lighter fractions (<2.2 g/cc). Mullite is not a naturally occurring mineral in coal, but is formed during the decomposition of clays. Whereas quartz was found to occur as single particles, the mullite was found to be associated with the larger and less dense glassy particles.

Although their chemical analyses of size-fractionated ashes do not show any major differences between the classes, marked differences are seen among density classes. Figure 4.1 was drawn using their tabulated data in terms of the glass composition for the major oxides in the various density classes. For the sub-bituminous ash, the calcia content increases sharply beyond the 2.3 g/cc density class. The Fe_2O_3 content increases steadily with density. In the bituminous ash, the heaviest class is high in alumina which replaces Fe_2O_3 as the second largest constituent. The SiO_2 content remains constant in the size classes $\lesssim$ 2.2 g/cc (the cenospheric ashes), and then decreases steadily, dropping to two-thirds of its average value in the highest density class, where the other three oxides constitute 50% of the mass. Thus, the increase in density is caused by an increase in the degree of substitution of Si in the glass by each of the other three elements, Al, Ca, and Fe.

4.3 Composition Distribution Functions

The mineral matter in coal is present in equilibrium, crystalline phases[§], generally having fixed compositions. Identification of these minerals (illite, kaolinite, calcite, etc.) is useful in tracing their chemical transformation through intermediate stages of coal combustion. However, by the end of char burnout, the molten mineral matter is essentially a mixture of various molten phases. The partitioning of these phases among ash particles of all

[§]It is conventional in coal research to use this geological/mineralogical term.

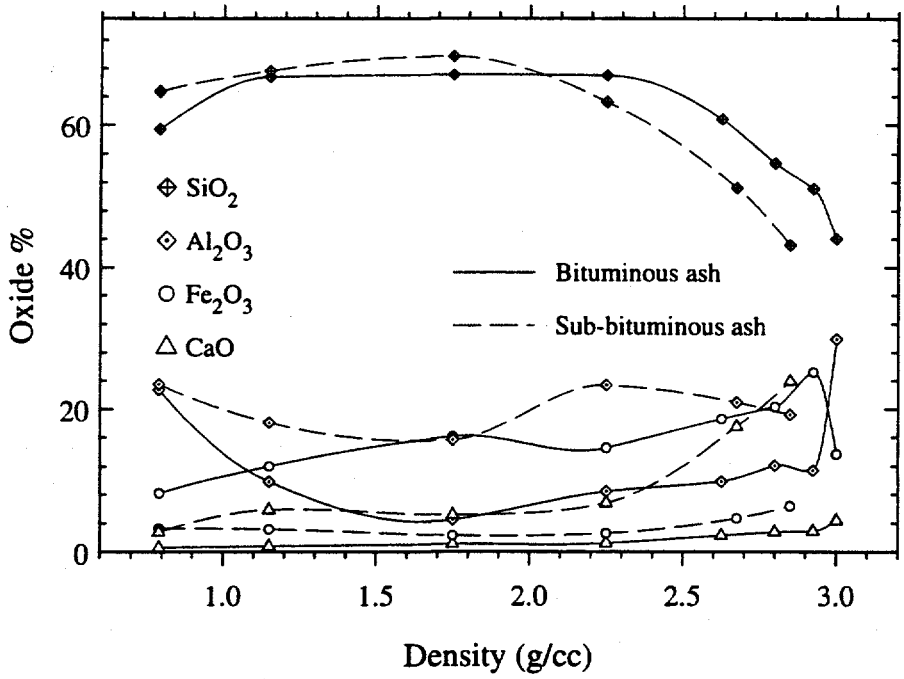

Figure 4.1: Chemical composition of ashes as a function of particle density class (data of Hemmings and Berry, 1986, and Hemmings *et al*, 1987). The composition is plotted against the mid-point of each class, except at the two extremes.

sizes depends on several factors, primarily among which are the size and contiguity of the mineral phases, maximum temperatures, char burnout rates and fragmentation mechanics, combustor residence times, and the oxidizing/reducing nature of the environment. As they leave the flame region of the combustor, the ash particles are rapidly quenched to a non-equilibrium glassy state.

The result of these complex processes is an ash composition distribution that is far more continuous than the original mineral phases. There are classifications of fly ash in the literature where a particle is assigned a 'mineral class' with an elemental ratio closest to that of the particle. Such classifications, which may be of some use in studies of ash formation mechanisms, is not relevant to optical characterization. It is noted that equilibrium mineral phase classification is valid for ash analyses based on low temperature ashing, where there is no melting of mineral matter.

Because of the continuous nature of ash composition distribution, it is appropriate and helpful to use mathematical functions to describe inter-particle compositional variation. The following four functions are proposed to describe the composition distribution within

a specific ash particle, as well as size-composition relationships.

1. The mass fraction (or %) of oxide o within an ash particle represented by X_o. For j detected oxides, $\sum_{o=1}^{o=j} X_o = 1$. For a CCSEM sample of p particles, the (number) average content of oxide o would then be given by $\bar{X}_o = \frac{1}{p}\Sigma_{k=1}^{k=p} X_{o,k}$.

2. The second function, $\delta_o(D)$, is so defined that $\delta_o(D)\,\mathrm{d}D$ represents the mass fraction (or %) of oxide o present in particles with diameters between D and $D + \mathrm{d}D$. Integrating $\delta_o(D)$ over all possible diameters yields the mass fraction of oxide o in the ash.

3. The function $\xi_o(x, D)$ is defined so that $\xi_o(x, D)\,\mathrm{d}x\,\mathrm{d}D$ represents the volume fraction of ash with mass percentage of oxide o between x and $x + \mathrm{d}x$ made up of particles with diameters between D and $D + \mathrm{d}D$. Cumulative functions based on $\delta_o(D)$ and $\xi_o(x, D)$ are developed later in the chapter.

4. Finally, there is a function, $\zeta_o(x)$, such that $\zeta_o(x)\,\mathrm{d}x$ represents the number fraction of ash particles with mass percentage of oxide o between x and $x + \mathrm{d}x$.

The CCSEM measurements detected twelve elements in the ash samples: Si, Al, Fe, Ca, Mg, Na, K, Ti, Ba, S, P, and Cl. For microprobe measurements on slags, appropriate detectors and standards were used to measure the composition in terms of these twelve elements. The elemental compositions were converted to oxide compositions using the following formulae: SiO_2, Al_2O_3, Fe_2O_3, CaO, MgO, Na_2O, K_2O, TiO_2, BaO, SO_3, and P_2O_5. Although it is the molar content of an oxide in glass that affects the latter's structure, and thus its optical properties, almost all published data pertaining to coal and ash composition are in terms of mass fractions. Hence, this representation is used in most of the results in this report, especially when comparisons are made with published data. However, in some of the more qualitative presentations of the same data (as in the case of ternary plots), the molar basis is used to familiarize the reader with the alternative representation.

4.4 Computer Controlled SEM/EDS (CCSEM) of Ash Particles

The primary objectives of the CCSEM study for chemical compositions of individual ash particles were to determine the composition distribution of the predominant oxides among

the particles (i.e., mean and standard deviation), and to establish the presence, or absence, of a size-composition correlation. Additionally, size distributions obtained from SEM measurements of geometrical diameters of ash particles was compared with size distributions obtained using the Coulter Multisizer.

SEM/EDS (energy dispersive X-ray spectroscopy associated with scanning electron microscopy, also called SEM/EDAX) is now a well-established technique for determining approximate chemical compositions. The technique is significantly faster than more accurate methods such as electron microprobe analysis. With the addition of computer control (CCSEM), it can be used to measure compositional variations in powders by make measurements on statistically significant sample sizes (>1000 particles), with respect to ten or more elements. EDS is used as an accessory with existing SEM facilities by the addition of an X-ray detector, and computer software for 'standardless' analyses.

In the CCSEM system, the electron beam scans the particle field in specified step sizes using the backscattered electron intensity to distinguish particles from the background (usually a graphite stub). On detecting a particle, the computer control reduces the step size and uses a suitable algorithm to detect the centroid of the projection of the particle on the stub. For spherical ash particles, this centroid is directly above the geometrical center of the particle. The electron beam is then focused around the centroid, and the whole particle may be 'bracketed' to obtain an 'average' X-ray spectrum that is accumulated by a windowless Si(Li) detector for a period of few seconds. A good description of the physics of SEM/EDS can be found in the Kevex handbook (1988), or in standard textbooks (e.g., Goldstein, 1984). Casuccio *et al* (1984) presents a good introductory summary.

The limitations in the accuracy of the measured composition of a single particle is quite acceptable for our purposes, since the data are used to create relatively broad composition classes. A detailed discussion of the semi-quantitative nature of EDS, particularly for measurements on single particles, is given in Appendix E.

4.4.1 Preparation of Ash Sample for SEM Analysis

Through the steady development of microanalytical techniques in the last fifteen years, the distribution of mineral matter in coal has been extensively studied (Huggins *et al*, 1980; Moza and Austin, 1983). The mineral matter embedded in the coal matrix is generally

present as irregular particles with median diameters[¶] >30 μm. In this case, EDS samples can be prepared by embedding coal particles in epoxy, and grinding and polishing to reveal mineral cross-sections.

However, in the case of fly ash particles, there are two problems which makes it necessary to adopt a different approach for sample preparation. First, collected ash is always present in a highly agglomerated state. To study the composition of single particles of diameter $\lesssim$ 5 μm, the ash must first be deagglomerated, using an effective method such as ultrasonic agitation of a liquid dispersion. Samples must then be prepared using small amounts of ash in order to minimize re-agglomeration. Conventional CCSEM systems reject agglomerates by limiting the departure from sphericity of detected 'particles'. However, the criteria used are often lax (Benson, 1989), allowing many agglomerates to be considered as 'particles'. Thus, in the absence of SEM micrographs, it is possible that some of the studies (e.g., Barta, 1989) may have presented compositions averaged over several small particles as being the composition of a single larger particle. From the results of Chapter 3, it is clear that fly ash has a very broad size distribution with the number of particles increasing with decreasing diameter. In such powders, the agglomeration problem is more pronounced, and several micron-sized particles can remain attached to a large particle without significant departure from sphericity, as detected by the CCSEM software.

Second, the ash particles are glassy, and it is unlikely that particles of diameter 1–10 μm can be ***polished*** using standard grinding and polishing techniques (using grits of similar size). It is more probable that the larger particles will be broken irregularly, while the small particles of diameter 1–3 μm will be detached from the epoxy base during polishing. Additionally, thin-walled cenospheres are easily broken and are soon filled with smaller ash particles and polishing material (commonly alumina), some of which may be retained even after washing (Koch, 1992). In any case, ash particle sections that are smooth enough for electron microprobe analysis do not appear achievable by embedding ash in epoxy and polishing. For this reason, it was decided to make EDS measurements on whole ash particles deposited on SEM stubs. However, initial samples, prepared at University of North Dakota Energy and Environment Research Center (UNDEERC), were found to be in a highly agglomerated state (see SEM picture in Figure 4.2), and could not be used.

A literature survey showed that the preparation of powder samples, representative of the bulk substance, for SEM study is an well-established art. The specific method chosen

[¶]i.e., the diameters of circles of area equal to that of the projected area of the particle.

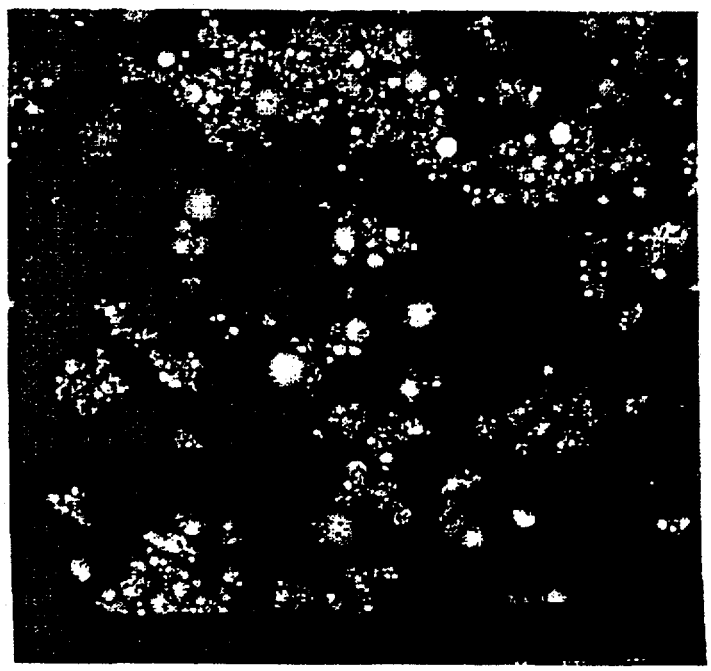

Figure 4.2: SEM sample prepared at UNDEERC. The ash appears to be inadequately deagglomerated.

depends on various factors such as the size range of the particles, the desired accuracy in representing the bulk material, and the degree of deagglomeration desired.

Brown and Teetsov (1978) discussed the most common (and also the most convenient) method of sprinkling the powder on to an adhesive tape mounted on the SEM stub. However, as shown in Chapter 3, for fly ash this method produces highly agglomerated samples, and many of the larger particles are lost during preparation. Lovell and Diamond (1986) describe the use of porous membrane filters for preparation of samples with better electrical contact between the particles and the stub. However, this method results in the formation of agglomerates and is not useful for CCSEM.

The necessity of using liquid suspensions for preparing well-deagglomerated samples is stressed by DeNee (1978). Initially, we prepared samples by ultrasonically deagglomerating the ash in distilled water. A few drops of the suspension were deposited on a SEM stub, and the water was evaporated under low vacuum. Although the resulting sample was deagglomerated, there was noticeable size segregation of the particles on the stub; the

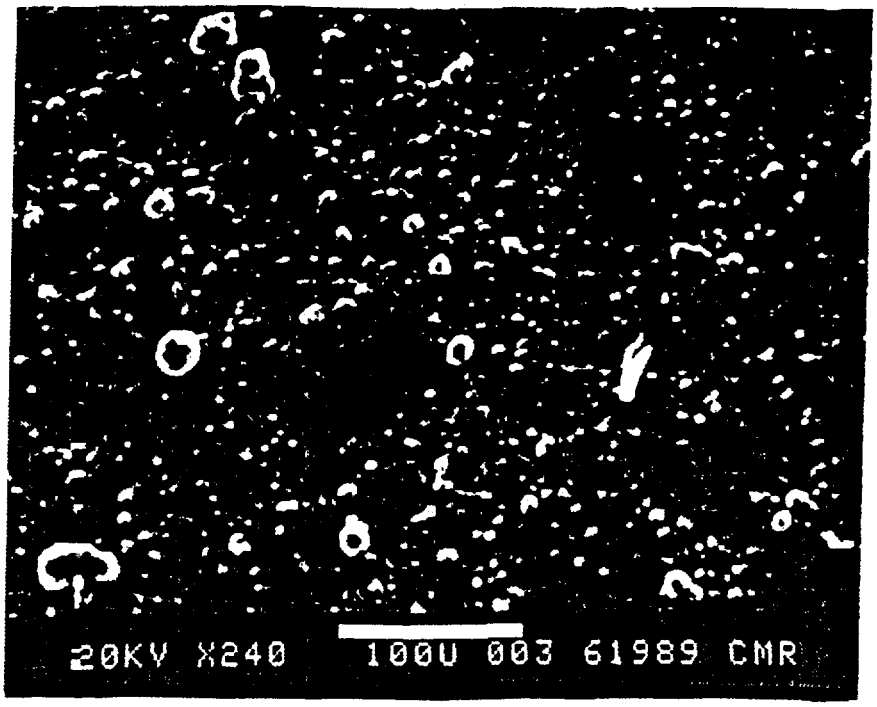

Figure 4.3: SEM sample prepared by depositing a few drops of deagglomerated ash suspension on the stub, and allowing the liquid to evaporate. Note size gradient that has developed from left to right.

larger particles concentrated at the center and the smaller particles predominantly at the periphery (Figure 4.3). This size gradient results from particle migration caused by a surface tension driven flow called the Marangoni effect (Scriven and Sternling, 1960). The liquid, after wetting the stub surface completely, gathers at the periphery with very little liquid at the center. While many of the smaller particles are carried along with the liquid, the larger particles settle rapidly in the central area of the stub.

The size gradient can be avoided by freezing the suspension rapidly, and then sublimating the dispersant under vacuum. This technique, referred to as freeze-drying, is discussed very briefly by Veale (1972), and in somewhat more detail by DeNee (1971). However, no description of the apparatus and other necessary information (e.g., degree of dilution of the suspension) are provided. Hence, further refinement of the technique was needed before satisfactory and reproducible results could be obtained. The choice of a suitable dispersant, and the procedure for preparing a SEM sample by freeze-drying is now discussed.

Table 4.1: Comparison of two proposed ash dispersants (CRC Handbook, 1985).

Property	C_3H_6O	CCl_4
Freezing point	−94.0°C	−22.6°C
Surface tension (dynes/cm) at vapor-liquid interface	23.7 @ 20°C	26.95 @20°C
Vapor pressure (mm of Hg)	400 @ 39.5°C	100 @ 20°C
Viscosity (centipoise)	0.316 @ 25°C	0.969 @ 20°C
Inexpensive?	Yes	Yes
Toxic?	Slightly	Yes

The criteria for selecting a liquid for dispersing the ash are
(a) a relatively high freezing point,
(b) low surface tension to allow the liquid drops to spread evenly over the stub surface,
(c) fairly high vapor pressure (solid in contact with its own vapor), allowing the dispersant to sublime in a reasonable time,
(e) low viscosity so that particles are more mobile and disperse better when agitated ultrasonically, and
(f) relatively inexpensive and preferably non-toxic.

Two liquids that meet many of the above conditions are acetone (C_3H_6O) and carbon tetrachloride (CCl_4). Their relevant properties are compared in Table 4.1. While both liquids are suitable, acetone is clearly preferable.

Initially, about 50 mg of a representative sample of the ash is dispersed in 10 ml of acetone in a beaker. No surfactants are added if the chemical composition of the ash is to be determined. After the sample is deagglomerated in an ultrasonic bath‖ for five minutes, about a dozen drops** of the suspension are transferred to another beaker containing 10 ml of acetone. The suspension is further ultrasonically agitated for a minute. The ash sample is now sufficiently dilute and dispersed, and is ready for the freeze-drying process.

A sketch of the of the freeze-drying apparatus is shown in Figure 4.4. Before liquid nitrogen is poured into the styrofoam bath, the chamber is pumped down to a pressure of a few torr to prevent atmospheric moisture condensing on the stub. The liquid nitrogen cools the aluminium block and the stub to a temperature well below the freezing point of

‖Nominal output frequency = 50 kHz.
**A standard eye-dropper is used for this purpose.

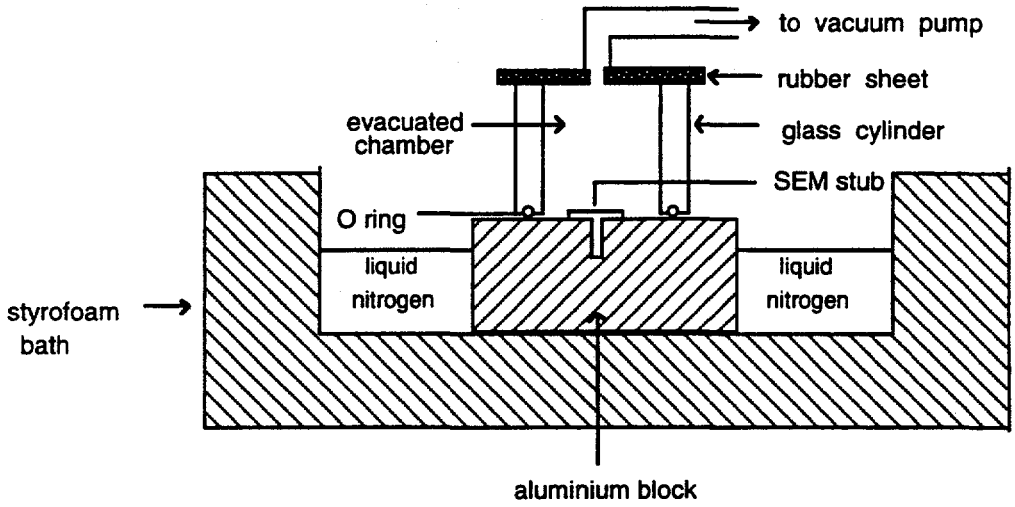

Figure 4.4: Cross-section of the apparatus for preparing CCSEM samples.

acetone liquid in five to ten minutes depending on the size of the block and the quality of the thermal contact between the stub surface and the block. More liquid nitrogen is added as required, since the initial charge boils off rather quickly.

Once the stub surface is sufficiently cooled, the glass cylinder is gently pried loose at the O-ring—aluminium block contact point. Two to three drops of the suspension is placed on the stub surface and the cylinder is replaced on the block. The vacuum pump is operated continuously. The exposure of the stub surface to the atmosphere is kept as short as possible to minimize condensation of water vapor. Additionally, some gaseous nitrogen may be directed towards the stub during the exposure. The liquid should freeze within three to four seconds; if it takes longer, it indicates that the stub had not been cooled to a sufficiently low temperature. The set-up is now left for an hour or so, during which time the solidified acetone sublimes. The transparent cylinder allows one to view the stub surface and determine whether the acetone has fully sublimed. The stub and the block are now warmed to room temperature[††] before the pressure is raised to atmospheric, again to prevent condensation of water vapor from the air on the stub. The stub is now ready to be coated for SEM microanalysis.

Figure 4.5 shows a typical sample prepared by this technique. Very few agglomerates are evident. The smaller particles (1–5 μm) are sufficiently separated for EDS analysis of

[††] A heat gun can be used to speed up the process.

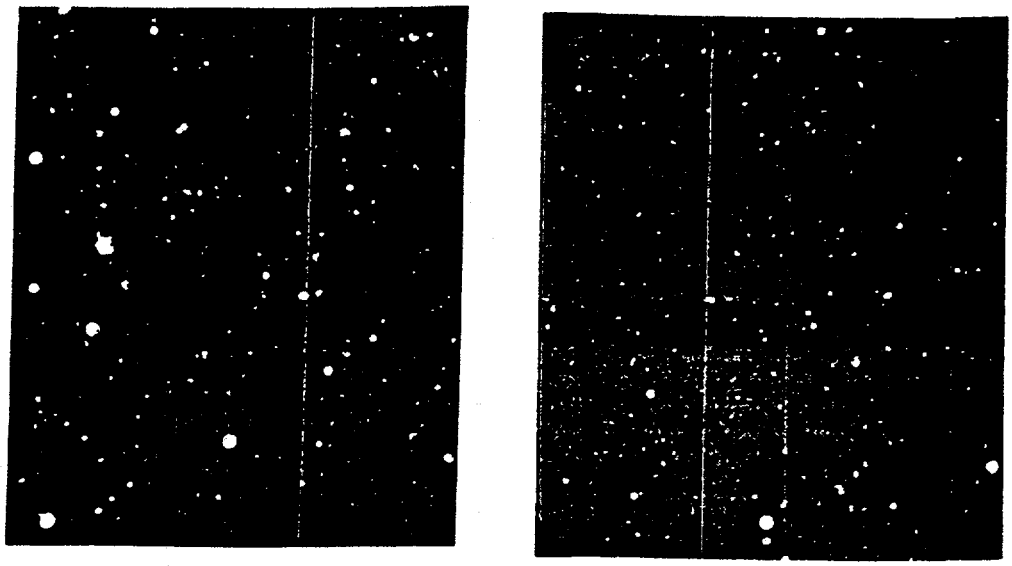

Figure 4.5: SEM sample prepared by freeze-drying of deagglomerated ash. Upper Freeport (left) and Eagle Butte (right) ash samples.

individual particles. It should be noted that the quality of the sample is very sensitive to the ash loading in the acetone. For example, doubling the initial ash loading (to 100 mg of ash in 10 ml of acetone) results in significant agglomeration on the stub.

4.4.2 Analysis of SEM data

The samples prepared on graphite stubs were coated with a thin layer of carbon to prevent charge buildup during SEM analysis before being sent to UNDEERC. For each sample, the results were given as characteristic X-ray counts, which are proportional to the elemental concentrations. Sample sizes ranged from 950 (for Kentucky #9) to 1887 (Eagle Butte), with an average of 1385 particles per sample. The elemental data for each composition were converted to oxide composition, on both mass and molar bases. Only particles of diameter larger than one micron were chosen for analysis by the CCSEM system. The diameter of the largest particle, later referred to as D_{max}, varied over the range 17–47 μm from sample to sample.

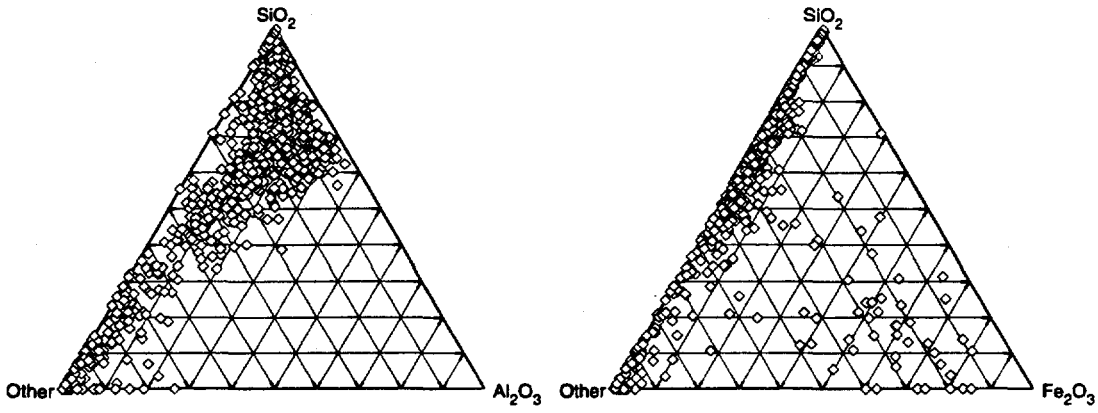

Figure 4.6: Ternary plots for molar composition distribution of Kentucky #9 fly ash. Each point represents a particle.

A convenient method of presenting CCSEM results is by ternary plots, as shown in Figure 4.6 for the Kentucky #9 bituminous ash. To determine the SiO_2:Al_2O_3 ratio for a particle, a straight line is drawn through the particle from the vertex labelled 'Other' to the opposite side. The desired ratio is the distance of the base of this line from the Al_2O_3 vertex, to the distance from the SiO_2 vertex. Figure 4.6 clearly shows the broad composition distribution of the ash. No particles having 50% or more alumina are seen. There is a clustering of particles in the general region of SiO_2:Al_2O_3= 3:1. In the SiO_2–Fe_2O_3 plot, it appears that there are very few particles that are rich in iron (more than >60% mole). The particles are concentrated close to the SiO_2–Other side of the triangle, suggesting that the iron in most ash particles is incorporated in the aluminosilicate matrix. Ternary plots for the other ashes are presented in Appendix G. Of interest is the calcia-rich Eagle Butte ash which has negligible particles that are pure aluminosilicates. Many of the high silica particles contain little or no alumina.

A useful means of looking for size-composition relationship is by averaging the compositions of ash particles over increments of one micron. In mathematical terms, the *average* concentration of oxide o for all ash particles assigned to the diameter bin i microns is given by

$$\bar{\delta}_o(i) = \frac{\int_{i-0.5}^{i+0.5} \delta_o(D)\ D^3\,\mathrm{d}D}{\int_{i-0.5}^{i+0.5} D^3\,\mathrm{d}D}$$

This differential distribution for the Illinois ash is shown in Table 4.2. Particles with diameter <8 μm constitute ≈92% by number of the sample, and have sufficiently large numbers

Table 4.2: Average oxide composition of Illinois #6 fly ash by mass as a function of particle diameter, D (in μm). The number of particles detected in each size class is shown in the second column.

D	No.	Si	Al	Fe	Ca	Na	K	Ba	Ti	Mg	P	S	Cl
1	270	39.1	12.1	18.9	2.5	0.2	2.8	0.8	1.4	0.2	0.6	20.8	0.3
2	213	46.9	13.3	12.9	2.3	0.4	3.0	0.9	1.3	0.2	0.5	18.0	0.4
3	142	53.0	14.4	10.9	3.8	0.1	2.9	0.9	1.5	0.2	0.4	11.6	0.3
4	116	53.8	15.9	10.1	3.1	0.2	2.7	0.7	1.2	0.2	0.3	11.5	0.3
5	72	58.2	14.8	11.6	1.7	0.2	2.5	0.8	1.1	0.1	0.1	8.7	0.2
6	60	60.7	14.5	9.4	2.3	0.1	2.9	0.5	1.1	0.1	0.1	8.0	0.2
7	37	62.7	12.1	8.8	3.8	0.2	2.4	0.6	0.9	0.1	0.2	8.1	0.2
8	35	62.0	15.2	11.3	2.7	0.2	3.0	0.5	0.9	0.1	0.2	3.6	0.3

of particles in each bin. The larger diameter bins contain too few particles, and should not be considered when drawing conclusions on size composition relationships[‡‡]. A minimum bin population of twenty-five particles was chosen arbitrarily for evaluating size-composition relationship. The diameter corresponding to this bin is D_{25}.

It is seen from the table that in the range 1–8 μm, there is a noticeable increase of SiO_2 content with increase in diameter, while no convincing correlation can be seen for the other major constituent oxides. The strongest size-composition dependence is shown by sulfur, which is, however, unimportant for optical properties of the ash. It is often reported that sulfates are preferentially deposited on small particles, which is confirmed by this data. Tables for other ashes are included in Appendix G.

Another way of presenting size-composition relationships is by using a cumulative composition function, $C_o(D)$, defined as

$$C_o(D) = \frac{\int_0^D \delta_o(x)\, x^3\, \mathrm{d}x}{\int_0^D x^3\, \mathrm{d}x}$$

Thus, $C_o(D)$ is the average mass fraction of oxide o for all ash particles with diameters $< D$ μm. Figure 4.7 shows the distributions $C_o(D_{25})$ for all six ashes. It is noted that only two ashes, Illinois #6 and Kentucky #9, have an average Fe_2O_3 content >5%. While the iron content shows a very small decrease with increasing diameter for the Illinois and Kentucky ashes over the whole size range, it shows no dependence on size for the other

[‡‡]For samples sizes of 1000–1500 particles, the numbers of particles drop sharply for diameters $\gtrsim 5$ μm. In Appendix F standard statistical methods are used to assess the limitations imposed by sample size.

four. Similarly, CaO shows a slight decrease with increasing diameter for some of the ashes. The positive size-concentration correlation for SiO_2 noted above holds for five of the ashes, excepting the Eagle Butte ash, which has more calcia and alumina than silica. Alumina content does not show any consistent trend with particle size. The fraction undersize graphs in Figure 4.7 show that there are very few particles in the samples with $D > D_{25}$.

The size-composition correlation for silica, however, is weak enough to be neglected for refractive index determination because the latter changes more slowly than SiO_2% with particle diameter. Overall, it is concluded that for the overwhelming volume of the ash (>90%) and from the viewpoint of optical properties, there is no significant size dependence of composition. As discussed later, the remaining small fraction (<10%) contains relatively large, iron-rich particles whose composition is not reliably determined for the CCSEM samples used here. Similar observations of size independence of composition with respect to the major oxides are reported by Mamane *et al* (1986) who studied Al/Si distribution as a function of particle diameter, and Hemmings and Berry (1986) who analysed the average composition of size-classified ash derived from sub-bituminous coal.

Particles in the larger diameter bins, not considered in the cumulative distribution calculations above, constitute $\lesssim$ 10% (by count) of the ash samples. Cumulative compositions over two diameter ranges, $C_o(D_{max})$ and $C_o(D_{25})$, are shown in Table 4.3 to illustrate the effect of a few large particles on the average composition. D_{max} is the bin containing the largest detected ash particle, and varies from 7 μm (Beulah) to 47 μm (San Miguel). It appears that the presence of a few large silica-rich particles results in a significant change in average composition, particularly for the Kentucky, Eagle Butte, and San Miguel ashes. The effect is particularly drastic for the Eagle Butte ash where five particles of diameter >10 μm, and with SiO_2 content of 28–35% promote SiO_2 from the third largest to the largest oxide constituent.

The distribution of the oxides among the ash volume can be expressed on a cumulative basis by integrating $\xi_o(x, D)$ as follows:

$$f_o(x) = \int_0^x \int_0^\infty \xi_o(x', D)\, \mathrm{d}D\, \mathrm{d}x'$$

Here, $f_o(x)$ is the volume fraction of ash with mass percent of oxide o less than x. Particles with diameter > D_{25} are omitted. When x=100%, $f_o(x)$ is unity for each of the oxides. Figure 4.8 presents $f_o(x)$ for all six ashes; its interpretation yields some useful information. Large or small slopes over an increment of Δx implies the presence of large or small proportion of particles with oxide content between x and $x + \Delta x$, respectively. Among all

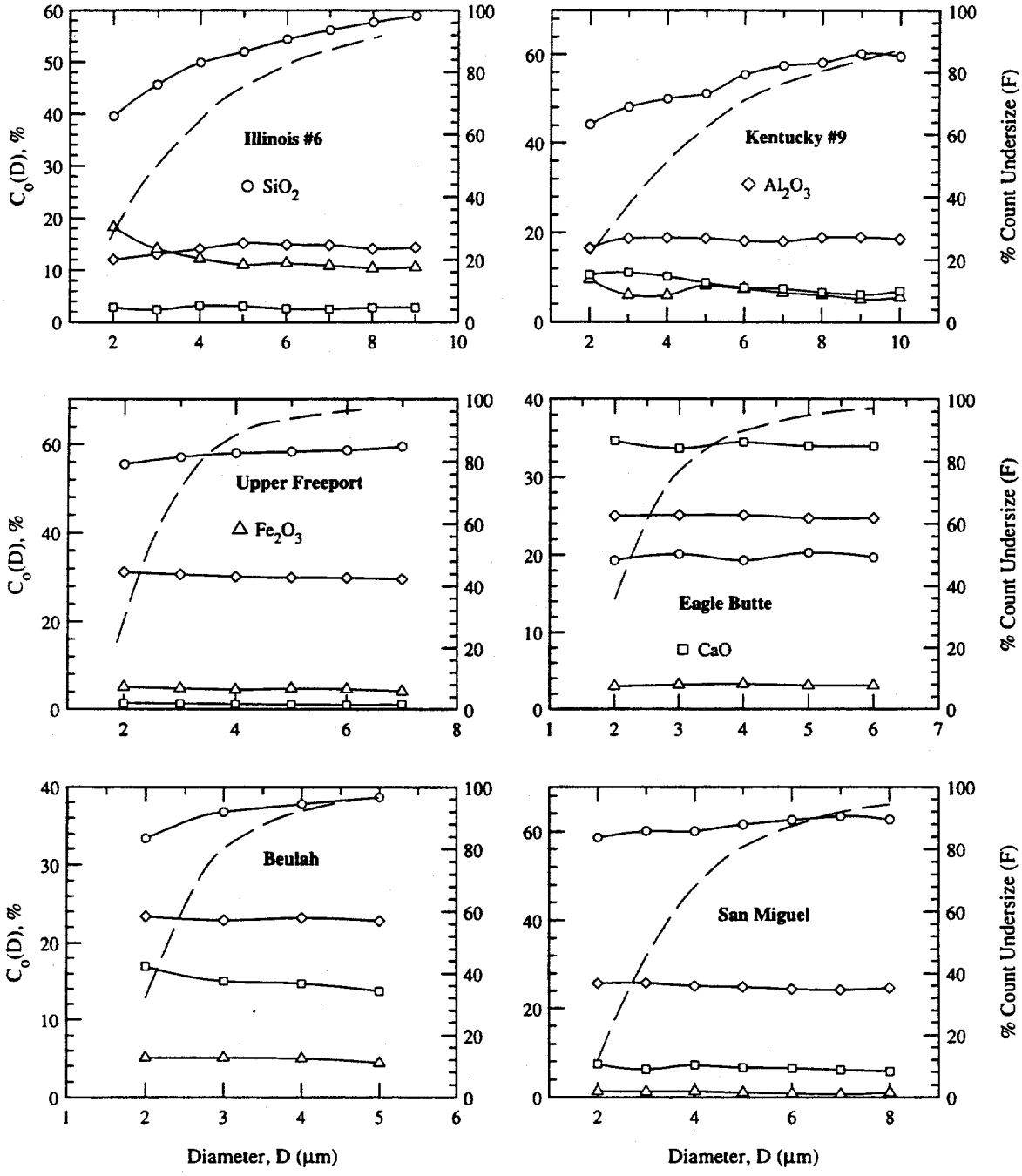

Figure 4.7: Cumulative undersize composition distribution for the six ashes. The right hand axis shows the count undersize, which is graphed as a dashed line.

Table 4.3: Comparison of cumulative compositions of ashes to show the effect of a few large particles on average composition obtained using CCSEM data. All composition figures are percentages by mass. For each ash, the composition figures in the first and second columns are $C_o(D_{max})$ and $C_o(D_{25})$, respectively, following D_{max} and D_{25} (μm), and sample populations (see text).

	Upper Freeport		Illinois #6		Kentucky #9		Eagle Butte		San Miguel		Beulah	
D (μm)	30	6	21	8	42	9	24	5	47	7	17	4
No.	1774	1716	1029	945	950	830	1887	1830	1558	1472	1111	1083
SiO_2	58.2	59.4	61.8	58.9	65.8	59.6	29.8	19.7	68.9	62.7	40.9	38.7
Al_2O_3	28.4	29.6	15.6	14.3	18.8	18.6	24.3	24.7	22.7	24.7	26.0	22.8
Fe_2O_3	4.9	4.1	8.3	10.6	4.8	5.6	2.6	3.1	0.5	1.1	3.5	4.4
CaO	1.4	1.1	2.1	2.8	3.4	7.0	27.8	34.0	3.0	5.8	10.3	13.7
MgO	0.3	0.4	0.1	0.1	0.0	0.1	6.8	10.7	0.1	0.2	3.2	4.0
Na_2O	0.3	0.4	0.2	0.2	0.3	0.2	2.1	1.0	2.4	2.6	3.7	5.6
K_2O	2.9	2.4	2.7	2.7	3.0	2.6	0.3	0.3	1.2	0.8	1.9	1.1
Cl	0.2	0.2	0.4	0.3	0.2	0.4	0.5	0.3	0.1	0.2	1.5	1.6
TiO_2	1.2	0.7	1.5	1.1	0.8	1.1	1.1	1.4	0.4	0.8	1.0	1.2
SO_3	1.0	1.0	6.3	8.2	2.2	3.9	3.6	3.4	0.3	0.6	7.2	5.6
P_2O_5	0.1	0.2	0.2	0.2	0.0	0.1	0.4	0.6	0.0	0.1	0.2	0.4
BaO	1.2	0.5	0.8	0.6	0.6	0.8	0.6	0.8	0.5	0.5	0.6	0.9

oxides, silica is distributed most broadly* (i.e., with the largest range of mass fractions), with Illinois ash having the broadest $f_o(x)$. Although, these distributions are presented on a differential basis later in the section, the following conclusions can be drawn from Figure 4.8.

The Kentucky and Illinois ashes contain a significant volume fraction of silica-rich particles (i.e., >80% SiO_2). Although Al_2O_3 is one of the two most predominant oxides, there are no alumina-rich particles (i.e., $\gtrsim$ 60%). For Fe_2O_3, it is seen that 90% of the ash volume contains $\lesssim$ 8% of the total Fe_2O_3 (by mass) for all the ashes, with the exception of Illinois #6 which has a much broader distribution and only 65% of the ash volume contains <8% of Fe_2O_3. Hence, for all ashes except Illinois #6, the fraction of ash volume containing a wide range of Fe_2O_3 mass fraction (20%–50%) is negligible. The distribution of CaO is similar to that of Fe_2O_3 in most of the ashes, except in Eagle Butte ash where it is the main constituent, and resembles the Al_2O_3 distribution of the other ashes.

Although the ash composition does not show any significant correlation with size, it is clear from the ternary plots that the oxide composition varies considerably from particle to particle. This oxide distribution is represented by $\zeta_o(x)$, where $\zeta_o(x)\,\mathrm{d}x$ is the number fraction of ash particles with mass percentage of oxide o between x and $x + \mathrm{d}x$. Inevitably, the differential function $\zeta_o(x)$ is spiky for CCSEM sample sizes in the range 1000–2000, especially $\zeta_{Fe}(x)$ and $\zeta_{Ca}(x)$. Relatively 'smoother' distributions can be obtained by integrating $\zeta_o(x)$ over small ranges of diameter to obtain a new frequency distribution, $\bar{\zeta}_o(x)$.

$$\bar{\zeta}_o(x) = \int_{x-\Delta x/2}^{x+\Delta x/2} \zeta_o(x')\,\mathrm{d}x'$$

No particles are excluded in this smoothed differential distribution, and a value of Δx = 5% is used in the calculations. The distributions for the four major oxides are presented graphically for the Illinois ash in Figure 4.9. The distributions of the four main oxides for all six ashes are included in Appendix G. The mode of the SiO_2 distribution, $\bar{\zeta}_{Si}(x)$, falls in the range 50–60% for all four ashes where SiO_2 is the largest constituent. The alumina distributions, $\bar{\zeta}_{Al}(x)$, are similar, with four distributions showing modes in the range x=20–30%. $\bar{\zeta}_{Al}(x)$ falls of precipitously beyond x=40%, reaffirming the conclusions from the ternary plot that there are few ash particles with Al_2O_3 content >50%. For both CaO and Fe_2O_3 increasing numbers of ash particles are seen to contain ever smaller fractions of these oxides. The two exceptions are the cases where calcia is a major component (>10%), *viz* the Beulah and Eagle Butte ashes.

*Even in the Eagle Butte ash where it is only the third largest component oxide.

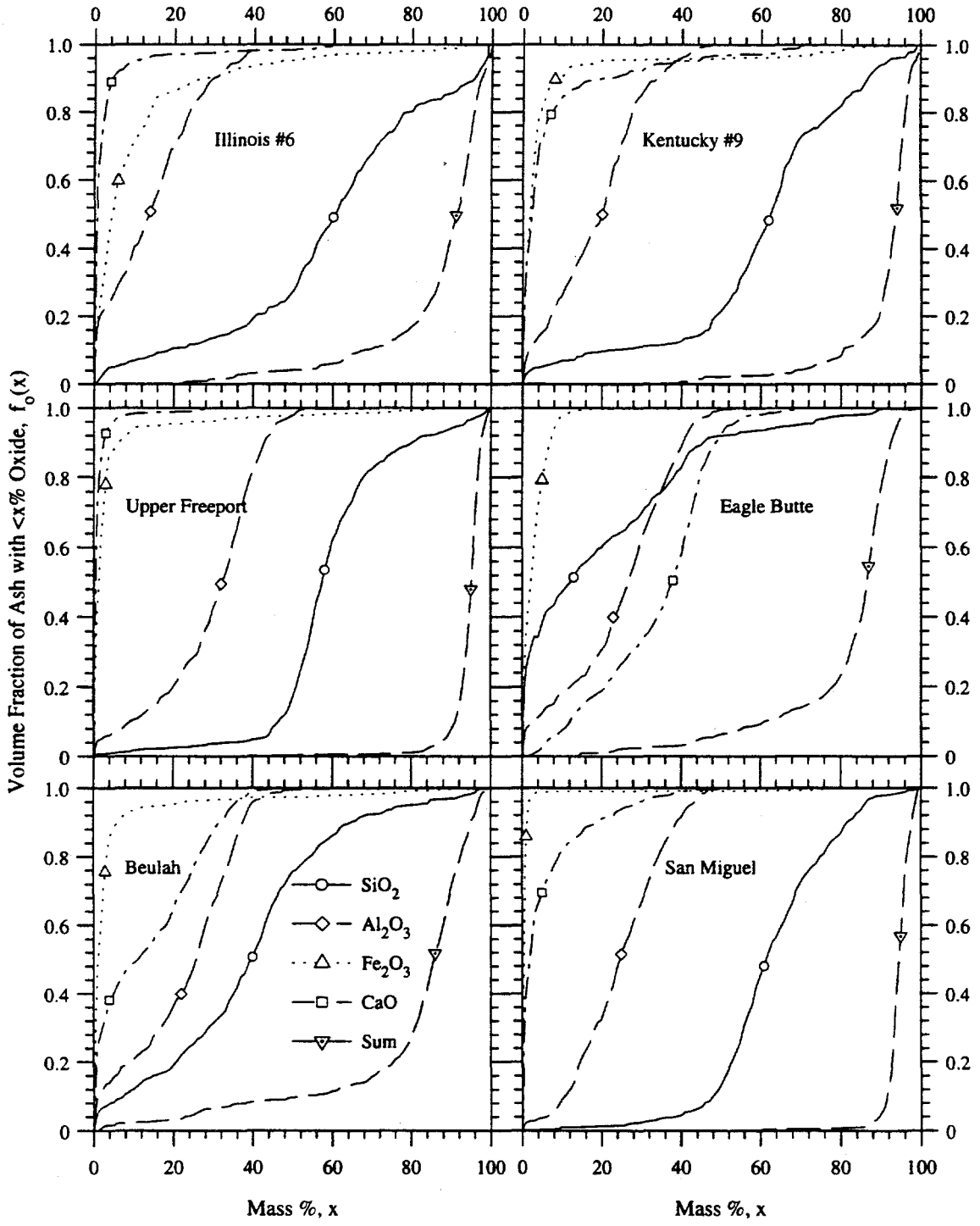

Figure 4.8: Volume-composition distribution shown on a cumulative basis for all six ashes. $f_o(x)$ represents the volume of ash with mass fraction of oxide o less than $x\%$, as a fraction of the total volume. To retain clarity, a limited number of data points are shown.

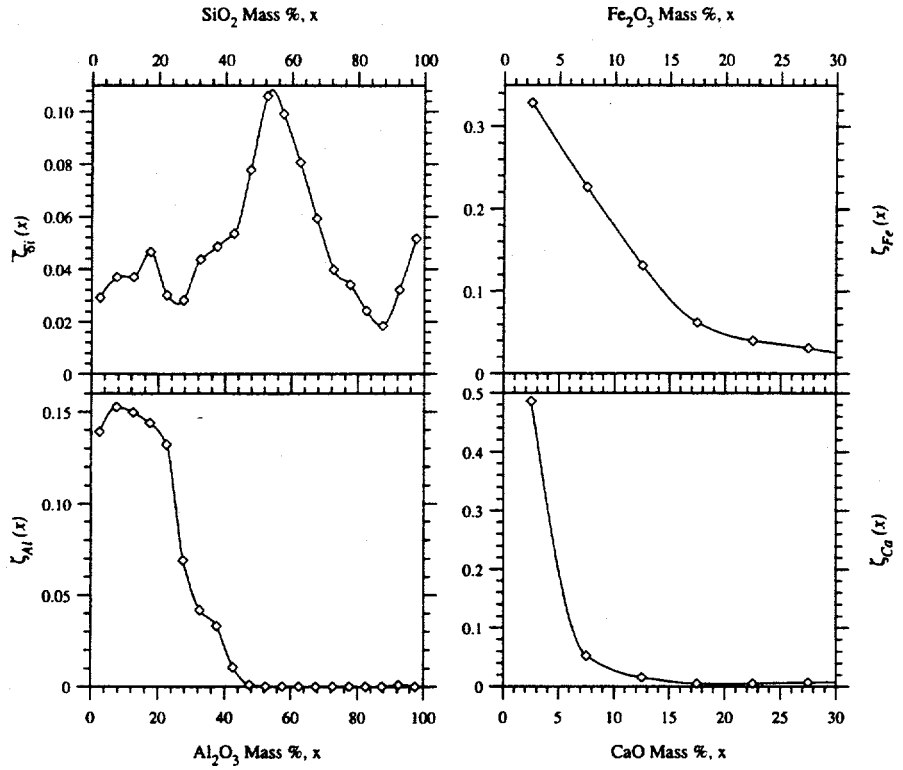

Figure 4.9: Oxide distributions in Illinois #6 ash expressed as number fraction with oxide mass percentage x, the data being averaged over increments of 5%. Note different ordinate scales.

Other useful measures of ash heterogeneity are the ratios, by mass, of SiO_2 to Al_2O_3, and SiO_2 to Fe_2O_3. Figure 4.10 shows these distributions for the Illinois ash averaged over each of twenty bins. A logarithmic scale is used to accommodate a large range of ratios. Again, such distributions for the other ashes are available in Appendix G. Clearly, with the exception of the Eagle Butte ash, there are very few ash particles with more alumina than silica. The most common SiO_2:Al_2O_3 ratios are in the range 1–2.5, with the low-silica ashes peaking close to unity. Overall, the ash particles show a wide range of silica-to-alumina ratio encompassing more than an order of magnitude. The SiO_2/Fe_2O_3 ratio is even broader, spanning more than two orders of magnitude (except for the San Miguel ash which has the lowest iron content). The breadth of the distributions suggest that the iron in the glass is not incorporated in any preferred proportions.

Having concluded that any composition–size correlation for the ashes is negligible, one

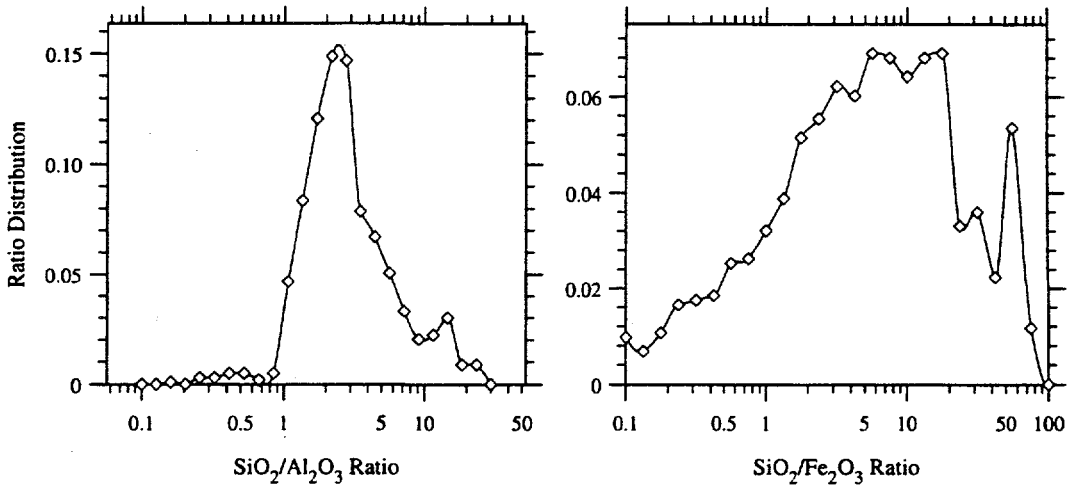

Figure 4.10: Distributions of oxide ratios in Illinois #6 ash expressed as number fraction with SiO_2/Al_2O_3 (or SiO_2/Fe_2O_3) ratio, x. The data has been averaged over increments of 5%. Note different ordinate scales.

can now work with the *number* mean composition, $\bar{X}_o$ and the associated standard deviation, s_o, for an oxide o[†]. Table 4.4 shows the computed values of $\bar{X}_o$ and s_o for the various oxides of all the ashes. The predominant oxides also have the broadest distributions as measured by s_o. It is noted that in four ashes, Fe_2O_3 is present in a greater range of mass fractions than Al_2O_3, although the latter constitutes a far larger proportion of the average ash mass.

Finally, it is noted that the TiO_2 contents of the ashes are quite small ($\approx$1%). Almost all of the TiO_2 appear to be distributed in the glassy matrix, although it is reported that a small fraction recrystallizes to form rutile (Del Monte and Sabbioni, 1984). Because TiO_2 is such a minor constituent, its contribution to the optical properties of the ash is negligible (Goodwin, 1986).

4.4.3 Composition Classes

The CCSEM data can used to create a reasonably small number of composition classes, and hence, refractive index classes that reflect the heterogeneity of the ash. There are two important considerations to be taken into account. First, there is no unique classification scheme, and the distribution functions and ternary plots presented in this Chapter must be used in a manner appropriate for the specific purpose. In most cases, it is likely that there

[†]The definitions $\bar{X}_o$ and s_o are conventional. However, they are also defined in Appendix F.

Table 4.4: Average compositions ($\bar{X}_o$) and standard deviations (s_o) for oxide distributions for the six ashes. All figures are percentages.

	Illinois #6		Kentucky #9		Upper Freeport		Eagle Butte		Beulah		San Miguel	
	$\bar{X}_o$	s_o	$\bar{X}_o$	s_o	$\bar{X}_o$	s_o	$\bar{X}_o$	s_o	$\bar{X}_o$	s_o	$\bar{X}_o$	s_o
SiO_2	50.3	25.6	54.1	23.7	57.4	15.0	19.9	20.16	36.6	19.62	61.4	15.18
Al_2O_3	13.9	11.1	17.9	11.1	30.3	11.5	24.7	12.41	23.2	11.93	25.1	10.51
Fe_2O_3	13.0	16.4	6.9	15.9	4.8	12.2	3.1	3.80	4.6	12.59	1.2	6.90
CaO	2.7	7.0	8.0	13.1	1.2	3.3	34.2	11.55	15.1	12.00	6.2	9.85
MgO	0.2	0.5	0.2	0.6	0.4	1.3	9.8	11.25	5.0	7.85	0.3	1.85
Na_2O	0.2	0.9	0.4	1.0	0.4	0.8	0.7	1.63	5.1	6.80	2.6	1.81
K_2O	2.8	2.2	2.7	2.3	2.3	1.3	0.3	0.58	1.0	1.98	0.8	0.8
Cl	0.3	0.7	0.6	3.6	0.3	0.7	0.3	0.59	1.2	4.96	0.2	0.47
TiO_2	1.3	2.9	1.4	2.3	0.9	2.1	1.5	2.69	1.4	3.37	0.8	1.73
SO_3	14.1	17.8	6.7	12.1	1.1	2.5	3.9	4.94	5.6	11.82	0.8	2.14
P_2O_5	0.4	1.3	0.3	1.8	0.3	1.5	0.7	1.54	0.4	1.35	0.1	0.57
BaO	0.8	1.9	0.9	1.5	0.5	1.3	0.9	1.71	0.9	2.17	0.5	1.13

will be no ash particles having the same composition as any of the classes.

Second, infrared optical constants are available only for the six oxides: SiO_2, Al_2O_3, Fe_2O_3, CaO, MgO, and TiO_2 (Goodwin, 1986). The simplest approximation to account for the component oxides for which there is no optical data is to re-normalize the ash particle composition after excluding these oxides (and Cl), i.e., $\sum_6 X_o$=100%, ($o \equiv$$SiO_2$, Al_2O_3, Fe_2O_3, CaO, MgO, and TiO_2) after setting X_o=0, ($o \equiv$$Na_2O$, K_2O, SO_3, BaO, P_2O_5). The last three components are present in negligible quantities, and can safely be neglected. Sulfur, present mainly as calcium and potassium sulfates, condenses on the ash well downstream from the flame, and can be ignored from the point of view of radiative heat transfer. This approximation means that we consider the refractivity of the neglected oxides (essentially, Na_2O and K_2O) to be equal to the average refractivity of the particle as determined by the mixture rule (Goodwin, 1986). It can be seen that this approximation is reasonable for the ash as a whole by examining the composition of slags presented later in Section 4.5.2 (Table 4.6). On average, these six oxides constitute 95% by mass of the slag, with a maximum of 95.9% and a minimum of 93.7% in the Beulah and Upper Freeport slags respectively. However, for that fraction of ash particles with unusually high Na_2O and K_2O contents[‡], the estimates probably slightly overpredict the actual refractivities.

The proposed classification scheme accounts for ash heterogeneity on the basis of concentration of the predominant component oxide, *viz* SiO_2 (which is also infrared-active) for all ashes except Eagle Butte, where it is CaO. A class is defined as containing all particles with a specified range of predominant oxide percentages. The two functions, $\zeta_o(x)$ and $f_o(x)$ provided guidance in choosing the ranges. The actual composition of the class is determined from the average (*viz* $\bar{X}_o$) oxide percentages for all particles in that class. The Illinois #6 ash is used as an example to illustrate the scheme. The actual compositions and the volume contributions by each class, are presented in Table 4.5.

Class 1 This class contains all particles with SiO_2 contents in the range $(\bar{X}_{Si} - \frac{1}{4}s_{Si}, \bar{X}_{Si} + \frac{1}{4}s_{Si})$, i.e., ≈(44%,57%). From $\bar{\zeta}_{Si}(x)$ in Figure 4.8, it is seen that this class contributes ~20% of the total ash volume.

Class 2 Particles with a higher SiO_2 content representing those in the range $(\bar{X}_{Si} + \frac{1}{4}s_{Si}, \bar{X}_{Si} + s_{Si})$. This class makes up close to one-third of the ash volume.

[‡]The fraction of ash particles with (Na_2O+K_2O)>12% are: <1% in San Miguel, Upper Freeport, and Eagle Butte; <2% in Illinois #6 and Kentucky #9; ≈20% in the Beulah ash.

Table 4.5: Chemical composition classes to account for heterogeneity in Illinois #6 ash. All figures are percentages. The category 'Others' sums up the contributions of the remaining six oxides. The extreme right column shows the contribution by the class to the total ash volume.

Class	SiO_2	Al_2O_3	Fe_2O_3	CaO	MgO	TiO_2	Others	Vol. %
1	51.2	23.0	9.2	1.2	0.2	1.1	14.2	18.9
2	64.4	19.0	6.1	1.1	0.1	0.9	8.4	33.2
3	89.3	3.0	1.8	0.6	0.1	0.4	4.8	21.4
4	35.7	14.1	19.9	2.9	0.2	1.8	25.3	13.5
5	11.8	5.5	29.7	8.0	0.3	2.2	42.5	12.0

Class 3 This class represents the highest-silica particles ($> \bar{X}_{Si}+s_{Si}$). The particles in this class are composed mostly (>90% by mass) of the three major oxides, SiO_2, Al_2O_3, and Fe_2O_3.

Class 4 Particles with SiO_2 content in the range $(\bar{X}_{Si} - \frac{1}{4}s_{si}, \bar{X}_{Si} - s_{Si})$.

Class 5 This class represents all low-silica particles with silica content $< (\bar{X}_{Si} - s_{Si})$, with a class-average SiO_2 content of 11.8%.

Because size-composition relationships are neglected[§], the size distributions obtained with the Multisizer, $F_3^{(a,b)}(D)$, is used for all composition classes. Ash densities for each of the five classes (needed for calculating n and k using the correlations) were calculated using effective densities of component oxides as described in Section 4.7.

It is noted that Class 5 (Class 4 for Eagle Butte) has the highest Fe_2O_3 content. Since the Fe_2O_3 content of Goodwin's and Ebert's synthetic slags were <20%, $n(\lambda)$ and $k(\lambda)$ values of Class 5 are extrapolated values, and hence, approximate. Additionally, ashes in Classes 4 and 5 have significant percentages of oxides for which optical properties are not available (*viz*, Na_2O and K_2O). However, the total volume fraction (of the total loading) contributed by the two classes is not very large (17%–35%).

The real and the imaginary parts of m for all five ash classes, obtained using correlations for melts, are shown in Figure 4.11 and 4.12, respectively. The shift in the vibration peaks towards longer wavelengths occur either with decreasing SiO_2 content or increasing

[§]It was noted that the contribution by each class to the whole ash on the basis of number (or count) was not very different from that based on volume.

temperature (see Ebert, 1993). In either case it is the result of bond weakening, and hence a lower resonance frequency. Seifert (1982) notes that an increase in network substitution, e.g., by Al, changes the Si–O–Al bond angle, and thus changes the effective proportion of bonding electrons for the Si–O bond, leading to the bond's weakening.

Composition and complex refractive index classes for the other five ashes can be found in Appendix I.

4.5 Bulk Slag Composition

4.5.1 Slag Preparation

Samples of each fly ash, weighing 40–50 g, were melted in alumina crucibles (1.5″ diameter) in a furnace. A description of the design and operation of the furnace is given by Ebert (1993). The slag was kept in a molten state at ≈1600°C for more than ten hours to maximize homogeneity, and to allow gases to diffuse out. Using a long alumina rod, the viscous melt was stirred gently through an opening at the top of the furnace, and a small amount withdrawn from the crucible. The rapid quenching[¶] resulted in the formation of homogeneous, glassy slag. The remaining melt was cooled at the rate of ≈ 10°C per minute. A higher cooling rate would probably have resulted in damage to the furnace due to thermal stresses.

In spite of some slight degree of crystallization, the resulting slag appeared to be quite homogeneous. The melt in contact with the crucible dissolved small amounts of alumina. However, EDS examination showed that the Al_2O_3 content of the slag showed little change beyond ≈3 mm from the slag boundary. An exception was the high-calcia Eagle Butte for which a platinum crucible was used because the slag dissolved significant quantities of the crucible. Samples were obtained from a core drilled from the center of the slag with a diamond impregnated core drill.

At the first attempt, the Illinois #6 slag was found to contain a large pellet of iron at the bottom of the crucible, produced by the reduction of the iron oxides. The most probable reducing agent was carbon monoxide generated by the oxidation of the small amount of char in the ash. The heavier iron sank to the bottom of the crucible, and formed a globular mass due to surface tension effects. This problem was overcome by initially oxidizing the char by

[¶]In air, followed by cooling in water to room temperature.

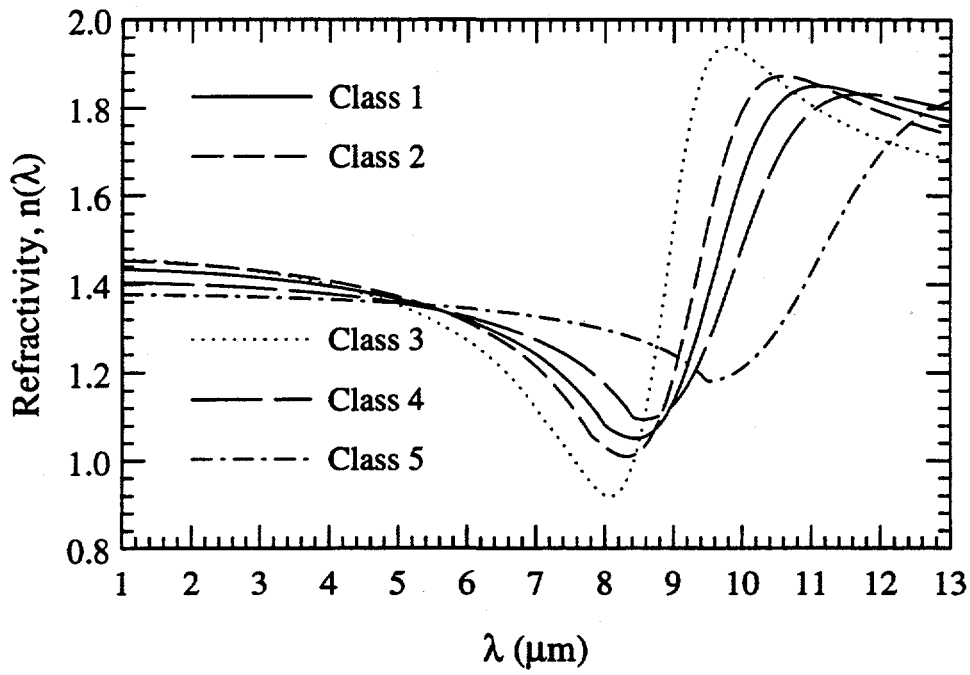

Figure 4.11: The real part of the refractive index, $n(\lambda)$, of the five classes of Illinois #6 ash.

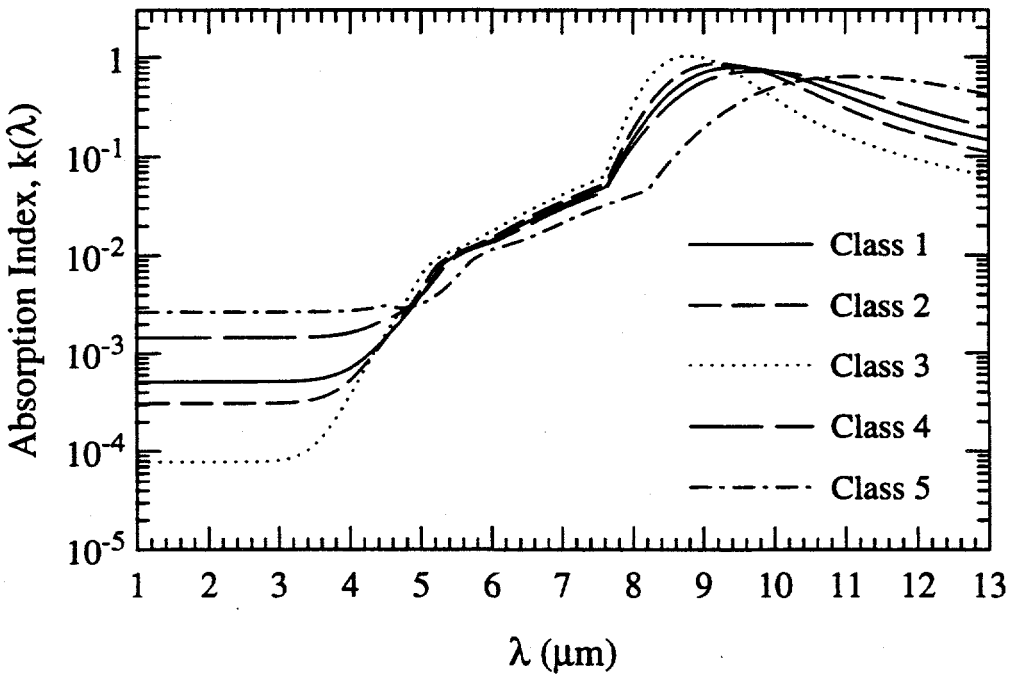

Figure 4.12: The imaginary part of the refractive index, $k(\lambda)$, of the five classes of Illinois #6 ash.

heating the ash to a temperature of ≈1000°C for forty-eight hours, and then proceeding as described above.

4.5.2 Slag Composition

The electron microprobe employs Bragg diffraction to examine one characteristic X-ray wavelength at a time. The technique is referred to as wavelength dispersive spectroscopy (WDS). The peak-to-background intensity for a specific element is compared with that from the same element present in a standard whose composition is well known, and is preferably similar to that of the sample. The relative concentrations of the various elements in the sample can be obtained by a quick scan of the characteristic X-ray spectrum using EDS, and this information used in choosing appropriate standards. Although microprobe analysis takes considerably more time than EDS, the results are accurate, limited mainly by the quality of sample preparation and the standards used. Detailed description of this well-established microanalytical technique can be found in Goldstein, *et al* (1984).

Microprobe samples were prepared by embedding small pieces of slags[‖] in epoxy followed by grinding, polishing, and lapping (so that the r.m.s. roughness was of submicron scale), and, finally, carbon coating. Preliminary studies showed that the slag cooled in the crucible showed evidence of density stratification in the form of increasing Fe_2O_3 and decreasing SiO_2 content with depth. A detailed study of axial and vertical variation of composition in synthetic slags prepared in this manner is given by Ebert (1993). Hence, the quenched fraction was used to prepare the sample, with the reasonable assumption that the stirring of the melt destroyed all stratification.

In all cases, the operating conditions of the JEOL 733 microprobe involved an accelerating potential of 15 kV, a nominal beam current of 10 nA, a probe diameter of 40 μm, an X-ray emergence angle of 40°C, and a sampling period of 30 seconds (per element, per sampling point). Three different detectors (TAP, PET, and LIF) were used to detect X-rays characteristic of the twelve elements studied in the CCSEM analysis. ZAF correction was incorporated to account for atomic number, absorption, and fluorescence, respectively (see Appendix E). Eight to ten points on the sample were analyzed for each slag, and the data averaged to yield an average slag composition.

The slag compositions obtained from the microprobe study are shown in Table 4.6.

[‖]Obtained by core drilling as described above.

The measurement uncertainty, shown next to the composition data, includes both X-ray counting uncertainties (statistical), and that arising from small composition variation from point to point.

Beulah and Illinois #6 ashes have the highest iron oxide content (17–19% by mass). The silica contents of the three bituminous ashes are ≈50% with a SiO_2:Al_2O_3 ratio of approximately 2:1. The San Miguel lignite ash is rich in silica (65%), while the SiO_2/Al_2O_3 ratio for the Beulah lignite slag is close to unity. The Eagle Butte sub-bituminous ash has an unusually high calcia content (CaO : SiO_2: Al_2O_3= 33:29:17).

The titanium contents of all the ashes are ≈1%, which is consistent with the CCSEM data. The sodium and potassium oxides, which lower the softening point of the ash, and cause slagging and fouling problems to heat exchangers in power plants, constitute less than 5% of the slag by mass, except in the cases of the two lignites and Kentucky #9. The Beulah ash, with 6.7% Na_2O, is well known in industry for its problematic fouling characteristics. All the sulfur is oxidized and lost during slag preparation.

For optical properties, the molar compositions shown in Table 4.7 are useful. Clearly, the four major constituent oxides shown in the Table, make up 85%–95% of the slags. The SiO_2/Al_2O_3 molar ratio varies considerably, from a low of 1.6 in Beulah, to a high of 5.1 in the San Miguel slag. In Chapter 2, we noted that the structure of glass is known to show considerable differences due to the varying quantities of glass modifiers (CaO, MgO, Na_2O, K_2O, BaO). The Upper Freeport ash has a relatively unmodified three-dimensional network structure while the presence of high quantities of CaO in the Eagle Butte ash results in significantly planar structure (Hemmings and Berry, 1988).

4.6 Comparisons of Ash Chemical Composition

A bulk ash composition can be obtained by combining the CCSEM data with the truncated lognormal function obtained in Chapter 3 using Multisizer size distribution data in the following way.

$$\vartheta_o = \int_a^b F_3^{(a,b)}(x)\,\delta_o(x)\,\mathrm{d}x \qquad a \le D \le b$$

The integration can be approximated to a summation using $\bar{\delta}_{i,o}$ of each of the n size bins

$$\vartheta_o = \sum_{i=0}^{n} \bar{\delta}_{i,o} \int_{i-0.5}^{i+0.5} F_3^{(a,b)}(x)\,\mathrm{d}x$$

Table 4.6: Compositions and associated uncertainities of slags obtained from electron microprobe analysis. All figures are mass percentages.

	Upper Freeport		Illinois #6		Kentucky #9		Eagle Butte		San Miguel		Beulah	
	Comp.	±	Comp.	±	Comp.	±	Comp.	±	Comp.	±	Comp.	±
SiO_2	51.36	0.23	49.39	0.72	47.19	0.34	28.53	0.63	64.66	0.47	31.70	0.49
Al_2O_3	27.51	0.32	21.09	0.20	28.95	0.43	17.44	0.23	21.51	0.24	33.51	0.87
Fe_2O_3	13.05	0.34	18.96	0.87	12.59	0.37	6.88	0.43	2.75	0.06	16.88	0.56
CaO	2.59	0.04	2.94	0.14	5.17	0.06	33.00	0.80	4.85	0.14	7.56	0.17
MgO	0.22	0.04	0.90	0.14	0.15	0.04	7.47	0.15	0.10	0.02	3.37	0.06
Na_2O	0.53	0.08	1.44	0.05	2.27	0.15	1.74	0.09	3.34	0.17	6.68	0.15
K_2O	3.16	0.04	2.17	0.10	2.24	0.16	0.00	0.00	1.80	0.04	1.49	0.10
Cl	0.00	0.00	0.64	1.31	0.00	0.00	1.05	1.61	0.01	0.01	0.02	0.02
TiO_2	1.08	0.10	0.68	0.18	1.06	0.08	1.11	0.28	0.91	0.06	0.67	0.12
SO_3	0.00	0.00	0.02	0.03	0.00	0.00	0.01	0.02	0.00	0.00	0.01	0.01
P_2O_5	0.40	0.04	0.19	0.22	0.25	0.07	0.27	0.33	0.03	0.03	0.39	0.06
BaO	0.08	0.02	1.58	0.71	0.12	0.03	2.50	0.27	0.12	0.04	0.62	0.05

Table 4.7: Bulk molar composition of slags.

	Illinois #6	Kentucky #9	Upper Freeport
SiO_2	62.89	59.47	64.90
Al_2O_3	15.83	21.51	20.50
Fe_2O_3	9.09	5.97	6.20
CaO	4.01	6.99	3.51
Others	8.19	6.06	4.89
SiO_2/Al_2O_3	3.97	4.99	3.17
SiO_2/glass modifiers	6.26	2.76	9.06

	Eagle Butte	Beulah	San Miguel
SiO_2	30.58	42.28	72.85
Al_2O_3	11.02	26.35	14.29
Fe_2O_3	2.78	8.47	1.17
CaO	37.90	10.80	5.86
Others	17.72	12.10	5.84
SiO_2/Al_2O_3	2.78	1.60	5.10
SiO_2/glass modifiers	0.58	1.93	6.68

This bulk composition does not account for cenospheres, and the composition of approximately half of the ash volume (i.e., for particles of diameter $\gtrsim 10\ \mu m$) is statistically unsound as discussed in Section 4.4.2. However, it is instructive to compare this composition with the accurate microprobe data on slags to test whether the discrepancies can be satisfactorily explained by the suggested artifacts of the measurement techniques.

The CCSEM and microprobe data were also compared with the average composition data of determined by PSI, Inc. (PSI, 1990) obtained using a very different technique, *viz*, ICP spectroscopy. In the latter, the ash is dissolved in acid, and a few drops introduced into an inductively-coupled thermal plasma. The emission spectra were analyzed to obtain the relative proportions of the detectable elements. Additionally, Foster-Wheeler and the AMAX Coal Company supplied ash compositions obtained by wet chemical analyses. Comparisons are presented for the Upper Freeport ash in Table 4.8, and in Appendix G for the other ashes. Because the slag preparation leads to a loss of the sulfur in the ash, both PSI and Foster-Wheeler data are normalized for zero–SO_3 content. No measurements of Cl and BaO were available for the PSI data. The microprobe data is in good agreement with the PSI and Foster-Wheeler data, considering the disparity in measurement techniques and the

Table 4.8: Comparison of bulk compositions of Upper Freeport ash. All figures are percentages, CCSEM data for 1774 particles. Column 3 and 4 show data obtained at PSI and Foster-Wheeler, respectively, after neglecting SO_3. Column 6 shows the bulk composition from CCSEM data, ϑ_o, after accounting for Fe_2O_3 deficit.

	1	2	3	4	5	6
	Microprobe	**PSI**	**PSI/SO_3**	**Foster**	**ϑ_o**	**ϑ_o/Fe_2O_3**
SiO_2	51.36	50.9	52.2	49.0	59.5	54.1
Al_2O_3	27.51	24.8	25.4	25.7	28.6	26.0
Fe_2O_3	13.05	13.6	13.9	16.7	4.4	13.1
CaO	2.59	2.2	2.3	2.9	1.4	1.3
MgO	0.22	1.4	1.4	1.0	0.3	0.3
Na_2O	0.53	0.3	0.3	0.3	0.4	0.3
K_2O	3.16	3.1	3.2	2.9	2.5	2.3
Cl	0.00	N.A.	N.A.	0.0	0.2	0.1
TiO_2	1.08	1.2	1.2	1.1	0.9	0.8
SO_3	0.00	2.4	0.0	0.0	1.0	0.9
P_2O_5	0.40	0.1	0.1	0.4	0.1	0.1
BaO	0.08	N.A.	N.A.	0.0	0.7	0.7

sampling uncertainties involved.

The Fe_2O_3 content of the CCSEM bulk composition is only about a third of that measured on the slag. This underprediction, occurring in all the ashes, is ascribed to the concentration of iron in large magnetic particles, and is discussed in the next Section. If ϑ_{Fe} and ϑ_S are set to the microprobe values and zero, respectively, and the data renormalized, ϑ_{Si} and ϑ_{Al} (the major constituents) are quite close to the other measurements (Columns 1, 3, and 4).

4.6.1 Iron Distribution in the Ashes

The visual appearance of the ashes is directly related to the iron content. San Miguel and Eagle Butte ashes that are low in iron are light-gray and yellowish-gray, respectively. The high iron ashes (>10% by mass) are darker, ranging from the dark-gray Kentucky ash to the black Illinois, Beulah and Upper Freeport ashes**. However, it is necessary to determine

**The dark color is a result of electronic absorption in the visible part of the spectrum by ferric ions in the glass.

whether the iron is distributed uniformly among the particles, or concentrated in certain size or composition classes. The location of iron in the ash is especially important for optical characterization because iron plays a dominant role in infrared radiation absorption in the important wavelength range 1–4 μm.

It was explained in Chapter 2 that iron, a glass intermediate, can be incorporated in the aluminosilicate matrix in varying quantities. Ramsden and Shibaoka (1982) noted that many of the large iron-rich particles in their ash sample (from bituminous coal) exhibited dendritic growth in a glassy matrix. They also found crystalline, iron-rich particles to be negligible in number. These observations are corroborated by Del Monte and Sabbioni (1984) who identified the iron oxides in large, iron-rich particles as composed of variable amounts of magnetite, hematite, and maghemite ($\gamma-Fe_2O_3$), often with more than one phase occurring in the same particle. These particles are formed primarily by the oxidation of the pyrite (FeS_2), and by the dissociation of the siderite ($FeCO_3$) present in the coal.

SEM micrographs of the highest density class of Illinois #6 ash (Figure 4.13) show that the large particles in this class (>50 μm) do appear to have dendritic growths. Using the data for size distributions of the density classes, it is seen that these particles compose $\lesssim$ 2% of the ash mass, and because of their high density, they compose a significantly lower fraction of the ash volume.

The CCSEM data show that the average mass fractions of Fe_2O_3 in all the ashes fall in the range 1%–13% (Table 4.9). However, ϑ_{Fe} is only 25%–70% of that determined by microprobe analysis. The reason for this discrepancy appears to be statistical. The high-iron ash particles belong to the higher density Classes 5 and 6 in the density classification scheme of Chapter 3. The ashes in these categories are also seen to have significantly higher median diameters than that of the unseparated ash. Consequently, they are fewer in number, and a sample size of one or two thousand particles is not statistically large enough to detect sufficient numbers of such particles in contrast to the microprobe data which is averaged over a large sample.

It is noted that a large sample is needed for an accurate estimate of the average iron content even if iron distribution is not weighted in favor of larger particles because Fe_2O_3 constitutes only 20% or less of the ash mass. The statistical analyses in Appendix F suggest that a sample size of >15,000 particles is needed for estimating the iron content of the Kentucky ash with a confidence interval of 0.5%.

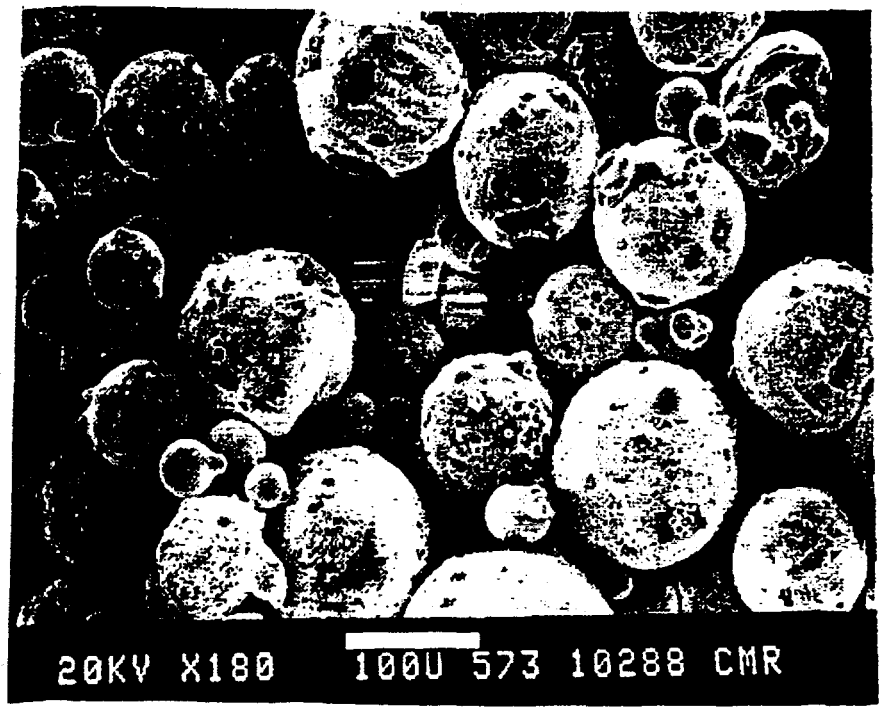

Figure 4.13: Large, iron-rich ash particles present in the heaviest density category (>3.2 g/cc) of Illinois #6 ash.

Table 4.9: Average Fe_2O_3 of ashes (by mass) obtained from CCSEM and electron microprobe analyses. All numbers are percentages.

Fly Ash	CCSEM, ϑ_o	Microprobe	Ratio, ϑ_o/Microprobe
Kentucky #9	6.9	12.59	0.55
Illinois #6	13.0	18.96	0.69
Upper Freeport	4.8	13.05	0.37
Eagle Butte	3.1	6.88	0.45
Beulah	4.6	16.88	0.27
San Miguel	1.2	2.75	0.44

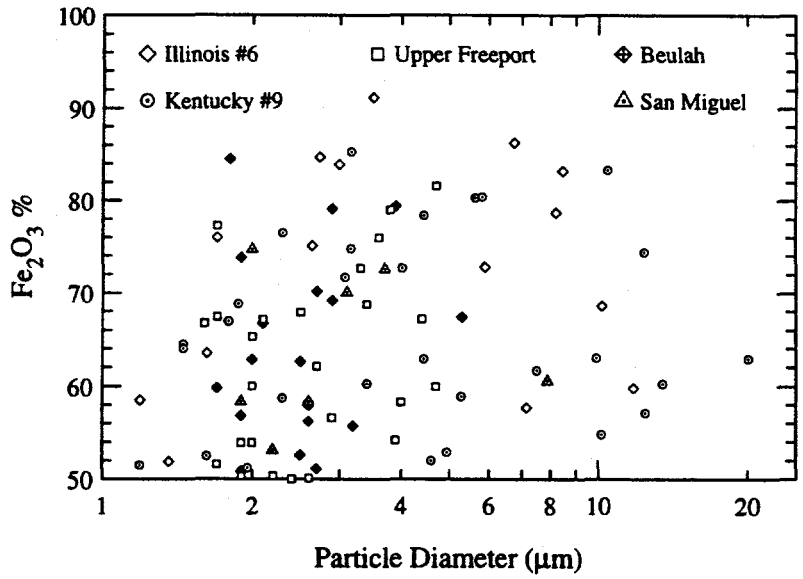

Figure 4.14: Diameter distribution of ash particles with Fe_2O_3 content greater than 50% by mass.

A search through the CCSEM data for ash particles with Fe_2O_3 mass >50% show that none of the particles have diameters >20 μm (Figure 4.14). Apparently, there is no size correlation, and the median diameter is in the vicinity of 3 μm for all the ashes. EDS data on fifteen magnetic Illinois ash particles[††] show that only three of the particles have a Fe mass fraction >80% (Table 4.10). From these studies, it is concluded that there are very few pure magnetite particles in the ash. However, this small sample of fifteen particles do not contain any of the large (> 20 μm) particles that are few in number but account for 50% or more of the total Fe_2O_3 content.

On the basis of the present study, and other published studies, it is concluded that the role of the iron in influencing near-infrared absorption is considerably diminished because approximately half of it is concentrated in larger particles (>20 μm) that are fewer in number (and are not detected by CCSEM analysis). This larger-sized fraction is either in the form of iron-rich glass, or occur as very large spheroidal particles (>50 μm) of iron oxides (primarily magnetite), often showing crystalline growth on an amorphous matrix.

[††]Separation was achieved with a hand-held magnet. The particles were chosen randomly while manually scanning the SEM field. EDS was performed at the Center for Materials Research (CMR) at Stanford. Multisizer measurements showed that the magnetic fraction had a size distribution that is 30% larger than that of the unseparated ash.

Table 4.10: Elemental composition of magnetic Illinois #6 ash obtained by EDS.

Particle #	D (μm)	Si	Al	Fe	Other
1	9	47.9	25.1	20.0	7.0
2	1	46.3	16.6	33.7	3.4
3	11	7.6	4.3	88.1	0.0
4	1	3.7	1.5	94.8	0.0
5	8	42.8	21.8	32.6	2.8
6	5	30.1	14.2	53.9	1.8
7	6	47.1	23.6	20.3	9.0
8	8	42.4	26.9	19.0	11.7
9	1.5	5.3	7.6	81.1	6.0
10	1.5	28.6	19.7	50.0	1.7
11	3.5	10.0	12.2	77.8	0.0
12	1	16.5	15.3	43.1	25.1
13	12	39.8	22.2	33.0	5.0
14	1.5	26.8	25.5	10.0	37.7
15	1	4.1	4.0	35.2	56.7

The remaining iron, detected in the CCSEM analysis, is incorporated in the glass over a broad range of distributions, and is included in the chemical composition classes created in Section 4.4.3. Thus, from the viewpoint of radiative transfer, the effective iron content is that amount detected by CCSEM analysis.

4.7 Densities of Individual Fly Ash Particles

In Chapter 2, it was stated that a knowledge of the density of an ash particle is needed to determine its optical properties, $n(\lambda)$ and $k(\lambda)$. Hence, it is necessary to obtain empirical relations that can predict the density of a slag from its composition, and the individual densities of its constituent oxides.

The densities of the slags were measured using the specific gravity bottle. Multiple measurements from different locations in each slag sample showed a reproducibility of $\pm 3\%$. This variation is ascribed to minor non-uniformities in slag composition and, possibly, the presence of small bubbles in the slag created by trapped gases.

Table 4.11: True and effective densities (ρ_o and ρ_e) of oxides present in fly ashes.

Oxide	Density (ρ_o), (State)	ρ_e
SiO_2	2.20 (Fused silica)	2.28
Al_2O_3	3.99 (Corundum)	2.5
CaO	3.32 (Lime)	3.9
MgO	3.65 (Periclase)	3.3
Na_2O	2.27	3.1
K_2O	2.32	2.8
BaO	5.72	7.0
TiO_2	3.84	3.8

The density of a slag, computed by linear combination of the densities of the component oxides (in crystalline or vitrified state) in proportion to their contribution to the composition, systematically overpredicts the measured density. This overprediction probably occurs because the atoms are packed more loosely in the multi-component glass (which is essentially a super-cooled liquid) than in the individual solid oxides. By measuring the densities of synthetic glasses prepared with varying proportions of constituent oxides, one can calculate an effective density (ρ_e) of each oxide in the glass. This effective density is not unique, i.e., ρ_e of SiO_2 in SiO_2–CaO–Na_2O glass is slightly different from ρ_e of SiO_2 in SiO_2–K_2O-Na_2O glass. Additionally, ρ_e for SiO_2 can change slightly for the same set of oxides depending on their relative proportions in the glass. Table 4.11 shows the effective densities as determined by Appen (1970) that are applicable to the mass fractions present in most ash particles. The computed density of a slag of specified composition, ρ_c, is obtained by adding the fractional density contributions of each of the nine oxides.

$$\rho_c = \sum_{j=1}^{9} X_{s,j}\, \rho_{e,j}$$

$\rho_{e,j}$ and $X_{s,j}$ are the effective density and normalized mass fraction[‡‡] of the j^{th} oxide in the slag, respectively.

The effective density is higher than that of the pure oxides for SiO_2, CaO, Na_2O, K_2O, and BaO. The effective density of iron oxide is not apparently available. However, using the available effective densities, it is possible to obtain a value of ρ_e for Fe_2O_3 so that the

[‡‡]Similar to X_o defined for an individual particle in Section 4.3.

Table 4.12: Comparison of slag densities calculated using effective and actual densities of component oxides, with measured densities. The composition and densities of the SA00–SA20 slags are given by Goodwin (1986). All densities in g/cc.

Slag	ρ_m	ρ_c using ρ_e	% Diff.	ρ_c using ρ_o	% Diff.
Upper Freeport	2.67	2.61	−2.15	3.14	17.78
Kentucky # 9	2.80	2.65	−5.47	3.18	13.71
Illinois # 6	2.69	2.77	2.93	3.27	21.64
Beulah	2.98	2.82	−5.44	3.45	15.71
Beulah (Cyclone)	2.92	2.77	−5.20	3.40	16.39
San Miguel	2.39	2.48	3.79	2.74	14.92
Eagle Butte	2.89	3.03	4.77	3.31	14.83
SA00	2.54	2.52	−0.66	2.88	13.24
SA05	2.60	2.58	−0.69	2.98	14.78
SA10	2.64	2.65	0.21	3.10	17.40
SA20	2.72	2.75	1.22	3.29	21.04

error is minimized. The average r.m.s. error, E, is computed from the calculated density (ρ_c) and the measured density (ρ_m) of each of J slags as follows:

$$E = \sqrt{\frac{\sum_{i=1}^{J}[(\rho_{m,i} - \rho_{c,i})/\rho_{m,i}]^2}{J}}$$

The effective densities of the primary constituent oxides, SiO_2, Al_2O_3, CaO, and Fe_2O_3 affect ρ_c most. Calculations showed that a lower ρ_e for CaO gave better predictions of slag densities. By trial and error, it was determined that ρ_e of 3.4 and 3.8 for CaO and Fe_2O_3, respectively, minimized E to 3.56%. It is reiterated that these values of ρ_e are not unique, but are engineering approximations for the complex physics of glasses. Nevertheless, they predict the densities of the slags quite well as can be seen in Table 4.12. The data for the four synthetic SAXX slags are taken from Goodwin (1986). Note that E=16.71% when actual oxide densities, ρ_o, are used instead of ρ_e. The term '% Diff.' in the fourth and sixth columns is defined as $(\rho_m - \rho_e)/\rho_m$.

In the absence of a database for computing more accurate densities of glassy ash particles, the values of ρ_e presented above have been used to estimate the refractivity. Because $n \sim \sqrt{\rho_c}$, the relative error in n is smaller than that in ρ_c.

An average density for the ash can be calculated using the effective densities of individual

Table 4.13: Comparison of measured slag and average ash densities with calculations using CCSEM data. All densities in g/cc.

Fly Ash	$\bar{\rho}_c$	ρ_m	% Diff.	ρ_{ash}
Kentucky #9	2.51	2.80	−10.36	2.15
Illinois #6	2.59	2.69	−3.72	2.12
Upper Freeport	2.53	2.67	−5.24	2.29
Eagle Butte	2.85	2.89	−1.38	2.76
Beulah	2.69	2.98	−9.73	2.37
San Miguel	2.43	2.39	+1.67	1.73

oxides and CCSEM composition data

$$\bar{\rho}_c = \frac{\sum_{p=1}^{N} D^3 \sum_{j=1}^{L} X_o \ \rho_{e,j}}{\sum_{i=1}^{p} D^3}$$

Here, N and L are respectively the CCSEM sample size and the eight component oxides for which ρ_e are available. The calculations ignore the sulfur content, the iron distribution, and the presence of cenospheres. The results are shown in Table 4.13 for comparison with the measured slag and ash densities. The quantity '% Diff.' in the table is defined as $(\bar{\rho}_c - \rho_m)/\rho_m$. Since cenospheres are not accounted for, $\bar{\rho}_c$ is greater than ρ_{ash}, the average ash density (see Section 3.5.1). For the Eagle Butte ash with only 3.6% cenospheres, $\bar{\rho}_c$ predicts the ash density with 3.3% accuracy. For the two low-iron ashes, Eagle Butte and San Miguel, $\bar{\rho}_c$ is within 2% of the slag density ρ_m. However, for the other four ashes, the deficit of the dense Fe_2O_3 in the sample (as discussed in Section 4.6.1), results in systematic underprediction of the slag densities.

4.7.1 Comparison of CCSEM Size Distributions with Multisizer Data

The geometric diameters of ash particles analyzed are determined using an image analyzing program that computes the average length of eight 'chords' passing through the 'center' of the particle as determined by an appropriate algorithm. The perimeter (or circumference), P, of the particle determined using the sixteen points corresponding to the end points of the eight chords, is used to determined the area, A. A shape factor, S, is computed thus

$$S = \frac{P^2}{4\pi A}$$

For a circle, S is unity. However, the measured value of S may depart slightly from unity due to measurement artifacts such as SEM astigmatism. Thus, any agglomerates can be excluded by limiting the acceptable values of S to a specified range. In this CCSEM study, particles outside the range $0.9 > S > 1.1$ were rejected.

The cumulative volume distribution obtained from the CCSEM data is plotted along with the Coulter Multisizer distributions for the San Miguel fly ash in Figure 4.15. The three Multisizer size distributions show, from left to right, the raw data obtained with the 30 μm orifice tube only (a), the combined data from the 30 μm and the 100 μm orifice tubes (b), and the combined data from the 30 μm, 100 μm, and the 280 μm orifice tubes (c). The differences between the size distributions obtained using the two methods are explained below in terms of artifacts related to the SEM sample preparation technique, and statistical limitations imposed by sample size. These two factors result in deficits of particles at the low and high ends of the diameter spectrum, respectively. While the median diameter from SEM data depends on which of the factors predominate, the standard deviation is necessarily smaller because the range of particles examined is narrower. Hence, the slope of the size distribution is slightly steeper compared to the Multisizer distribution in all cases.

It is virtually impossible to prepare a fully deagglomerated ash sample for CCSEM. The freeze-drying method produces relatively well deagglomerated samples, with very few particle clusters per SEM frame. Such agglomerates were rejected in the UNDEERC study by limiting the maximum acceptable shape factor to 1.1. However, these clusters typically consist of numerous small ash particles (1–5 μm) attached to one or two larger particles. This phenomenon can easily be confirmed by examining transparent glass microspheres under an optical microscope. The fines are seen to adhere to the surface of the larger spheres. As a result, there is a deficit of small fly ash particles among those analyzed by CCSEM. The Multisizer data shows that the median diameters by count, D_n, of all the ashes except San Miguel are < 1 μm. However, the size distributions in the Tables of CCSEM results peak in the range 1–2 μm. This artifact explains the departure of the CCSEM curve from the Multisizer curve in the smaller diameter range.

The difference in the two distributions in the large diameter ranges is due to statistical reasons. In Figure 4.15, the median diameter of distribution (a) is smaller than that obtained from the CCSEM data because the 30 μm orifice cannot correctly size particles that are larger than 21 μm. However, the median diameter of the complete size distribution

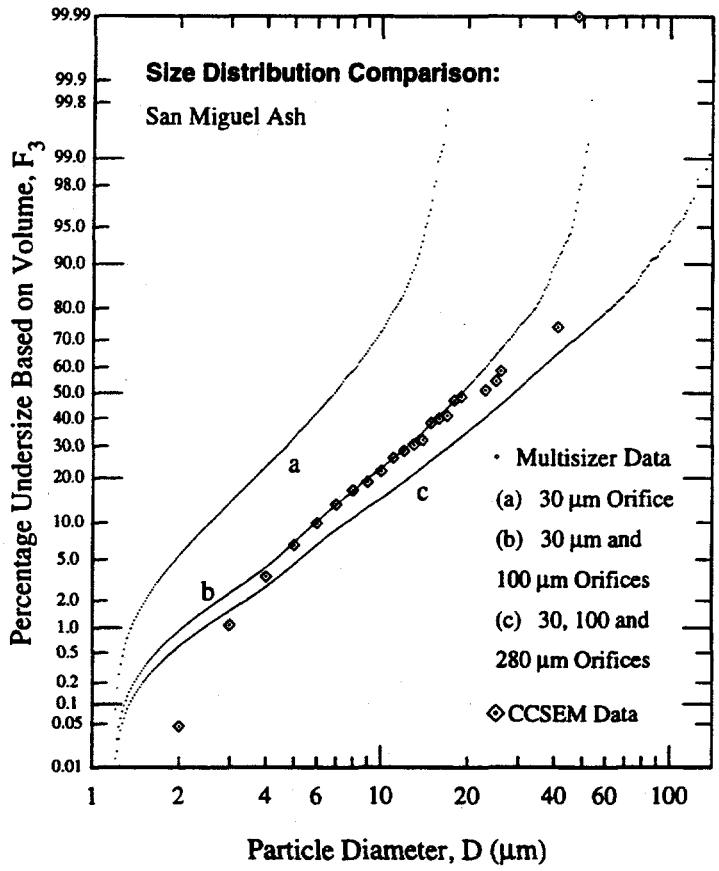

Figure 4.15: Comparison of San Miguel ash size distribution obtained with Coulter Multisizer measurements (using three different sets of orifices) with CCSEM size data.

(distribution c) is larger than that from the CCSEM data. The reason is that the large particles are better represented in the Multisizer sample (280 μm orifice) than in the CCSEM sample. This difference is a result of the relatively small CCSEM sample size of 1558 particles compared to the Multisizer sample size of >200,000 particles. The Multisizer sampled 23 particles of diameter >50 μm. Using this data, it is seen that, on average, a random CCSEM sample size of ≈4000 particles is necessary to encounter one particle of diameter >50 μm*. Additionally, it is possible that some of these 'rare' large particles are rejected as part of agglomerates. This deficit of large particles shifts the CCSEM size distribution to the left. The Multisizer sample for size distribution b had all ash particles of diameter > 53 μm removed by sieving, so it is not surprising that this distribution is quite close to the CCSEM distribution.

*The largest particle sized by CCSEM was a San Miguel ash particle of diameter 47 μm.

The conclusions for the other ashes are very similar (see Appendix G). As explained earlier in this section, the anti-clockwise rotation of the size distribution curve about the median diameter for the Illinois #6 ash is a result of the deficit of particles at both size extremes. For the Kentucky #9 ash, the effect of the shortage of small particles predominates, and the median diameter from the CCSEM data is about 40% larger than that of the Multisizer distribution. The discussion in this section is applicable to all powders of broad size distribution, and illustrates the limitations of size distribution measurements using microscopes. Also, it probably accounts for discrepancies between ash size distributions measured using SEM and Coulter Counter (see Chapter 3, Section 3.1) reported by Fisher *et al* (1978), but were not explained.

4.8 Minor Ash Constituents

The compositions of particles rich in each of the four major oxides have been examined. Only six ash particles in the Illinois #6 sample, three in the Upper Freeport sample, and one each in Kentucky #9, Eagle Butte, and Beulah samples were found to be composed of pure silica. Additionally, only the bituminous ashes contain significant[†] number of particles with SiO_2 content > 95% by mass (Upper Freeport=1.7%, Kentucky=2.7%, and Illinois=5.7%, as number fractions). There is no apparent size correlation for these silica-rich particles.

The Kentucky and Illinois samples do not contain any particles with Al_2O_3 content >50%. The rest contain such particles in negligible amounts (0.1%–0.8%). These alumina-rich particles are almost entirely composed of two oxides, Al_2O_3–SiO_2 in the cases of San Miguel and Upper Freeport, and Al_2O_3–CaO in Eagle Butte and Beulah samples.

Del Monte and Sabbioni (1984), and Hemmings and Berry (1986) have observed rare CaO particles which may have formed from the pyrolysis of dolomite. None of the samples in this study contain particles with CaO content > 80%, indicating that pure CaO particles constitute a negligibly small fraction. In fact, only the Eagle Butte (4.1%) and Kentucky samples (2.4%) have significant quantities of particles with CaO mass percentage >50%. About a third of these particles contain Al_2O_3 and CaO primarily (>90%). In those cases where the samples contain significant numbers of calcia- or alumina-rich particles, no correlations with particle diameter are observed.

[†]Any class of particles discussed in this Section that constitutes less than 1% of the total CCSEM sample is considered insignificant.

Measurements with a high temperature Elemental Analyzer showed that the char contents of the six ashes were well below 1% by mass. More accurate measurements of such small quantities of char was not possible with the available instrumentation. These low estimates are consistent with the results of density classification presented in Chapter 3, and confirm that the influence of the char on ash optical properties and the transmittance measurements (of Chapter 6) is negligible.

4.9 Summary

The chemical compositions of single ash particles were determined for all six ashes using CCSEM. A technique for sample preparation was developed using freeze-drying of deagglomerated ash samples. The CCSEM data revealed strong variations in composition from particle to particle. It was concluded that there was no strong size-composition correlation in any of the ashes.

Composition distribution functions were developed to represent the distribution of each of the four major oxides (SiO_2, Al_2O_3, Fe_2O_3, and CaO). A scheme for creating composition classes to account for ash heterogeneity was presented. Refractive index classes for molten ash suspensions were created for each ash using the chemical composition classes, the effective densities of the classes, and the correlations for optical properties developed by Ebert (1993).

Accurate bulk compositions of slags were obtained from electron microprobe analysis to compare the chemical composition of the ashes relative to each other, with results published elsewhere, and with the corresponding CCSEM compositions. Such cross-checks at all stages of the characterization work has not only helped in testing the reliability of the data, but has also revealed measurement artifacts hitherto unreported in the literature. For example, it is seen that size distributions obtained from SEM image analysis underpredict the breadth of the size distribution and overpredict the median diameter. Comparison of the bulk slag composition with the CCSEM composition also shows that more than half of the total iron in the ash is present in particles that are significantly larger than the median ash diameter ($>20\ \mu m$).

Chapter 5

Extinction by Ash Dispersions: Preliminary Measurements and Analyses

5.1 Introduction

The objective of the second part of this work is to design and conduct a bench-scale experiment for extinction measurements on ash suspensions at room temperature, under controlled laboratory conditions. The experiment is intended to test the validity of the overall approach, i.e., is it possible to predict the radiative properties of an ash provided its size and composition distributions are known from microanalytical studies?

This chapter begins with a discussion of the optical design of conventional transmissometers, followed by an alternative design for a transmissometer suitable for the conditions of this experiment. A description of the infrared optical system (used for both the extinction and reflectance measurements) is then presented. Reflectance measurements on the liquid dispersants $CHBr_3$ and CS_2 are used to determine their spectral refractive indices in the near-infrared. Measurements are also made on water to test the accuracy of the method by comparison with available data. Finally, the results of calculations to determine the sensitivity of the measured transmittance to various factors (optical properties, size distribution, loading, etc.) are discussed.

It was decided to perform the experiment at room temperature because it is extremely difficult to make valid and accurate emission/absorption and scattering measurements on

ash dispersed in a high temperature environment. A major consideration here was the conclusion that there is no satisfactory method for dispersing and adequately deagglomerating a sample of ash powder into a gas stream to reproduce the conditions of the ash aerosol before it was collected from the exhaust stream of the coal combustor. This conclusion was based on extensive experience of redispersing ash, and other fine, insulating powders into a gas stream for laboratory research in electrostatic precipitation at Stanford (Self, 1989).

On the other hand, it *is* possible to produce stable, well-deagglomerated dispersions of fly ash in liquids using ultrasonic agitation. Moreover, by stirring it is possible to maintain stable liquid dispersions at concentrations much higher than is possible with gaseous dispersions. This fact allows one to perform optical extinction and scattering experiments on a much smaller volume of dispersed ash (contained in an optical test cell) than is possible with a gaseous dispersion. This technique also permits the use of suitably high ash loadings to achieve measurable extinction over a short path length.

In gases, scattering dominates and obscures absorption. Scattering depends strongly on $(n_r(\lambda)-1)$ because it is the refractive index of the ash *relative* to the medium that determines the scattering cross-section in Mie theory. Unlike $k_r(\lambda)$, $n_r(\lambda)$ is relatively insensitive to C, λ, T. Extinction measurements on liquid suspensions significantly reduces scattering relative to absorption, providing a more critical test with regard to the optical property values.

5.2 Optical Design of Transmissometer

The theoretical basis for measuring absorption or extinction (i.e., the net effect of absorption and scattering) assumes a perfectly collimated incident plane wave. In practice, a perfectly collimated beam is not realizable, but one uses a beam of small divergence angle. A small angle is not critical for absorption measurements. However, a small divergence angle is necessary when measuring extinction due to scattering because it is important to reject light scattered at small angles to the axis (Hodkinson, 1966). The rejection of scattered light is especially difficult for large size parameter, $x_r = \pi D/\lambda_r$, when typically half of the scattered light is contained in the forward diffraction lobe of angular width, $\theta_d \approx (1/x_r)$.

In the standard design of transmissometer, a well-collimated beam is used. This is particularly appropriate for measuring extinction in optically-thin aerosols where the path length through the scattering medium has to be long compared to the beam diameter.

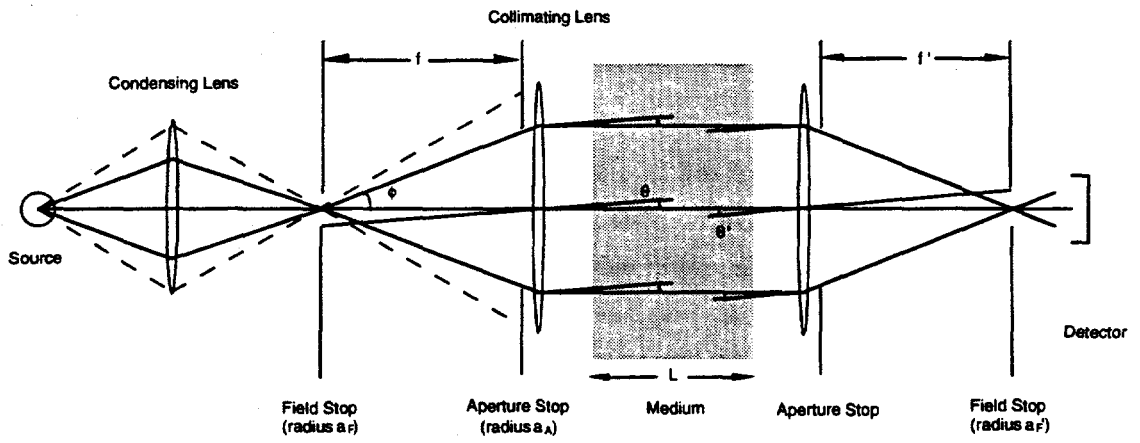

Figure 5.1: Standard design of a transmissometer for measuring extinction over large path lengths.

However, in measuring stronger absorption, or scattering through denser dispersions, where the path length may be comparable with or smaller than the beam width, an alternative design is possible in which the cell is placed at an image point of the optical system. The two cases are discussed below, the second design being found suitable for use in the planned measurements (Self, 1991).

5.2.1 Standard Design

Figure 5.1 shows a transmissometer, the conventional experimental set-up for transmittance (or extinction) measurement. For measurements in the infrared, mirrors are usually preferable to lenses. Although the transmitting and receiving optics are shown identical, this is not necessary. For spectral measurements, the field stop on the receiving side would be either the entrance or the exit slit of a monochromator, depending on which is smaller. Because of its convenience, it is usual practice to image the source on to the transmitting field stop where its size can be controlled by adjusting the radius, a_F. The magnification by the condensing lens must be sufficient for the image to be larger than the stop and the lens diameter large enough to more than fill the aperture of the optical system (as determined by the limiting aperture stop).

As shown in the figure, the transmitting field stop is placed at the focus of the collimating lens to produce a nominally parallel beam so that the image of the stop is at infinity. The

beam has a radius, a_A, that is determined by the aperture stop. The divergence of the beam, in terms of its half-angle, θ, and in the paraxial ray approximation ($\tan\theta \approx \sin\theta \approx \theta$) is

$$\theta = \frac{a_F}{f}$$

Here a_F is the radius of the field stop and f is the focal length of the collimating lens. A conserved quantity called etendue, ε, which is a measure of the light transmitting capacity of an optical system, is evaluated at any image point as the product of the beam area, A and the solid angle, Ω, i.e., $\varepsilon \equiv A\Omega$ (Jenkins and White, 1981). To evaluate ε for the 'collimated' beam (i.e. for the image at infinity) one uses $A = \pi a_A^2$, and $\Omega = \pi\theta^2$. Hence

$$\varepsilon = \frac{\pi^2 a_F^2 a_A^2}{f^2}$$

The power transmitted by the system is $P = I_s\varepsilon$, where I_s is the total source radiance (units: $W/m^2/Sr$). The spectral power over an increment of $\Delta\lambda$ transmitted is

$$\Delta P_\lambda = I_{s,\lambda}\,\varepsilon\,\Delta\lambda$$

where $I_{s,\lambda}$ is the spectral radiance of the source (units: $W/m^2/Sr/\mu m$). When all the power is transmitted (i.e., no absorption or reflection losses), ΔP_λ is conserved, and because ε is a conserved quantity, the radiance, $I_{s,\lambda}$, is invariant through the system.

It is noted that for a system with more than one field or aperture stop, the etendue is set by the limiting field and aperture stops; the others are superfluous. Generally, for a given source radiance, one needs to maximize the etendue of the optical system so as to maximize the power to the detector and optimize the signal/noise ratio. However, if the divergence of the 'collimated' beam is set to a small value, the etendue can only be increased by increasing the radius of the beam, which is determined by the aperture stop.

For absorption measurements (no scattering) one does not, in principle, need any field or aperture stops on the receiving side. In practice however, one usually places the limiting stops on the receiving side in order to minimize stray light. Also, for spectral measurements the limiting field stop is often the monochromator slit and the aperture is set by the F-number (or F/#, the solid angle of acceptance) of the monochromator because it is necessary to fill the grating to obtain its full spectral resolution. Thus the etendue is set by that of the monochromator and is coupled to the spectral resolution. Also, in this case, the geometry is not cylindrically symmetric about the axis and one must consider both the width and height of the slits. Usually, the slit height, h, is larger than the width, s, and one can

increase the etendue without losing spectral resolution by increasing the height but, if the slit is the limiting field stop, the angular divergence, θ_h, parallel to the slit will be larger than that (θ_s) perpendicular to the slit.

For measuring extinction due to scattering, it is essential to reject forward scattered light. A considerable amount of past literature contains erroneous results for extinction measurements because the forward scattered light was not adequately rejected (Hodkinson, 1966). Thus it is necessary to use field stops on both the transmitting and receiving optics. Usually, the best one can do is to match these field stops, so that light scattered at angles greater than the beam divergence half angle θ is rejected. For example, if the acceptance angle of the receiving field stop is $\theta' = a'_F/f'$, then by making $\theta' = \theta$, forward scattered light is rejected for scattering angles greater than $\sim \theta'(= \theta)$. However light scattered at angles $\leq \theta'(= \theta)$, as well as the unscattered light will be accepted. In this respect, measurements of extinction due to scattering can never be perfect, and for a fixed collection angle θ', are increasingly inaccurate for large size parameter.

For a spectral transmissometer where the limiting field stop is set by the monochromator it is essential to use a field stop on the transmitting side which (nearly) matches that of the monochromator.

5.2.2 Alternative Design

It is clear from the previous section that in the case of the conventional transmissometer, the ratio of the beam radius to the medium thickness is small, i.e., $a_F/L \ll 1$. However, for the present application we are constrained by the cell design to $L \simeq 1$ cm, and a beam radius, $a_F \simeq 1$ cm (which is sufficiently large to yield an acceptable signal/noise ratio). Hence, instead of designing for a collimated beam passing through the medium (i.e., with the image of the transmitting field stop at infinity), a design is considered in which a magnified image of the source (or entrance field stop) is produced at the center of the medium, as shown in Figure 5.2. The radius of the magnified image of the transmitting field stop at the center of the medium is $M\, a_F$, where $M = s_2/s_1$ is the magnification. At the field stop the etendue is $\varepsilon = (\pi a_F^2)(\pi \phi^2)$, where $\phi = a_A/s_1$, i.e., $\varepsilon = \pi^2 a_F^2 a_A^2/s_1^2$. At the image the etendue is $\varepsilon = \pi(M a_F)^2(\pi\theta^2)$, where $\theta = a_A/s_2$, i.e., $\varepsilon = \pi^2 M^2 a_F^2 a_A^2/s_2^2$. Clearly, these are equal because $s_2^2 = M^2 s_1^2$.

As with the standard design, one can control the width and divergence of the beam in

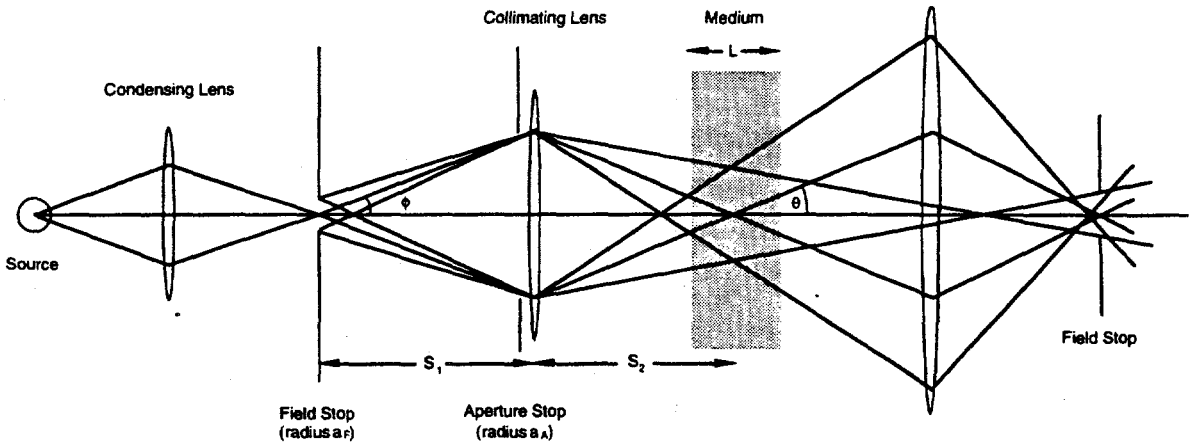

Figure 5.2: Proposed alternative design of a transmissometer for measuring extinction over short path lengths.

the medium. However, whereas in the standard system the beam radius is controlled by the aperture stop and the divergence angle is controlled by the field stop ($\theta = a_F/f$), in the alternate system, the beam width is determined by the image of the field stop, while the divergence angle is controlled by the aperture stop ($\theta = a_A/s_2$). This makes little difference in the case of an absorbing medium, but in the case of scattering, it is necessary to consider the forward scattered light.

It is clear that in the absence of an aperture stop on the receiving side (and for a sufficiently large receiving lens), light scattered at arbitrarily large angles in the forward direction will pass through the image of the transmitting field stop on the receiving side, i.e., through the actual receiving field stop if it is matched to that of the transmitting one. This follows because the image at the center of the cell and its image at the receiving field stop are conjugate points, so that any scattered ray passing through the first must pass through the second. In order to limit the collection of scattered light to angles $< \theta$, the divergence of the input beam, one should use a matched aperture stop on the receiving side.

To summarize, the designs of the two systems differ as follows. In the standard design, one uses field stops (preferably matched) on both the transmitting and receiving sides. In addition, one may use an aperture stop on either side to control the beam diameter. However, in the alternate design, one should use aperture stops (preferably matched) on both the transmitting and receiving sides. In practice one would use a field stop on the

receiving side (the monochromator entrance slit for a spectral system) and arrange for the transmitting field stop (or the source itself) to be large enough so that its image at the receiving field stop is rather larger than the receiving field stop.

It appears that the alternate design has an advantage for extinction measurements in short cells (as in our application), and for spectral systems where it is preferable to use the monochromator slit as the receiving field stop. For the standard design it would be difficult to make a transmitting field stop to closely match the monochromator slit as receiving field stop. In contrast it is much easier to match aperture stops for the alternate system.

5.3 Choice of Dispersing Media and Cell Design

Suitable liquids and window material (for the test cell) are needed to allow extinction experiments over the wavelength range of interest, say λ=1–13 μm. While there is no liquid that is transparent over the whole range, it was found that by using three separate liquids, namely carbon tetrachloride (CCl_4), carbon disulfide (CS_2) and bromoform ($CHBr_3$), the full wavelength range could be covered (more details in Section 5.6). Moreover, it was also established that there is negligible chemical reaction between fly ash constituents and these liquids.

For windows, barium fluoride (BaF_2) is suitable because it transmits over the full wavelength range of interest*. Its refractive index is close to those of the three liquids (Section 5.6), which minimizes reflection at the window–liquid interface. Additionally, BaF_2 does not react with the chemicals, or with atmospheric water vapor†.

A schematic of the cell is shown in Figure 5.3. The windows (5 cm diameter, 3 mm thick) cover both the test chamber containing the dispersed ash and the reference chamber containing the pure liquid. Thus the signal passing through both the suspension and the reference signal are measured under the same conditions. The cross-sections of the two chambers are limited by the window diameter. The test chamber diameter was maximized after ensuring that the reference chamber could accommodate a beam of diameter approximately 5 mm. The path length, L, of the suspension and reference liquid between the two windows is 9 mm. Two pairs of Viton O-rings are used to seal the cells and cushion

*Its *Reststrahlen* absorption peak is located in the far-infrared at 53 mm.

†Although most of the experiments were performed using BaF_2 windows, sapphire windows were used in some of the preliminary studies. The latter possess superior mechanical properties, but transmit only up to $\approx$6 μm.

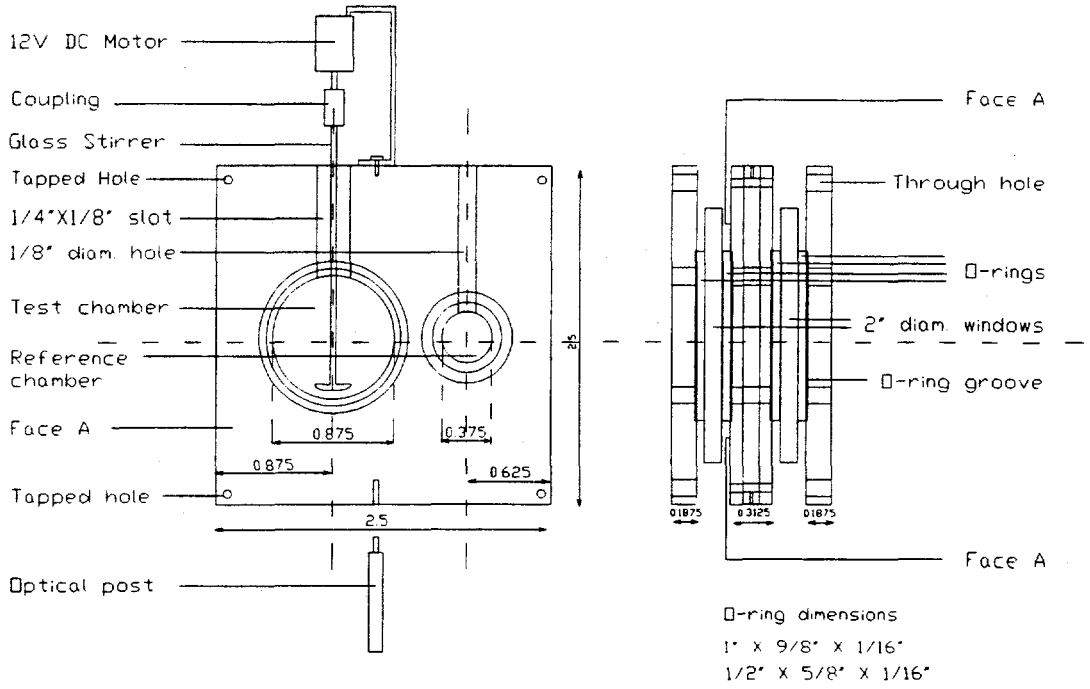

Figure 5.3: Sectional schematic of experimental cell.

the windows. The output shaft of a small D.C. motor, mounted on the top of the cell, is coupled to the glass stirrer. The stirrer is operated at speeds in the range 3000–4000 r.p.m., sufficiently high to prevent heavy particles from settling, but not so high as to generate bubbles. The voltage-speed characteristics of the stirrer system, in the range of interest, is almost linear as shown in Figure 5.4.

5.4 Transmittance Measurements: Infrared Optical System and Experimental Set-up

Based on the discussion of Section 5.2.2, an optical configuration (Figure 5.5) was designed to maximize the signal while minimizing the collection of light scattered at small angles to the forward direction by large particles. An image of the source filament was located at the center of the cell. The cell itself can be moved back and forth on an optical rail perpendicular to the path of the beam, so that the latter can pass through the ash suspension and the reference liquid alternately. The ratio of the detected signal powers in the two paths is the measured transmittance, T, from which the extinction is found as, $E = 1 - T$. The components of the optical system are described in the rest of this section.

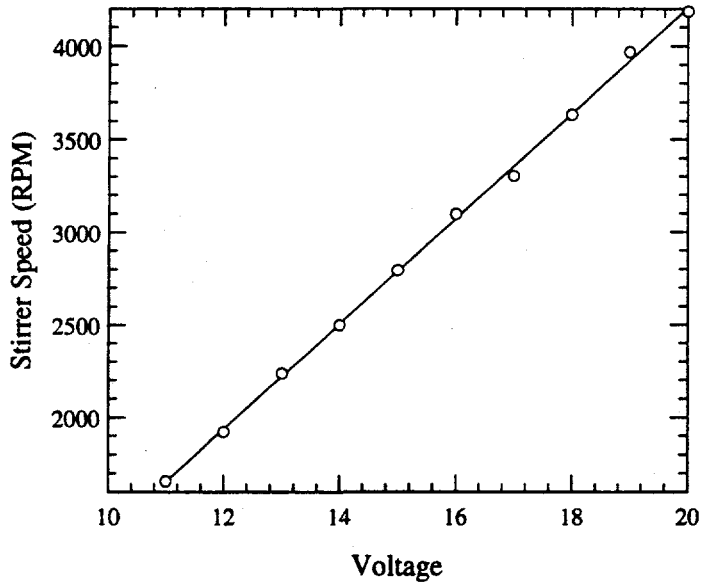

Figure 5.4: Voltage-speed relationship for the stirrer-motor system used to keep the ash particles in suspension.

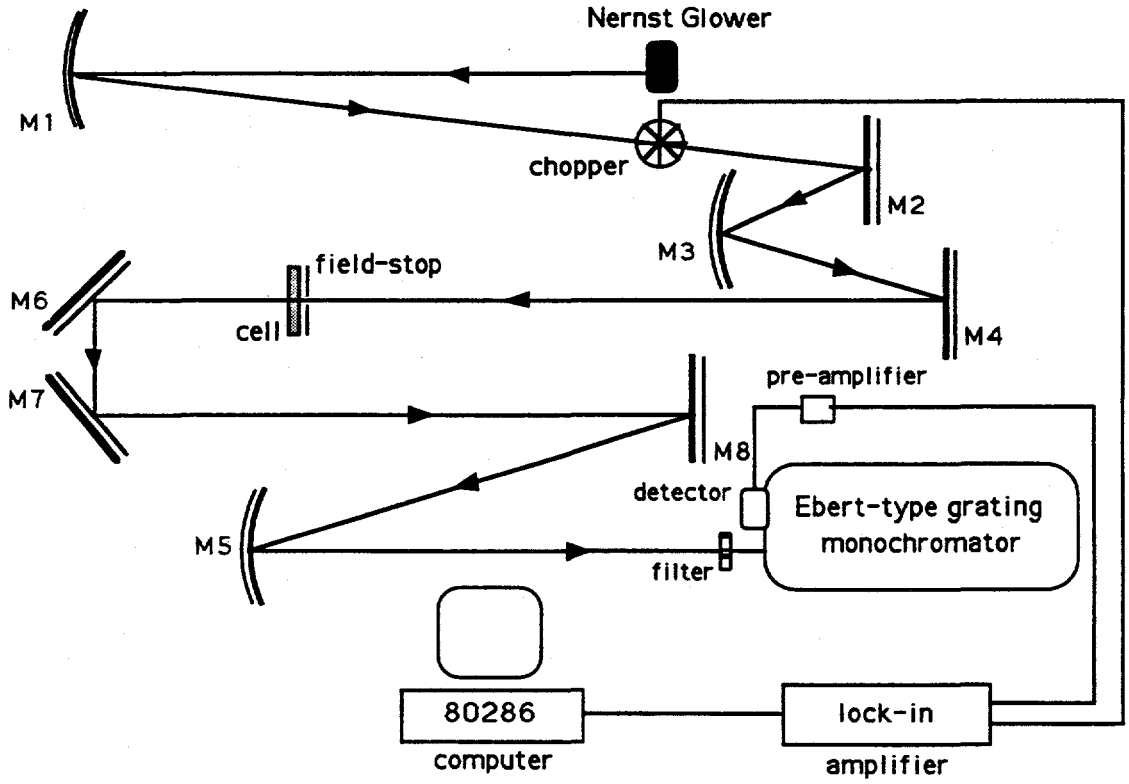

Figure 5.5: Experimental set-up for transmittance measurements.

A Nernst Glower (Electro-optical Industries model 304) is used as the broadband radiation source. Introduced in 1900, the Glower's composition is typically 90:7:3 parts by weight of oxides of the rare earth elements zirconium, yttrium, and erbium, respectively (Martin, 1966). These oxides have overlapping *Reststrahlen* bands, resulting in high emissivity at long wavelengths. The mixture, together with some binding material, is extruded in the form of filaments that are about an inch in length and $\approx$1 mm in diameter, with platinum wires at the ends for electrical connection. The Glower initially carries a small current, and is radiantly heated by a pair of (electrically heated) Nichrome filaments. The Glower's resistance decreases with temperature (i.e., it has a negative temperature coefficient of resistance), and when the temperature is sufficiently high, the tungsten filaments are switched off. The ceramic filament then glows brightly in the visible, and operates at an effective blackbody temperature of 1700–1800°C with a spectral emission profile that resembles black body radiation. The temperature of the filament is kept constant by adjusting the power-supply current (usually in the range 0.3–0.6 A) using radiometric feedback control.

Apart from its ability to emit far into the infrared ($\approx$50 μm), another advantage of the Nernst Glower is that it can operate under atmospheric conditions, thus eliminating the need for windows. Its main disadvantage is the unpredictability of its lifespan[‡] often caused by thermal stresses (it has to be contained in a housing for protection from draughts), and electrical contact problems. Because it is fragile and sensitive to impurities, it has to handled carefully using tweezers or gloves.

The source radiation is modulated using a mechanical chopper (PAR model 125A), the chopping frequency being synchronized with the lock-in amplifier. While it can operate at any of twenty-four frequencies in the range 13–1015 Hz, the chopper was operated at $\approx$670 Hz in these experiments. This frequency is sufficiently distant from high multiples of the line frequency, a primary source of interference/noise.

All the mirrors used are front-surface gold mirrors having a reflectance $\gtrsim$ 99% over the wavelength range of interest. The concave spherical mirrors M1, M3, and M5 are each 4″ in diameter and have focal lengths of 0.5 m, while the mirrors M2, M4, and M6 are plane. The mirror M1 images the filament at the chopper. The latter, in turn is used as the object for concave mirror M2, which magnifies and images it at the center of the cell. The field stop is adjusted to obtain a circular image. The image at the center of the cell (diameter

[‡]The Glower lifespan can last from a few hours to a year or more of intermittent use, the filament often fracturing with little warning. Three Glower elements were used over the period of this study.

≈5 mm) is used as the object for concave mirror M3 which images it at the entrance slit of the monochromator. The overall magnification is close to unity. Several plane mirrors (M2, M4, M6, M7 and M8) are used to fold the beam.

The detector, located at the exit slit of the monochromator, is a liquid nitrogen cooled (77 K), photoconductive[§] HgCdTe (mercury cadmium telluride) infrared detector (Judson model J15-D) with a cut-off wavelength of 13 μm, and maximum responsivity at 12 μm. (The detector cut-off wavelength is defined as the long wavelength point of the spectral response profile where the response is 10% of peak.) The detector surface, of area 1 mm^2, is protected by a zinc sulfide window. The noise is further reduced by the use of a cold shield which limits the detection half-angle to 10°.

An Ebert-type monochromator (Jarrell-Ash model 82-020) is used with multiple sets of gratings for wavelength selection over a wide range. The monochromator has a focal length of 0.5 m, and a numerical aperture or F/# of 8.6. Slit widths of ≈1 mm maximize power to the detector while yielding adequate spectral resolution. The gratings were used in first order for all the measurements. To prevent detection of higher order radiation at shorter wavelengths, a longpass filter is placed at the entrance slit. Six different filters were used, each having an average transmittance >0.75, over relevant wavelength ranges. Table 5.1 shows how the gratings and filters were combined to form six contiguous spectral sub-ranges. The Table also shows the blaze wavelength and the number of lines per mm for each of the four reflection gratings. The maximum wavelength at which a longpass filter will block second order diffraction lobes is $2\lambda_c$, where λ_c is the nominal cut-off frequency which is defined as the wavelength below which the filter transmittance is $\lesssim 0.05$. A stepper motor, controlled by a personal computer, is used to select monochromator dial settings corresponding to desired wavelengths.

The output signal from the detector pre-amplifier is the input to the lock-in amplifier (SRS model SR550) which is synchronized with the chopper. This phase-sensitive detection system rejects a large fraction of the unmodulated background radiation, yielding remarkably good signal/noise ratio, even beyond 11 μm, where the signal intensity is quite low. In essence, the amplifier acts as a very high Q (narrow bandwith) filter sampling at the chopper frequency, with an effective bandpass that is inversely proportional to the time constant of

[§]A photoconductive detector carries a steady bias current (an optimal value 30 mA for best signal to noise ratio in this case) driven through a load resistor. The detector responds to infrared radiation through small changes in its resistance which is proportional to the signal. Because of its low impedance (63 Ω), a low-noise pre-amplifier (gain=60 dB,) is used to detect the voltage changes.

Table 5.1: Scheme for forming measurement ranges A–F by combining various gratings and filters to span the wavelength range 1–13 μm, showing the grating blaze wavelengths, ruling density in lines/mm, wavelength resolution ($\Delta\lambda$), the cut-off wavelengths for each filter, and the maximum and minimum wavelength for each of the six ranges.

Sub-range	Blaze λ (μm)	Ruling (lines/mm)	$\Delta\lambda$ (μm)	Cut-off λ (μm)	λ_{min} (μm)	λ_{max} (μm)
A	1.2	590	0.010	0.84	1.0	1.5
B	2.6	295	0.019	1.5	1.6	2.4
C	4.0	148	0.038	2.0	2.4	3.8
D	4.0	148	0.038	3.5	3.8	6.2
E	10.0	50	0.113	6.125	6.25	11.8
F	10.0	50	0.113	7.85	11.8	14.0

the final rectifier/detection circuit. A time constant of two seconds was used for all signals $\gtrsim$ 1 mV. With decreasing signal strength, this period is progressively increased, to a maximum of thirty seconds close to 13 μm where the signal falls to $\lesssim$ 50 μV.[‖] An integration time period of approximately five times the time constant is used for all measurements.

The digitized output from the lock-in is sent to the PC *via* a parallel port using GPIB (IEEE 488) protocol. Software available from previous work (Ebert 1993) is used for real-time display of the signal. A mouse-control is used to advance the stepper motor, and for beginning and ending data acquisition. The software also facilitates data file manipulation, the setting of spectral ranges (see Table 5.1), and the display of transmittance (or reflectance) *vs* wavelength plots as the spectral scan proceeds, among other functions. The computer control of the system considerably enhances the overall speed of data acquisition, enabling greater spectral resolution (a constant wavelength increment of 0.1 μm was used over the range 1–13 μm) than would have been possible with manual control.

[‖]Signals as small as $\approx$10 μV have been recorded by Ebert (1993) using the same lock-in detection system. However, when large time constants are used, one tends to record low frequency noise caused by the wandering of the input signal occurring over comparable time periods. Additionally, there are linearity limitations below $\lesssim$ 50 μV imposed by the contribution of extraneous scattered light (which has been chopped) to the signal. Apart from the above two factors, there are several others that set the lower 'limit' of signal measurement by the lock-in.

5.5 Near-normal Reflectance Measurements for $n(\lambda)$ of CS_2, and $CHBr_3$

5.5.1 Experimental Apparatus and Procedure

The refractive indices of all three liquids were determined using the standard technique of near-normal reflectance measurements. The measurement procedure and the apparatus is described in details by Ebert (1993), and Goodwin (1986), and is summarized here. It is clear from Figure 5.6 that most of the components of the experimental set-up are the same as those used in the transmittance measurements (Figure 5.5). However, in this optical train, the mirror M3 forms an image of the glower at the surface of the liquid in the alumina crucible. The reflection of the image is collected by the M5, which forms an image at the entrance slit of the monochromator. After the signal is recorded, M4 is swung out of the beam path allowing for the measurement of the signal reflected from the gold reference mirror *via* the plane mirror M4REF.

The reference signal is corrected for reflection at the gold mirror by normalizing the signal value with the spectral reflectivity of gold, which has an approximately constant value of 0.992 over the wavelength range of interest (Lynch and Hunter, 1985). All three liquids have high vapor pressures and the surface level in the crucible changed continuously due to evaporation. However, the evaporation rate was significantly decreased by placing the aluminium crucible (containing the liquid) at the bottom of a 18″ long hollow tube. Additional liquid was added every half-hour to bring the liquid level up to the point at which the optical system had been aligned.

Because of the small departure from normal incidence, there is a systematic underprediction of ~0.1% in the measured reflectance, $R(\lambda)$, for this configuration, which is acceptable for our purposes.

5.5.2 Reflectance Measurements on Water

Measurements were made on water** to test the method by comparison with data available in the literature (Hale and Querry, 1968, Irvine and Pollack, 1973). The reflectance data shown on Figure 5.7 indicates anomalous dispersion in the vicinity of the strong absorption

**Apart from water, there do not appear to be any other liquids whose optical properties have been determined with high accuracy over the wavelength range of interest.

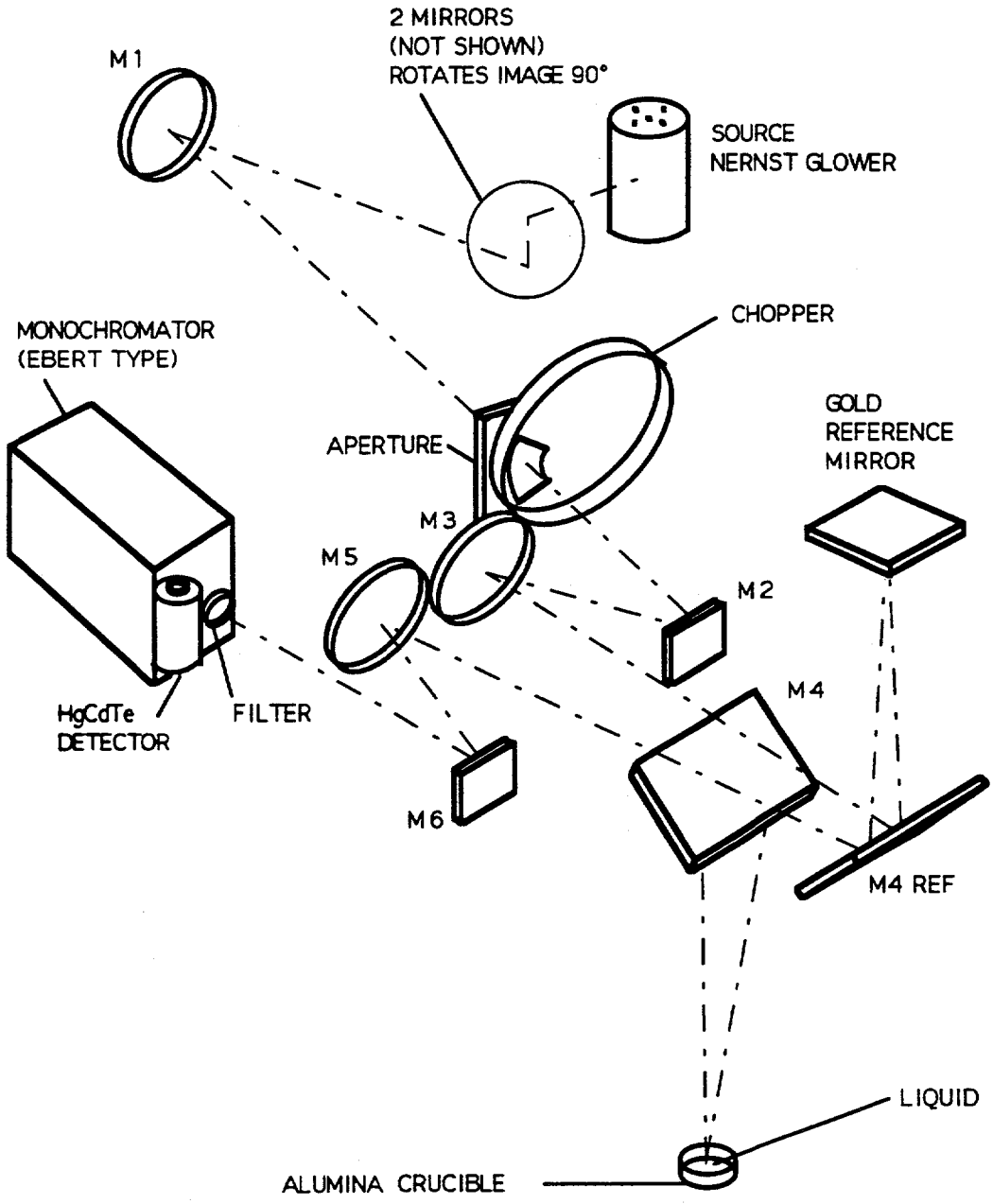

Figure 5.6: Experimental set-up for near-normal reflectance measurements.

bands at 2.8 μm and 5.7 μm, where $k \geq 0.1$. The refractive index data obtained using the Kramers-Kronig relations discussed in Chapter 2 are plotted on Figure 5.8. In the wavelength range 1–11 μm, the current results agree very closely with those reported in the references, showing only small differences near the absorption bands where $n(\lambda)$ changes rapidly.

The largest discrepancy between these measurements and the published data is for λ >11 μm, where the two published data sets show significant disagreement, with $n(\lambda)$ reported by Irvine and Pollack being on average ~4% larger than reported in Hale and Querry. The current reflectance measurements yield values of $n(\lambda)$ slightly larger than Irvine and Pollack's data. However, this is expected since the Kramers-Kronig procedure is not accurate close to the end of the measured wavelength range for the following reason. In the wavelength range 11–13 μm the imaginary part of the refractive index is increasing in value, with $k(\lambda$=11 $\mu m)$~0.1 and $k(\lambda$=13 $\mu m)$~0.3. At longer wavelengths, $k(\lambda)$ continues to increase to a peak of $\approx$ 0.43 near 17 μm. The measured reflectance does not include this strong absorption band beyond 13 μm, resulting in an underprediction of $k(\lambda)$ by the Kramers-Kronig procedure. The effect of this neglect is significant close to the end point (λ=13 μm), but is minor at shorter wavelengths. From Equation 1.12 (Chapter 2), we see that underprediction of $k(\lambda)$ results in overprediction of $n(\lambda)$ if ($n(\lambda)$-1) and $k(\lambda)$ are of similar magnitude. Therefore, overprediction of $n(\lambda)$ by the Kramers-Kronig method is expected in the wavelength range 11 μm< λ <13 μm. A more detailed discussion of this discrepancy is given by Ebert (1993).

The results of water reflectance measurements indicate a high degree of accuracy, and is the basis of our confidence in the accuracy of the data for $CHBr_3$, CS_2, and CCl_4.

5.5.3 Reflectance Measurements on $CHBr_3$

Figure 5.9 and 5.10, respectively show the reflectance and refractive index data for $CHBr_3$. It is clear that anomalous dispersion occurs only at the strong absorption bands located at 3.3 μm and 8.7 μm (Tarpley and Vitiello, 1952). A magnified view of the former band is shown in the window. Except at these two wavelengths, where there are rapid changes, the value of $n(\lambda)$ decreases steadily from 1.58 to 1.51 over the wavelength range 1–13 μm. Because $n(\lambda)$ undergoes large changes over this wavelength range, as many as seven cubic polynomial fits have been used to fit the data over separate wavelength ranges. However, when interpolating, it is advisable to determine new polynomial fits using tabulated values

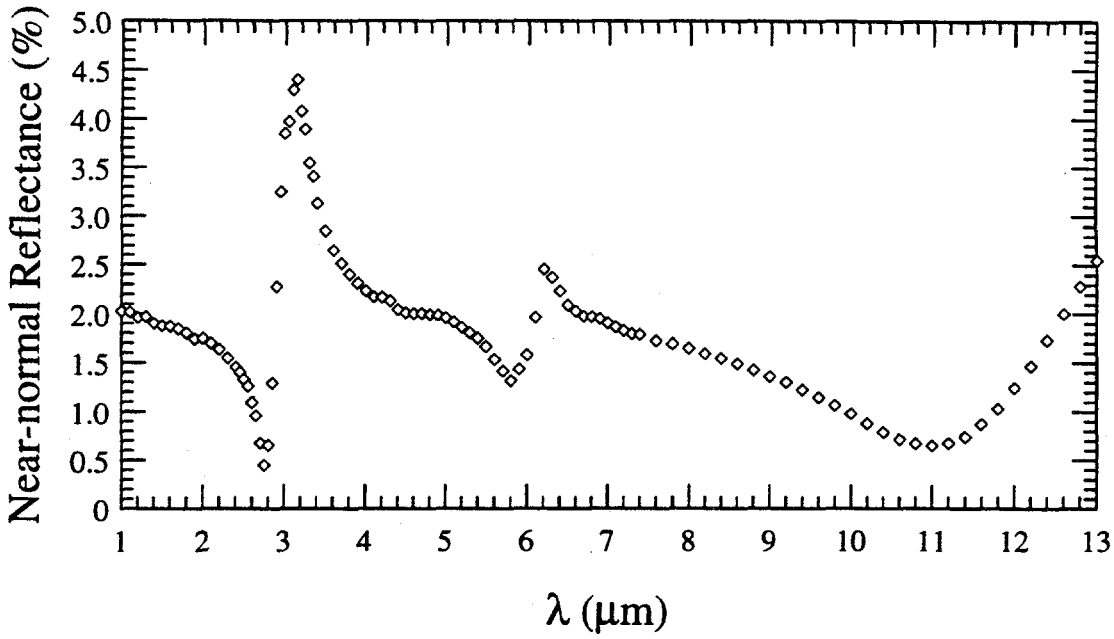

Figure 5.7: Near-normal reflectance of water in the wavelength range 1–13 μm. Note that the y-axis is expanded.

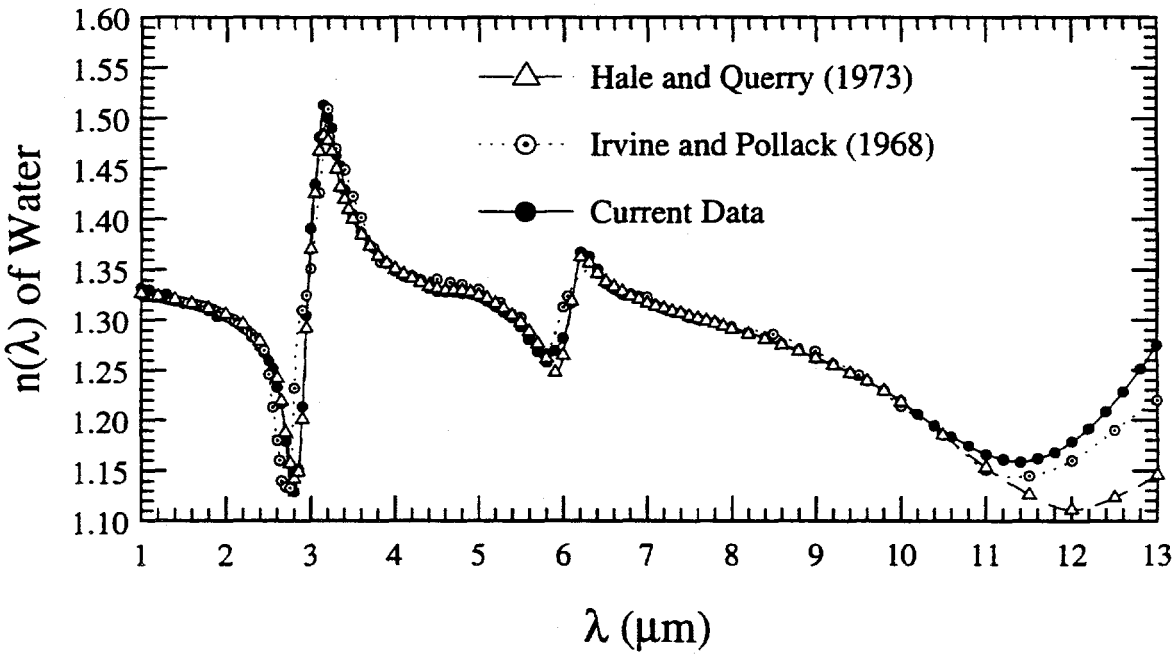

Figure 5.8: Spectral refractive index of water in the wavelength range 1–13 μm. Note that the y-axis is offset.

Table 5.2: Harmonic oscillator parameters for bromoform refractive index.

Oscillator	ω_o (cm^{-1})	λ_o (μm)	ω_p	γ
1	3011.27	3.32	49.50	11.75
2	1137.60	8.79	112.87	13.17
3	580.62	17.22	220.39	29.99

of $n(\lambda)$ (See Appendix H) in the proximity of the wavelength of interest.

Following the Lorentz-Lorenz model (see Section 2.3), a three-oscillator fit to the $n(\lambda)$ data of the following form, is shown in Figure 5.11.

$$m^2 = n_\infty^2 + \sum_{j=1}^{3} \frac{\omega_{pj}^2}{\omega_{oj}^2 - \omega^2 - \mathrm{i}\,\gamma_j\,\omega}$$

The value of the constant term n_∞, used to account for short wavelength absorption, is 1.578. The best-fit values of the resonance frequency (ω_o), the resonance wavelength (λ_o), plasma frequency (ω_p), and the damping coefficient (γ), for each of the three oscillators, are shown in Table 5.2. The locations of the absorption peaks corresponding to C–H stretch and bending modes compare favorably with 3017 cm^{-1} (3.31 μm) and 1148 cm^{-1} (8.71 μm), respectively, given by Pouchert (1985). The third oscillator accounts for the effect of absorption beyond 13 μm, especially that due to C–Br stretch vibration at 653 cm^{-1} (Pouchert, 1985). As the plot of the error in Figure 5.11 shows, the fit to the data is quite good (except close to the absorption band at 8.7 μm) indicating that a simple oscillator model can reasonably model the vibrational absorption.

In the vicinity of the strong CO_2 absorption bands at 4.3 μm and that of water vapor at 2.9 μm, the signal-to-noise ratio (SNR) was very small due to absorption in the air path. Hence, no reflectance measurements were made at wavelengths close to these bands. Water has another weaker, broader band centered close to 6.0 μm. As a result, the SNR in the range 5.6–6.4 μm was lower than average, leading to slightly increased scatter in the data.

The precision of the measurements, based on reproducibility, depends on both signal/noise and the accuracy of the monochromator wavelength setting, especially in regions of strong absorption where $n(\lambda)$ changes rapidly with wavelength. Hence, the precision is lower in the vicinity of absorption bands of atmospheric CO_2 and water vapor, and near regions of anomalous dispersion. By multiple measurements at each wavelength, the precision of $n(\lambda)$, averaged over wavelength ranges, was determined to be 0.1% (1.0–2.5 μm),

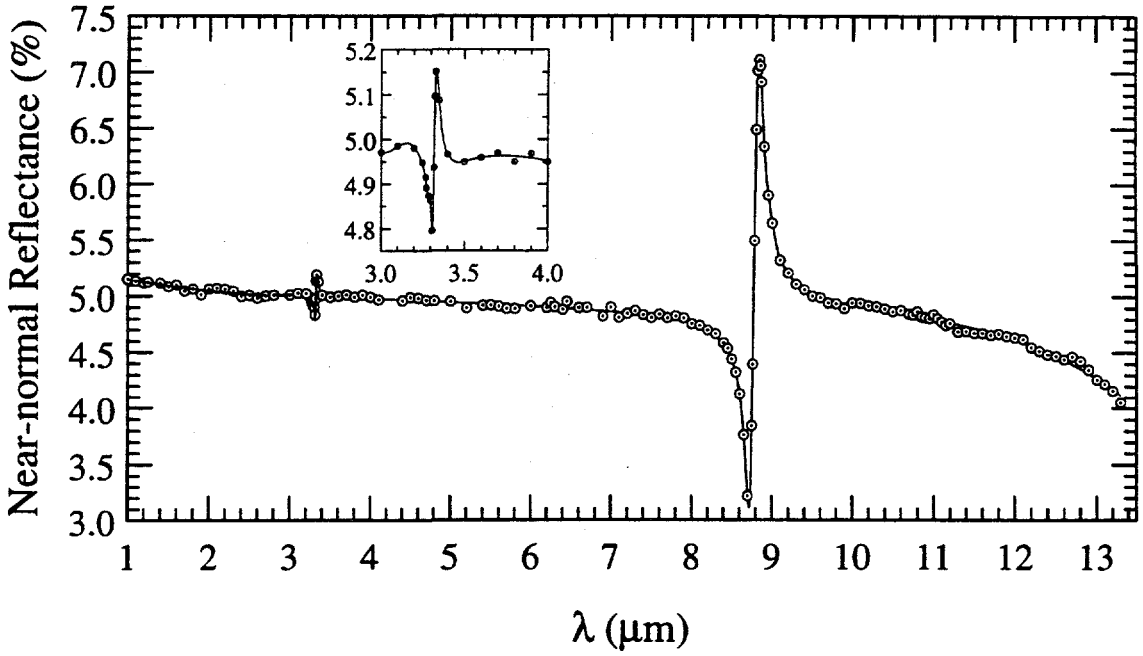

Figure 5.9: Near-normal reflectance of bromoform in the wavelength range 1–13 μm. Note that the y-axis is expanded.

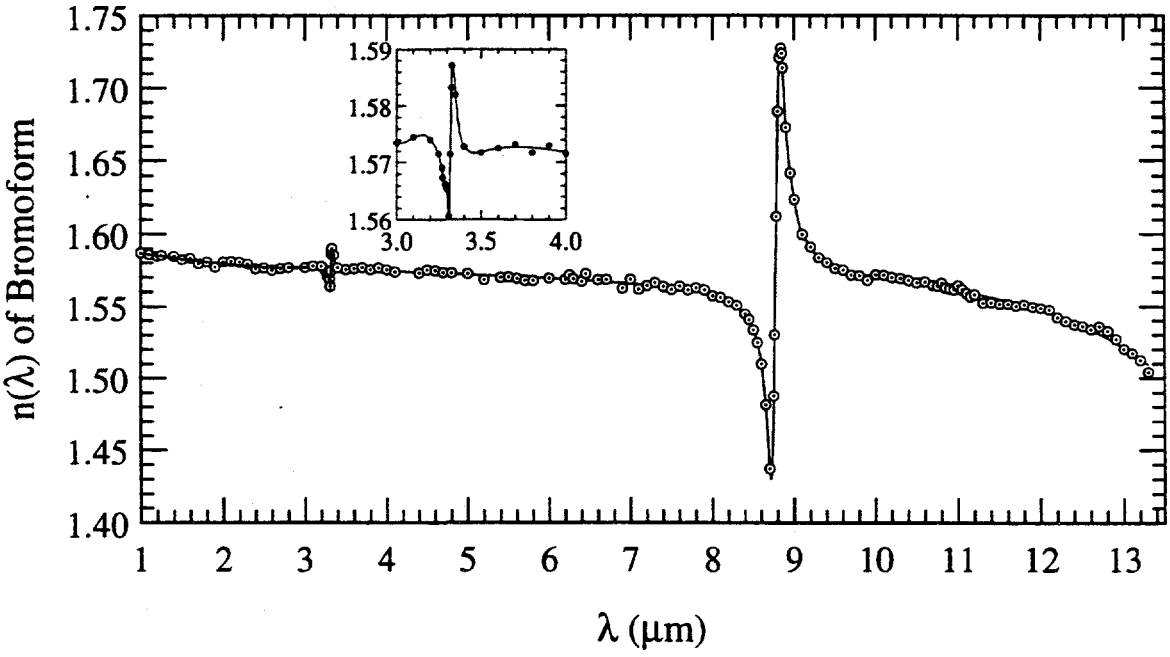

Figure 5.10: Spectral refractive index of bromoform in the wavelength range 1–13 μm. Note that the y-axis is expanded.

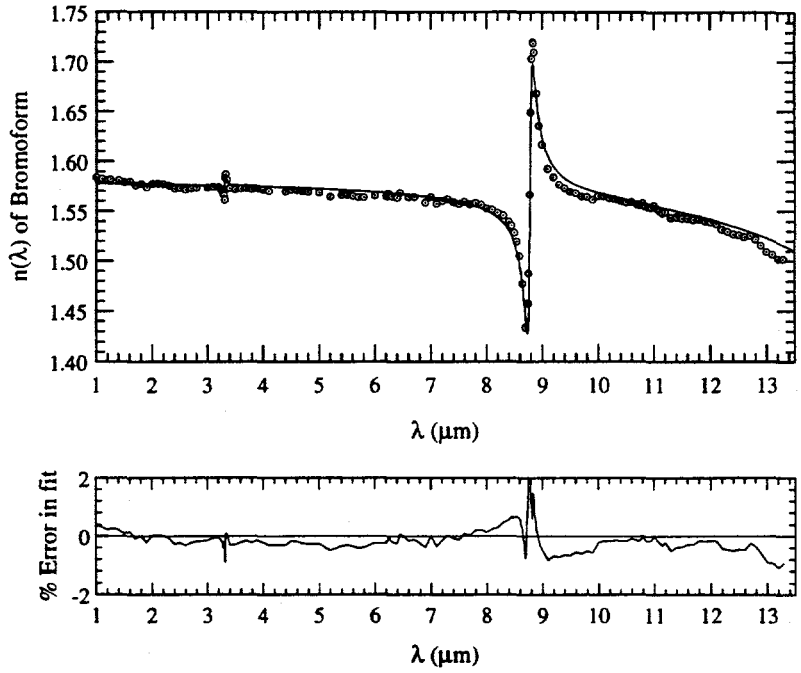

Figure 5.11: Three-oscillator Lorentz-Lorenz model fit to bromoform $n(\lambda)$ data. Also shown is the fitting error.

0.2% (2.6–8.5 μm), 0.5% (8.6–8.9 μm), 0.2% (9.0–11.5 μm) and 0.8% (11.6–13.0 μm).

5.5.4 Reflectance Measurements on CS_2 and CCl_4

Figures 5.12 and 5.13 show the spectral reflectance and $n(\lambda)$, respectively, for CS_2 in the range 7.4–11.2 μm. The present data for CS_2 lie within $\pm 0.5\%$ of values by Pfund (1935) over this wavelength range. The precision is estimated to be same as for bromoform over corresponding wavelength ranges, except in the 8.6–8.9 μm range, where it is better than 0.5%*. The scatter in the data beyond λ=10 μm is caused both by decreasing signal strength as well as by slight optical misalignment caused by the liquid surface receding due to evaporation. The data for $n(\lambda)$ are tabulated in Appendix H.

Since there are no strong absorptions features, and hence no corresponding regions of anomalous dispersion, Lorentz-Lorenz fits are not warranted. Simple polynomial expressions can be used to correlate $n(\lambda)$ with λ. The following best-fit cubic polynomials are fitted to the data for interpolation (λ in microns) for CCl_4 and CS_2 respectively.

*For bromoform, the signal/noise was low in this range because of absorption.

$$n(\lambda) = 1.459 - 3.064 \times 10^{-3}\,\lambda + 2.044 \times 10^{-4}\,\lambda^2 - 4.909 \times 10^{-5}\,\lambda^3 \qquad 1.0 < \lambda < 9.0$$

$$n(\lambda) = 4.203 - 7.389 \times 10^{-1}\,\lambda + 7.114 \times 10^{-2}\,\lambda^2 - 2.297 \times 10^{-3}\,\lambda^3 \qquad 7.0 < \lambda < 11.5$$

Refractive index data for CCl_4, measured by Ebert (1993) are shown in Figures 5.14. They appear to be within 0.5% of those of Pfund. The structures in the data of Ralajchak are probably noise-related, since there are no strong absorption bands in the wavelength range 1–6 μm.

The values of $n(\lambda)$ obtained using the simplified Fresnel relation (Equation 1.13, Chapter 2) are found to agree with those obtained using the Kramers-Kronig relations to within 0.1%, except near the strong absorption bands of bromoform, where the relation between the complex refractive index and $R(\lambda)$ includes a significant contribution from $k(\lambda)$ (Equation 1.12, Chapter 2).

5.6 Spectral Transmittance Measurements on CCl_4, CS_2, and $CHBr_3$

Spectrophotometric grade samples of the three liquids (99+%) supplied by Aldrich Chemical Company, Inc. were used for all measurements without further purification. For transmittance measurements on the pure liquid kept in the larger chamber, the control chamber was empty. The ratio of the signal intensity with the beam passing through the liquid chamber, to that with the beam passing through the empty chamber, is the apparent spectral transmittance, T_{exp}. The true transmittance is obtained after accounting for reflections at the window–air and window–liquid interfaces, and absorption by the windows as described below.

The expression for the effective transmittance of a sequence of multiple windows separated by air/vacuum, taking into account the reflectances at the interfaces, and absorption in the windows, is derived in Siegel and Howell (1981). A slightly modified expression is used here because of the presence of the liquid between the windows, although the same nomenclature is used. The dependence of all properties on wavelength is implied throughout, although not shown, for simplicity. This treatment assumes that the window surfaces

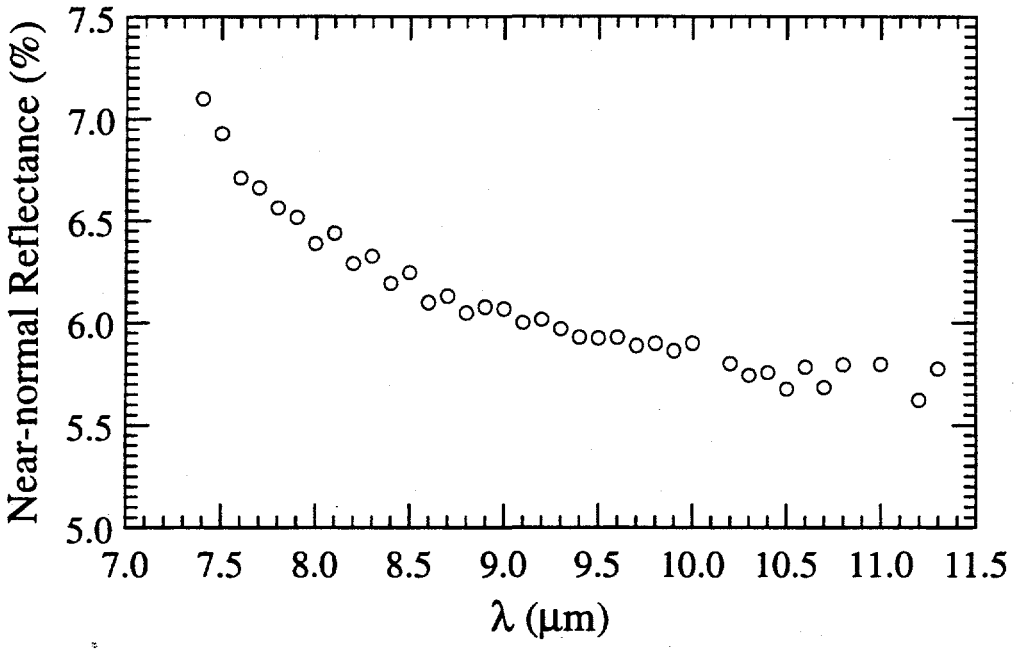

Figure 5.12: Near-normal reflectance of carbon disulfide in the wavelength range 7.3–11.2 μm. Note that the y-axis is expanded.

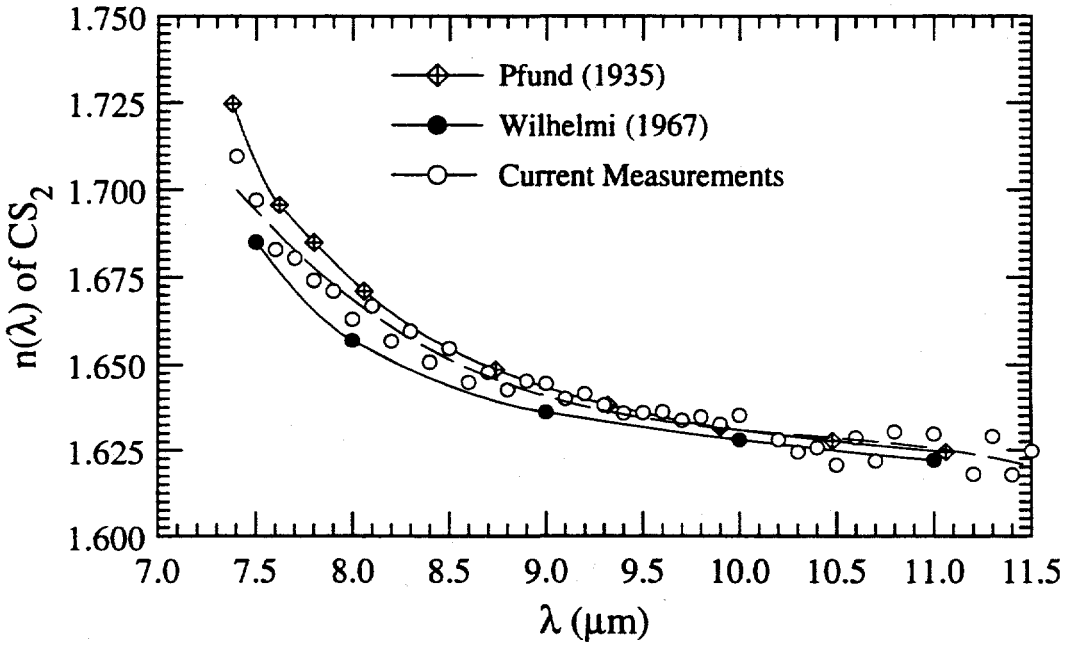

Figure 5.13: Spectral refractive index of carbon disulfide in the wavelength range 7.3–11.2 μm compared with published data. Also shown are polynomial fits to the data. Note that the y-axis is expanded.

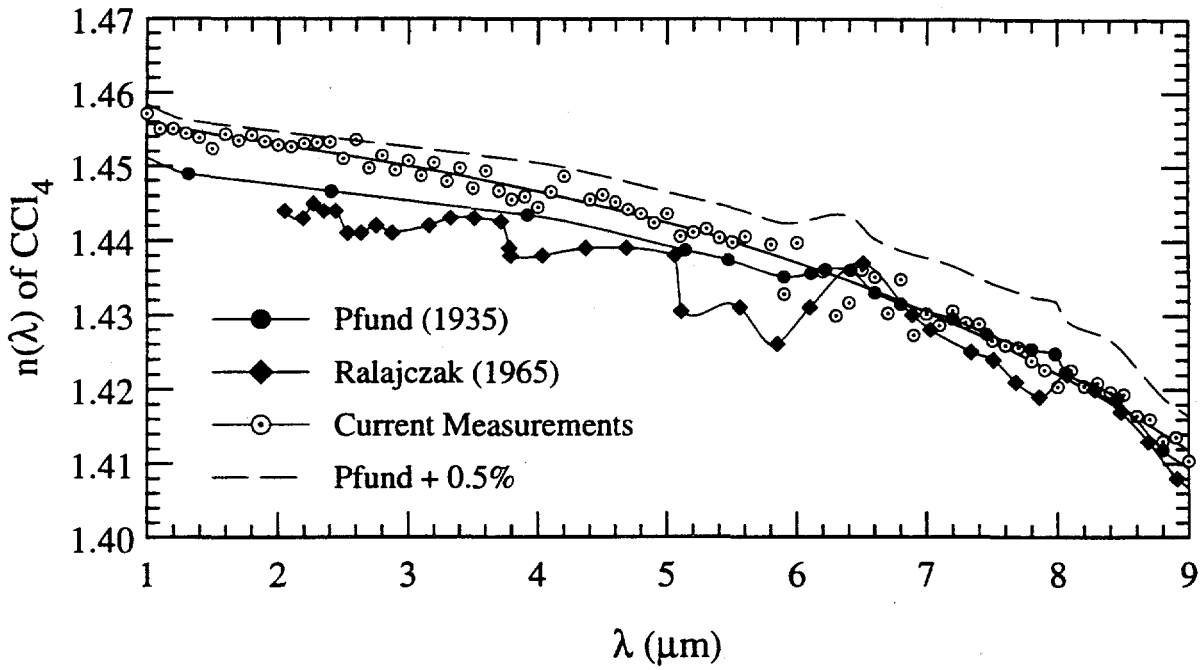

Figure 5.14: Spectral refractive index of carbon tetrachloride in the wavelength range 1–9 μm, (Ebert 1993) compared with published data. Also shown are polynomial fits to the data. Note that the y-axis is expanded.

are not so accurately parallel, and the coherence length of the radiation is not long enough that interference effects have to be taken into account.

If $(T_t)_l$ is the ratio of the energy transmitted through the chamber containing the liquid to the energy incident, and $(T_t)_{air}$ is the energy transmitted through the empty chamber, then

$$T_{exp} = \frac{(T_t)_l}{(T_t)_{air}} \tag{5.1}$$

The denominator is given by

$$(T_t)_{air} = \frac{T_w^2}{1 - R_w^2}$$

Here T_w and R_w are the apparent transmittance and reflectance of one BaF_2 window in air after taking into account multiple reflections at the two interfaces (i.e., the ratio of the energy transmitted through the window to the energy incident). They are calculated as follows.

$$T_w = \frac{\tau_w (1 - \rho_w)^2}{1 - (\rho_w \tau_w)^2}$$

$$R_w = \rho_w \left[1 + \frac{\tau_w^2 (1 - \rho_w)^2}{1 - (\rho_w \tau_w)^2} \right]$$

The normal reflectivity for a single interface, ρ_w, is given by the Fresnel relation

$$\rho_w = \left(\frac{n_w - 1}{n_w + 1} \right)^2 \tag{5.2}$$

Let T_{wl} and R_{wl} be the apparent transmittance and reflectance of one BaF_2 window with air on the incident side and the liquid on the other. Then

$$T_{wl} = \frac{\tau_w (1 - \rho_w)(1 - \rho_{wl})}{1 - \rho_w \rho_{wl} \tau_w^2}$$

and

$$R_{wl} = \rho_w + \frac{\tau_w^2 \rho_{wl} (1 - \rho_w)^2}{1 - \rho_w \rho_{wl} \tau_w^2}$$

The reflectivity of the window–liquid interface, ρ_{wl}, is obtained using the relative refractive index, n_w/n_l, in Equation 5.2. For the second window, where the incident radiation is on the liquid side, the corresponding apparent reflectance is

$$R_{lw} = \rho_{wl} + \frac{\tau_w^2 \rho_w (1 - \rho_{wl})^2}{1 - \rho_w \rho_{wl} \tau_w^2}$$

The transmittance is symmetric and, hence, $T_{lw} = T_{wl}$ Finally, one can use the above expressions to obtain $(T_t)_l$

$$(T_t)_l = \frac{\tau_l T_l T_{wl}}{1 - \tau_l^2 R_l R_{wl}}$$

Once $(T_t)_l$ is known from Equation 5.1, the transmittance of the liquid slab, τ_l, can found by solving the quadratic equation shown above.

The spectral refractive index of BaF_2 used in these calculations was obtained from Malitson (1964). He used the following Sellmeier-type dispersion equation to fit his data between 0.3 μm and 10.4 μm.

$$n(\lambda)^2 - 1 = \frac{0.643356\,\lambda^2}{\lambda^2 - (0.057789)^2} + \frac{0.506762\,\lambda^2}{\lambda^2 - (0.10968)^2} + \frac{3.8261\,\lambda^2}{\lambda^2 - (46.3864)^2}$$

This relation was used to interpolate and extrapolate for values of $n(\lambda)$ over the range 1–13 μm (Figure 5.15). As seen in the transmittance plot, the latter falls off sharply beyond $\approx$11 μm (although the window can be used up to $\sim$14 μm). Hence, $n(\lambda)$ probably changes more rapidly between 11–13 μm than predicted by the above relation. However, sensitivity calculations show that the effect of small changes in $n(\lambda)$ for BaF_2 has negligible effect on the calculated transmittance of the liquid.

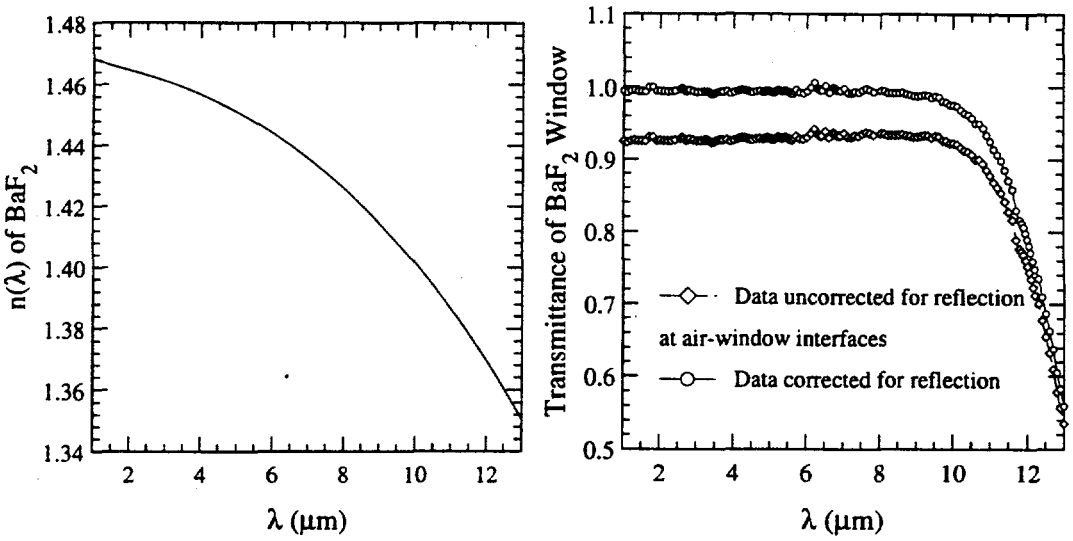

Figure 5.15: The graphs show the real part of the refractive index of barium fluoride BaF_2 in the near-infrared (Malitson, 1964), and the transmittance of a 3 mm thick BaF_2 window.

The transmittance of the window, τ_w, was measured over the wavelength range 1–13 μm. The data, after correction for reflection at the air-window interface, is shown in Figure 5.15. The transmittance is greater than 97% up to 10 μm, and over 50% even at 13 μm.

The corrected spectral transmittance data for a slab 9 mm thick of each of the three liquids are shown in Figure 5.16. The liquids used are CCl_4 in the range 1–6 μm, $CHBr_3$ in the ranges 6.4–7.4 μm and 11–13 μm, and CS_2 in the range 7.4–11 μm. Clearly, taken together, they provide a window for measurements in the infrared in the wavelength range 1–13 μm with a few small gaps (6–6.4 μm and 11.2–11.7 μm). It should be noted that almost all of the absorption bands shown are weak. However, the transmittance is low in the region of the absorption bands because of the relatively large path length (for a liquid). Nevertheless, one can make extinction measurements on ash suspensions at specific wavelengths where the liquids are sufficiently transmitting and obtain spectral data over the wavelength range 1–13 μm because the ash does not contribute any narrow band features. Even when the transmittance of the liquid is low (e.g., at λ>12 μm), the use of chopper and lock-in amplifier with integration times of 3 or 4 seconds yielded good signal/noise ratio.

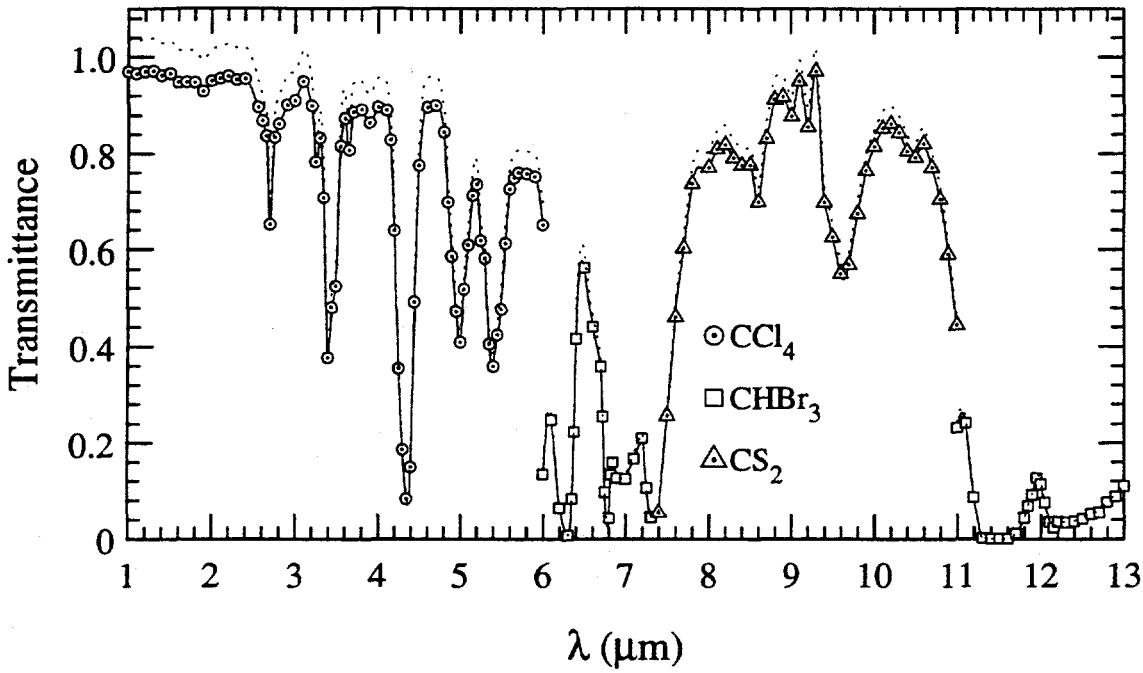

Figure 5.16: Transmittance of 9 mm slabs of CCl_4, CS_2, and $CHBr_3$ over the wavelength range 1–13 μm. The dotted line shows the transmittance before reflections at the air-window and liquid-window interfaces are taken into account.

5.7 Preliminary Calculations of Extinction

This section begins with a discussion of some details of the Mie calculations which are applicable to all the calculations in this and the following chapter. Next, calculated extinctions by liquid and air suspensions of fly ash are compared. Finally, results of sensitivity studies are presented and analyzed.

5.7.1 Mie Calculations

Computer codes developed by Ebert (1993) were used for all Mie calculations[††]. The scattering and absorption coefficients are integrated over the diameter range 0.2 μm–50.0 μm. This range was chosen symmetrically about the median of the lognormal area distribution. The width of the diameter range is limited by the increasing computer time for calculations

[††]The reader should consult this reference for detailed description of the analytical and numerical techniques involved in the Mie calculations. The computed efficiencies were found to compare quite well with those obtained using the program of Wiscombe (1987).

for large size parameter ($x = \pi D/\lambda$). All the ash particles are assumed have the composition of synthetic slag SA10[‡‡] (Goodwin, 1986). The optical constants are calculated using the room temperature correlations formulated by Goodwin. The parameters of the lognormal function describing the size distribution for the base calculations are $D_v = 10\ \mu m$ and σ_g=2.5. A volumetric loading, V_a, of 1.7×10^{-4} was used, and calculations were performed at wavelength increments of 0.1 μm. The path length, L, (the cell thickness) is 9 mm.

As explained in Chapter 2, the computed efficiencies are size-weighted mean efficiencies. For a (truncated) lognormal size distribution as defined in Chapter 3, the expression for each efficiency is

$$\bar{Q}_\lambda = \int_a^b Q_\lambda\, f_2(D)\, \mathrm{d}D$$

The normalized area distribution, $f_2(D)$, is given by

$$f_2(D) = \frac{dF_2^{(a,b)}(D)}{d(\ln D)} = \frac{\frac{1}{\sqrt{2\pi}\ln\sigma_g}\exp\left[-\frac{1}{2}\left(\frac{\ln D/D_a}{\ln\sigma_g}\right)^2\right]}{\int_{\ln a}^{\ln b}\frac{1}{\sqrt{2\pi}\ln\sigma_g}\exp\left[-\frac{1}{2}\left(\frac{\ln x/D_a}{\ln\sigma_g}\right)^2\right]d(\ln x)} \qquad a \le D \le b$$

The scattering coefficient was obtained from

$$\sigma_\lambda = \frac{3}{2}\frac{V_a\,\bar{Q}_{s,\lambda}}{D_{32}}$$

Here, D_{32} is the Sauter mean diameter. Similar expressions are applicable to absorption and extinction coefficients using the appropriate efficiencies.

Much of the computational effort in Mie calculations is spent in determining the phase function, Φ_λ. To reduce the computational time, calculations for Φ_λ are performed at twenty-six equally spaced angles spanning a polar angle of only 5°. However, this is quite sufficient since the collection cone half-angle of the optical system is very small, $< (1.0 \times 10^{-3})°$. In all cases given in this section (unless otherwise stated), the transmittance refers to an effective transmittance which is the ratio of the sum of the actual transmitted radiation *and* the scattered radiation (included within the collection angle) to the incident radiation. As shown later, the scattered radiation collected by the detector is negligible.

5.7.2 Ash Suspended in Liquid Media *vs* Ash in Air

In Figure 5.17, the values of $n_r(\lambda)$ and $k_r(\lambda)$ for ash in CCl_4 are compared to the values in vacuum (i.e., n, k). Since the refractive indices of the slag and CCl_4 are quite close,

[‡‡]This slag has a nominal composition of SiO_2=50.64%, Al_2O_3=25.04%, Fe_2O_3=9.51%, and CaO=14.82%.

$n_r(\lambda)$ is close to unity. Also presented are the spectral absorption and scattering efficiencies obtained from Mie calculations. Because the number of terms needed for the convergence of the efficiencies is directly related to $|n_r(\lambda) - 1|$, the calculations for ash suspended in a liquid medium take significantly less than for air suspensions. In Figure 5.17, it is seen that scattering is much smaller for liquid suspensions, $Q_{s,\lambda}$ becoming several orders of magnitude smaller as $n_r(\lambda)$ $(=n_{ash}/n_{CCl_4})\rightarrow 1$ at $\lambda\sim 5.6$ μm. The absorption efficiency, $Q_{a,\lambda}$, is also reduced substantially for ash in CCl_4 compared to ash in air, although both follow the same general trend.

The contribution of scattering to extinction decreases with increasing wavelength for two reasons. First, with increasing λ the effective size parameter decreases. Provided D is not very much greater than λ (so that $Q_{s,\lambda}$ is not near the diffraction limit of 2), the increase in λ causes $Q_{s,\lambda}$ to decrease. Second, the relative refractive index, $n_r(\lambda)$, decreases at a large relative rate with increasing λ, going to unity at ≈ 5.6 μm, at which point scattering is zero*, and then increasing again in the region where $n_{ash} < n_{CCl_4}$. For this reason, $Q_{s,\lambda}$ for ash in CCl_4 changes by more than three orders of magnitude over the wavelength range 1–6 μm, while $Q_{s,\lambda}$ for the ash dispersed in air decreases by only 50% over the same range. In practice, allowing for heterogeneity of ash composition from particle to particle (neglected in these calculations), the sharp minimum where $n_r(\lambda)\rightarrow 1$ will be less pronounced because various particles satisfy the condition $n_r(\lambda)=1$ at different wavelengths.

Figure 5.18 compares the scattering and absorption coefficients, and the resultant transmittances for a 9 mm thick slab of fly ash dispersed in CCl_4, over the wavelength range of interest, 1–6 μm. Despite the decreased scattering by ash in CCl_4 compared to ash in air, the extinction at all wavelengths, except in the range 5–6 μm, is still mostly due to scattering. It is clear that the transmittance of ash in CCl_4 is significantly greater than in air. Because in CCl_4 the scattering decreases steadily with wavelength (unlike in air where it peaks at ≈ 2 μm), the transmittance in the former case increases from 60% to close to 100%. In actual ashes, where $n_r(\lambda)$ of individual ash particles becomes unity at different wavelengths, the transmittance will not be so sharply peaked, but will be broader.

Figures 5.19 and 5.20 show calculations for ash in CS_2 for λ=8–11 μm. For ash dispersed in air, both Christiansen wavelengths can be seen in this range. However, for ash suspended in CS_2, $n_r(\lambda)=1$ occurs at a longer wavelength (≈ 9.8 μm), and it increases monotonically

*Since calculations are not performed at the Christiansen wavelength where $n_r(\lambda)=1$, the point where $Q_{s,\lambda}$ drops to zero is not shown on the plot. At this wavelength, the particle and the medium are optically indistinguishable, the former becoming fully transparent provided absorption is small.

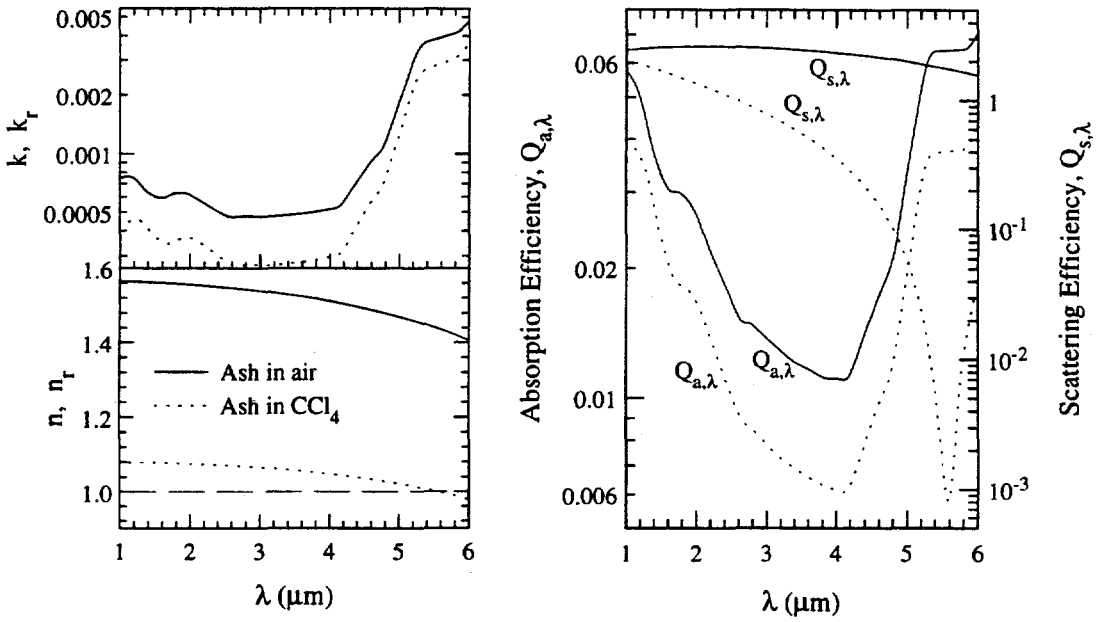

Figure 5.17: Optical properties of SA10 slag, and absorption and scattering efficiencies of SA10 fly ash, comparing the case of ash suspended in CCl_4 with that in air. Volume loading, $V_a = 1.7 \times 10^{-4}$. Note y-axis limits.

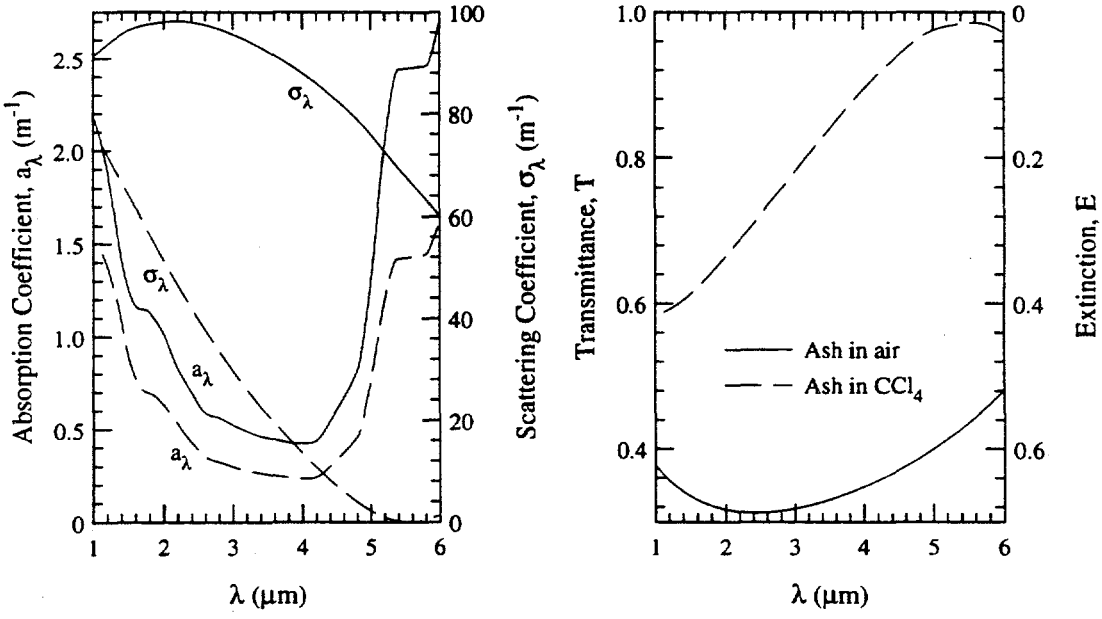

Figure 5.18: Radiative properties of SA10 fly ash in CCl_4 and air. D_v=10.0 μm, σ_g=2.5. $V_a = 1.7 \times 10^{-4}$. Path length = 9 mm.

over the wavelength range. The value of $|n_r(\lambda) - 1|$ does not vary much over the full wavelength range, resulting in a much smaller variations of $Q_{s,\lambda}$ and σ_λ compared to ash dispersed in air.

Due of the presence of the two strong silica absorption bands, $Q_{a,\lambda}$ and $Q_{s,\lambda}$ (and hence α_λ and σ_λ) have comparable values. Hence, in this wavelength range, scattering and absorption make comparable contributions to extinction. Since $k \sim n$, the minimum in $Q_{s,\lambda}$ is much less pronounced (compared to ash in CCl_4), even with no compositional heterogeneity of the ash. Another notable point is that $|n_r(\lambda) - 1|$ is larger for ash in CS_2 compared to ash in air in the range λ=8–8.5 μm. Consequently, the scattering (and hence, extinction) is higher in this range for ash dispersed in liquid.

5.7.3 Sensitivity Analyses

For meaningful comparison of the measured extinction with that predicted from calculations, it is necessary to test the sensitivity of the measured quantity, the transmittance, T, of the ash suspension, to uncertainties in the values of the relevant parameters, such as the size distribution and the optical properties of the ash. For instance, to find the sensitivity of T to σ_g, we need to calculate $\Delta T/T$ where

$$\Delta T \approx \frac{\partial f(n, k, D_v, \sigma_g, \lambda, \theta, V_a, L, \omega)}{\partial \sigma_g} \Delta \sigma_g$$

Here the function $f(n, k, D_v, \sigma_g, \lambda, \theta, V_a, L, \omega)$ expresses the dependence of T on optical properties, size distribution parameters, wavelength, temperature, ash loading, path length and the solid angle of the beam, in that order. Of all the parameters, the wavelength can be determined with the greatest accuracy, and $\Delta\lambda$ (the resolution) is much smaller than the wavelength increments over which there are measurable changes in T. Optical properties change very slowly with temperature. Hence, T is practically insensitive to θ in the experiment.

For evaluating the sensitivity to size distribution and optical properties, several Mie calculations were performed with small step increments in any one of the above listed parameters while keeping the remaining ones unchanged. Initially, results are presented separately for each parameter, and then summarized by comparing their relative effects. For convenience, all the figures are grouped at the end of the section. The cases of ash dispersed in CCl_4 and CS_2 are considered, since with these two liquids one can span $\approx$80% of the wavelength range of interest.

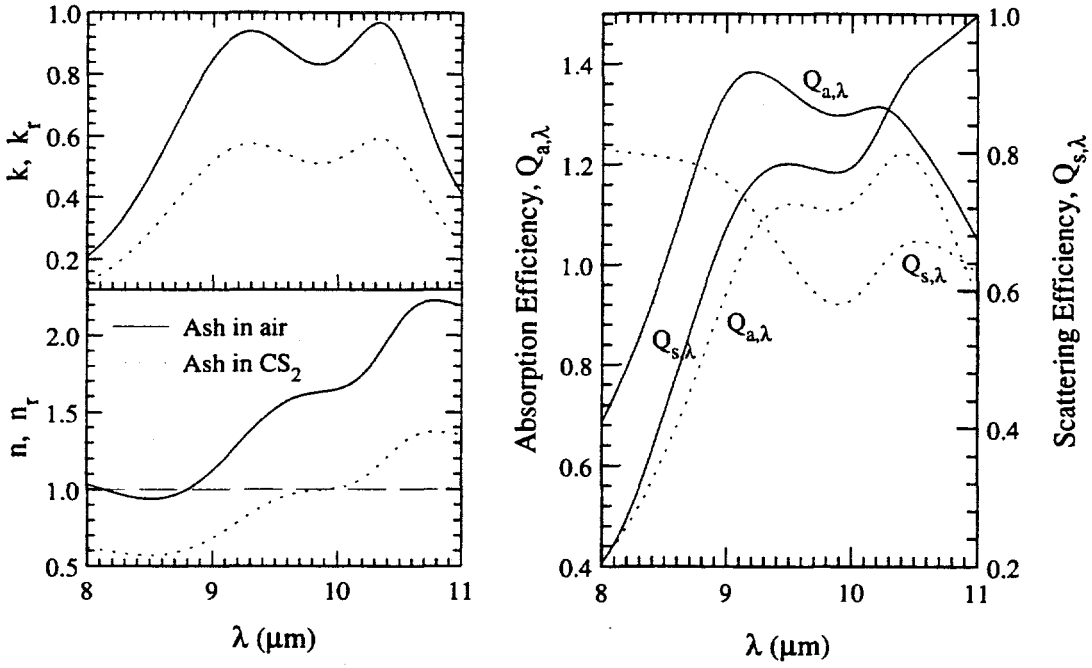

Figure 5.19: Optical properties of SA10 slag, and absorption and scattering efficiencies of SA10 fly ash, comparing the case of ash suspended in CS_2 with that in air. Volume loading, $V_a = 1.7 \times 10^{-4}$.

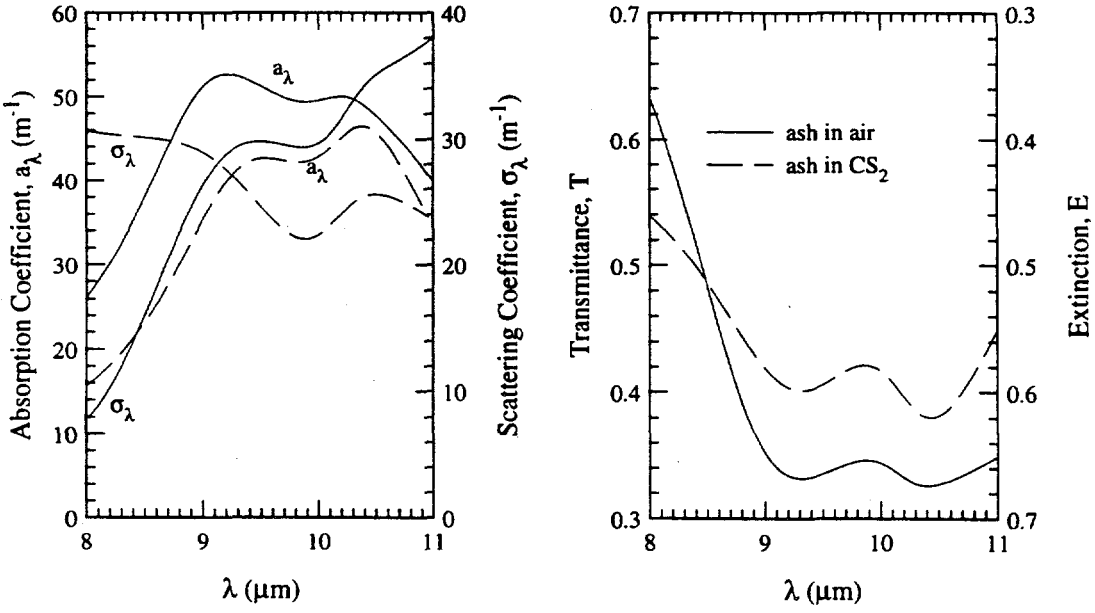

Figure 5.20: Radiative properties of SA10 fly ash in CS_2 and air. D_v=10.0 μm, σ_g=2.5. $V_a = 1.7 \times 10^{-4}$. Path length = 9 μm. Note y-axis limits.

Figures 5.21 and 5.22 show for ash in CCl_4 how the transmittance changes for ±20% variation in D_v and ±6% in σ_g, respectively. T is seen to be insensitive to small changes in σ_g, and it is somewhat sensitive to the median size only in the wavelength range 1–2 μm (for which $x \gg 1$). Larger values of D_v means an increase in the size parameters overall for the ash. However, for constant ash loading, the effect of the increased values of $Q_{a,\lambda}$ and $Q_{s,\lambda}$ on T are offset by the inverse dependence of the extinction coefficient on D_{32} (Equation 2.12), which also increases with increasing D_v. Consequently, T actually increases with increasing D_v in the range 1–3 μm.

Figure 5.23 shows that T is very sensitive to $n_r(\lambda)$ which is a result of the proximity of $n_r(\lambda)$ to unity. The scattering coefficient is strongly affected by a few percent change in $n_r(\lambda)$. The reason is that (as stated earlier) the extent of scattering is dependent on $|n_r(\lambda) - 1|$. Depending on how close $n_r(\lambda)$ is to unity, a few percent change in its value causes large changes in $|n_r(\lambda) - 1|$. The location of the minimum $Q_{s,\lambda}$ is shifted to shorter wavelengths with decreasing $n_r(\lambda)$ since the ratio $n_r(\lambda)(=\frac{n_{ash}}{n_{CCl_4}})$ reaches unity at smaller λ. Thus the experiment should be a very sensitive test for $n_r(\lambda)$ in this wavelength range. In contrast, from Figure 5.24, it is seen that T is rather insensitive to $k_r(\lambda)$. This is to be expected because in this wavelength range the contribution to $Q_{e,\lambda}$ by $Q_{a,\lambda}$ is small, $Q_{s,\lambda}$ being more than an order greater than $Q_{a,\lambda}$.

The sensitivity study for ash dispersed in CS_2 is discussed next. Figures 5.25 and 5.26 show the effect of changes in the size parameters on transmittance in the range λ=8–11 μm. As described earlier, D_v affects T through the size parameter, and the Sauter mean diameter. T shows some sensitivity for both parameters, particularly close to the absorption peaks where absorption dominates scattering, with approximately equal changes in T for equal fractional increments (or decrements) in their respective values. The real and imaginary parts of the refractive index are, of course, related, and small changes in one affect the other especially in the region of absorption bands where their values are comparable. This is clear from Figures 5.27 and 5.28 where it is seen that σ_λ is sensitive to $n_r(\lambda)$ except close to the absorption bands. Overall, it appears that T (and E) is moderately sensitive to the accuracy of the optical constants in the wavelength range 8–11 μm.

The sensitivities of T to the remaining three parameters: collection angle, path length, and ash loading are shown in Figures 5.29, 5.30, and 5.31, respectively. The transmittance is sensitive to the half-angle of the collection cone only at short wavelengths ($\approx$1–3 μm). This is because most of the ash particles appear large to radiation of shorter wavelengths

(i.e., $x \gg 1$), resulting in a larger component of forward scattered light reaching the detector. Additionally, the contribution of scattering to extinction decreases in the long wavelength range due to increased absorption. In any case, the collection angle in this optical arrangement is negligibly small (see Section 5.7.1), and so is the amount of forward scattered light collected by the detector. Because both V_a and L appear as factors in the optical thickness term in the exponential in the expression for T (Equations 2.11 and 2.12), they can significantly affect the measured value of T.

The results of sensitivity analyses are summarized in Figures 5.32, 5.33, and 5.34 at three specific wavelengths†, λ=1.6 μm, 5.8 μm, and 9.8 μm. It is apparent that T is far more sensitive to $n_r(\lambda)$ in the range 1–6 μm compared to the other parameters over the entire wavelength range. T is moderately sensitive to the optical constants and the size parameters at longer wavelengths. It is moderately sensitive to the path length, L, and the volumetric ash loading, V_a, over the entire wavelength range of interest. These calculations are invoked in interpreting the results of transmittance measurements in the next chapter.

5.8 Summary

An experiment to measure the room-temperature infrared transmittance of fly ash suspended in a transparent liquid has been designed. The spectral refractive indices of CS_2 and $CHBr_3$ needed for Mie calculations were determined for λ=1–13 μm using the near-normal reflectance technique.

From Mie calculations, it is established that performing the experiment in a liquid medium reduces scattering due to a decrease in the real part of the complex refractive index of the ash relative to that of the medium. Despite this reduction, scattering still plays the predominant role in the extinction of radiation in wavelength range 1–6 μm. This dominance of scattering makes direct emission measurements from a hot, gaseous ash dispersion difficult in this wavelength range because scattered light is collected in the detection optics unless the medium is optically very thin. However, in the range 8–11 μm, where the absorption efficiency (due to silica) is comparable to the scattering efficiency, the transmittance is sensitive to both $n_r(\lambda)$ and $k_r(\lambda)$.

†The wavelengths are arbitrarily chosen to span the range λ=1–13 μm.

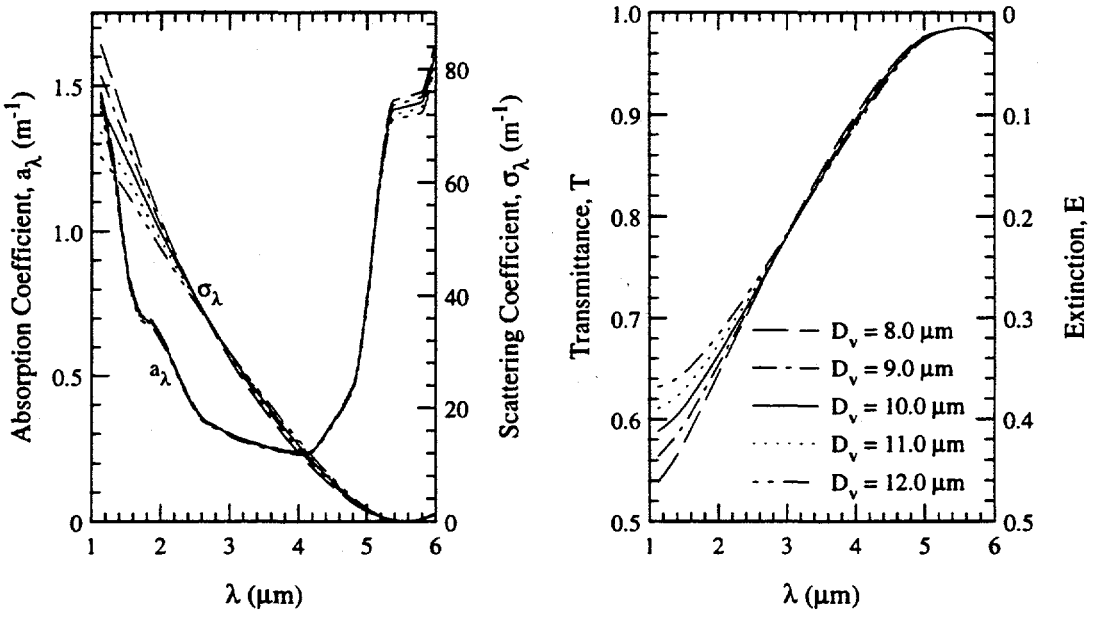

Figure 5.21: Sensitivity of the absorption and scattering coefficients (α_λ, and σ_λ, respectively), transmittance T, and extinction, E, to the ash median diameter, D_v. SA10 ash dispersed in CCl_4. σ_g=2.5, V_a=2.0×10^{-4}. Path length=9 μm. Note y-axis limits.

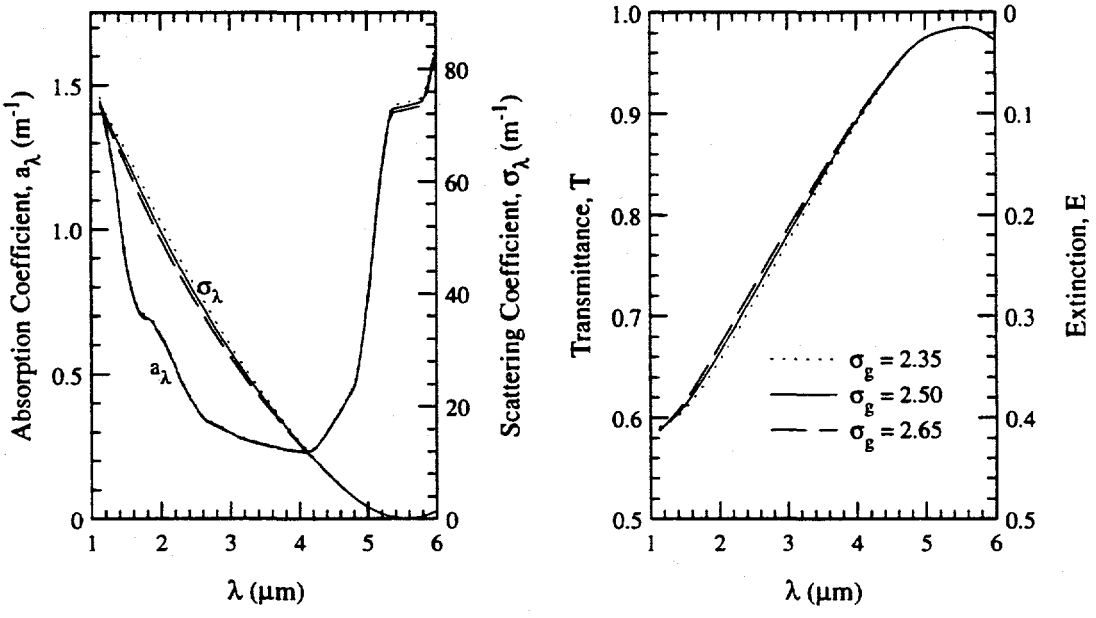

Figure 5.22: Sensitivity of the absorption and scattering coefficients (α_λ, and σ_λ, respectively), transmittance T, and extinction, E, to the geometric standard deviation of the ash size distribution, σ_g. SA10 ash dispersed in CCl_4. D_v=10.0 μm. V_a = 2.0×10^{-4}. Path length = 9 μm. Note y-axis limits.

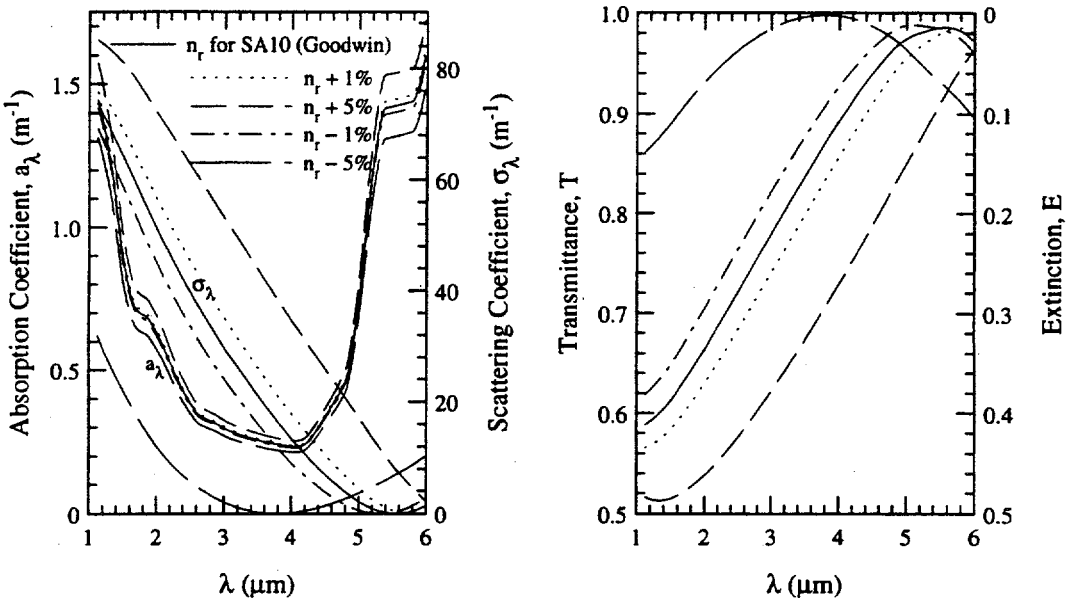

Figure 5.23: Sensitivity of the absorption and scattering coefficients (α_λ, and σ_λ, respectively), transmittance T, and extinction, E, to the real part of the refractive index of the ash relative to that of CCl_4, $n_r(\lambda)$. D_v=10.0 μm, σ_g=2.5, V_a=2.0×10^{-4}. Path length=9 μm. Note y-axis limits.

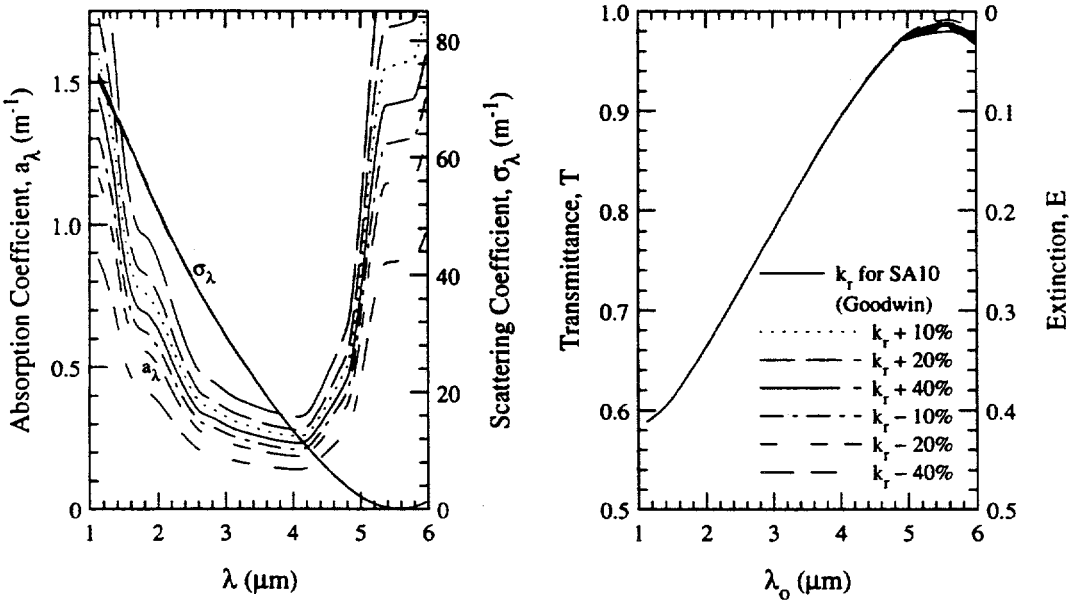

Figure 5.24: Sensitivity of the absorption and scattering coefficients (α_λ, and σ_λ, respectively), transmittance T, and extinction, E, to the imaginary part of the refractive index of SA10 ash relative to that of CCl_4, $k_r(\lambda)$. D_v=10.0 μm, σ_g=2.5, V_a=2.0×10^{-4}. Path length=9 μm. Note y-axis limits.

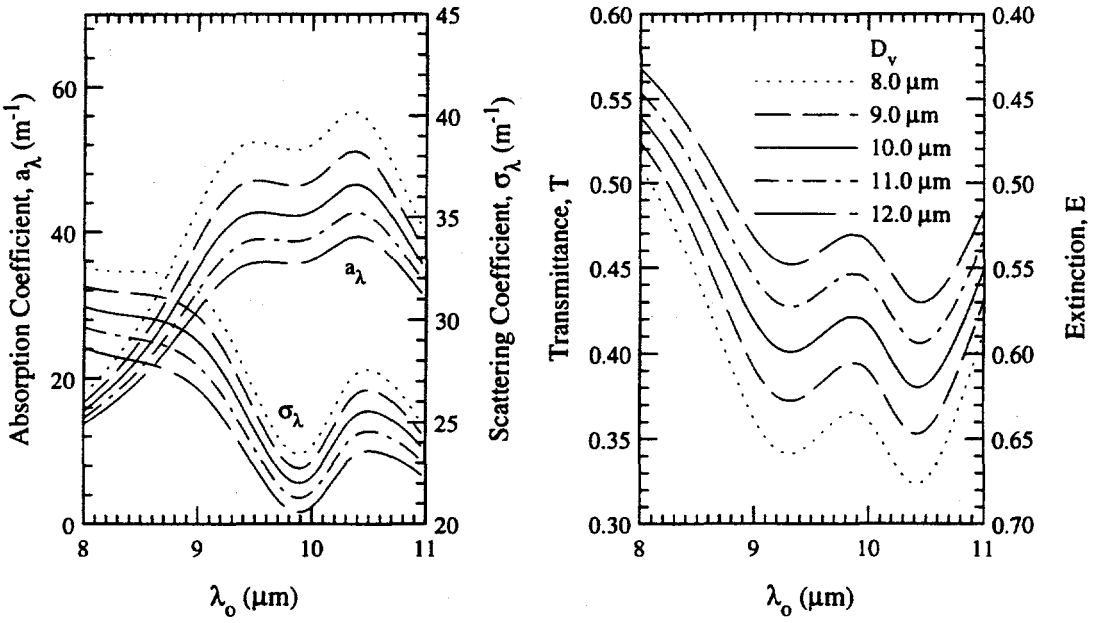

Figure 5.25: Sensitivity of the absorption and scattering coefficients (α_λ, and σ_λ, respectively), transmittance T, and extinction, E, to the ash median diameter, D_v. SA10 ash dispersed in CS_2. σ_g=2.5, V_a=2.0×10^{-4}. Path length=9 μm. Note y-axis limits.

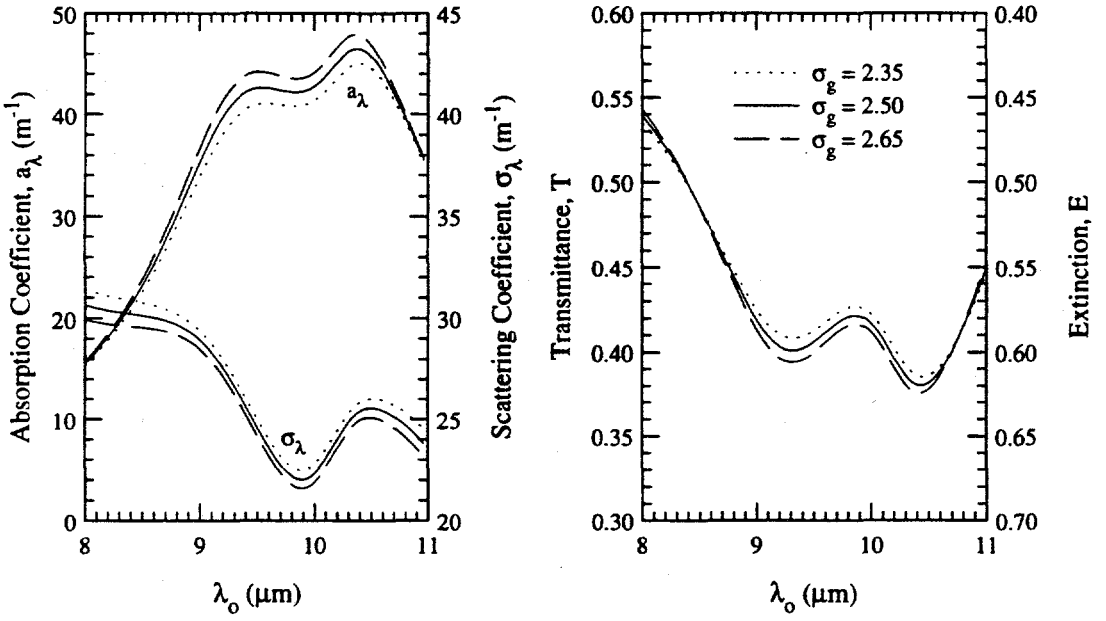

Figure 5.26: Sensitivity of the absorption and scattering coefficients (α_λ, and σ_λ, respectively), transmittance T, and extinction, E, to the geometric standard deviation of the ash size distribution, σ_g. SA10 ash dispersed in CCl_4. D_v=10.0 μm. V_a = 2.0×10^{-4}. Path length = 9 μm. Note y-axis limits.

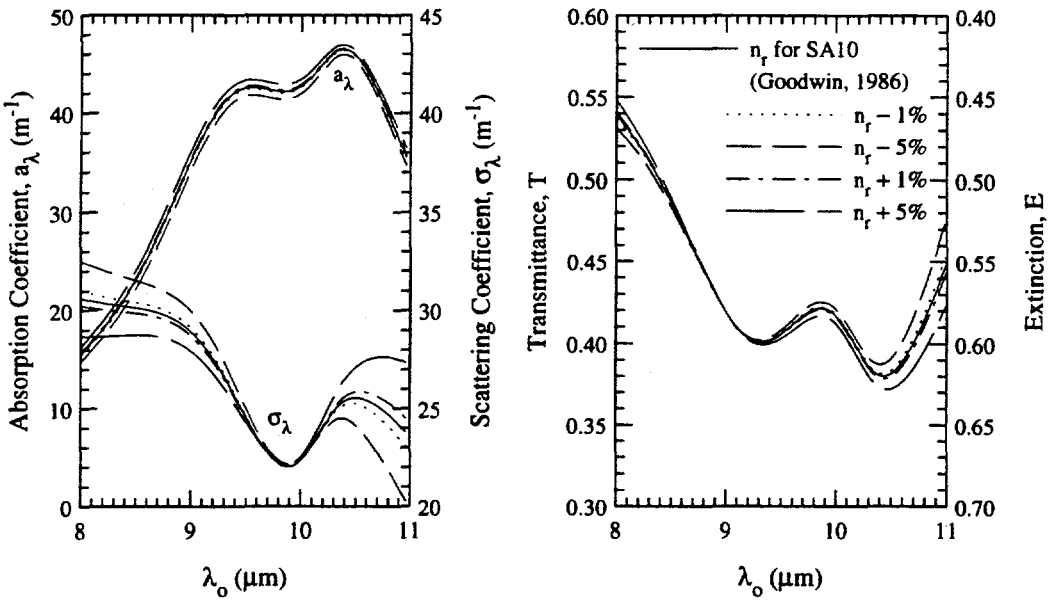

Figure 5.27: Sensitivity of the absorption and scattering coefficients (α_λ, and σ_λ, respectively), transmittance T, and extinction, E, to the real part of the refractive index of the ash relative to that of CS_2, $n_r(\lambda)$. D_v=10.0 μm, σ_g=2.5, V_a=2.0×10^{-4}. Path length=9 μm. Note y-axis limits.

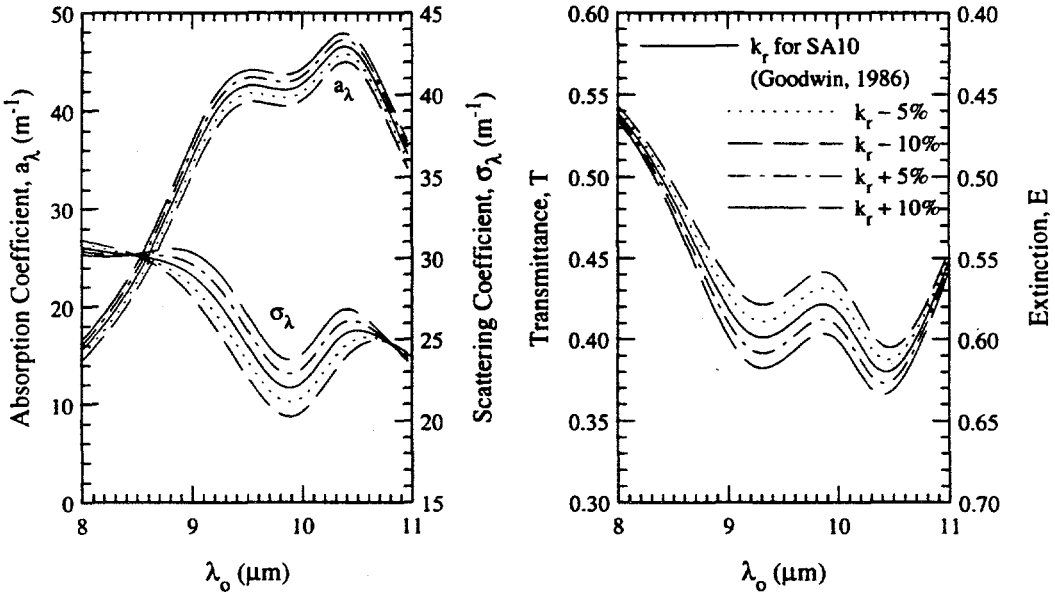

Figure 5.28: Sensitivity of the absorption and scattering coefficients (α_λ, and σ_λ, respectively), transmittance T, and extinction, E, to the imaginary part of the refractive index of the ash relative to that of CS_2, $k_r(\lambda)$. D_v=10.0 μm, σ_g=2.5, V_a=2.0×10^{-4}. Path length=9 μm. Note y-axis limits.

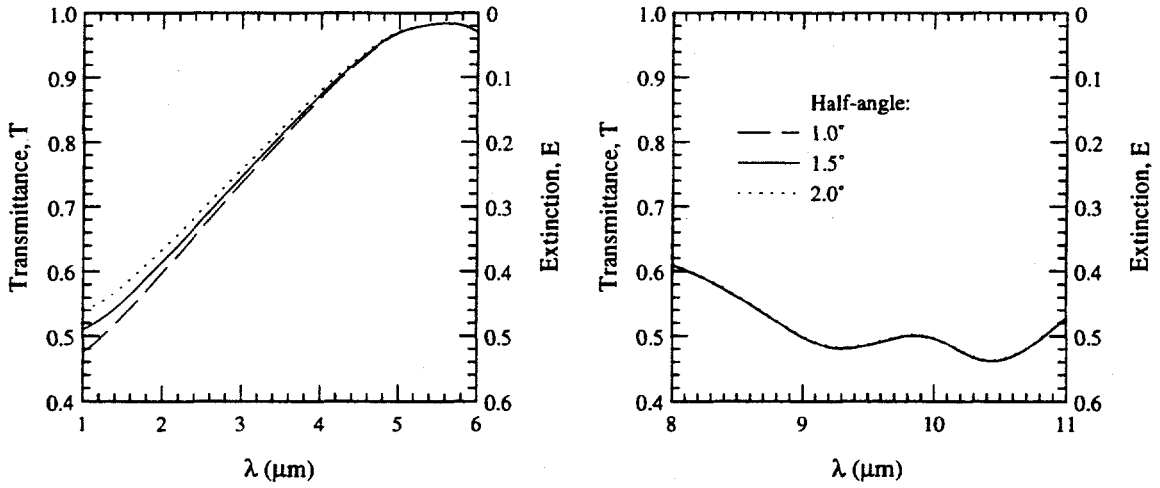

Figure 5.29: Sensitivity of transmittance, T, and extinction, E, to the detector collection angle. SA10 ash in CCl_4 and CS_2. D_v=10.0 μm, σ_g=2.5, V_a=2.0×10^{-4}. Path length=9 μm. Note y-axis limits.

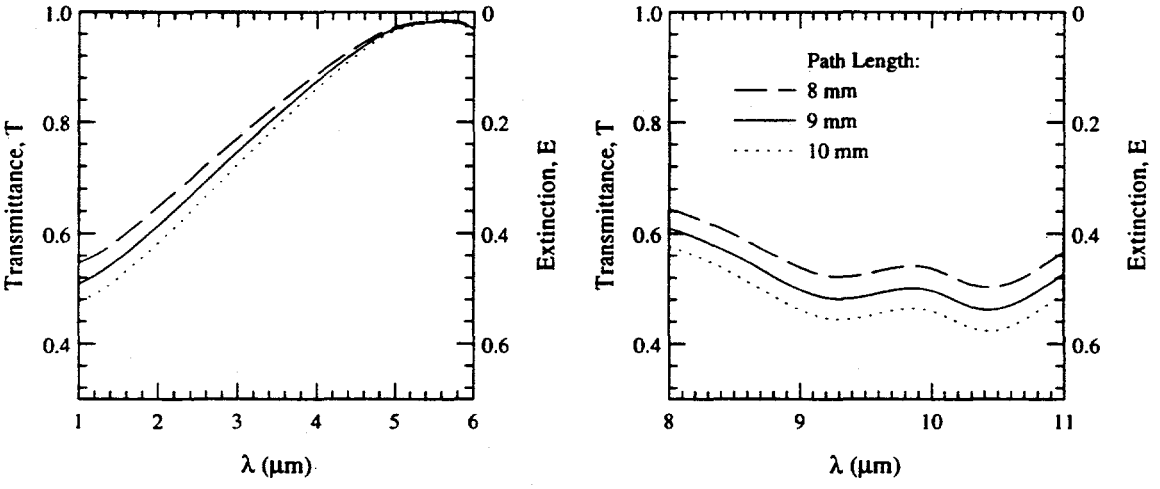

Figure 5.30: Sensitivity of transmittance, T, and extinction, E, to path length, L. SA10 ash in CCl_4 and CS_2. D_v=10.0 μm, σ_g=2.5, V_a=2.0×10^{-4}. Note y-axis limits.

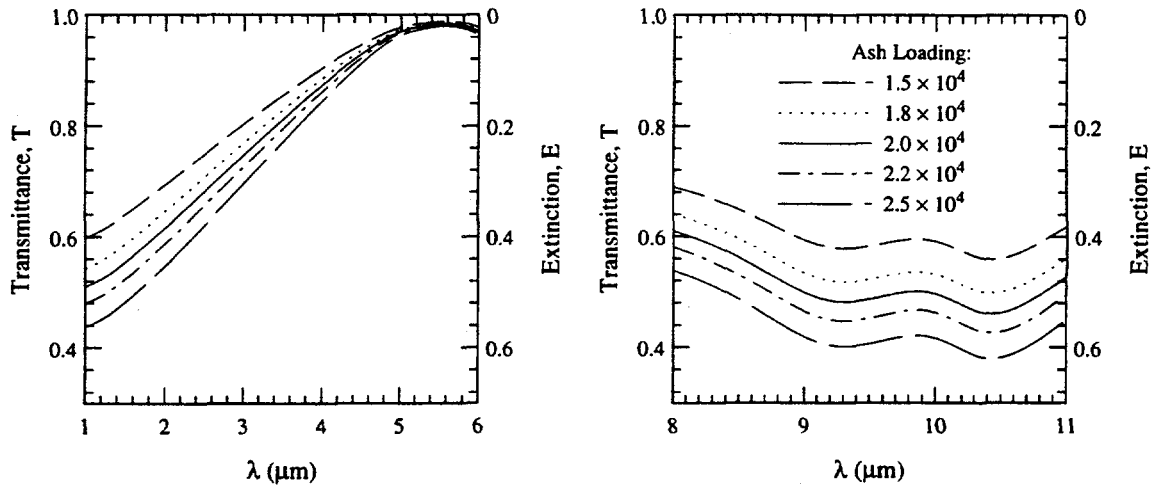

Figure 5.31: Sensitivity of transmittance, T, and extinction, E, to volumetric ash loading, V_a. SA10 ash in CCl_4 and CS_2. D_v=10.0 μm, σ_g=2.5. Path length=9 μm. Note y-axis limits.

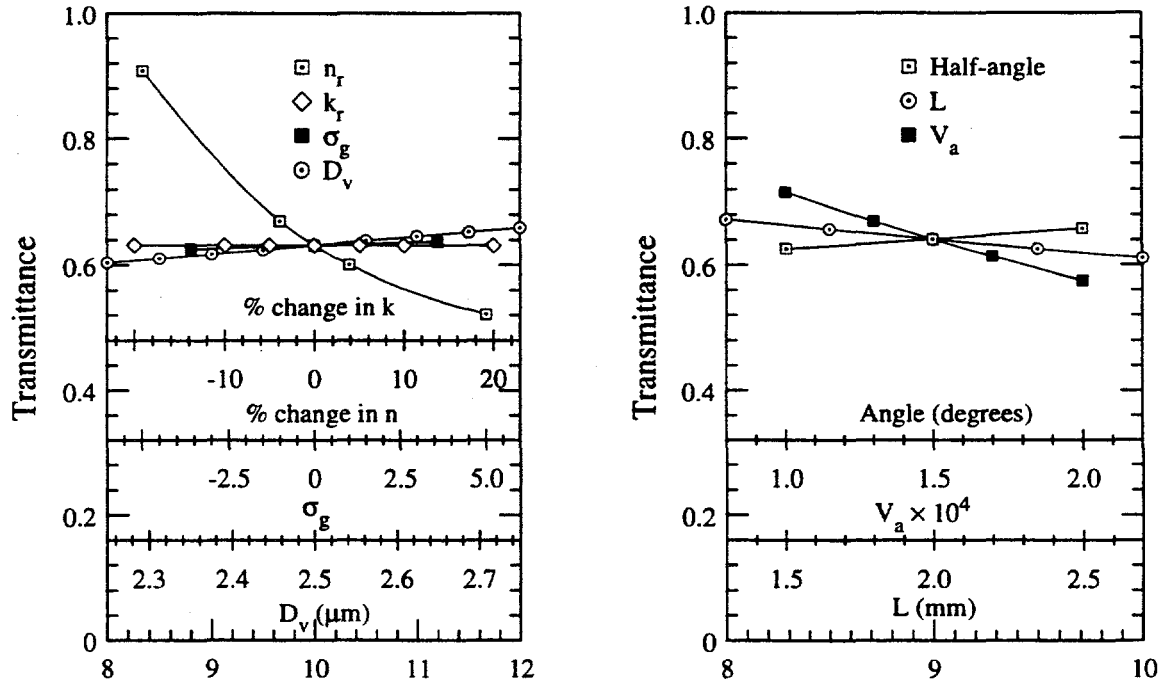

Figure 5.32: Sensitivity of measured transmittance to the various parameters at λ=1.6 μm. SA10 ash in CCl_4. Note y-axis limits.

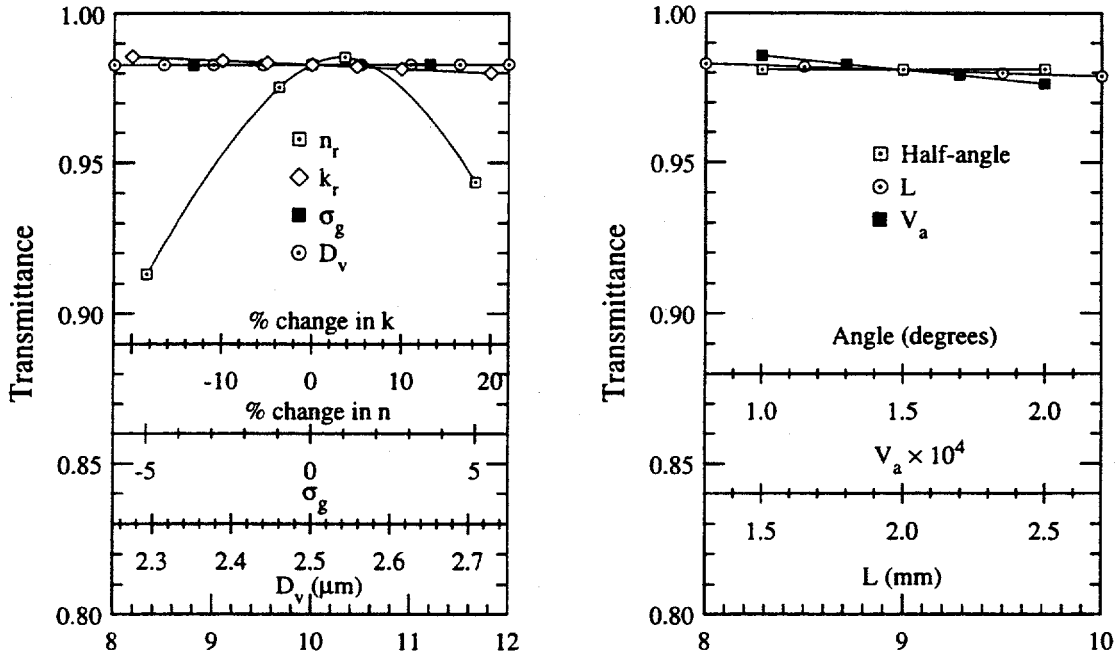

Figure 5.33: Sensitivity of measured transmittance to the various parameters at λ=5.8 μm. SA10 ash in CCl_4. Note y-axis limits.

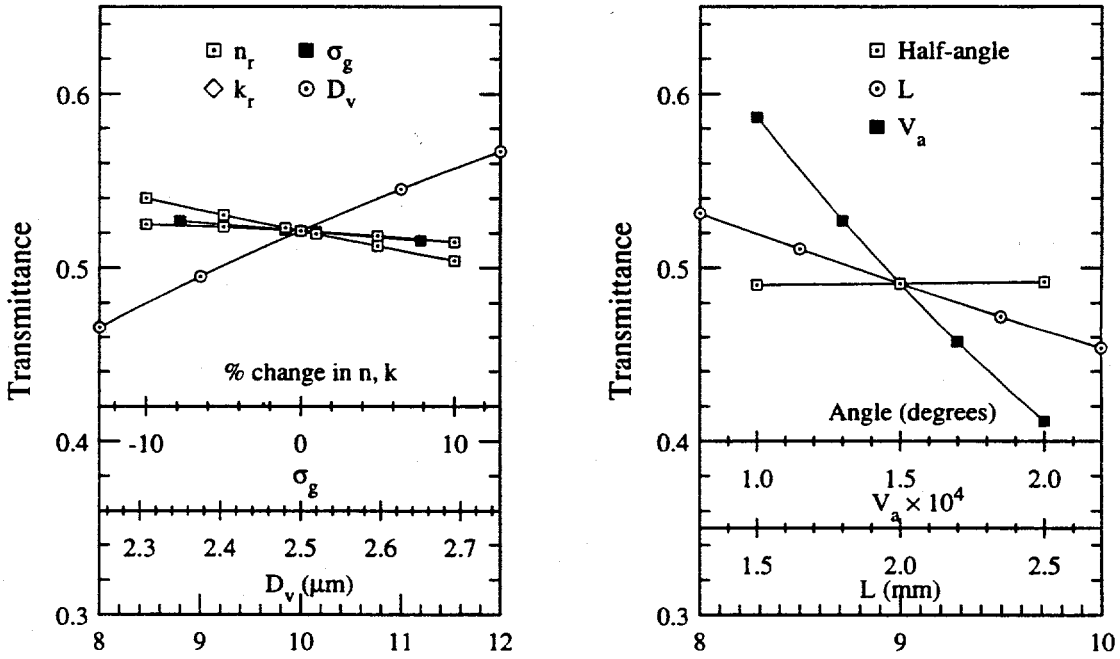

Figure 5.34: Sensitivity of measured transmittance to the various parameters at λ=9.6 μm. SA10 ash in CS_2. Note y-axis limits.

Chapter 6

Extinction Measurements on Ash Dispersions

6.1 Introduction

Results of extinction measurements on ash suspensions are presented in this chapter. Measurements were made on the ashes from four of the coals: one bituminous (Upper Freeport), the sub-bituminous one (Eagle Butte), and the two lignites (Beulah and San Miguel). Some practical details and artifacts related to the experiment are discussed initially, followed by results for each ash given in separate sections. The data are compared with predictions from Mie calculations. Differences are explained primarily in terms of the cenospheric content and the heterogeneity of ash composition.

As defined in the previous Chapter, the transmittance of the dispersed ash is the ratio of the signal intensity (power) transmitted through the ash suspension to that through the pure liquid. The three chemicals, whose optical properties were described in Chapter 5, were used over separate wavebands to span the range 1–13 μm: CCl_4 (1–6.2 μm), $CHBr_3$ (6.7–7.4 μm, 11.8–13.5 μm), and CS_2 (7.4–11.2 μm). The optical configuration for the experiment and details of the apparatus were also discussed in Chapter 5. Volumetric loadings (V_a) of 2–5×10^{-4} were used to achieve extinctions as high as 60%. A liquid medium allows the use of such high loadings, about two orders of magnitude larger than typical combustor loadings (Ebert, 1993). As a result, easily measurable values of extinction were obtained for short path lengths, and small changes in extinction could be observed more readily.

6.1.1 Preparation of Ash Suspension

Ash sample masses in the range 25–100 mg, and liquid samples of mass 100–300 g, were used in preparing suspensions*. Weighing errors due to uncontrolled moisture content of the ash and the weighing paper were minimized by initial drying at ≈75°C for half an hour, and by the use of dessicant in the balance chamber. The average ash densities given in Chapter 2, and accurate values of densities for the three liquids from the CRC Handbook (CRC, 1985), were used in calculating the liquid mass needed for a desired volumetric loading, V_a. For a monodispersion of D_v=10 μm, a loading of V_a=2×10^{-4} indicates a concentration of ≃ 4·× 10^5 particles/ml. The suspension was ultrasonically agitated for two to three minutes to ensure proper deagglomeration each time a sample (≈5 ml) was withdrawn with a pipette.

Although the suspensions were stored in sealed glass bottles and refrigerated, a slight loss in mass of the two more volatile liquids, CCl_4 and CS_2, was recorded. Hence, the net weight was recorded before and after a sample of the suspension was withdrawn from the container. After a period of storage, additional chemical was added to compensate for the evaporative loss, and the total mass (i.e., of suspension and container) increased to the previously recorded value.

6.1.2 Signal Fluctuation and Drift, Linearity, Reproducibility, etc.

The 'raw' signal (i.e., without the experimental cell in the beam path) output from the lock-in amplifier is shown in Figure 6.1. Its spectral nature represents the Nernst glower emissivity convolved with gaseous absorption along the path length, and the responsivities of the optical system, detector, and the electronics. It is seen that the signal decreases significantly at 4.3 μm due to absorption by atmospheric CO_2, and at 2.9 μm and in the range 5.8–6.1 μm due to atmospheric water vapor. In many cases, no transmittance measurements were made at these wavelengths.

After allowing a period of one hour for the Nernst glower and detection electronics to stabilize, signal drift was observed to be negligible. The random noise associated with the data was estimated by successive measurement of the 'raw' signal at a fixed wavelength,

*An electronic balance (Mettler AE163) with a least count of 1 μg was used for all ash mass measurements. A less accurate balance (least count 0.1 g) which permitted faster measurements was deemed sufficient for determining the total weight of the suspension and glass container.

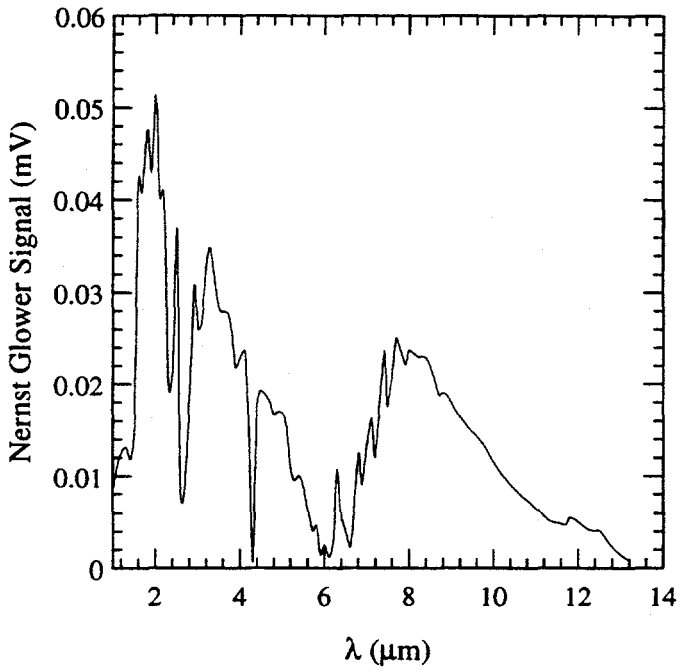

Figure 6.1: Lock-in signal in mV without the cell in the path of the beam. Note carbon-dioxide and water vapor absorption bands at 4.3 μm, and at 2.9 μm and 6.0 μm, respectively.

and was found to average $\approx \pm$ 0.3% (r.m.s.) over the range λ=1–13 μm. When the transmittance of the suspension was measured successively, the noise increased slightly. This increase is caused by the ash particles moving in and out of the detection volume during the measurement period. This noise was minimized while avoiding the inconvenience of using a large time constant by using as large a spot size (and, hence, detection volume) as possible. A spot size of 6 mm diameter (averaging over $\approx 1 \times 10^5$ particles) limited the noise to $\pm$0.4%, r.m.s. of the signal.

System linearity was tested using the sapphire and BaF_2 windows. If $T_1, T_2, ...T_n$ are the individual transmittances through n windows measured separately, then for a linear system the transmittance of n windows together is $T_{comb} = T_1\, T_2....T_n$. Non-linearity can occur for several reasons, primarily related to the detector and the amplifying electronics (in the absence of electrical interference effects). Measurements at J number of wavelengths using two or more windows showed that the r.m.s. linearity, defined below, averaged 1.12% over

the wavelength range 1–13 μm.

$$\text{R.M.S.Linearity} = \sqrt{\frac{\sum_1^J \left[1 - \frac{T_{exp}}{T_{comb}}\right]^2}{J}}$$

Here T_{exp} is the experimentally measured combined transmittance.

An important issue in this experiment was the minimization of any change in the transmitted signal resulting from changes in the ash loading. There are two opposing factors causing a drift in the signal as described below.

When the ash suspension is introduced into the test cell and the stirrer turned on, a small fraction of the ash is lost quickly (in ≈1 minute) resulting in an increase in the transmittance of ≈5–10% (depending on ρ_{ash}). Most of this lost fraction is trapped in the O-ring groove in the chamber wall, and in the gap between the window and O-ring. A smaller fraction, which settles at the lowest point of the circular chamber, is minimized by installing the stirrer slightly eccentrically with respect to the center of the chamber, and operating it at the highest possible speed without generating bubbles (≈3000 r.p.m.). The settling continued at a much reduced rate after the first few minutes.

The effect of the settling is countered by the loss of the liquid medium by evaporation, which increases V_a. The vapor escapes through the clearance between the seal and the stirrer at the top of the cell. The evaporation rate is diminished by the presence of a ≈1 cm high vapor column around the stirrer passage above the liquid surface. The overall effect of these two factors was a gradual increase in transmittance with time, the magnitude of the increase depending directly on ρ_{ash}. However, the change was small (≈2–4%) and repeatable over the period needed for scanning the total wavelength range (about an hour).

For each ash, at least two separate measurements were made, starting with fresh samples from the stored suspension. No significant differences between the data sets were seen with respect to their spectral nature (i.e., the slopes, maxima, and minima of the transmittance graphs). However, the precision in magnitude of the extinction is limited by the uncertainty in the effective value V_a. From repeat measurements, the spectrally-averaged reproducibility of the measured transmittance was determined to be 5–10% over the wavelength range. Such uncertainty is probably as good as one can expect to obtain from such an experiment due to the difficulty of controlling V_a. It would certainly be much worse for ash dispersed in a gas. Finally, T measured at positions on either side of the stirrer were identical, an indication of the uniformity of the suspension over the test chamber volume.

6.1.3 Measurements Close to Absorption Bands of the Liquid Medium

Initial measurements on ash dispersed in CCl_4 showed a number of absorption features in the transmittance spectrum (Figure 6.2(a)). Since there are no ash absorption bands at these wavelengths, they could not easily be explained. Closer examination showed that these unexpected features occurred near the absorption bands of CCl_4. However, as discussed in Chapter 5, Mie theory should be valid for ash dispersed in the three liquids in the vicinity of the absorption bands in the wavelength ranges under consideration, since the bands are relatively weak. It was concluded that the features must result from some experimental artifact.

The problem was traced to a lack of parallelism of the inside surfaces of the cell windows. The resulting difference in path lengths results in unequal absorption by the liquid in the test and reference chambers. This differential absorption is significant because of the considerable path length (9 mm nominal) for a condensed phase. The expression for the ratio, R_T, of the transmittance of CCl_4 in the test chamber to that in the reference chamber, is given by

$$R_T = \exp(\pm\, \alpha_\lambda\, d\, \tan\theta)$$

The separation between the two paths and angle between the windows are denoted by d and θ, respectively. Ideally, $\theta = 0$, and $R_T = 1$.

Figure 6.2(b) shows that R_T departs sharply from unity close to the CCl_4 absorption bands. Figure 6.2(c) shows that small angles ($\theta < 0.5°$) give rise to structures similar to those observed. The absorptivity of CCl_4, α_λ, was calculated from the transmittance data (Chapter 5). The differences between Figures 6.2(b) and 6.2(c) are probably a result of path length differences attributable to additional non-parallelism caused by slight bending of the windows.

In principle, one should be able to normalize the transmittance of the suspension, T, by R_T and eliminate the effect of the unequal absorption. This, however, was not possible in practice because the difference in path length changed between the times R_T and T were measured, as result of one or more of several factors such as O-ring relaxation, thermal expansion/contraction of the windows, etc. These 'environmental' changes reinforce the importance of simultaneous measurements of the test and reference transmittances.

It was concluded that the best approach was to minimize θ. For all the experimental runs, θ was restricted to $\lesssim 0.5°$. This was achieved by adjusting the windows in place

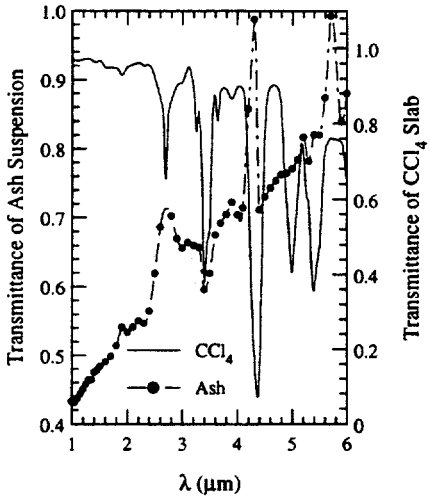

(a) Transmittance of CCl_4 slab, and initial transmittance measurements on Upper Freeport dispersed in CCl_4. Note expanded y-axes.

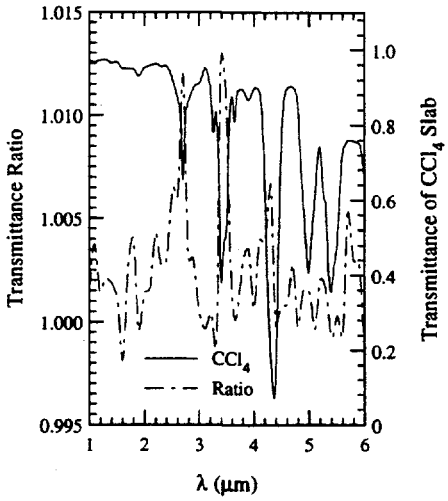

(b) Spectral variation of R_T, the ratio of transmittance through both cell chambers containing CCl_4. Note expanded ordinate scale.

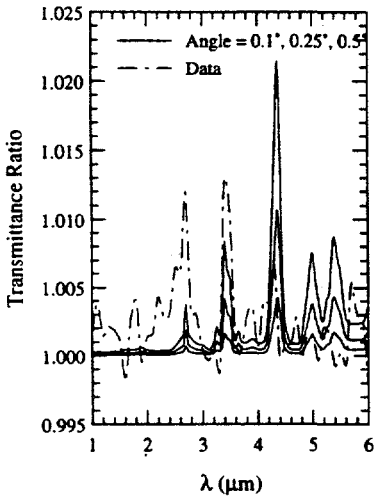

(c) Effect on R_T of unequal path lengths caused by nonparallelism of windows. Figure shows comparison with calculations for various angles. Note expanded ordinate scale.

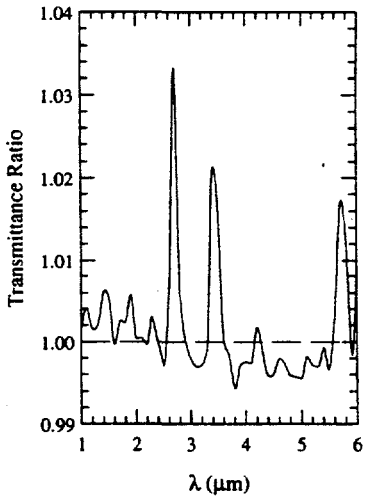

(d) Acceptable spectral values of R_T. Spectral variation of R_T, the ratio of transmittance with both cell chambers containing CCl_4. Note expanded ordinate scale.

Figure 6.2: Preliminary measurements on pure CCl_4 and ash dispersions.

(see Chapter 5) until the reflections of a HeNe laser beam from the inside surfaces of the two windows coincided on a screen stationed some two meters from the cell. Figure 6.2(d) shows a typical spectral plot of R_T that was considered acceptable. The deviation of R_T from unity is <1% (r.m.s.). No data was taken at wavelengths where $R_T > 2\%$.

6.2 Measurements on Upper Freeport Ash

6.2.1 Ash dispersed in CCl_4

Figure 6.3 shows data for T and $E(\equiv 1-T)$ over the entire range 1–6 μm for Upper Freeport ash in CCl_4. Also shown for comparison are calculations for ash of a single composition (that of slag prepared by melting this ash).

The transmittance increases almost linearly with wavelength in the region 1–3 μm. Such reduction in extinction is to be expected due to two effects: a decrease in size parameter, and a decrease in (n_r-1) with wavelength. However, the slope is smaller than that predicted from Mie calculations. The small increase in E at $\lambda\sim 2.7\mu m$ was seen in all the ashes, and is probably a result of absorption by OH (stretch) present in the ash. Unfortunately, measurement of OH content is not possible with common microanalytical methods, and hence its effect on E (albeit minor) cannot be easily quantified. Beyond 3 μm, the spectral transmittance becomes significantly flatter, while the calculations predict $T(\lambda)$ to continue increasing to a maximum of nearly unity at $\lambda\approx 5.6$ μm. As discussed in Chapter 5, the relative refractive index, $n_r(\lambda)$, passes through unity at this wavelength for the assumed homogeneous composition, at which point the scattering falls to zero, and the small extinction is due entirely to absorption.

Clearly there is a significant discrepancy between the measured and calculated extinction in Figure 6.3, which must be attributed to insufficiently realistic modeling of the heterogeneous ash in the Mie calculations. As discussed separately below, the two respects in which the calculations are deficient are the neglect of heterogeneity of ash composition (and hence of refractive index) and neglect of the effect of cenospheres.

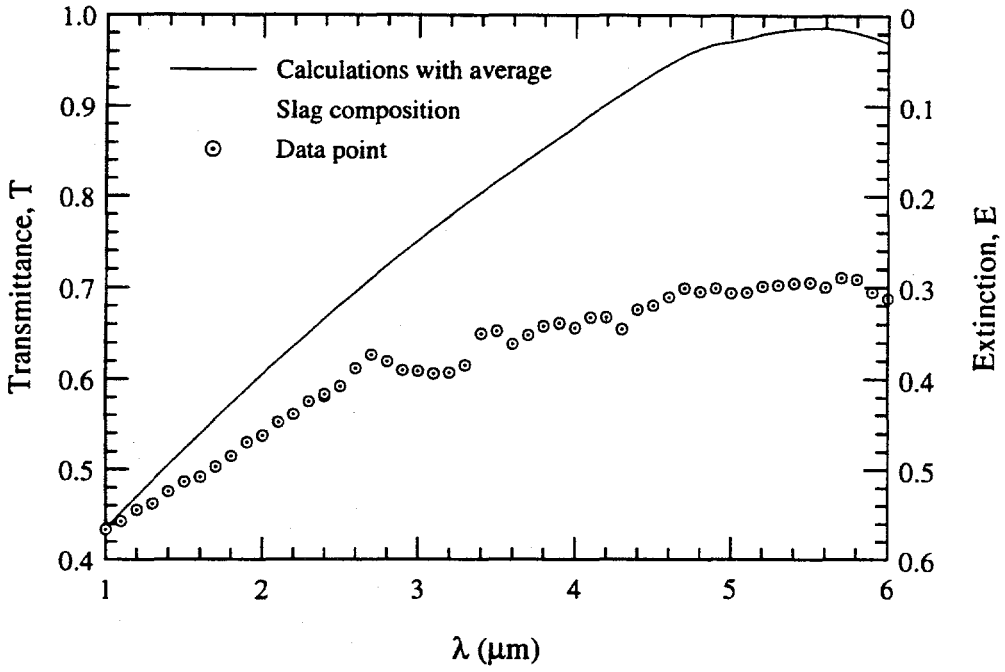

Figure 6.3: Transmittance measurements on Upper Freeport dispersed in CCl_4 (Density=2.29 g/cc). Note expanded ordinate scale.

Effect of Cenospheres on $T(\lambda)$

The difference between the data and the prediction is especially large in the wavelength range (3–6 μm). To investigate this discrepancy, it was decided to make separate transmittance measurements on the two main components identified from ash characterization, *viz*, the cenospheric and non-cenospheric fractions. As discussed in Chapter 3, the ash fraction lighter than 2.2 g/cc (comprising about a quarter of the ash by mass) consists almost entirely of cenospheres while the fraction with ρ >2.2 g/cc contains very few cenospheres. The average densities of the two fractions, measured with the specific gravity bottle, are $\rho_{<2.2}$=2.01 g/cc and $\rho_{>2.2}$=2.36 g/cc.

Transmittance data for the cenospheric and non-cenospheric fractions are shown in Figure 6.4. It is apparent that the transmittances for the two components are significantly different, especially in the shorter wavelength range. The cenospheric ash has a relatively flat spectral transmittance, $T(\lambda)$ increasing by only ~8% over the wavelength range. On the other hand, the data for the non-cenospheric fraction agrees with the calculations very well in the range λ=1–3 μm. These results indicate that for the whole ash, the cenospheric

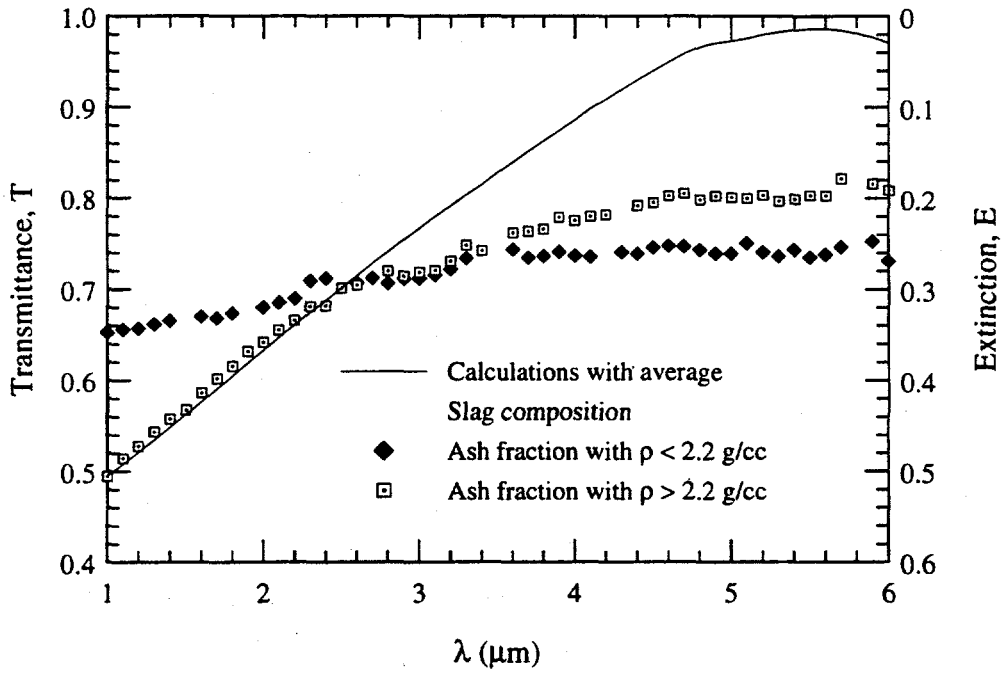

Figure 6.4: Transmittance measurements on density classified Upper Freeport ash in CCl_4. Note expanded ordinate scale.

component is primarily responsible for the reduced slope of the transmittance curve in the range 1-3 μm. The difference between data and predictions for the non-cenospheric ash at longer wavelengths will be addressed later in this section.

The calculations in the previous chapter showed that for (solid) particles with $n \sim 1.5$ and $k \ll 1$ in a gas, $Q_{s,\lambda} \gg Q_{a,\lambda}$ resulting in scattering dominating over absorption. In a liquid when $n_r \equiv (n/n_l) \sim 1$, i.e., $|(n_r - 1| \ll 1$, scattering is much reduced, and $Q_{s,\lambda}$ may be comparable to $Q_{a,\lambda}$. Extinction, too, is significantly reduced, tending to zero at the Christiansen wavelength where $n_r \rightarrow 1$.

Although scattering is reduced in liquid, the absorption at these wavelengths is very small ($k_r \ll 1$), and scattering still constitutes over 80% of the total extinction. Moreover, for cenospheres in a gaseous environment, Mie scattering results from interference of scattering (of comparable amplitudes) from the outer surface and the inner (bubble) surface. In a liquid environment, while scattering at the outer surface is much reduced, scattering at the inner surface is not reduced. Hence, the cenosphere in the liquid looks rather like a bubble to the incident radiation, with $n_r(\lambda) \approx \frac{1}{n_l} \simeq \frac{1}{1.4} \simeq 0.7$, independent of wavelength.

Thus for cenospheres we only have a slow decrease in scattering with increase in λ which is primarily due to the decreasing size parameter, $\pi D/\lambda_r$, and hence a decrease in $Q_{s,\lambda}$. The solid (or material) part of the cenospheres plays a secondary role in the increase of T with wavelength (similar to the non-cenospheric ash) in this range. It is important to note that this effect of cenospheres on the measured transmittance, while prominent in the case of ash dispersed in a liquid, would essentially be absent for a gaseous dispersion.

It is noted that the above analogy between a cenosphere and a bubble in liquid may not be extended to the long wavelength range ($\sim$10 μm) of the *Reststrahlen* band of silica where absorption is relatively large ($k_r \sim 1$). The reason is that when k_r is large, radiation is attenuated in the wall of the cenospheres, even when the latter is thin. In this case, a negligible fraction of the incident radiation is reflected from the bubble surface and escapes back into the liquid. A simple semi-quantitative analysis using extinction by an absorbing slab indicates that for $k_r \lesssim 0.1$, radiation will generally 'be aware'[†] of bubble(s) even for thick-walled cenospheres (thickness>15 μm). However, in the range $0.1 \lesssim k_r \lesssim 1$, cenospheric particles behave increasingly as solid particles.

It was seen in Chapter 3 that each cenosphere contained either a single (concentric or eccentric) bubble, or multiple bubbles. While Mie calculations for single concentric bubbles are possible (Bohren and Huffman, 1983), those for such complex geometries are formidable to the point of being impractical. However, a simple model may be formulated to explain the trend seen in the transmittance measurements using suitable approximations. Because $(n_r(\lambda)-1)$ is very small, the first approximation is to assume that $n_r(\lambda)=1$, so that the incident electromagnetic wave 'sees' only the bubble and not the glassy ash. Secondly, it is assumed that all cenospheres are concentric hollow spheres characterized by a single value of R_c, the ratio of inner diameter to the outer diameter of the cenosphere. Assuming the shell is made of material of the non-cenospheric fraction ($\rho_{>2.2}$) while the whole hollow sphere has a density equal to the average of the $\rho_{<2.2}$ material, it can be shown that this diameter ratio is given by

$$R_c = \sqrt[3]{1 - \frac{\rho_{<2.2}}{\rho_{>2.2}}} = \sqrt[3]{1 - \frac{2.01}{2.36}} = 0.53$$

By this model, cenospheres suspended in the liquid are represented by air bubbles with diameters reduced by a factor of R_c. If we further assume that all the bubbles are large ($D \gg \lambda_r$), then we have $Q_e \simeq 2$ (van de Hulst, 1957) independent of size parameter. The

[†]i.e., at most 1% of initial intensity would escape as reflection from bubble.

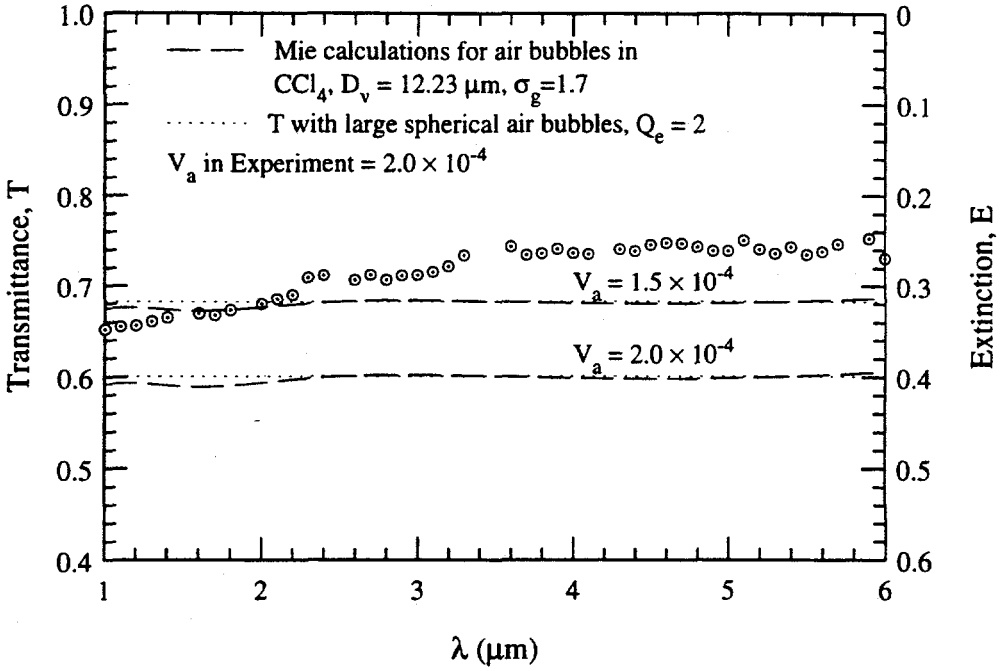

Figure 6.5: Transmittance measurements on the cenospheric fraction of Upper Freeport. Note expanded ordinate scale.

last assumption can be relaxed by assigning to the bubbles the size distribution of the cenospheric fraction (D_v reduced by R_c).

Mie scattering calculations were performed for air bubbles in CCl_4. The results are shown in Figure 6.5 along with the transmittance data for the cenospheric fraction. The volume median diameter of the bubbles is given by $D_{v,b} = R_c D_v = 0.53 \times 23.1 = 12.2\ \mu m$. Since R_c is the same for all ash particles, the geometric standard deviation of the air bubbles is $\sigma_{g,b}=\sigma_g$. After accounting for the unavoidable settling of a fraction ($\sim$25%) of the ash particles, the approximate model does a fairly good job of predicting the measured extinction of the cenospheric fraction. The difference between the Mie calculations and the large sphere model is small, and is maximum where the size parameter for most particles falls in the Mie scattering regime, i.e., $x \sim 1$. The slight decrease in the measured extinction in the range λ=3–6 μm is probably due to the effect of reflection at the outer liquid–cenosphere surface, and its reduction due to the closeness of $(n_r - 1)$ to unity in this range.

Effect of Ash Heterogeneity

While the presence of cenospheres largely explains the difference between transmittance data and predictions for the wavelength range 1–3 μm, the key to explaining the flat spectral dependence of the transmittance in the range 3–6 μm lies primarily in the compositional heterogeneity of the ash. The above calculations assumed that all particles have the same composition. As discussed earlier, for a chemically homogeneous ash, the transmittance of the ash dispersion increases to almost 100% because $n_r(\lambda)$ for all particles becomes unity at the same wavelength. However, as the CCSEM data show, chemical composition varies significantly from particle to particle. Hence, $n_r(\lambda)$ reaches unity at different wavelengths for different particles, which results in a flattening of the maximum in the spectral transmittance.

Extinction calculations were made for ash particles belonging to the five refractive index classes formulated in Chapter 4. Calculations of the combined extinction by these classes (Figure 6.6) shows a decrease in the maximum value of T. However, average compositions are used for each class, and, hence, the use of many more classes would reduce the calculated T to a value closer still to the data. Though the magnitude of the predicted T in Figure 6.6 is somewhat larger than the data, it is within uncertainty bounds imposed by the modeling of $n_r(\lambda)$, a part of which results from uncertainties in determining ρ_c (see Section 4.7). Figure 6.7 shows the sensitivity of T to the ash density, which, as discussed in Chapter 4, can be predicted as a function of composition only to an accuracy of 5%. This sensitivity to density is also seen when the data is compared with calculations using average CCSEM composition and two different average densities, the measured slag density and that calculated using effective densities of individual oxides (Figure 6.8). The transmittance calculated from the slag and average CCSEM compositions are very close.

6.2.2 Ash dispersed in CS_2

Extinction in the wavelength range 8–13 μm is dominated by the absorption mechanisms of SiO_2. The absorption band centered at $\lambda \sim 9\ \mu m$ is attributed to the vibrational stretch of the bridging oxygen atom (Si–O–Si) (Simon, 1960). There is a second band due to the stretch vibrational mechanism of the non-bridging oxygen atom ($Si–O^-$) centered at $\approx 10.2\ \mu m$. The band centers shift to slightly shorter wavelengths with increasing concentration of SiO_2 in the ash.

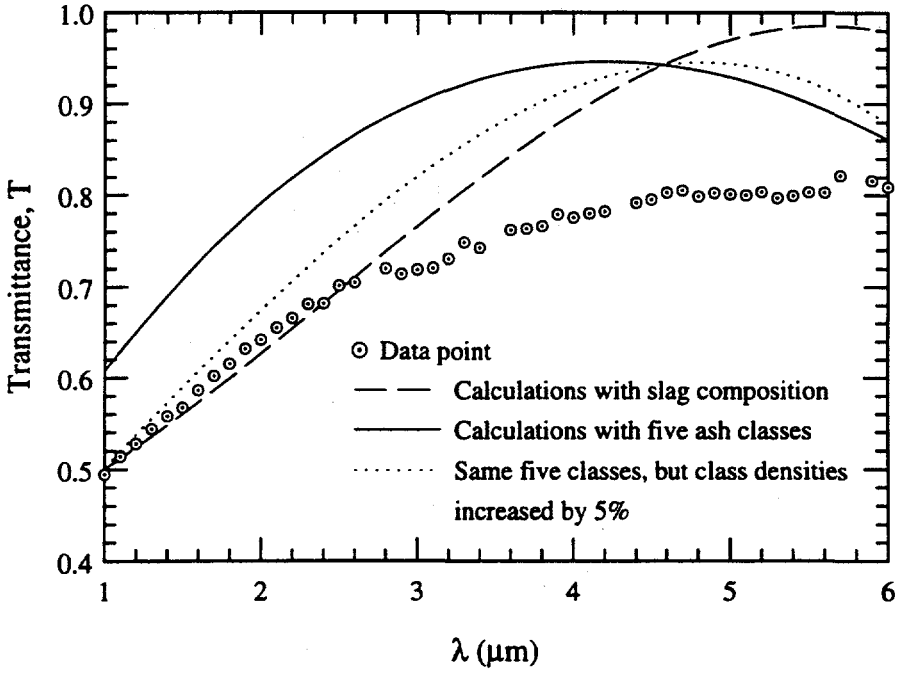

Figure 6.6: Comparison of transmittance data for non-cenospheric fraction of Upper Freeport ash with calculations for five refractive index classes. Note expanded ordinate scale.

Transmittance measurements for Upper Freeport ash (cenospheric, non-cenospheric, and whole ash) suspended in CS_2, over the wavelength range 7–11 μm, are shown in Figure 6.9. It is seen that extinction by cenospheres is significantly lower than that by the solid ash particles. The reason for this smaller extinction is that the cenospheres have larger diameters, and hence their area is less for the same V_a. In all three cases, there is a single broad *Reststrahlen* absorption band centered at $\lambda \sim 9.4\ \mu m$.

Calculations based on the size distribution of Upper Freeport ash, using room-temperature optical constants presented by Goodwin (for slag SA05[†]) and those obtained from high-temperature correlations developed by Ebert, are shown in Figure 6.10 and 6.11, respectively. Two distinct absorption peaks attributable primarily to the stretch vibrations of the bridging and non-bridging O atoms, predicted from Goodwin's room temperature measurements of $n(\lambda)$ are absent in the measured transmission (Figure 6.10). However, the spectral behaviour is similar to calculations using high temperature data $n(\lambda)$ measured by

[†]Goodwin's slags spanned a narrow range of SiO_2 content. Hence, no empirical relationships could be established between the SiO_2 content and the location and magnitude of the absorption peak.

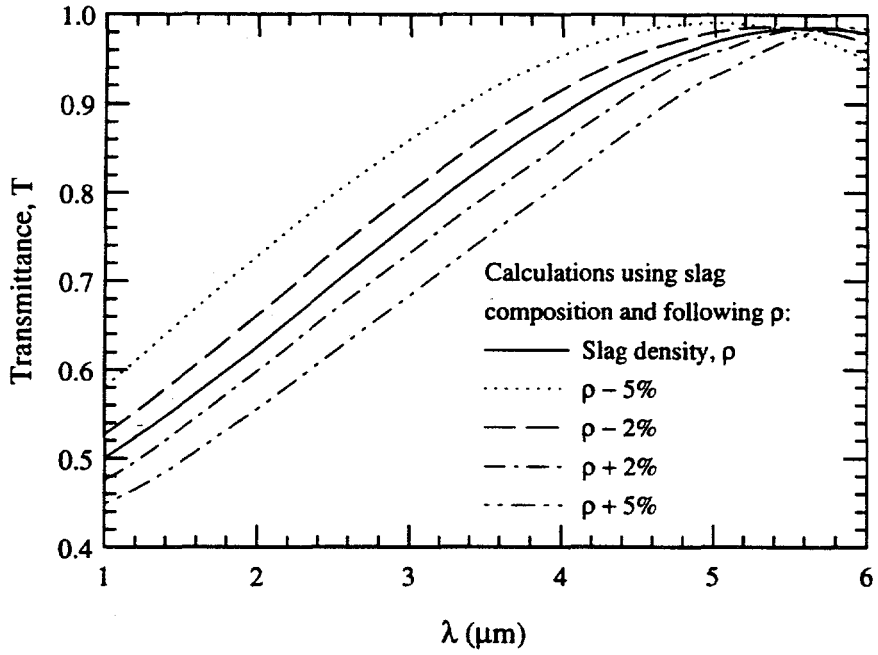

Figure 6.7: Sensitivity of T to ash density. Calculations for Upper Freeport ash. Note expanded ordinate scale.

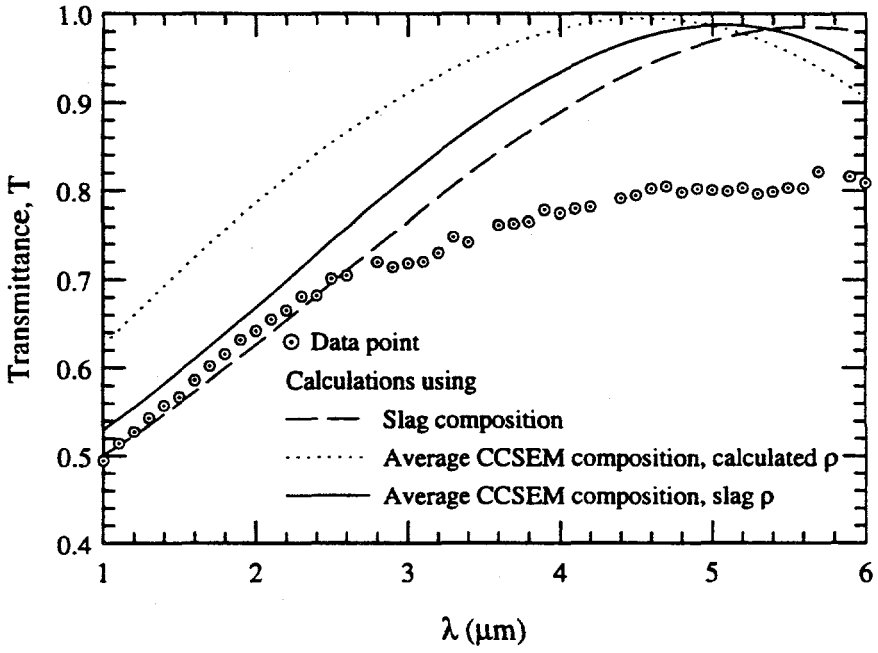

Figure 6.8: Comparison of T for Upper Freeport ash in CCl_4 calculated using slag and average CCSEM compositions, the latter using slag density (2.67 g/cc), and calculated density (2.48 g/cc). Note expanded ordinate scale.

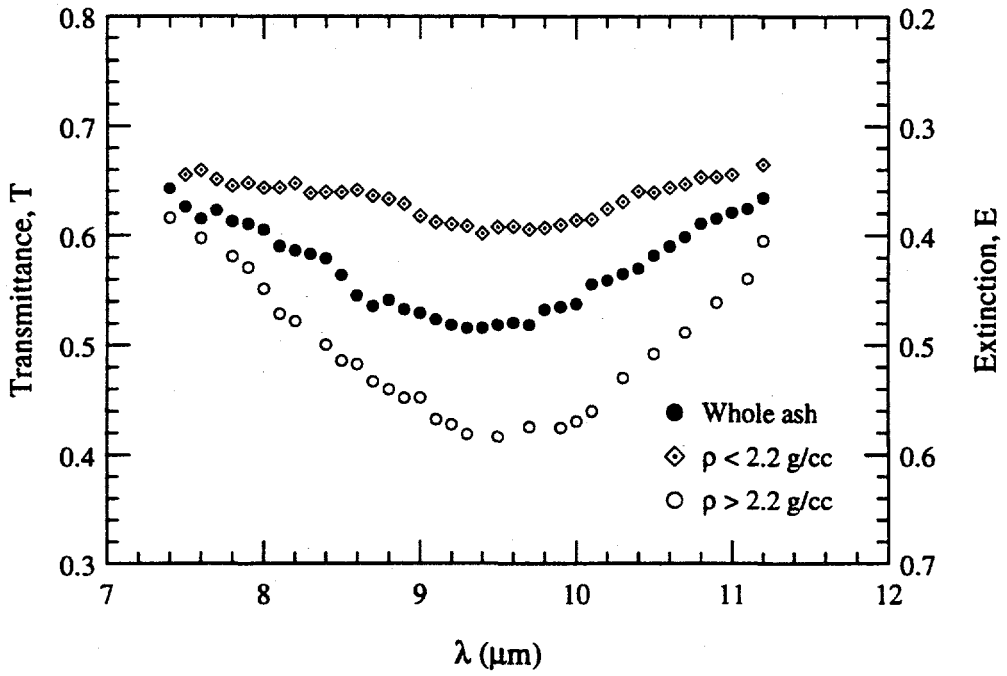

Figure 6.9: Transmittance measurements on cenospheric, non-cenospheric, and whole (unseparated) Upper Freeport dispersed in CS_2. Ash loading=2×10^{-4}. Note expanded ordinate scale.

Ebert (Figure 6.11). This difference is discussed in the next paragraph. The figures also show the contributions to extinction by both the absorption and scattering components. This range is the only part of the wavelength spectrum where the extinction is dominated by absorption. The scattering continues to decrease with increasing λ. Keeping in mind the sensitivity of T to $n_r(\lambda)$, $k_r(\lambda)$, and ash loading in this wavelength range, the differences between the calculations and experimental data are quite small.

A shift in the vibrational absorption peaks towards longer wavelengths occurs with increasing temperature, and also with decreasing SiO_2 content. In either case it is the result of bond weakening, and hence a lower resonance frequency. Seifert (1982) notes that an increase in network substitution, e.g., by Al, changes the Si–O–Al bond angle, and thus the effective proportion of bonding electrons for the Si–O bond, which leads to its weakening. Increasing thermal agitation of the molecules also weakens the bonds, resulting in dissociation of a fraction that increases with temperature. This depolymerization of the glass structure produces more non-bridging oxygen. From his high temperature optical property data, Ebert (1993) suggests that the shifted SiO_2 absorption peak merges with

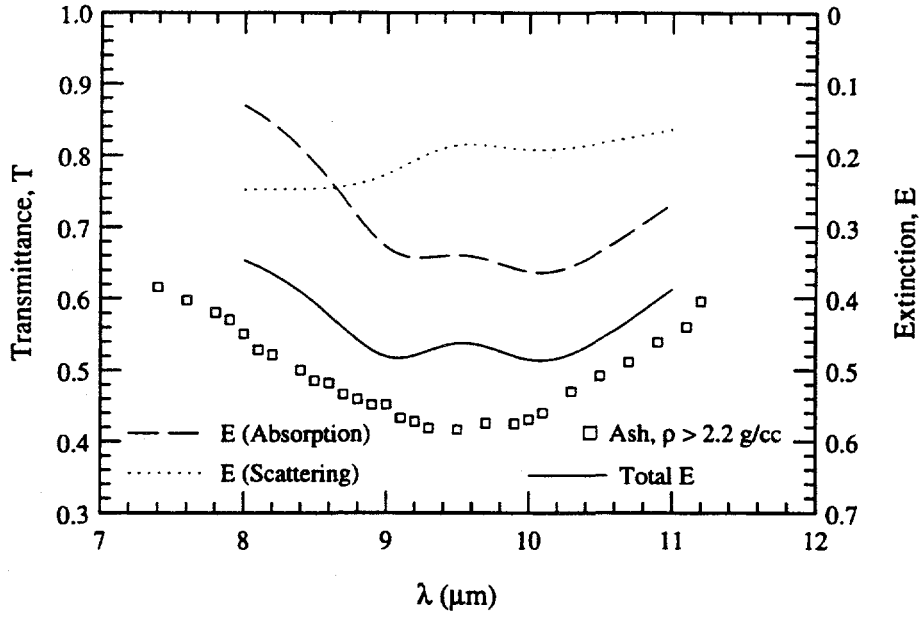

Figure 6.10: Non-cenospheric Upper Freeport ash dispersed in CS_2 (density>2.2 g/cc). Ash loading=2×10^{-4}. Comparison with calculations using Goodwin's correlations for room temperature optical properties. The scattering and absorption components of extinction are shown. Note expanded ordinate scale.

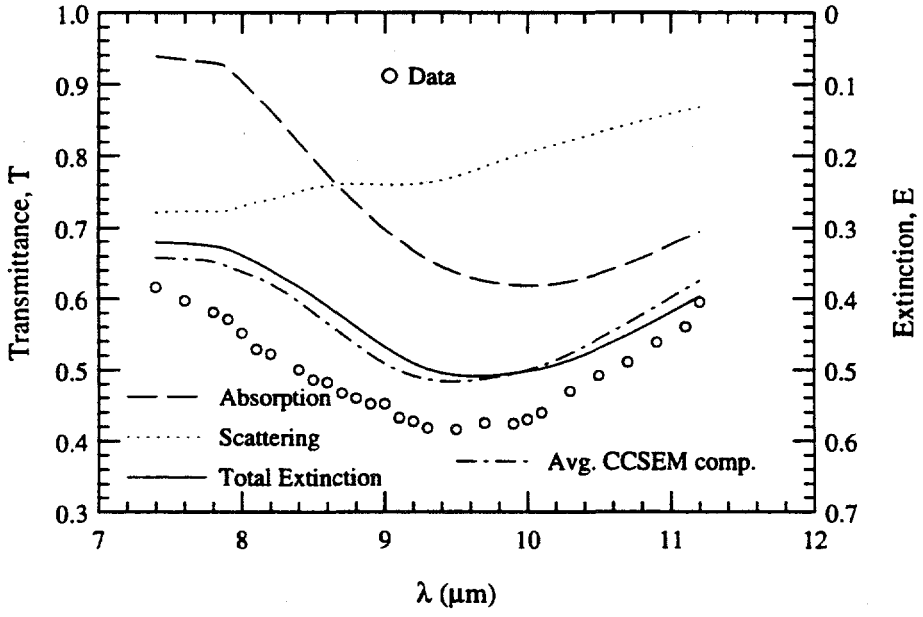

Figure 6.11: Non-cenospheric Upper Freeport ash dispersed in CS_2 (density>2.2 g/cc). Ash loading=2×10^{-4}. Comparison with calculations using Ebert's correlations for high temperature optical properties. The scattering and absorption components of extinction are shown. Note expanded ordinate scale.

the SiO^- peak, and only one broad absorption band is seen.

It should be noted that the two mechanisms described above are not the sole sources of absorption. There are multiple absorption bands that are combinations and overtones of the original vibration bands resulting from weak anharmonicity in the vibration modes. In these circumstances, it is not possible to pinpoint all the possible reasons why a single absorption band is observed.

It has also been noted that for high quench rate melts, e.g., $\gtrsim$ 500 K/s, at atmospheric pressure, there are no detectable structural differences between the glass and the melt, within the sensitivity limits of the spectroscopic techniques used (Sweet and White, 1969; Mysen *et al*, 1985). However, there indeed *are* some structural changes, such as those responsible for different heat capacities between the glass and melt. It is probable that such changes, which cannot be monitored at the transition point using currently available analytical tools, do not significantly affect the overall structure of the broad absorption band.

From the scattering component of E in Figures 6.10 and 6.11, it is noted that $Q_{s,\lambda}$ decreases throughout this wavelength range. Thus, part of the increase in E due to SiO^- absorption is offset by a decrease in scattering. Absorption by SiO^- does not result in a separate extinction peak at λ~10.5 μm. The single, broad absorption peak (which coincides with the extinction peak) matches the prediction for high temperature ash very well, suggesting that the quench rates of the ash particles were sufficiently high to prevent any perceptible structural change from the melt (at least, from the viewpoint of radiative properties). This is to be expected in coal-fired combustors. By contrast, the quench rates of the bulk slags produced by Goodwin and Ebert in a laboratory furnace are very much lower. Thus the structure and optical properties of these solid slags may be significantly different from those of the corresponding molten slags.

6.2.3 Ash dispersed in $CHBr_3$

Measurements using bromoform were made over two wavelength ranges (6.5–7.3 μm) and (11.8–13.5 μm) which together span ~20% of the total wavelength range. In Figure 6.12, it is seen that extinction by the ash suspension is relatively constant since there are no absorption bands over these ranges. The Mie calculations using high temperature optical properties (Ebert, 1993) are in general agreement with the data within uncertainity limits

(note expanded ordinate scales). For the longer waveband, the calculations show E decreasing with λ because of the edge of the absorption band at $\sim$10 μm. The spectral flatness of the data is probably because of the effect of cenospheres. Due to decreasing size parameter, the effect of non-cenospheric component decreases at long wavelengths. The contribution of the cenospheric component (bubbles) remains dominant ($Q_{e,\lambda}$ remains $\sim$2).

Finally, the transmittance spectrum over the full range 1–13 μm is shown in Figure 6.13. The data for CS_2 and $CHBr_3$ were normalized with respect to the CCl_4 data in order to obtain a continuous curve. This normalizing implies an adjustment of the ash loading, and is presented only to provide a comparison of the nature of the spectral changes in E for ashes dispersed in the three liquids.

6.3 Measurements on San Miguel Ash

Transmittance data for San Miguel ash in CCl_4 and CS_2 are shown in Figure 6.14 and 6.15, respectively. This ash is almost entirely cenospheric. As with the lighter density fraction of Upper Freeport ash, both the cenospheric and the heterogeneous nature of the ash cause the maximum T in CCl_4 to be significantly broader and smaller than unity. Due to the high silica content, the scattering, and hence E, reaches a minimum at $\approx$3.8 μm, where $n_r(\lambda) \rightarrow 1$ for the average composition.

The spectral extinction in the 7.5–11 μm range is similar to that of Upper Freeport, exhibiting a broad absorption band centered at $\approx$9.8 μm. Ebert's correlations for the high temperature optical properties take into consideration the ash's high silica content, and accordingly shift the calculated absorption peak to slightly shorter wavelengths compared with Upper Freeport ash. Considering that E is diminished for cenospheres compared with solid ash particles (see Section 6.2.2), the spectral behaviour of T is in good agreement with the data. No measurements with bromoform were possible because the ash tended to float to the surface and re-agglomerate (as a result of the large density difference between the two).

6.4 Measurements on Eagle Butte Ash

Figure 6.16 shows transmittance data for Eagle Butte ash dispersed in CCl_4, along with Mie calculations. In contrast to the San Miguel ash, this ash contains very few cenospheres

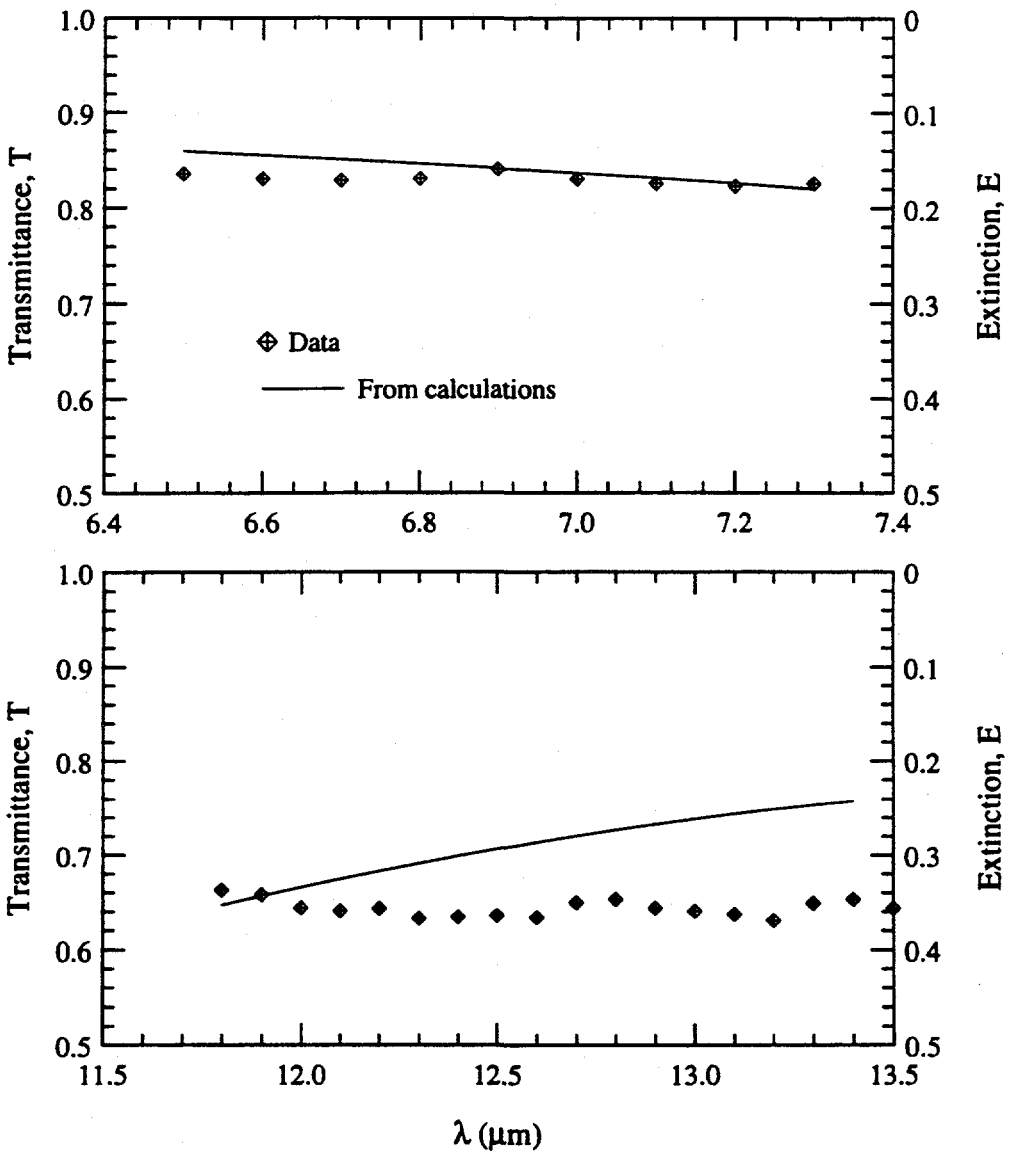

Figure 6.12: Comparison of T for Upper Freeport ash in $CHBr_3$ calculated using slag composition, and optical property correlations of Ebert (1993). Note expanded ordinate scale.

(<4% by mass). Hence, the departure from the calculated transmittance in the wavelength range 3–6 μm is attributed almost entirely to ash heterogeneity. Due to the high refractivity of this calcia-rich ash, $n_r(\lambda)$ does not pass through unity in the range λ=1–6 μm, so there is no transmittance maximum. The comparison with calculations need not necessarily mean that Goodwin's correlation is better than Ebert's since the synthetic slags in neither case included a range of CaO as large as in the Eagle Butte ash.

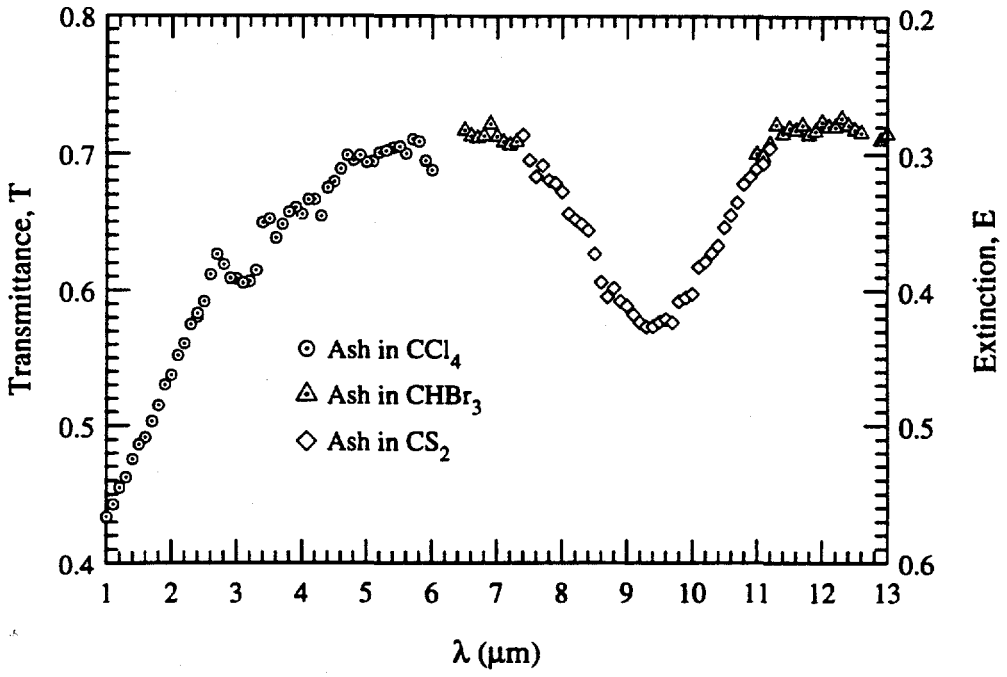

Figure 6.13: Transmittance measurements on Upper Freeport ash, combined over the wavelength range 1–13 μm. Note expanded ordinate scale.

In the longer wavelength range (7–12 μm), the form of the measured extinction (in CS_2) is quite different from the previous two ashes (Figure 6.17). This is hardly surprising, since the composition of the Eagle Butte ash is unusual in that a quarter of the particles in the CCSEM sample had no silica, while half the particles contained 15% or less. The optical property correlations of Ebert are not very accurate for particles of such low SiO_2 content. Unlike the previous ashes, the spectral transmittance shows at least two distinct absorption bands. The very broad extinction peak centered at 10.7 μm is predicted quite well by the high temperature correlations, and is a result of absorption due to stretch vibrations of both the bridging (Si–O) and non-bridging (SiO^-) oxygen atoms. As explained earlier, in low-silica particles characteristic of this ash, the absorption peak due to the bridging O is shifted to longer wavelengths and merges with the SiO^- peak. In the Eagle Butte melt, too, the peaks are indistinguishable (Ebert, 1993).

The second extinction feature, centered at ≈8.8 μm, appears to have a double peak. We were not able to satisfactorily explain this feature, although it may arise from the scattering component; a result of $n_r(\lambda)$ for a fraction of ash particles passing through unity.[‡]

[‡]It is too strong to be assigned to any combination modes of different pairs of vibration mechanisms.

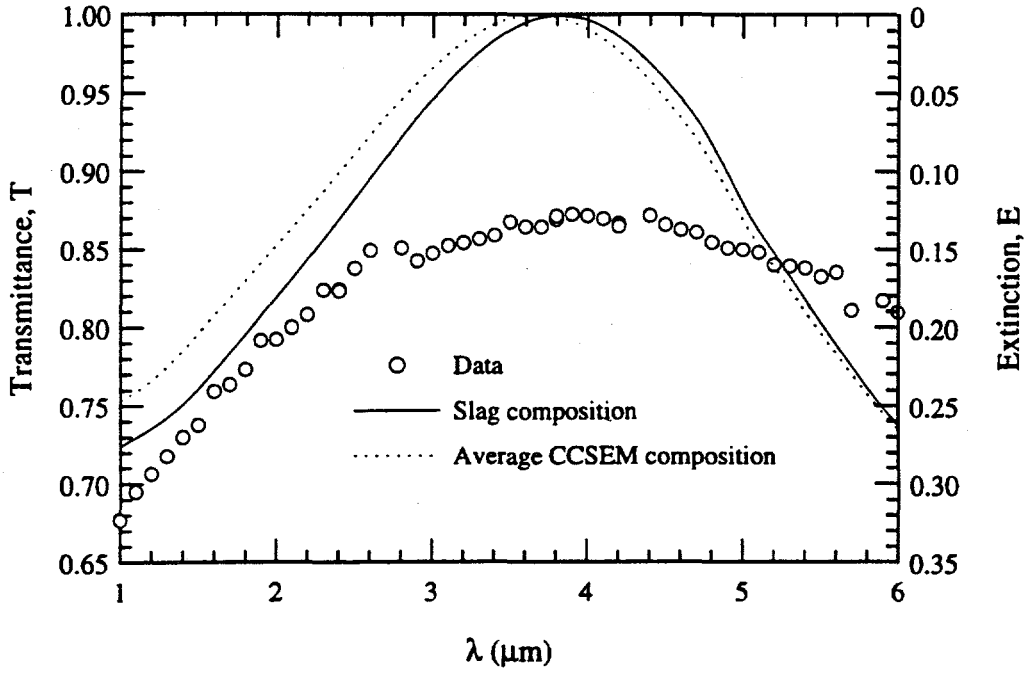

Figure 6.14: Transmittance measurements on San Miguel ash dispersed in CCl_4. Ash loading=5×10^{-4}. Note expanded ordinate scale.

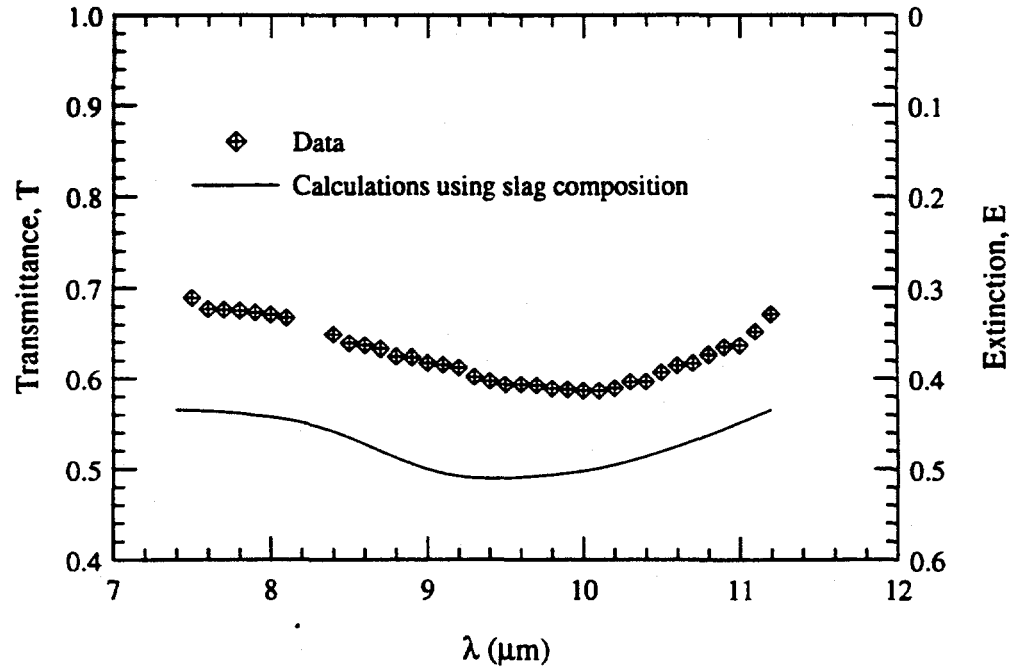

Figure 6.15: Transmittance measurements on San Miguel ash dispersed in CS_2. Ash loading=5×10^{-4}. Note expanded ordinate scale.

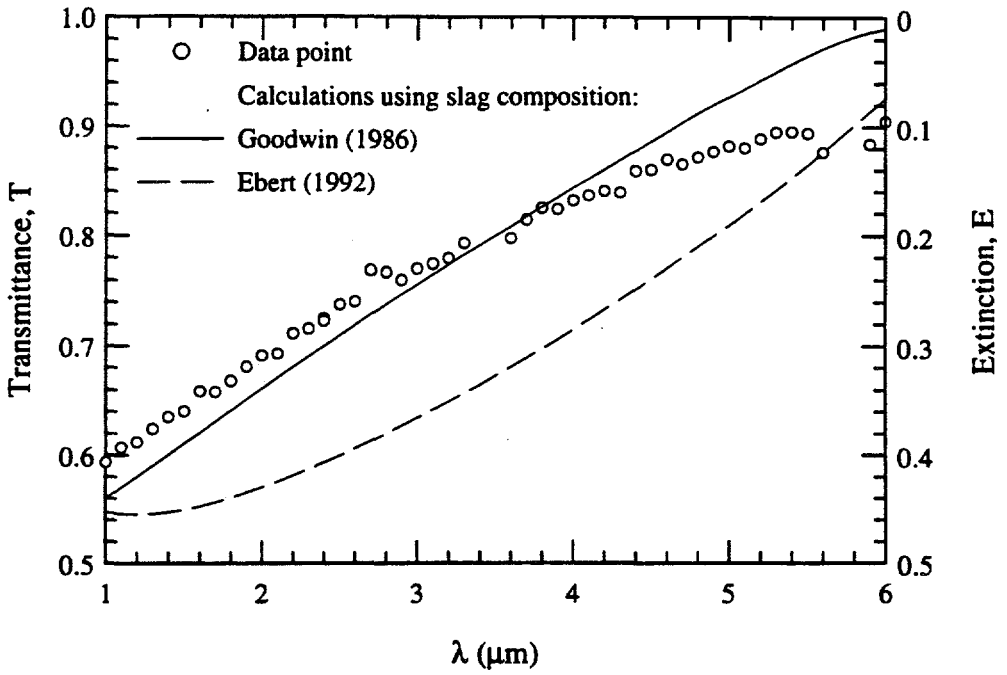

Figure 6.16: Transmittance measurements on Eagle Butte ash dispersed in CCl_4. Ash loading=2×10^{-4}. Note expanded ordinate scale.

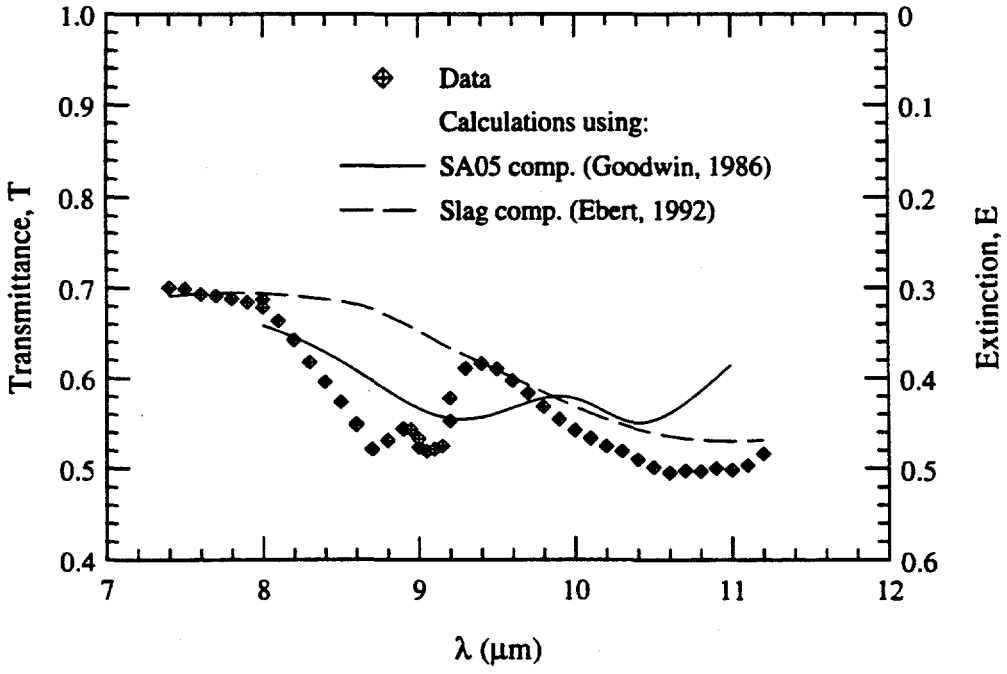

Figure 6.17: Transmittance measurements on Eagle Butte ash dispersed in CS_2. Ash loading=2×10^{-4}. Note expanded ordinate scale.

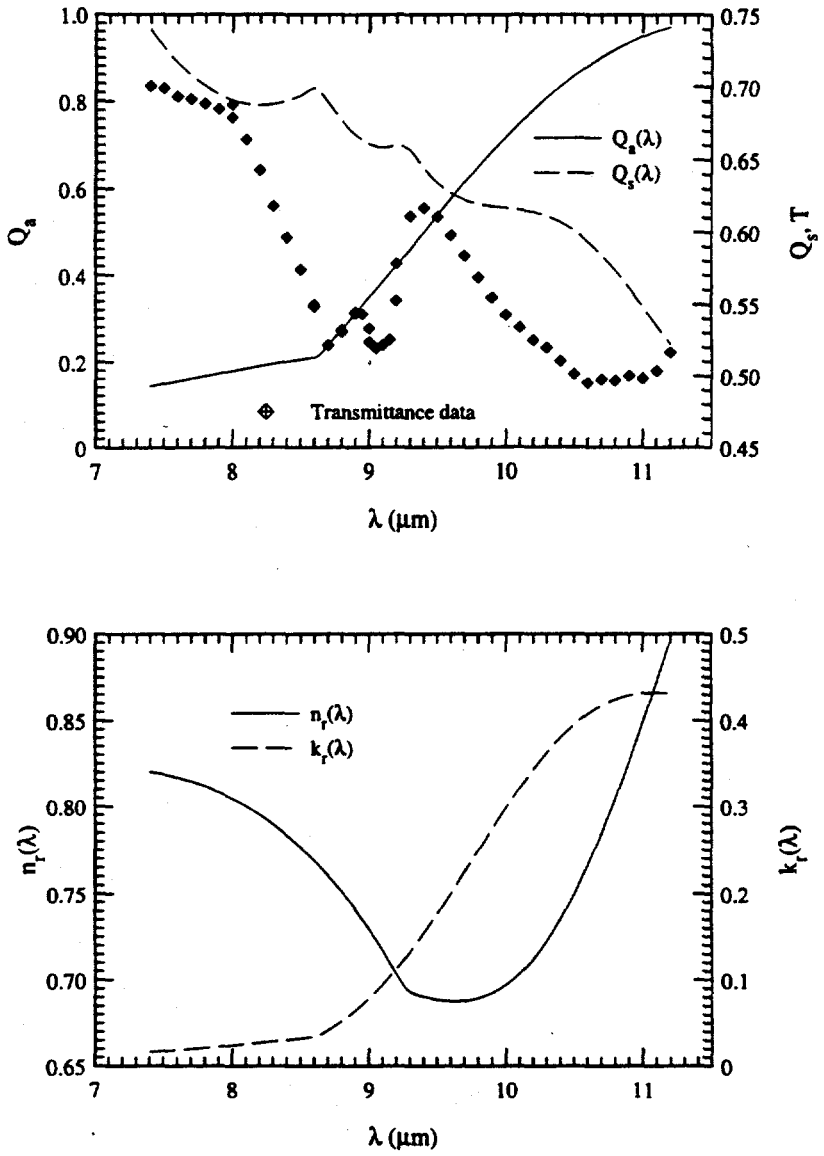

Figure 6.18: Optical constants, and scattering and absorption efficiencies calculated using Ebert's correlations for Eagle Butte slag in CS_2.

In Figure 6.18, the absorption and scattering efficiencies from Mie calculations are shown together with $n_r(\lambda)$ and $k_r(\lambda)$ from Ebert's high temperature correlations. The discontinuities in the (otherwise monotonically decreasing) $Q_{s,\lambda}$ and $Q_{a,\lambda}$ curves are a result of patching together correlations for $n_r(\lambda)$ and $k_r(\lambda)$ that are valid over separate wavelength ranges. As a result of the high refractive of $CHBr_3$, $n_r(\lambda)$ has relatively low values in this range, and reaches a minimum at 9.6 μm.

The broad absorption band on which these scattering features are superimposed, however, is more difficult to explain. As discussed earlier, a Si–O stretch absorption peak shifted to this location would imply the presence of a relatively large class of high-SiO_2 particles. But CCSEM data shows that less than 10% of the ash has more than 50% silica. Although Goodwin's correlations (which do not account for peak shifts with varying silica content) for SA05 slag predicts a bridging O absorption peak at 9.2 μm (Figure 6.17), the composition differences between the two slags are too great for meaningful comparison. It is again reiterated that both sets of correlations are not valid for almost a quarter of the (zero-silica) ash. For better understanding, more comprehensive studies on the optical properties of high-calcium aluminosilicate glasses are needed. Additionally, CCSEM data on much larger samples (10,000–15,000 particles) are needed for more accurate compositional classification of the ash. All we can conclude from the transmittance data is that there exists a significant fraction of ash particles with strong bonds probably involving bridging oxygens associated with Si or Al in tetrahedral coordination.

In contrast to SiO_2, CaO (the predominant oxide) is distributed more evenly throughout the sample. In fact, CaO is present in all the particles. While only 8% are composed of <15% CaO, 20% of the particles contain >80% of the oxide by mass. Engelhardt *et al* (1985) studied the structures of about fifty glasses in the CaO–Al_2O_3–SiO_2 system. In glasses of composition similar to average Eagle Butte (molar proportions of CaO : Al_2O_3: SiO_2= 48 : 14 : 38), three of the four oxygen atoms in SiO_4 were bridging ones, with either two or all three O atom connecting the Si atom to Al atoms. As the molar concentration of Ca decreases to <15%, all four O atoms become bridging atoms, with either one or two connecting the Si atom to Al atoms. This low concentration of non-bridging O atoms in most of the particles may contribute to the absence of the corresponding absorption band in the two earlier ashes which containing low mass fractions of glass modifiers. However, it is also known that the presence of significant amounts of network modifiers (e.g., >10% Na_2O, molar) in this glass forming system of SiO_2–Al_2O_3 leads to the creation of non-bridging oxygen, SiO^- (Seifert *et al*, 1982).

Comparison of extinction of ash in $CHBr_3$ with calculations for both long and short wavelengths are shown in Figure 6.19. The increase in E beyond λ=12.8 μm may be due to the wing of the broad fundamental vibration band of Al_2O_3, centered at 15.7 μm. However, the correlations used here do not account for this mechanism, since its location at mid-infrared wavelengths make it unimportant from the viewpoint of radiation transfer.

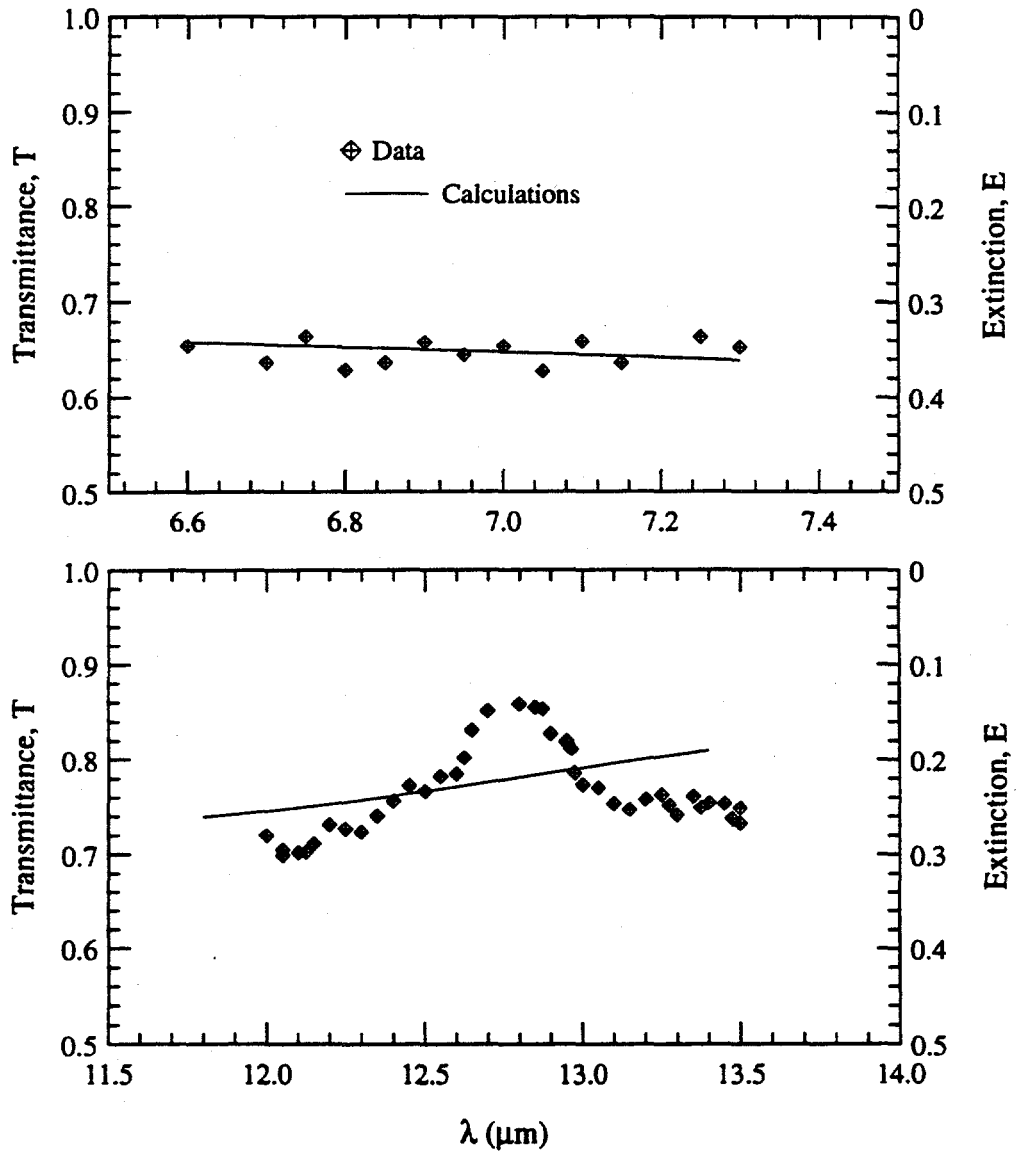

Figure 6.19: Transmittance measurements on Eagle Butte ash dispersed in $CHBr_3$. Ash loading=2×10^{-4}. Note expanded ordinate scale.

6.5 Measurements on Beulah Ash

The Beulah lignite ash resembles the Eagle Butte ash in its low glass former/modifier content and comparable Al_2O_3 content. It, too, has relatively few cenospheres ($\approx$7%, by mass), and, therefore, measurements were made only on the unseparated ash. It differs from the Eagle Butte ash in its high iron (18%) and Na_2O (6%) contents. Figure 6.20 show the

transmittance data for ash dispersed in CCl_4. As in the case of Eagle Butte ash, predictions from Mie calculations agree with the data in the 1–3 μm range. As with all the ashes, the heterogeneity of optical properties lowers the transmittance in the 3–6 μm range.

In Figure 6.21, the nature of $T(\lambda)$ in the high-absorption wavelength range is somewhat similar to the Eagle Butte ash. Both ashes are relatively low in silica, and have significant modifier content. Again, two distinct absorption peaks, located at $\sim$9.0 μm and 10.2 μm, are clearly distinguishable. The narrow extinction feature at 8.7 μm, seen in the Eagle Butte ash, is also seen here. The discussion for the Eagle Butte ash is applicable here. Neither set of correlations appear to predict the extinction peaks accurately. The composition of the SA05 ash too different from the Beulah ash for meaningful comparison of its calculated transmittance with the data, although it appears to offer the best predictions. Calculations for Goodwin's high iron–low silica slag SB20, which has the composition closest to that of Beulah slag, show little agreement with the data. The transmittance data in bromoform shown in Figure 6.22 is relatively featureless, and the calculations agree within uncertainity bounds.

To further investigate the effect of the SiO^- stretch vibration on transmittance, measurements were made on glass spheres of high modifier content. The spheres (from Duke Scientific Corp.) are nominally monodisperse (diameter 8 μm) with the following average composition: SiO_2=73%, Na_2O=13%, CaO=10%, MgO=3.3%, Al_2O_3=0.4%, K_2O=0.1%, Fe_2O_3<0.2%. The data for $T(\lambda)$ in Figure 6.23 clearly shows significant absorption by SiO^- at $\lambda\sim$10.8 μm.[§]

6.6 Summary

Measurements on four ashes with distinctly different characteristics have been compared with Mie scattering calculations to test the proposed procedure for predicting their radiative properties. For gaseous fly ash suspensions, scattering dominates absorption in its contribution to extinction. However, scattering is considerably diminished by performing the experiment in a liquid medium, making the extinction, E, more sensitive to absorption. Even so, E is still sensitive to $n_r(\lambda)$, especially in the range 1–6 μm. The experiments show that both ash heterogeneity and the presence of cenospheres must be taken into account to

[§]Due to lack of data on optical properties of Na_2O and K_2O, it is not possible to do Mie calculations for such powders containing significant amounts of either (or both) oxides.

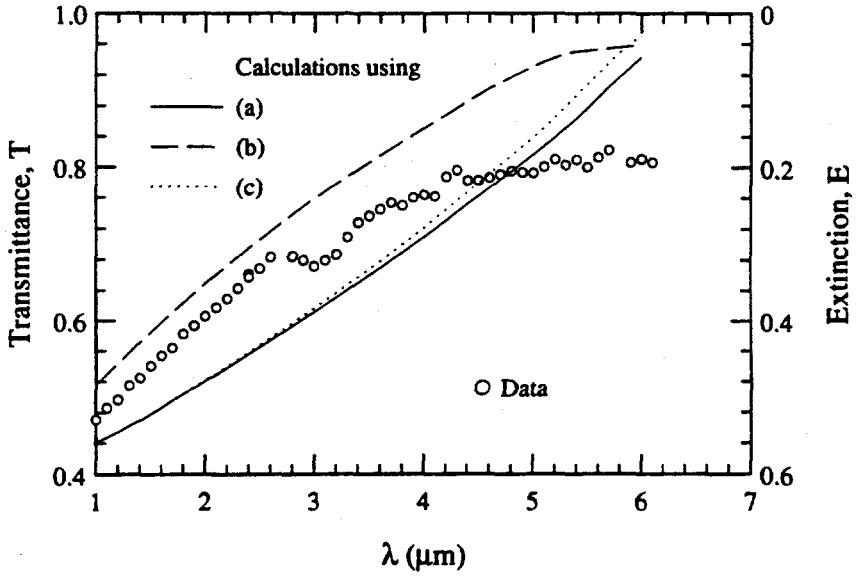

Figure 6.20: Transmittance measurements on Beulah ash dispersed in CCl_4. Ash loading=2×10^{-4}. (a) Ebert's correlations, slag composition, (b) Goodwin's correlations, slag composition, (c) Ebert's correlations, average CCSEM composition. Note expanded ordinate scale.

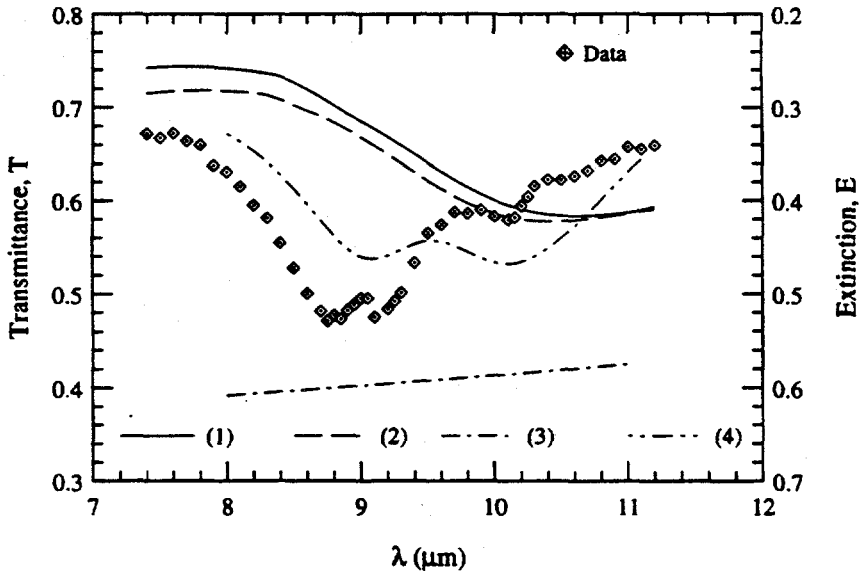

Figure 6.21: Transmittance measurements on Beulah ash dispersed in CS_2. Ash loading=2×10^{-4}. (1) Ebert's correlations, slag composition, (2) Ebert's correlations, average CCSEM composition. (3) Goodwin's correlations, SA05 slag composition, (4) Goodwin's correlations, SB20 slag composition. Note expanded ordinate scale.

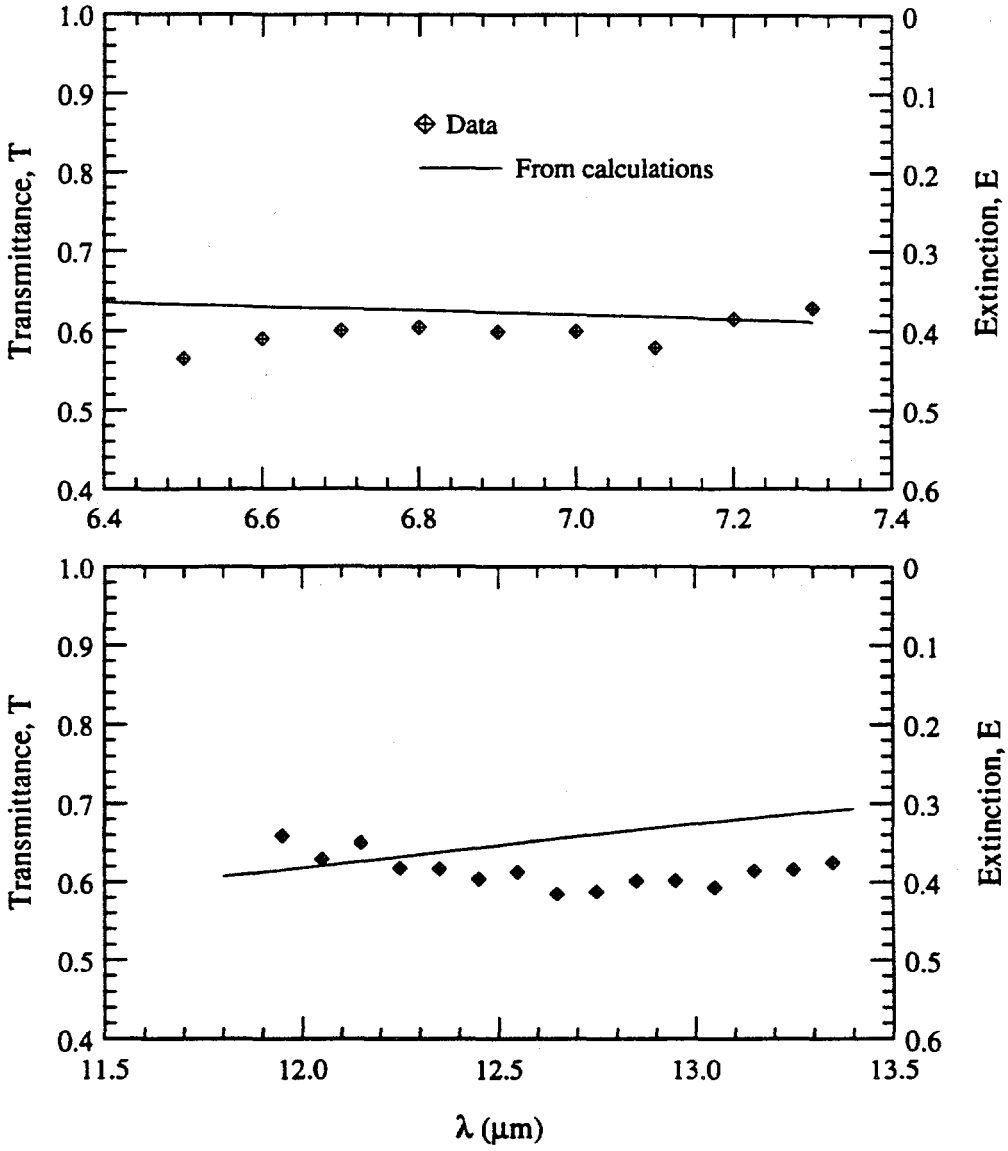

Figure 6.22: Transmittance measurements on Beulah ash dispersed in $CHBr_3$. Ash loading=2×10^{-4}. Note expanded ordinate scale.

interpret the measurements in CCl_4 in this wavelength range. These effects, however, are less important for ashes dispersed in air where the slope of $(n_r(\lambda)-1)$, as a function of λ, is much smaller.

At longer wavelengths (>4 μm), the relative strengths of various absorption mechanisms related to silica depend on the concentrations of glass modifiers like CaO (as seen in

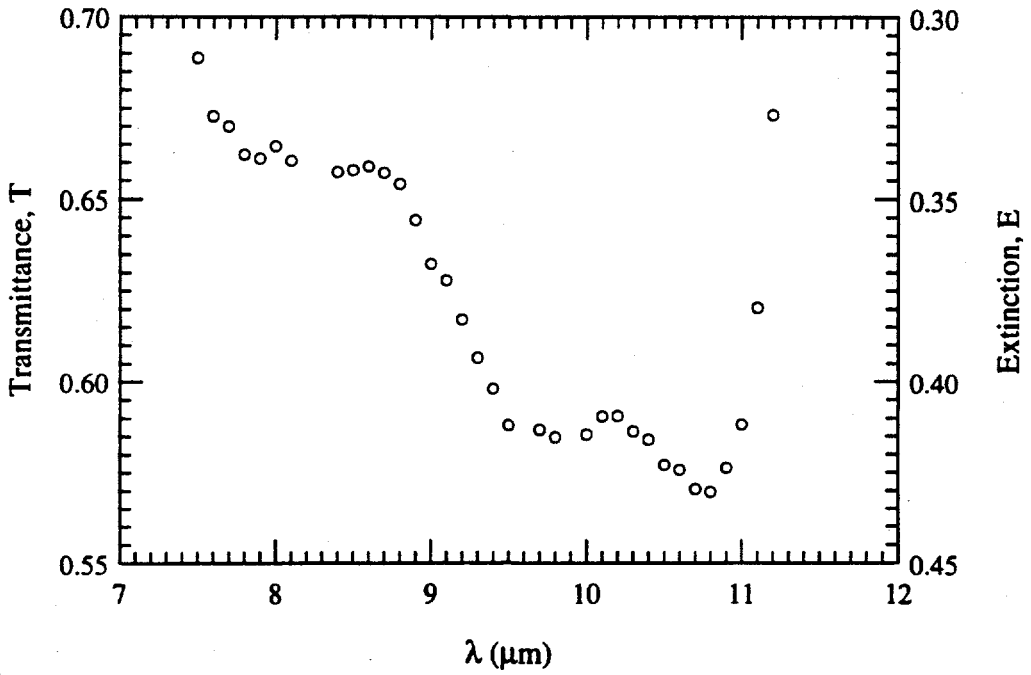

Figure 6.23: Transmittance measurements on glass microspheres (density=2.42 g/cc) dispersed in CS_2. Loading=2×10^{-4}. Note expanded ordinate scale.

the Eagle Butte and Beulah ashes). Spectral extinction in this range for high-silica ashes (Upper Freeport and San Miguel) is predicted better by the high temperature optical properties (of melts) presented by Ebert (1993), than by room-temperature data obtained with solid slags (from slowly cooled melts) by Goodwin (1986). This contrast suggests that the glassy ash largely retains the melt structure as a result of rapid quenching in coal combustors. Overall, both the spectral nature and the absolute magnitude of the extinction are predicted with reasonable accuracy by Mie theory.

Chapter 7

Summary and Conclusions

This experimental study of the optical-radiative properties of coal fly ash forms part of a larger effort to develop a fundamental scientific basis for the reliable prediction of the ash's role in radiative heat transfer in pulverized coal-fired combustors. Earlier studies by Goodwin (1986) and concurrent work by Ebert (1993) have identified and analyzed the wavelength dependent absorption mechanisms of iron and silica which control the infrared optical properties of the ash. Iron is primarily responsible for absorption in the short wavelength infrared region ($1\ \mu m < \lambda < 4\ \mu m$), while SiO_2 is responsible for strong absorption in the longer wavelength region through its broad *Reststrahlen* band centered at approximately $9\ \mu m$. Those studies confirmed that fly ash, while not dominating the radiative transfer process, substantially influences it by scattering the radiation emitted by combustion product gases, CO_2 and H_2O. They established a database of optical properties for synthetic slags of controlled compositions, at both room and combustor temperatures. Their correlations for predicting the optical constants (n, k) from slag composition is the basis for determining the optical properties of *particulate ash* using data obtained with *bulk slags*.

The present work addresses two areas of the overall problem that complement these two studies. In the first part of this dissertation, six ashes, typical of those generated in U.S. power plants, have been comprehensively characterized with respect to factors controlling their optical properties. Previously published studies have often made unrealistic assumptions about size and chemical composition distributions of fly ash. The final results of this ash characterization effort are accurate determination of the ash size distributions, the establishment of several refractive index classes (classes within which all ash particles are assigned the same composition, and hence, the same (n, k) values), and estimates of

the cenospheric contents of the ashes. This information is the input necessary for realistic Mie calculations for the scattering and absorption efficiencies of the ashes studied. These efficiencies, in turn, are the necessary input for radiation transfer calculations in pulverized coal-fired combustors.

The second part of the dissertation describes an experiment designed to test the validity of the entire approach to the problem, *viz*, that the radiative properties of an ash dispersion can be reliably calculated *if* its size and composition distributions are known in sufficient detail. While there are several analytical and numerical studies in the literature related to the radiative properties of dispersed fly ash, no controlled experiments appear to be have been performed to test these predictions. Rather than try to reproduce combustor conditions where meaningful radiation measurements to determine the contribution by individual components (i.e., soot, char, ash, and gases) are virtually impossible, we designed a bench-scale experiment, and made extinction measurements under controlled conditions on well-characterized ashes.

The two parts of this dissertation, while seemingly independent, are actually closely related. The principal underlying assumptions in modeling ash radiative properties is that fly ash particles, as a result of their formation process, are preponderantly spherical, glassy (and hence isotropic), and reasonably homogeneous, thus fulfilling the requirements of Mie theory. These assumptions are necessary to render the problem tractable, and it is indeed a fortunate happenstance that fly ash satisfies them remarkably well. There is a significant body of literature* on the physical and chemical characterization of ashes, most of which concludes that ash is indeed predominantly spherical and glassy. However, the fraction of the ash composed of particles that are inhomogeneous†, by virtue of being cenospheric (containing gas bubbles) is often not insignificant. The present characterization work provides estimates of this fraction in the six ashes studied, and comparison of the data from the extinction measurements with predictions from Mie theory shows whether additional measures need to be taken to account for this fraction.

Four of the ashes were generated in a pilot-scale combustor while the remaining two were obtained from full-scale power plants. Three originated from bituminous coals (Illinois #6, Kentucky #9, and Upper Freeport), two from lignites (Beulah and San Miguel), and one

*The literature is disseminated primarily by the environmental, combustion, and ash utilization research communities. The last group appears to have treated the subject most comprehensively.

†There are several factors that determine the fraction of the ash constituted by this component, primary among which are the coal type, combustor operating conditions, and ash composition.

(Eagle Butte) from sub-bituminous coal.

Physical characterization included optical and scanning electron microscope examinations of ash samples, which confirmed the closely spherical nature of the ash. The non-spherical fraction, which includes a variety of morphological types (char, unmelted adventitious mineral matter, etc.), tend to be quite large and prominent when examined by optical microscope. Even if all the large particles (say, >30 μm) are assumed to be non-spherical, it was established from size distribution measurements that they constitute only a small fraction of the ash (<10% by volume, <1% by count), with the exception of the San Miguel ash.

The Coulter Multisizer was used to determine the ash size distribution over the diameter range 1–200 μm. To size over such a large range, it was necessary to obtain data using several orifices. The data were later combined by normalizing at overlapping size ranges to obtain the composite distribution. To use smaller orifices, the larger particles had to be removed from the sample. A wet-sieving apparatus was designed to facilitate accurate separation of the particles by size. One outcome of the study of the Multisizer performance was that its acceptable lower limit of size measurement was found to be ~3.5% of the orifice diameter, rather than 2% as stated by the manufacturers. Suitable software was written to process the Multisizer data, and to compute and display size distributions on the basis of number, area, or volume in both differential and cumulative forms.

A lognormal distribution function, truncated outside the measurement limits, was found to fit the size distribution data very well. This function allows detailed size information to be stored compactly using four quantities: the parameters of the best-fit lognormal functions, D_v and σ_g, and the diameter measurement limits (a, b). For all but one of the ashes, D_v and σ_g are found to be in the range 9–15 μm and 2.0–3.0, respectively. The exception is the predominantly censopheric San Miguel ash which has a large D_v of 32.3 μm.

From the standpoint of radiative transfer, the primary source of inhomogeneity in the individual ash particles is the presence of cenospheres. Density classification by centrifugal separation was used to separate the cenospheric fraction. The ashes were classified into six classes of equal width spanning the density range <1.6 g/cc to >3.2 g/cc. For most ashes, 80% by mass have densities in the range 2.0–2.8 g/cc. Of the two exceptions, the calcia-rich Eagle Butte is significantly denser than the rest (~75% of the mass having ρ >2.8 g/cc), and the highly cenospheric San Miguel ash with ~88% of the mass having ρ <2.0 g/cc. Density classification also confirmed that the char contents of all six ashes were negligible,

which eliminated the inclusion of char in the optical characterization process.

Since the least dense of the oxides in ash, SiO_2, has a density of 2.2 g/cc, it is reasonable to assume that all particles having ρ <2.2 g/cc must contain voids that reduce their average densities. It was concluded that this fraction is a good estimate of the cenospheric content of an ash. Separation with a liquid of density 2.2 g/cc showed that the San Miguel ash consists almost entirely of cenospheres (>95% by mass), and the Eagle Butte ash contained the smallest fraction of cenospheres (3.6%). For the remaining ashes, the cenospheric fraction was found to vary in the range 5–25% by mass, with no clear dependence on coal rank. This quantification of the cenospheric fraction was particularly important for the transmittance measurements because, in liquid dispersions, extinction by cenospheres was found to differ significantly from that by solid ash particles.

The average ash densities, ρ_{ash}, needed for preparing ash suspensions of known volumetric loading for transmittance measurements, were also measured. For the bituminous ashes, ρ_{ash} lies in the range 2.15–2.30 g/cc. As expected, the lowest and highest densities are those of San Miguel (1.73 g/cc) and Eagle Butte (2.76 g/cc), respectively.

The size distributions of all density classes of the classified ashes were measured with the Multisizer. It was found that the median diameters of the lighter particles (primarily cenospheres) tend to be significantly larger than those of the whole (unseparated) ash. This is also true for the denser ash fractions (>2.8 g/cc). The latter class contains iron-rich particles that are relatively large, as well as a wider range of diameters of particles that are low-silica, high-calcia and/or high-alumina. The cenospheric ash fractions have median diameters that are two to three times larger than those of the non-cenospheric fractions. The size distribution data for the majority of the density classes were found to be described very well by truncated lognormal functions.

In addition to yielding accurate information on ash size and density distributions, the physical characterization results showed that a substantial amount of the total iron is present in a relatively few large particles (which are believed to result from the combustion of pyrite-rich particles in the coal grind). This information together with the results from chemical analysis helped in evaluating the relative importance of Fe_2O_3 in radiative transfer.

Detailed information on the chemical compositions of the ashes is needed because their optical properties (n, k) depend on the corresponding properties of the component oxides. While bulk compositions may be useful in comparing properties such as the slagging/fouling characteristics of various ashes, they may be insufficient for optical characteristics because of

significant variation of chemical composition from particle to particle. Computer Controlled Scanning Electron Microscopy and associated Energy Dispersive X-ray Spectroscopy (CCSEM/EDS), an established semi-quantitative microanalytical tool, was used to determine the chemical composition of individual ash particles for statistically significant sample sizes (>1000 particles). Deagglomerated samples on SEM stubs were prepared by freeze-drying a suspension of ash in acetone that had been ultrasonically dispersed.

The CCSEM data confirmed that there were significant variations in composition from particle to particle. However, no significant size-composition correlation was seen in any of the ashes. Composition distribution functions were formulated to represent the distribution of each of the four major oxides (SiO_2, Al_2O_3, Fe_2O_3, and CaO). To quantitatively describe ash heterogeneity, chemical composition classes were created for each ash. The fractional mass of the dominant oxide (SiO_2 for all ashes except Eagle Butte, for which it is CaO) was used as the basis for the classification scheme. The ranges of the major oxide present in each of the five classes are ($\bar{X}_o \pm s_o/4$), ($\bar{X}_o + s_o/4$, $\bar{X}_o + s_o$), ($> \bar{X}_o + s_o$), ($\bar{X}_o - s_o$, $\bar{X}_o - s_o/4$), and ($< \bar{X}_o - s_o$), where $\bar{X}_o$ and s_o are respectively the mean and standard deviation of the distribution of the major oxide[‡]. The average composition, in terms of the twelve oxides in each class, was obtained from the CCSEM data. Each class was assigned an appropriate volume fraction, and the size distribution of the whole ash[§]. Using correlations of (n, k) with compositions of bulk slags developed by Ebert (1993) and Goodwin (1986), refractive index classes were developed from these chemical composition classes. Mie scattering calculations for the refractive index classes yield five sets of absorption and scattering coefficients at each wavelength of interest. When weighted by the volume contributions of the classes, the sums of the coefficients represent the radiative properties (α_λ, σ_λ) of the ash.

Slags were prepared by quenching ash melts. Their bulk compositions, accurately obtained from electron microprobe analysis, compared favorably with results published by PSI (1990) and those provided by Foster-Wheeler, as well as those determined by CCSEM. Such cross-checks at all stages of the characterization work not only helped to test the reliability of the data, but has also revealed artifacts hitherto unreported in literature. For example, it was found that size distributions obtained from CCSEM image analysis underpredicted the breadth of the size distribution and overpredicted the median diameter (An explanation is given in Chapter 4).

Comparison of the bulk composition with the CCSEM composition also shows that more

[‡]Many of the oxide distributions were found to be close to normal (Gaussian) distributions.

[§]This is a reasonable assumption because of the absence of any significant size-composition relationship.

than half of the total Fe_2O_3 in the six ashes is present in particles that are significantly larger than the median diameter (>20 μm). This observation, along with the dominance of scattering over absorption/emission (in the near-infrared wavelength range where Fe_2O_3 has absorption bands), indicates that Fe_2O_3 plays a smaller role in radiative transfer compared to the case where Fe_2O_3 is distributed more uniformly throughout the ash.

To determine the refractivity (n) of an ash particle of known composition using available correlations, its density must be known accurately. A 'mixture' rule was adopted to obtain densities of individual ash particles using *effective* densities of each of the major constituent oxides. The effective densities of an oxide, when present in glasses of various compositions, are available in the literature.

The correlations used to determine the optical properties of the ash classes are valid for specific compositional ranges of SiO_2 ($\gtrsim$ 10%, by mass) and Fe_2O_3 ($\lesssim$ 20%). Additionally, data on the infrared optical constants over relevant wavelength ranges are available for six of the twelve oxides detected in the ash. Hence, the correlations are, strictly speaking, not applicable for ash particles which contain a significant fraction of any of the remaining six oxides, say >20% by mass. Ignoring these oxides means assigning them the average optical properties. While this averaging may be acceptable in the 1–8 μm range, it is not applicable to the anomalous region, where the *absolute* silica content determines the optical constants. However, in most ashes, at least four of the five classes (with the exception of the class with the lowest silica content) satisfy the validity requirements of the correlations.

In the second part of the dissertation, a controlled, bench-scale experiment was designed to measure the transmittance of suspensions of the characterized ashes. The ash was dispersed in liquid media to achieve proper deagglomeration, and an ash loading that is both steady and sufficiently high to produce measurable extinction in a short path. Since the measurements were made at room-temperature, there was no complication introduced from radiation emitted by the ash or the suspension medium, as there is for measurements under combustion conditions. The premise behind this experimental test is that if the measured infrared radiative properties of a well-characterized ash, suspended in a liquid at room temperature, can be accurately modeled by Mie scattering calculations, then similar calculations will also reliably predict the radiative properties of the same ash at high temperatures in a coal combustor. Provided correct spectral quantities are used (i.e., the size parameters and optical constants of ash particles are calculated *relative* to the liquid, not vacuum), and measurements are not made close to strong absorption bands of the liquid,

the above analogy should be valid.

Different sensitivities are introduced in performing the experiment on a liquid suspension rather than in gaseous one. They are summarized below, and are further discussed later in this chapter.

- Because $n_r(\lambda)$ (the spectral refractive index of the ash relative to the liquid) is near unity, scattering is reduced relative to absorption. Even so, scattering is still dominant except in the silica absorption band (8–11 μm).
- The reduced scattering makes it easier to measure small absorption that would otherwise be obscured by scattering.
- At the Christiansen wavelength, where $n_r(\lambda) \rightarrow 1$, scattering$\rightarrow$0. This makes the measurements very sensitive to heterogeneity of composition of the non-cenospheric component.
- Use of liquid media enhances scattering by cenospheres relative to non-cenospheric component, especially at wavelengths where $n_r(\lambda) \rightarrow 1$.

Thus, the use of a liquid rather than gas actually provides a more critical test of the capability of predicting measured extinction because it makes the experiment more sensitive to certain features of the ash (such as chemical heterogeneity and the presence of cenospheres).

A suitable transmissometer was designed to allow (almost) simultaneous measurement of transmittance through the ash suspension, and through the suspending liquid used as reference. Use of the same BaF_2 windows for both the suspension and the reference chambers of the cell eliminated uncertainties related to window properties. Three liquids were chosen as dispersing media to span the wavelength range 1–13 μm: CCl_4 (in the range 1–6 μm), $CHBr_3$ (6.4–7.4 μm and 11.8–13 μm), and CS_2 (7.4–11.2 μm). These liquids have no strong absorption bands in the relevant ranges, and taken together, they provide a window across the entire wavelength range of interest. Because of a lack of accurate information on the refractive index, $n(\lambda)$, of CS_2 and $CHBr_3$, measurements were made over appropriate wavelength ranges using the near-normal reflectance technique. The accuracy of the measurements was estimated by comparing $n(\lambda)$ obtained for water with published data.

Extensive sensitivity calculations were performed to determine the uncertainty bounds of the measured extinction, E. In the near-infrared wavelength range ($\approx$1–8 μm), E is much

more sensitive to the real part of the refractive index, $n_r(\lambda)$, than to other parameters such as D_v, σ_g, $k_r(\lambda)$, etc. The reason for this high sensitivity to $n_r(\lambda)$ is the dependence of scattering on $(n_r(\lambda)-1)$. Since $n(\lambda)$ for CCl_4 is not very different from that of the ash particles in this wavelength range where scattering is the dominant component of extinction, small changes in $n(\lambda)$ of the ash cause large changes in $(n_r(\lambda)-1)$, and hence in E. Clearly, the uncertainty in predicting transmittance is much smaller for ash dispersed in the gaseous medium of a combustor. In the range 8–13 μm which contain the absorption bands of SiO_2, E is sensitive to both $n_r(\lambda)$ (although to a lesser degree), and $k_r(\lambda)$.

Extinction measurements were made on four of the six ashes chosen to cover a variety of coal ranks and ash characteristics: Upper Freeport (bituminous, high iron, and $\approx$25% cenospheric, by mass), Eagle Butte (sub-bituminous, high calcia, and containing few cenospheres), Beulah (lignite, high iron, and of relatively low cenospheric content), and San Miguel (lignite, low iron, almost entirely cenospheric).

For cenospheres, scattering at the ash–void interface is considerably greater than at the liquid–ash interface. Hence, in this experiment, the cenospheric fraction contributes a larger fraction of the total extinction compared to ash dispersed in gases. In the latter case, scattering at both surfaces of the cenospheres' shells are of comparable magnitude. Mie scattering calculations for cenospheres, a large fraction of which contain irregular, eccentric, and multiply-connected voids, are not feasible. However, since cenospheres are predominantly large and thin-walled, a reasonable first approximation model for cenospheres dispersed in a liquid medium is that of air bubbles. Calculations for air bubbles in CCl_4, both in the Mie regime and in the diffraction limit (where $Q_{e,\lambda} \simeq 2$) were successful in explaining the relatively flat spectral transmittance of the two ashes with significant cenospheric content, San Miguel and Upper Freeport, when compared with predictions made ignoring the presence of cenospheres.

In the experiment, the effect of ash heterogeneity was very pronounced in the range λ=3–6 μm, where $n_r(\lambda)$ passes through unity for the vast majority of the ash particles. Use of an average ash composition to predict extinction is misleading because σ_λ becomes zero at $n_r(\lambda)$=1. In reality, particles of different compositions attain the extinction minimum at different wavelengths, resulting in a much flatter spectral transmittance in this wavelength range. The observed transmittance was predicted more accurately by adding the individual extinctions by ash fractions in each of five refractive index classes.

In the range 8–13 μm, the ashes exhibited two distinct types of spectral behaviour. The

high-silica ($\gtrsim$ 50% by mass) ashes, Upper Freeport and San Miguel, showed a single broad absorption band centered at $\sim 9\ \mu m$, which is accurately modeled using high temperature optical property data presented by Ebert (1993). In contrast, room temperature measurements made on slowly cooled slags (Goodwin, 1986) indicate the presence of two absorption mechanisms, *viz*, the stretch vibrations of the bridging and the non-bridging oxygen in SiO_2. This difference suggests that the high quench rates typical of molten ash droplets result in a glass structure which is closer to that of the melt than that of a slowly cooled glass. Such structural differences based on quench rates have been noted by Mysen *et al* (1985).

A significant fraction of oxygen atoms in the two low-silica ashes, Eagle Butte and Beulah are non-bridging (SiO^-). Their spectral extinctions show two distinct absorption bands. For the Eagle Butte ash, the broad band at the longer wavelengths (10.0–10.5 μm) is predicted, but the current model fails to explain the other band centered at $\sim 9\ \mu m$. This band is characteristic of absorption by the bridging oxygen, Si–O–Si, in high silica ashes. However, these ashes contain few silica-rich particles. Despite this anomaly, the extinction profiles for these two ashes are accurately predicted over most of the wavelength range.

Clearly, one direction in which our understanding of ash optical properties could be usefully enhanced is through the study of low silica-high calcia and high-alumina glasses. By expanding the database of optical constants of synthetic slags, more accurate correlations for $n(\lambda)$ and $k(\lambda)$ could be obtained for ashes with a much wider range of composition. As suggested by Ebert (1992), a convenient method for measuring optical constants of a large number of slags may be to quench melts very rapidly (>100 K/s), and then make FTIR measurements at room temperature, preferably in vacuum to eliminate interference by water and carbon dioxide absorption bands. Also, fundamental studies on the optical properties of amorphous Na_2O and K_2O are needed for more accurate modeling of ashes such as Beulah[¶]. Since glass structure, and hence ash optical properties, depend on the rate of cooling, basic studies on the effect of quench rate on the structure of aluminosilicate glasses are also desirable.

In Chapter 3, an inverse relationship between D_n and σ_g was observed. From the viewpoint of ash formation mechanics, it makes physical sense that increased coaelescence of molten mineral matter on char surface leads to larger and narrow ash size distributions. If this relationship is confirmed through more detailed size studies, then it should be incorporated into current ash formation models.

[¶]In the Beulah ash, these two oxides make up $\approx$8% of the mass.

Since cenospheres constitute a significant mass fraction in some ashes, a relatively simple model needs to be developed to account for scattering (and to a smaller extent, absorption) by this fraction. Mie solutions for coated spheres[‖], described by Bohren and Hoffman (1983), might be used as a starting point. CCSEM analyses of the cenospheric and non-cenospheric fractions might be carried out to determine whether their compositional differences are significant.

The practical problems related to optical measurements at combustor temperatures (even in an inert gaseous medium, let alone gases that are combustion products) are formidable. They include difficulties related to ash dispersion, ash load fluctuations, collection of radiation emitted by hotter upstream particles scattered into the detection path, which make it very difficult to obtain reliable results. The set of transmittance measurements presented here may serve as a benchmark for future experiments in this direction.

To summarize, the primary result made available by this work are sets of spectral optical constants that describe the radiative properties of six fly ashes generated by pulverized coals typically burnt in power plants in the U.S. The overall conclusion is that Mie calculations can be used to reliably predict overall ash radiative properties on a spectral basis provided the ashes are adequately characterized. The various aspects of the characterization technique have been documented in considerable detail (e.g., in Appendices D and G), making possible future application to other ashes. Some related conclusions and achievements are listed below.

- A method for sizing insulating powders of broad size distribution (diameter $\gtrsim 1\ \mu m$) using the Coulter Multisizer, and characterizing the distribution by a truncated log-normal function was developed.
- Detailed information was obtained in regard to the size–density relationship for the ashes.
- The cenospheric content of the ashes was determined by density separation.
- A freeze-drying method was refined to prepare well-deagglomerated ash samples for SEM study.
- The variation of ash composition from particle to particle was quantified, and composition classes were created to reflect this heterogeneity.

[‖]i.e., sphere composed of two concentric but different dielectrics.

- A large fraction of iron in the ash is found to be present in a small fraction of large particles. Consequently, prediction of total iron content based on CCSEM studies may significantly underestimate the true value.
- The refractive indices of CS_2 and $CHBr_3$ were measured in the wavelength ranges 7–11 μm and 1–13 μm, respectively, where no literature data was available.
- A transmissometer was designed, constructed, and used to measure extinction over short path lengths.

Appendix A

Experimental Study of the Coulter Multisizer

This Appendix describes the results of tests carried out on the Coulter Multisizer to determine the lower limit of size measurement, the precision, and the effect of measurement conditions such as particle concentration, sample size, etc. It was noted in Chapter 3 that all information pertaining to ash size distribution is contained in four numbers, *viz*, the two parameters of the truncated lognormal function (D_v, σ_g), and the limits of size measurement, (a, b). Hence, all tests are conducted using the same orifice (100 μm) and on the same suspension sample (wherever applicable) of Kentucky #9 ash. Conclusions are reached after comparing (D_v, σ_g) for various cases.

Figure A.1 presents a closer look at the Multisizer orifice. The orifices are accurately machined cylindrical apertures in a sapphire wafer set in a glass frame. The orifice 'tubes' used here have wafer thickness (L) to aperture diameter (D) ratio of $\approx$0.75:1 except for the 30 μm and 50 μm orifices, where the ratios are $\approx$1.5:1 and $\approx$1:1, respectively.

It can easily be shown (see, e.g., Allen, 1981) from geometrical considerations*, and from the definition of resistivity, that the change in resistance of the orifice, ΔR, due to the particle passing through it is given by

$$\Delta R = \frac{\rho_f}{A^2} \left(\frac{1}{\frac{1}{1-\rho_f/\rho_s} - \frac{a}{A}} \right) (a\,\Delta l)$$

*The spherical particle is approximated by a volume-equivalent cylindrical particle to avoid solving the three dimensional electrical problem

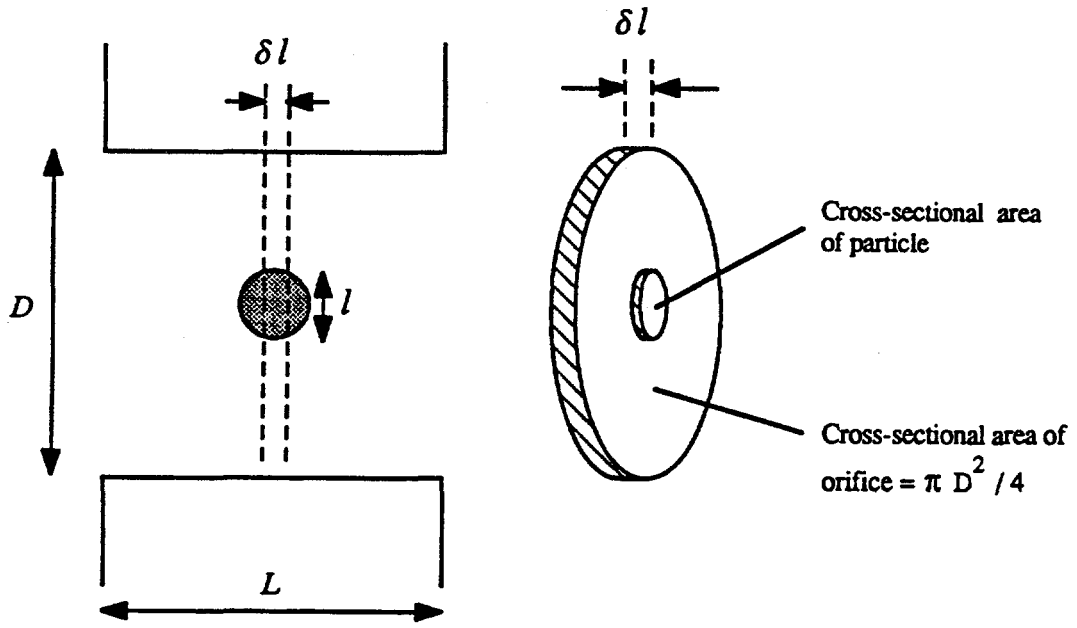

Figure A.1: Schematic of the Coulter Multisizer Orifice.

Here ρ_f/ρ_s is the ratio of fluid to particle resistivities. If $\rho_s/\rho_f \rightarrow 0$, as in the case of insulating particles in an electrolyte, then ΔR (and, hence, the voltage signal, for constant current supply) is proportional to the differential particle volume ($a\,\Delta l$), modified by the term a/A.

$$\Delta R = \frac{\rho_f}{A^2}\left(\frac{1}{1-\frac{a}{A}}\right)(a\,\Delta l)$$

For $(a/A) \ll 1$, binomially expanding the denominator yields

$$\Delta R = -\frac{\rho_f}{A^2}\left(1+\frac{a}{A}\right)(a\,\Delta l)$$

And thus

$$\Delta R \propto (a\,\Delta l)$$

This proportionality between the change in resistance and the elemental volume continues to be applicable after integration over the particle volume.

The linear relationship between signal and particle volume is strictly valid for small values of a/A. In practice, the Multisizer unit counts particles of diameter up to $\approx$60% of the orifice diameter (i.e., $a/A = 0.36$). The actual cut-off diameter varies with orifice size, from a minimum of 62.5% for the 70 μm orifice to a maximum of 74.5% for the 30 μm orifice.

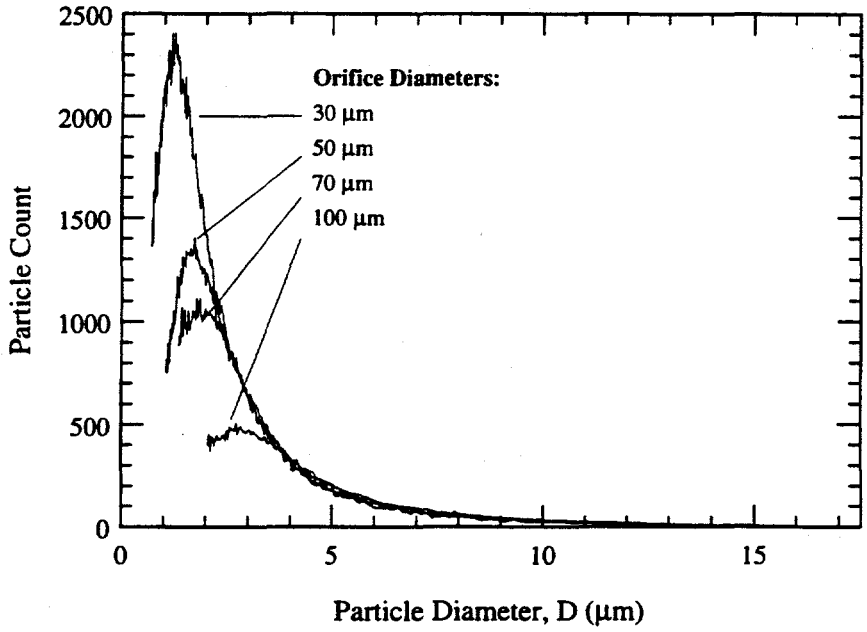

Figure A.2: Differential size distributions of Illinois #6 ash obtained with five different Multisizer orifices. The ordinate shows the number of particles sampled in each size channel.

A.1 Lower Limit of Size Measurement

While the upper limit of size measurement is set by the departure from linearity between the voltage signal and the particle volume, it is suggested in the literature that the lower limit is set by the signal-to-noise ratio (Allen, 1981; Coulter, 1986). The nominal lower limit is stated by the manufacturer as 2% of the diameter of the orifice, although this limit varied slightly from 1.96% for the 70 μm orifice to 2.33% in the case of the 30 μm orifice.

To test the specified lower limit, a sample of Illinois #6 baghouse ash was sized using four orifices of diameters 30, 50, 70 and 100 μm. The ash was initially sieved using the wet-siever (described in Section 3.4.2) with mesh size of 16 μm to prevent blockage of the smaller orifices by larger particles. The four differential size distribution functions, which are measures of the number of particles per differential size range dD at diameter D, were determined using the Multisizer. Since the four orifices measure the same ash dispersion, the measured distributions should, in principle, differ only by a constant multiple. Hence, the data were normalized by equating the number of particles of a certain size (in this case 4 μm), where sufficient numbers of particles were present for all four data sets.

Figure A.2 shows the size distributions on a differential basis. The total sample size

for each orifice was approximately 150,000. Quite correctly, the curves fall to zero near $D = 16\ \mu m$. Within the limits of instrumental accuracy, and statistical uncertainty associated with sample size, the plots show that each orifice gives accurate results down to $D_{particle} \approx (0.035)D_{orifice}$. At $D_{particle} \approx (0.03)D_{orifice}$, each curve shows a maximum count, and then decreases for smaller diameter, i.e., the mode of the distribution shifts to smaller diameters with decreasing orifice diameter. This trend indicates that the Multisizer sensitivity decreases for $(D_{particle}/D_{orifice}) < 0.035$, i.e., it does not record all the signals. It is apparently not a question of signal/noise because if noise pulses were being recorded the count rate would increase. Therefore, we conclude that the manufacturer's recommended minimum size measurement limit (2% of $D_{orifice}$) is understated and that the smallest particle which can be accurately measured is closer to 3.5% of $D_{orifice}$. The minimum particle diameter measured by our smallest orifice of diameter 30 μm was 1.2 μm—sufficiently small for our purpose.

A.2 Statistical Estimate of Repeatability

Assuming that the particle suspension is distributed uniformly throughout the sampling beaker, the statistical accuracy with which the sample's size distribution represents that of the original suspension depends mainly on the sample population size and, to a lesser extent, on the nature of the size distribution[†]. Additionally, the sample size also affects precision, i.e., $D_{50\%}$ of a set of data with a large population per sample will be closer to each other than those of a data set with significantly smaller population per sample. In practice, size distributions are obtained from a single measurement of sample size that is reasonably large (100,000–200,000 particles).

A measure of the statistical limitation imposed by a specific sample size can be obtained by calculating the repeatibility or precision with which the median diameter, $D_{50\%}$, can be measured. To this end, thirty successive size measurements of sample size ≈100,000 were made on the same suspension. From the Central Limit Theorem[‡] we know that when the number of measurements, n, is very large, the average of the means, $\bar{D}_{50\%}$, approaches the actual $D_{50\%}$ of the suspension. Additionally, this distribution of the means is approximately

[†]This is strictly from statistical considerations, and does not take into account possible inaccuracies inherent in the measurement process itself, such as non-proportionality of signal with particle volume, and coincidence error.

[‡]A more detailed discussion of the Limit Theorem and other statistical issues can be found in Appendix 8 in connection with the analysis of CCSEM data.

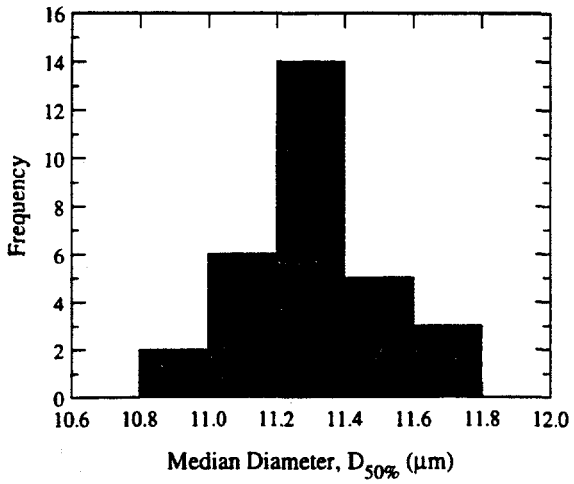

Figure A.3: The distribution of volume median diameter, $D_{50\%}$, of thirty sets of size data obtained successively from the same sample (of Kentucky #9 ash) in the Multisizer beaker, using an orifice of diameter of 100 μm. The mean and standard deviation of $D_{50\%}$ are $\bar{D}_{50\%}$=11.32 and $\sigma_m = 0.18$, respectively.

normal with a standard deviation, σ_m, that approaches $\sigma/\sqrt{n}$ for large values of n. Here σ is the standard deviation of the suspension's size distribution. Of course, apart from n and σ, the variation of $D_{50\%}$ will also be affected by other factors such as size of individual sample, electronic noise, coincidence error, etc. Hence, it is appropriate to define an instrument precision using σ_m, based on a limited number of repeat measurements, for a typical sample size, and operating conditions.

The bargraph in Figure A.3 shows that the distribution of $D_{50\%}$ does resemble a normal distribution for the test with $n = 30$. Using the value of σ_m and from considerations of the three-sigma bounds, one can conclude that in 99.7% cases, the value of $D_{50\%}$ obtained from one measurement is within $\pm 1.1\%$ of the 'actual' volume median diameter of the suspension. When best-fit lognormal functions are fitted to these thirty distributions, the corresponding precisions for D_v and σ_g are found to be $\pm 1.1\%$ and $\pm 0.6\%$, respectively.

Clearly, all measurements that test the effect of varying any of the Multisizer operating parameters (sample size, concentration, etc.) must be repeated several times for statistically acceptable conclusions. However, only one measurement per test case was considered practical in most cases. It was decided, somewhat arbitrarily, that the effect of varying an

operating condition is significant only if the range[§] of values of lognormal parameters obtained from the data is considerably larger (say, >5%) than the repeatability range (2.2%).

A.3 Coincidence Correction

The Coulter principle assumes that at any given moment during the sizing process, there is only a single particle in the electrical sensing zone (a space extending somewhat beyond the orifice volume). However, there is always a finite probability that more than one particle may pass through the sensing volume simultaneously. This probability, P_n, that there are n particles simultaneously in the sensing zone, can be represented by the Poisson distribution.

$$P_n = \frac{m^n}{n!} e^{-m}$$

Here, m is the average number of particles (in the suspension) in a volume equal to that of the sensing zone, i.e., $m = N\,A\,L$, where N is the particle concentration per unit volume. P_n has an exponential dependence on m and

$$\frac{P_n}{P_1} = \frac{m^{n-1}}{n!}$$

Consequently, the probability of pairs, triplets, etc., passing simultaneously through the orifice can be drastically lowered by the use of sufficiently dilute solutions ($m \ll 1$). However, a high degree of dilution has the adverse effects of raising the sampling time to impractical levels, and necessitating background subtraction, which may not be possible in some circumstances. In practice, it is found that conveniently high loadings that result in coincidence errors/loss of 5–10%[¶] can be used to accurately predict size distribution if corrections based on statistical corrections are incorporated. The electronic unit of the Multisizer makes these corrections in the form of an inverse problem after accurately sensing the particle loading, i.e., given the ash loading and the size data with coincidence errors upto 20%, it can calculate the original distribution.

Tests of the effect of varying the suspension concentration showed no change of the lognormal function parameters in the range 2%–8% coincidence error. However, above ≈8% coincidence error, D_v increased and σ_g decreased steadily. At 20% level, D_v and σ_g were respectively ≈10% above and ≈10% below the values obtained with the dilute suspensions. This trend is to be expected since the smaller particles comprising the bulk of the ash by

[§]Range=(Maximum value−Minimum value)/Average value

[¶]A coincidence error of 5% implies that the sample size is undercounted by 5%.

count, are more prone to coincidence error, thus decreasing the range of detected particle sizes (and hence a smaller σ_g). Since two or more small particles may be detected as one large particle, the value of D_v increases. Another effect that tends to shift the distribution curve slightly towards larger diameters is the occurrence of pulses above the threshold limit that are actually the sum of two or more pulses that are individually below the limit, caused by the simultaneous passage of two particles very close to each other.

Although the Multisizer handbook indicates that coincidence errors as high 15% can be corrected, the above data confirms the observations of Allen (1981) that the coincidence correction should be kept well below 10% and preferably close to 5%.

A.4 Miscellaneous Tests

To test the effect of sample size, the lognormal function parameters were obtained for size data of nominal samples sizes 25,000, 50,000, 100,000, 200,000, and 400,000. While σ_g was independent of sample size, the values of D_v increased progressively in the first three cases, probably because the sample sizes in the first two cases were too small to detect sufficient numbers of the larger particles. Based on these results, it was concluded that sample sizes in the range 100,000–150,000 were acceptable. It is noted that the corresponding 'raw count' range is 200,000–300,000 for two reasons. For unexplained reasons, the raw count reported by the Multisizer's electronic unit was $\approx$35% higher than the total count in all the size channels. Additionally, raising the lower limit of measurement to $\approx$3.5% of the orifice diameter results in rejection of another 10–15% of the particles.

The importance of ultrasonic deagglomeration was confirmed from several tests in which (a) the ash sample was directly added to the Multisizer beaker without deagglomeration, (b) an ash suspension was separately deagglomerated manually using a stirrer, and (c) same as (b) with the addition of a few drops of surfactant. In all these cases, the resulting D_v was 10–15% higher than that obtained with a well deagglomerated sample (ultrasonically agitated after adding surfactant). The value of σ_g was insensitive to the sample preparation, probably because sufficient numbers of the small particles are always deagglomerated from the larger particles by fluid mechanical action.

The suspension in the Multisizer beaker was found to be very homogeneous from size data obtained with the orifice at varying horizontal and vertical positions, except close to the liquid surface (and away from the stirrer), where there appeared to be a paucity of

larger particles.

Each ash sample, obtained originally in quantities in excess of two pounds, had been stirred in its dry agglomerated state to ensure homogeneity. Size distribution of samples obtained from five different parts of the storage container showed no difference in lognormal parameters. Neither did the parameters corresponding to size data obtained with four separate samples taken from the same deagglomerated suspension.

Appendix B

Density Classification by Centrifugal Separation

Experiments on centrifugal separation of controlled mixtures* revealed that there is a systematic carryover of a portion of the denser fraction into the lighter fraction. This occurs because of the fluid-mechanical entrapment of heavier and smaller particles among the lighter and larger particles. While the extent of this carryover depends somewhat on the size and composition distribution of the powder, it was determined that the sample loading was, by far, the most important factor. The carryover decreased significantly with decreased loadings (i.e., with more dilute suspensions). However, very small samples result in proportionately greater errors in striking a mass balance. Additionally, very dilute suspensions make it impractical to separate sufficient quantities of ash. Balancing these contrary factors, it was decided to use ash loadings of ~0.6 mg per ml of liquid (i.e., volume loadings of $\approx 2.5 \times 10^{-3}$, for an average ash density of 2.5 g/cc)†.

Several tests were carried out which caused us to modify the standard centrifugal separation technique described by Browning (1961). It was found that ultrasonic deagglomeration of the suspension, gravitational settling preceding centrifugal separation, and a low rate of increase of particle acceleration, all contributed to more accurate separation. In powders similar to fly ash, whose chemical composition (and, hence, density) varies significantly from particle to particle, the fraction with density very close to that of the separation liquid

*Using chemicals of different densities and color such as copper sulfate and magnesium powders.

†This loading is an order of magnitude higher than loadings typically used in the transmittance measurements

may finally be collected in the either the float or the sink. This uncertainty may finally be the limiting factor for separation accuracy, especially, if the ash contains a significant mass fraction of particles with density in the vicinity of the liquid density.

The following sequence of steps describes the centrifugal separation process used for density classification:

1. Ultrasonically disperse 0.5 g of ash in 80 ml of liquid, with a few drops of surfactant to aid deagglomeration. Divide it equally between the two 50 ml centrifuge tubes.
2. Place the tubes in the shields and insert the latter in the trunnion rings attached to the arms of the centrifuge. Gently stir the suspension with a thin spatula and allow for ten minutes of gravitational settling.
3. Turn on the centrifuge and gradually increase the speed of rotation to the maximum[‡] over a period of one minute. Stop after five minutes.
4. Gently stir the float material to free any denser particles that may have got trapped. Repeat (3) for four minutes.
5. Decant the top two-thirds of the liquid into a previously dried and weighed filter cone.
6. Add more liquid to the tubes to the initial level and repeat (3) for three minutes. Now decant all the liquid into the filter paper used in (5).
7. Extract the sink material, now embedded at the bottom of the tubes using a jet of acetone or ethanol, and pour it into another filter paper[§].
8. Dry each filter paper with its ash in an oven, and enclose it in an airtight plastic bag.
9. Weigh and calculate the separated ash masses.

The entire operation takes about thirty minutes. The process is speeded up by the use of additional pairs of centrifuge tubes and of a vacuum pump to aid filtering. Because the density of most of the ash falls in the range 2–3 g/cc, the liquid of density 2.4 g/cc is used for initial separation. Centrifugal separation is next performed with liquids of density 2.0 g/cc and 2.8 g/cc on the float and sink respectively. Separation is carried out in this manner for the other density classes. Repeated separations are performed until a minimum of 1 g of

[‡]A maximum speed of 2000 rpm corresponded to an acceleration of ≈1000 g for the centrifuge used.
[§]Previously dried and weighed.

ash is available for the subsequent centrifugal separation processes. The reproducibility of the separation process varies from class to class; 2–3% for density classes containing >25% of the ash mass to 10–15% for classes containing <5% of the ash.

Appendix C

The Truncated Lognormal Distribution

Consider F_j, the integral of the j^{th} moment of the lognormal distribution, about the diameter x, over all possible diameters:

$$F_j = \int_{-\infty}^{\infty} x^j \frac{1}{\sqrt{2\pi}\ln\sigma_g} \exp\left[-\frac{1}{2}\left(\frac{\ln x/D_n}{\ln\sigma_g}\right)^2\right] d(\ln x) \qquad \text{(C.1)}$$

By successively substituting the variables $u = \frac{\ln x/D_n}{\sqrt{2}\ln\sigma_g}$ and $z = u - \frac{j\ln\sigma_g}{\sqrt{2}}$, C.1 can be integrated to obtain

$$F_j = \exp\left(j\ln D_n + \frac{1}{2}j^2\ln^2\sigma_g\right) \qquad \text{(C.2)}$$

The cumulative j^{th} moment of the truncated lognormal distribution is written as

$$F_j^{(a,b)}(D) = \frac{\int_{\ln a}^{\ln D} x^j \frac{1}{\sqrt{2\pi}\ln\sigma_g} \exp\left[-\frac{1}{2}\left(\frac{\ln x/D_n}{\ln\sigma_g}\right)^2\right] d(\ln x)}{\int_{\ln a}^{\ln b} x^j \frac{1}{\sqrt{2\pi}\ln\sigma_g} \exp\left[-\frac{1}{2}\left(\frac{\ln x/D_n}{\ln\sigma_g}\right)^2\right] d(\ln x)} \qquad a \le D \le b \qquad \text{(C.3)}$$

By dividing the integrand in both the numerator and the denominator of Equation C.3 by F_j (from Equation C.2) and replacing x^j by $\exp(j\ln x)$, Equation C.3 may be put in the form:

$$F_j^{(a,b)}(D) = \frac{\int_{\ln a}^{\ln D} \frac{1}{\sqrt{2\pi}\ln\sigma_g} \exp\left[-\frac{1}{2}\left(\frac{\ln x/\bar{D}_j}{\ln\sigma_g}\right)^2\right] d(\ln x)}{\int_{\ln a}^{\ln b} \frac{1}{\sqrt{2\pi}\ln\sigma_g} \exp\left[-\frac{1}{2}\left(\frac{\ln x/\bar{D}_j}{\ln\sigma_g}\right)^2\right] d(\ln x)} \qquad a \le D \le b$$

where

$$\bar{D}_j = D_n \exp\left(j \ln^2 \sigma_g\right)$$

$F_j^{(a,b)}(D)$, too, is a truncated lognormal distribution with the same geometric standard deviation, σ_g, and a median diameter, $\bar{D}_j$. The Sauter mean diameter, D_{32}, is found to be: $D_{32} = F_3/F_2 = D_n \exp\left(\frac{5}{2} \ln^2 \sigma_g\right)$.

Appendix D

Detailed Ash Size Distributions

Plots of the size distributions of the ashes, on the basis of number, area, and volume (both differential and cumulative), are included in this Appendix. Data for ash fractions with density greater and less than 2.2 g/cc (i.e., non-cenospheric and cenospheric fractions, respectively) are also given.

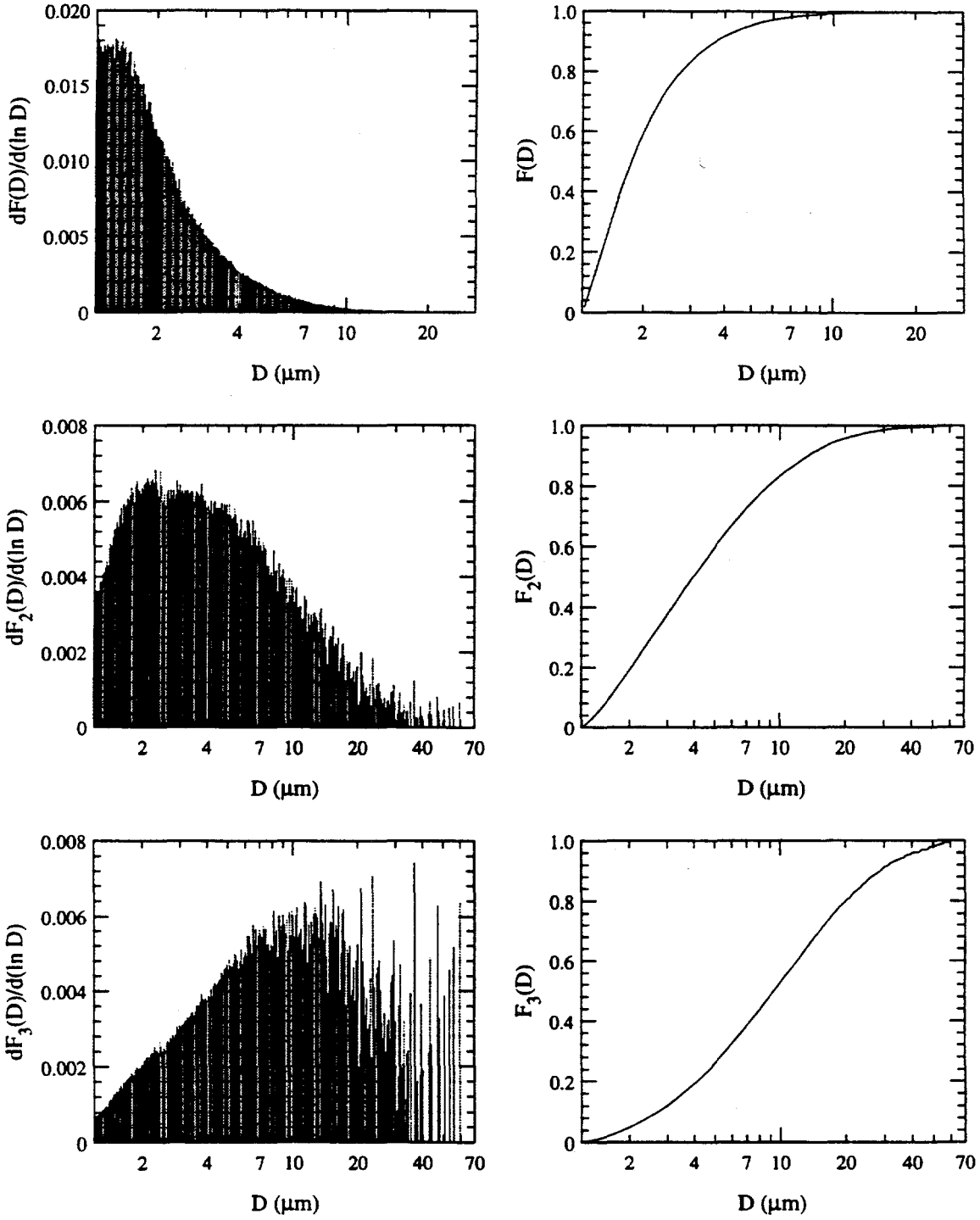

Figure D.1: Differential and cumulative size distributions of Upper Freeport baghouse ash on the basis of number (count), area, and volume. Total particle count = 283,474.

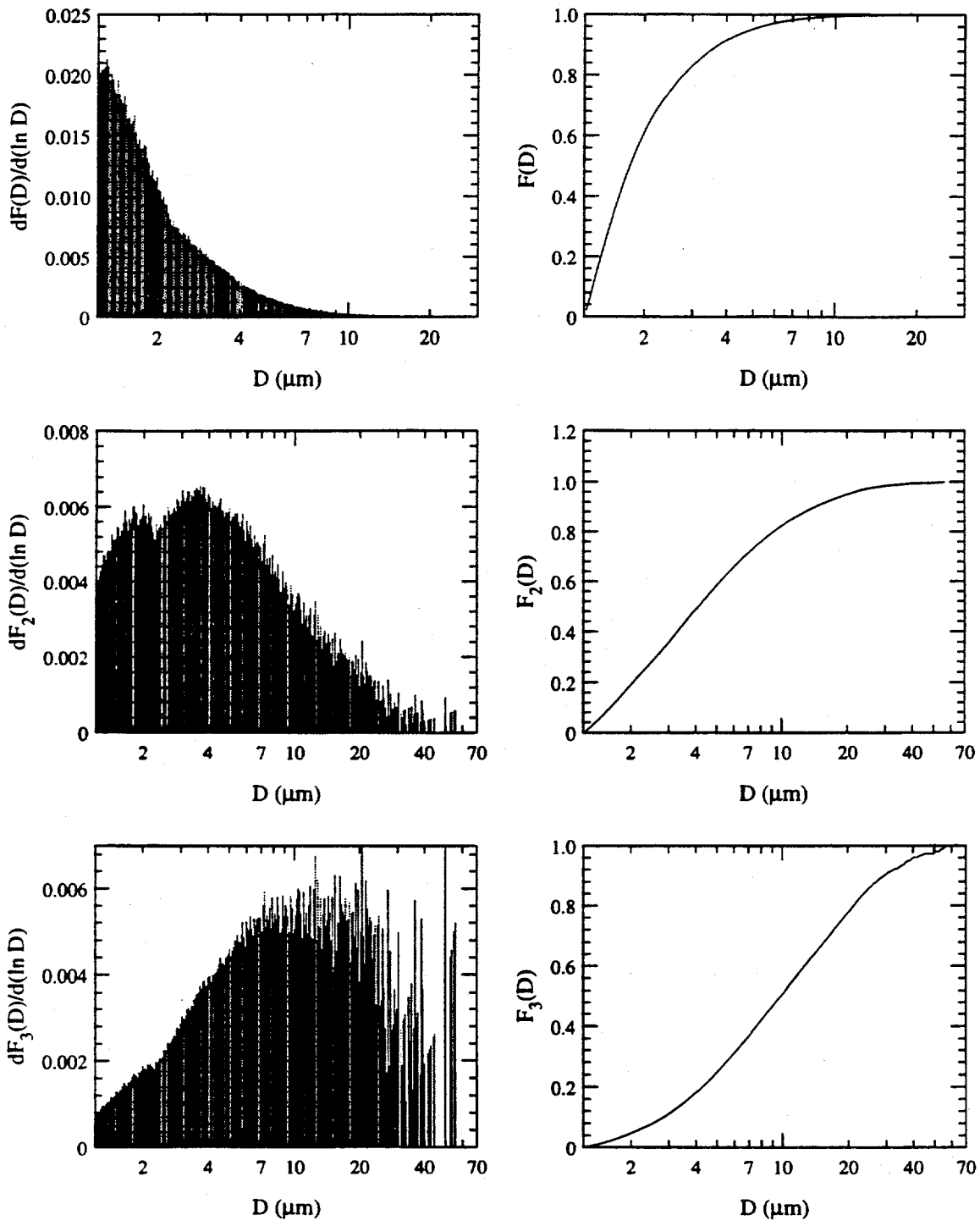

Figure D.2: Differential and cumulative size distributions of Illinois #6 baghouse ash on the basis of number (count), area, and volume. Total particle count = 301,405.

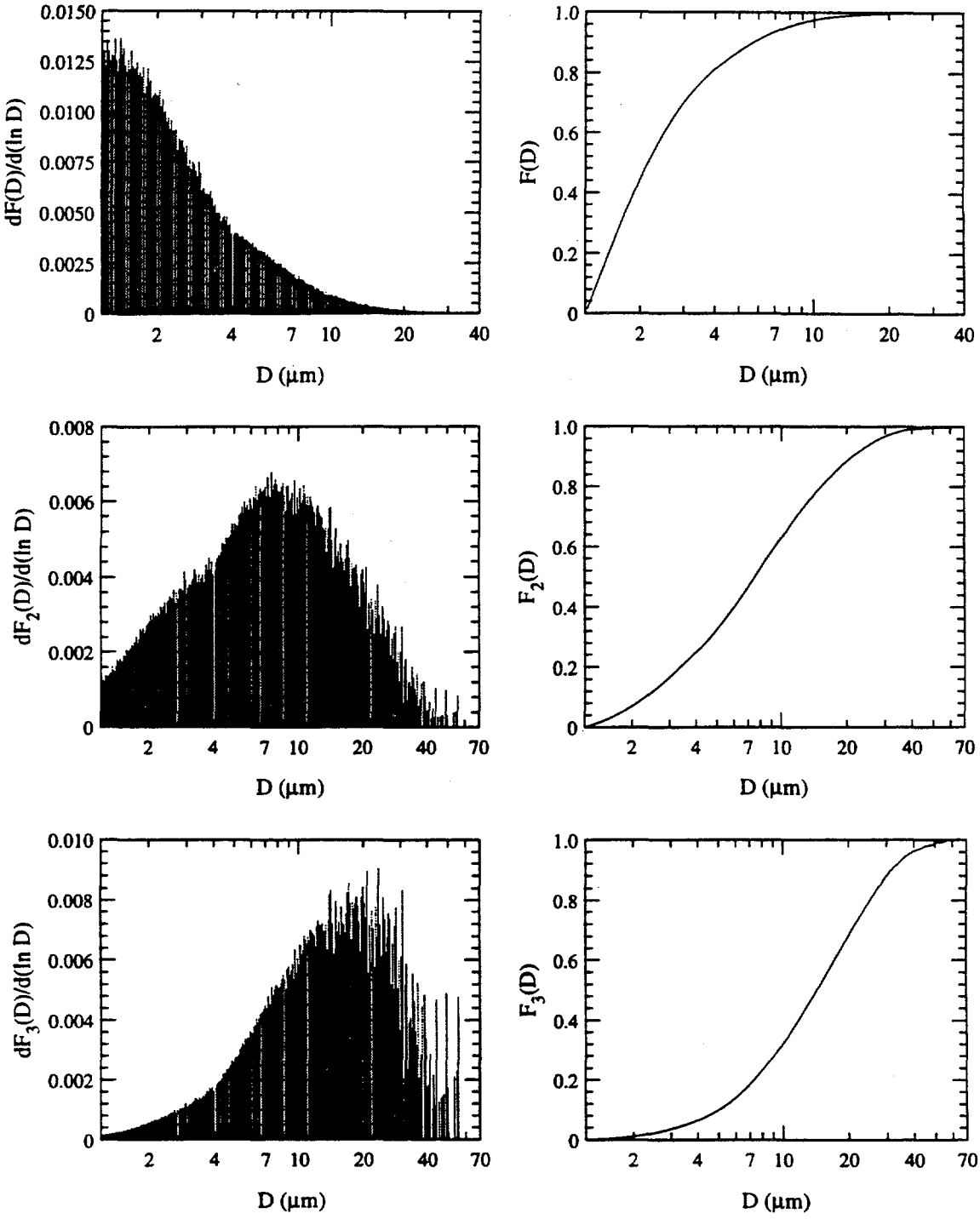

Figure D.3: Differential and cumulative size distributions of Illinois #6 cyclone ash on the basis of number (count), area, and volume. Total particle count = 279,356.

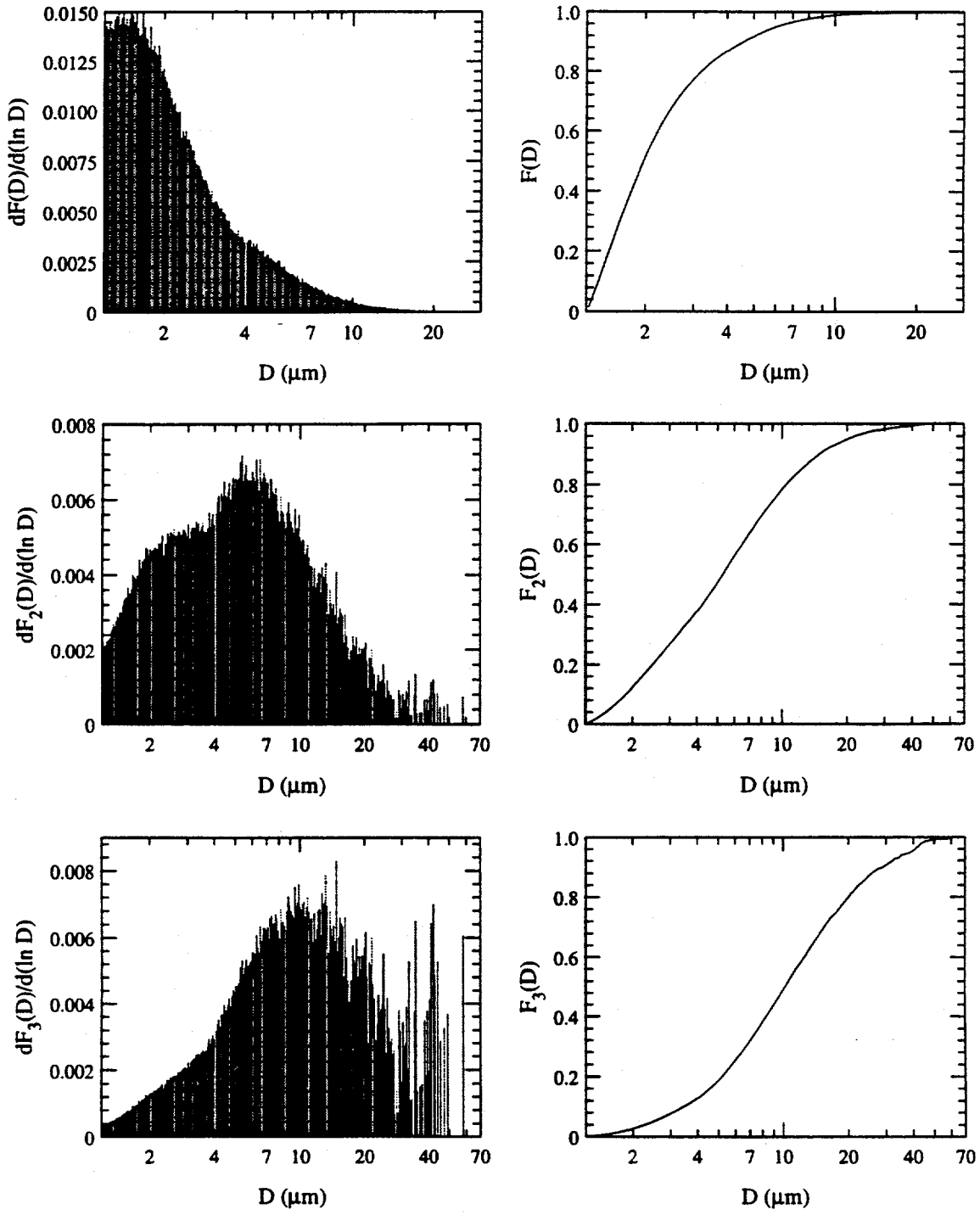

Figure D.4: Differential and cumulative size distributions of Kentucky #9 baghouse ash on the basis of number (count), area, and volume. Total particle count = 355,527.

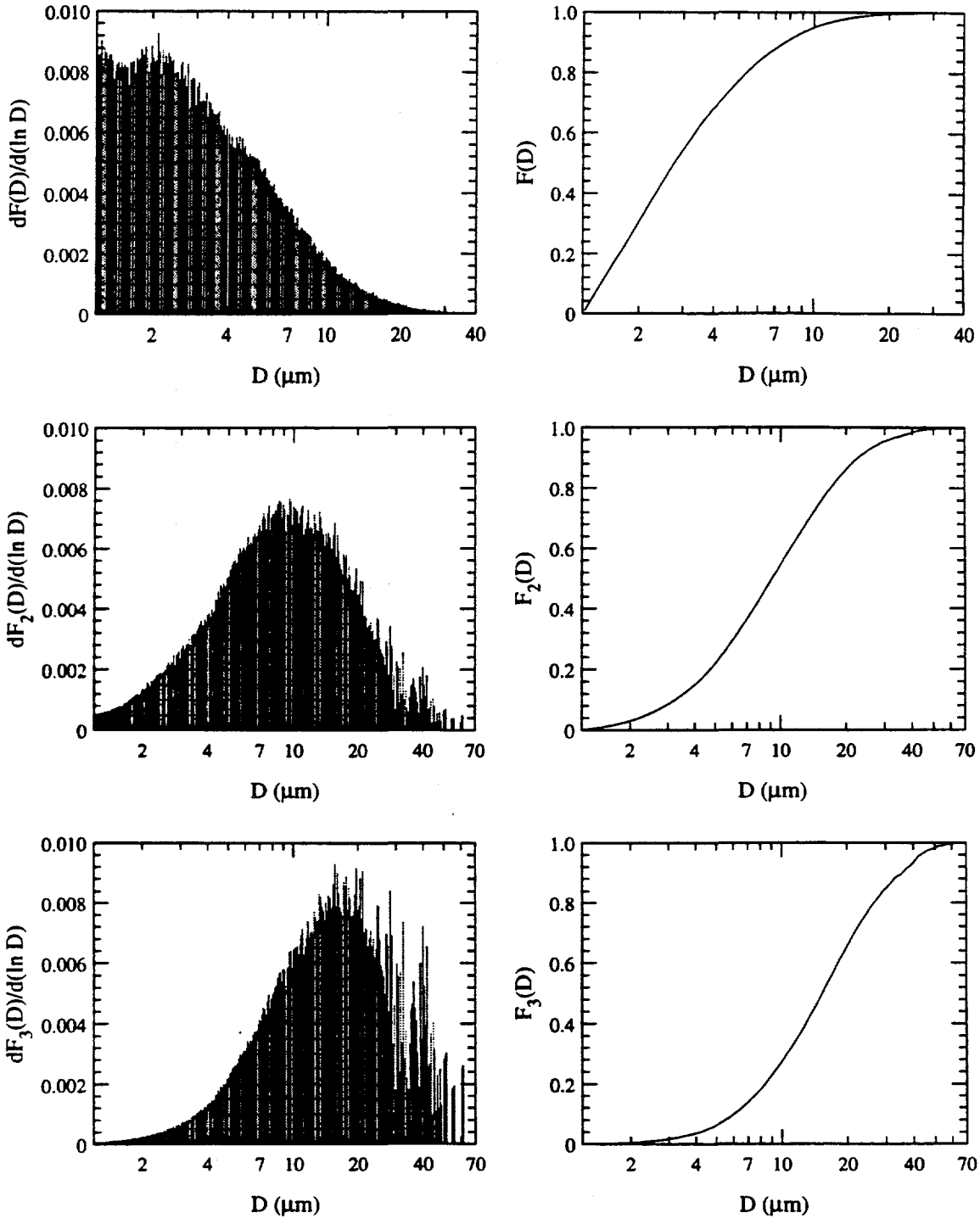

Figure D.5: Differential and cumulative size distributions of Kentucky #9 cyclone ash on the basis of number (count), area, and volume. Total particle count = 287,824.

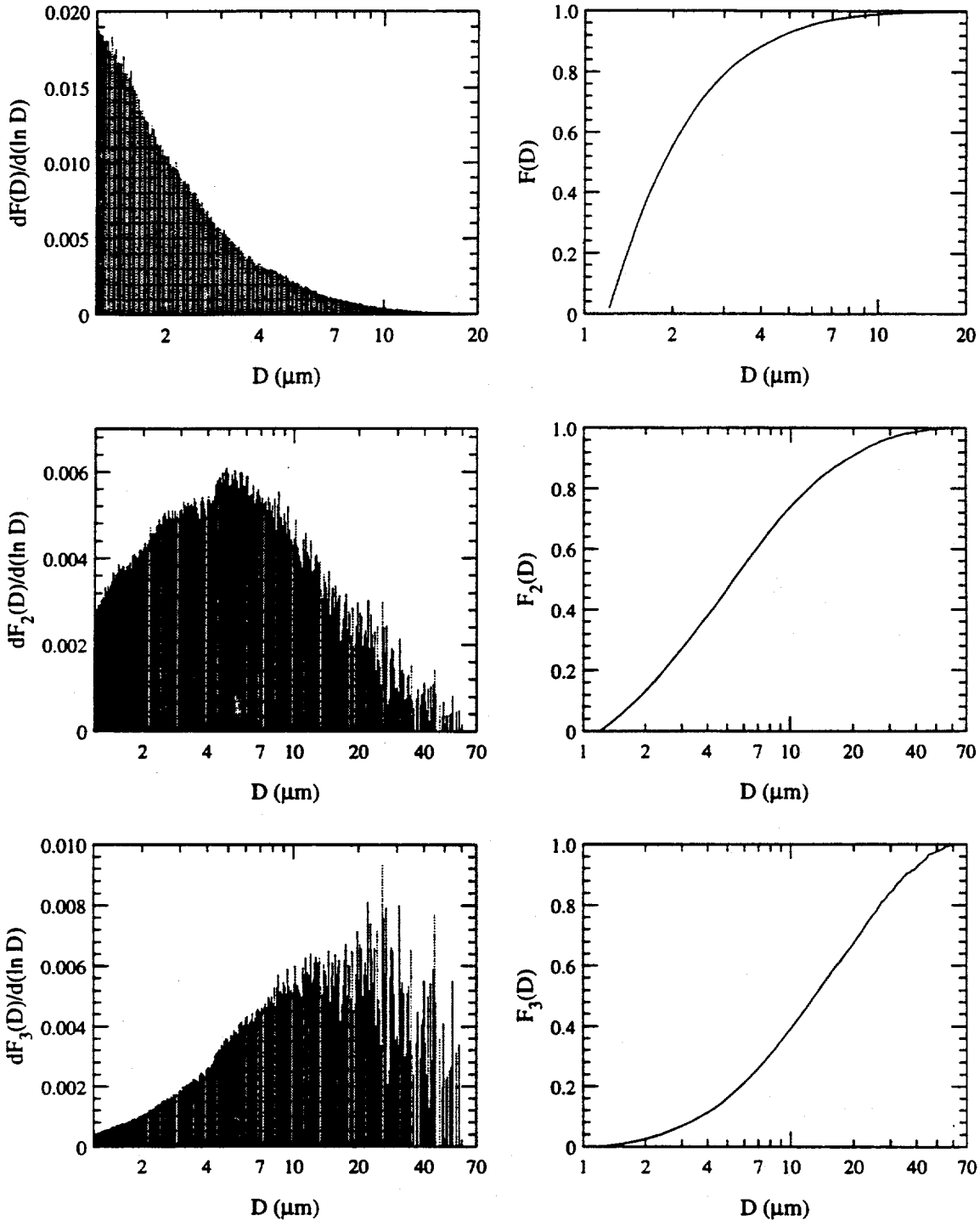

Figure D.6: Differential and cumulative size distributions of Eagle Butte cyclone ash on the basis of number (count), area, and volume. Total particle count = 432,383.

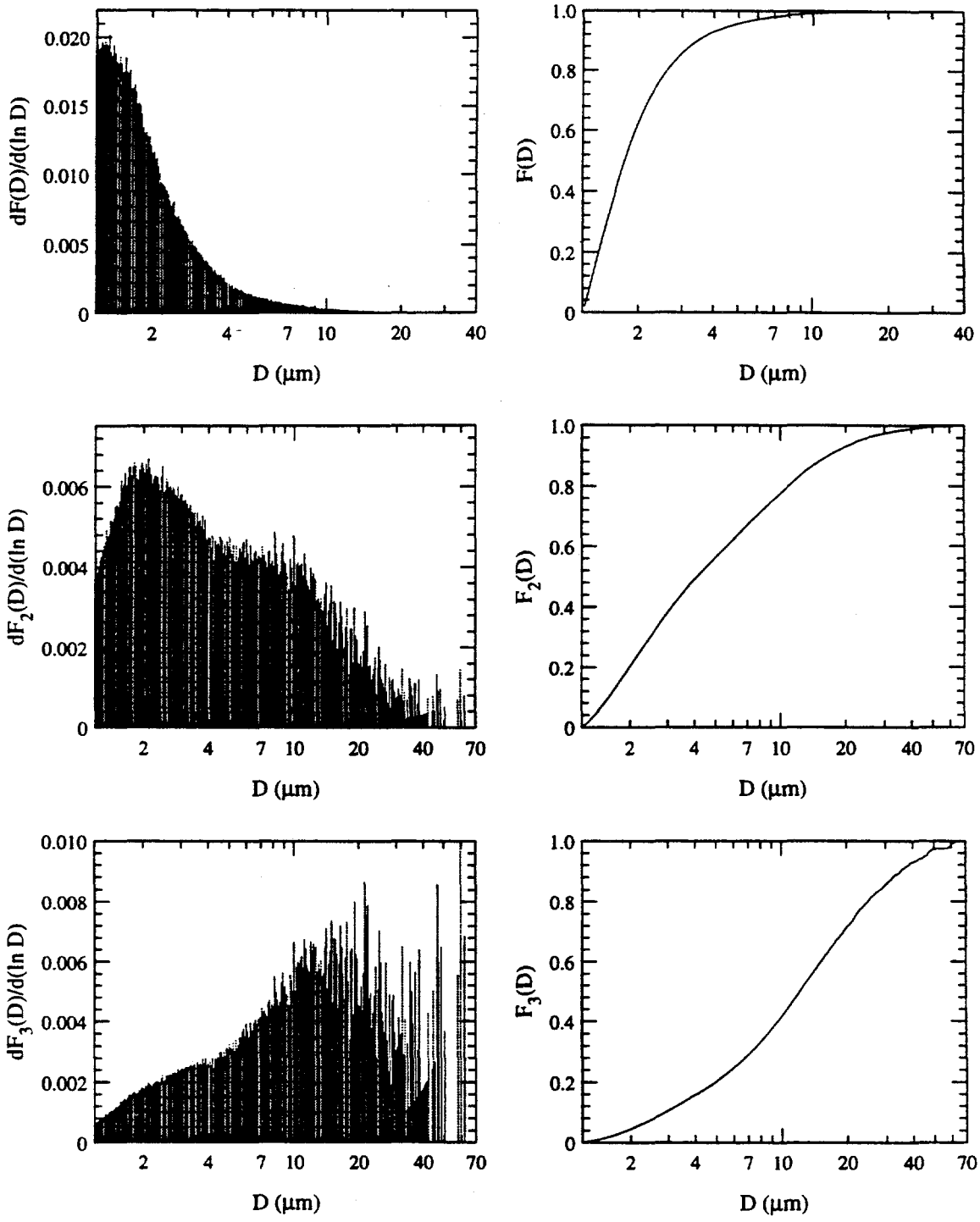

Figure D.7: Differential and cumulative size distributions of Beulah baghouse ash on the basis of number (count), area, and volume. Total particle count = 251,534.

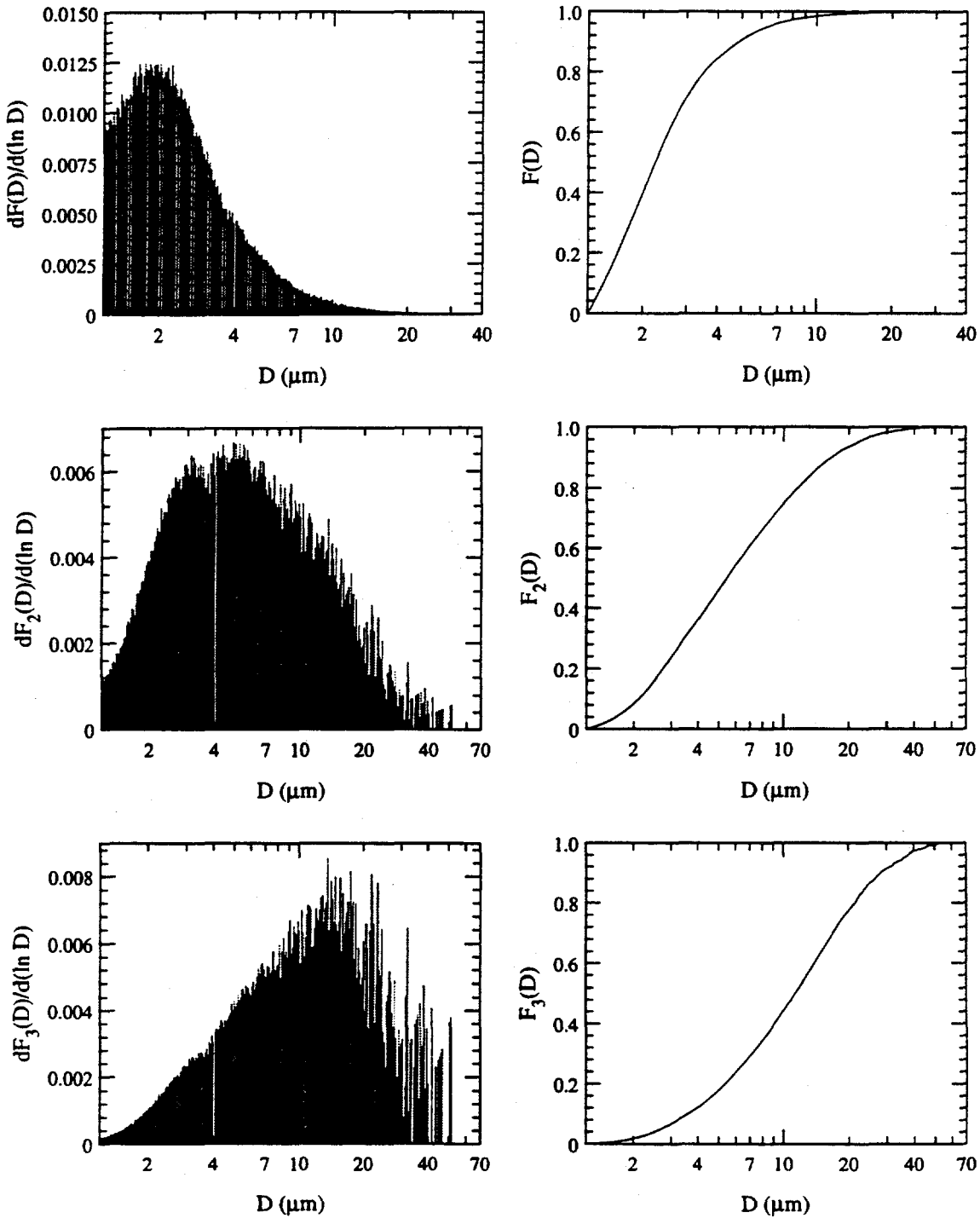

Figure D.8: Differential and cumulative size distributions of Beulah cyclone ash on the basis of number (count), area, and volume. Total particle count = 286,125.

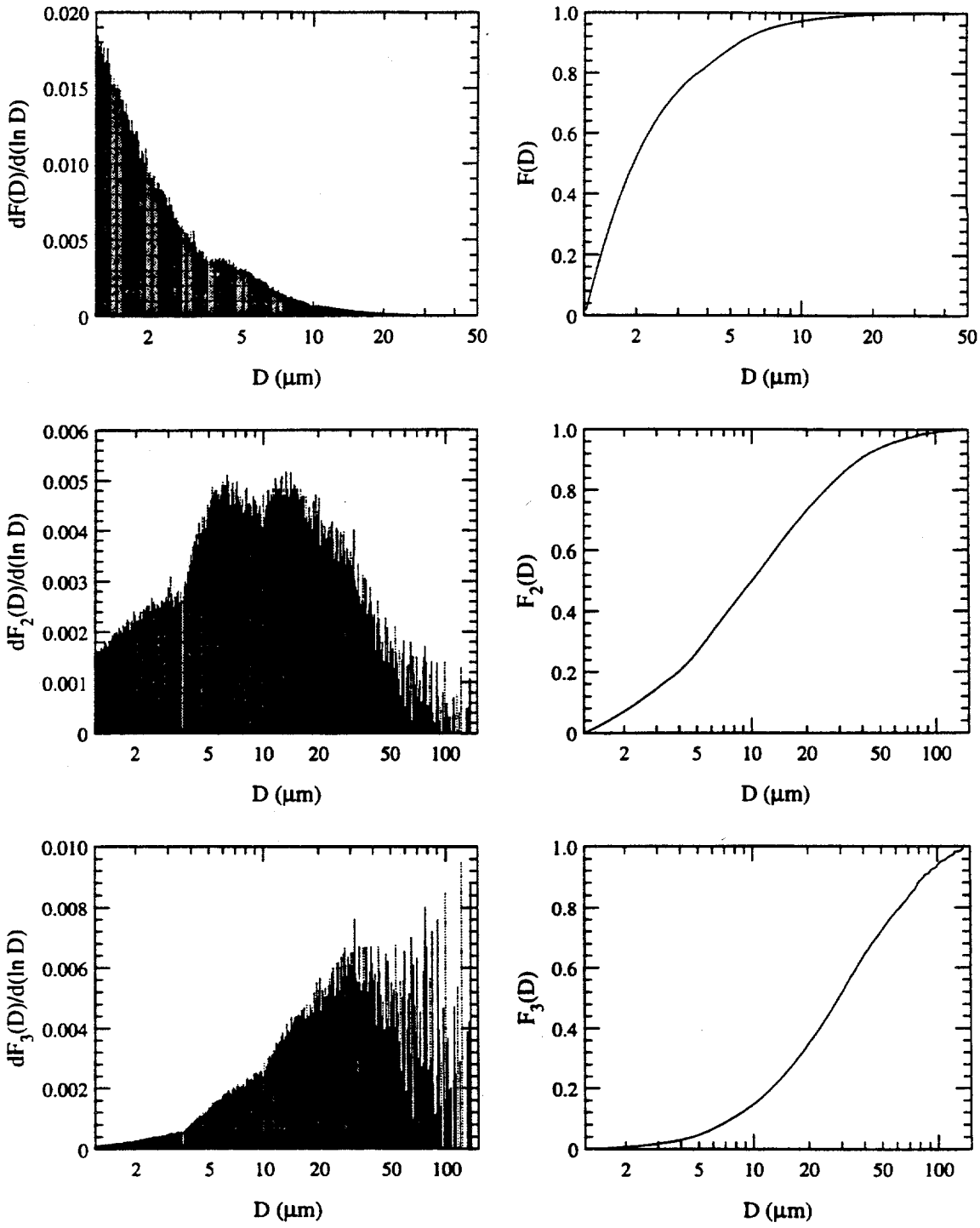

Figure D.9: Differential and cumulative size distributions of San Miguel ash on the basis of number (count), area, and volume. Total particle count = 235,822.

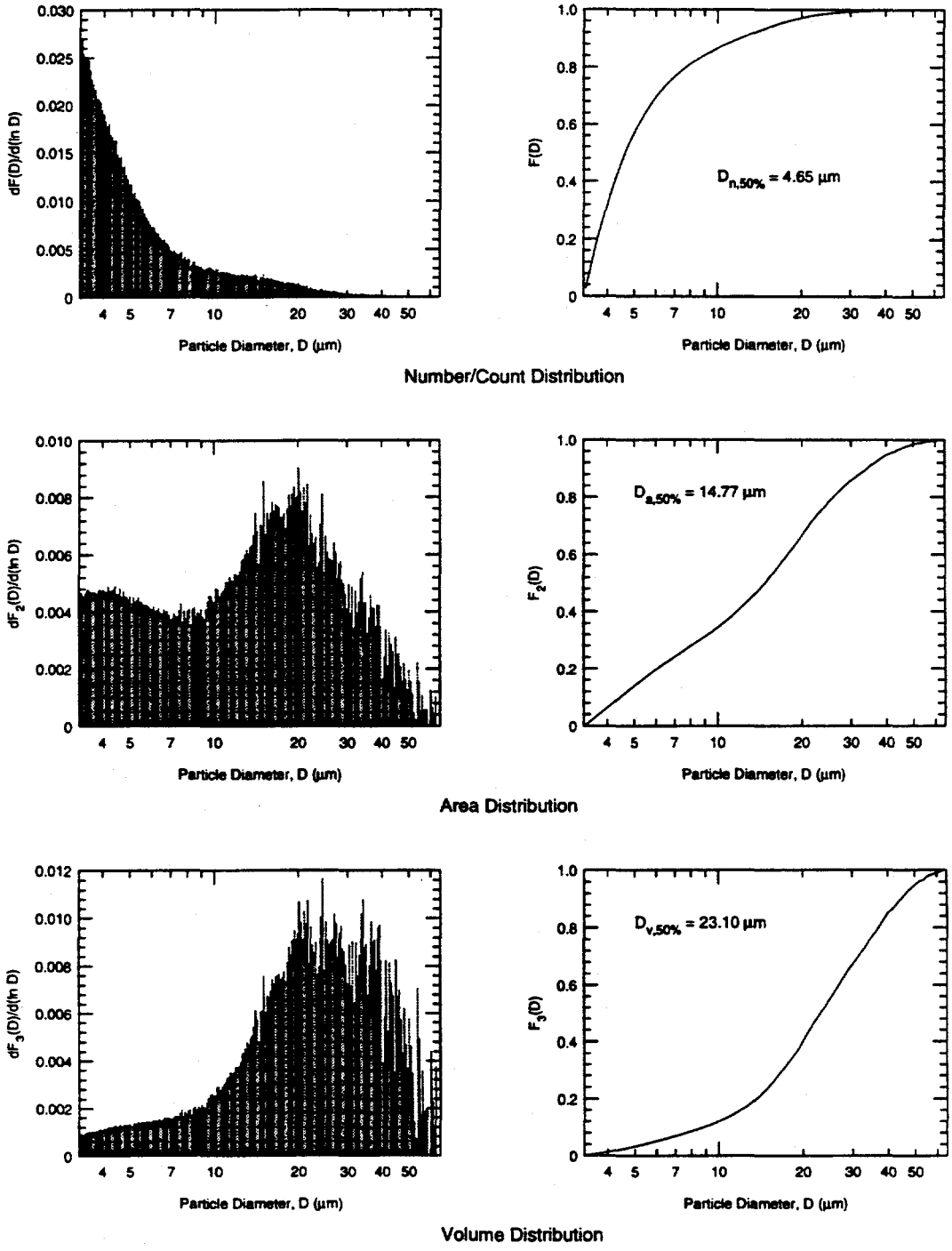

Figure D.10: Differential and cumulative size distributions of Upper Freeport baghouse ash (density < 2.2 g/cc) on the basis of number (count), area, and volume. Multisizer orifice = 100 μm. Total particle count = 178,595.

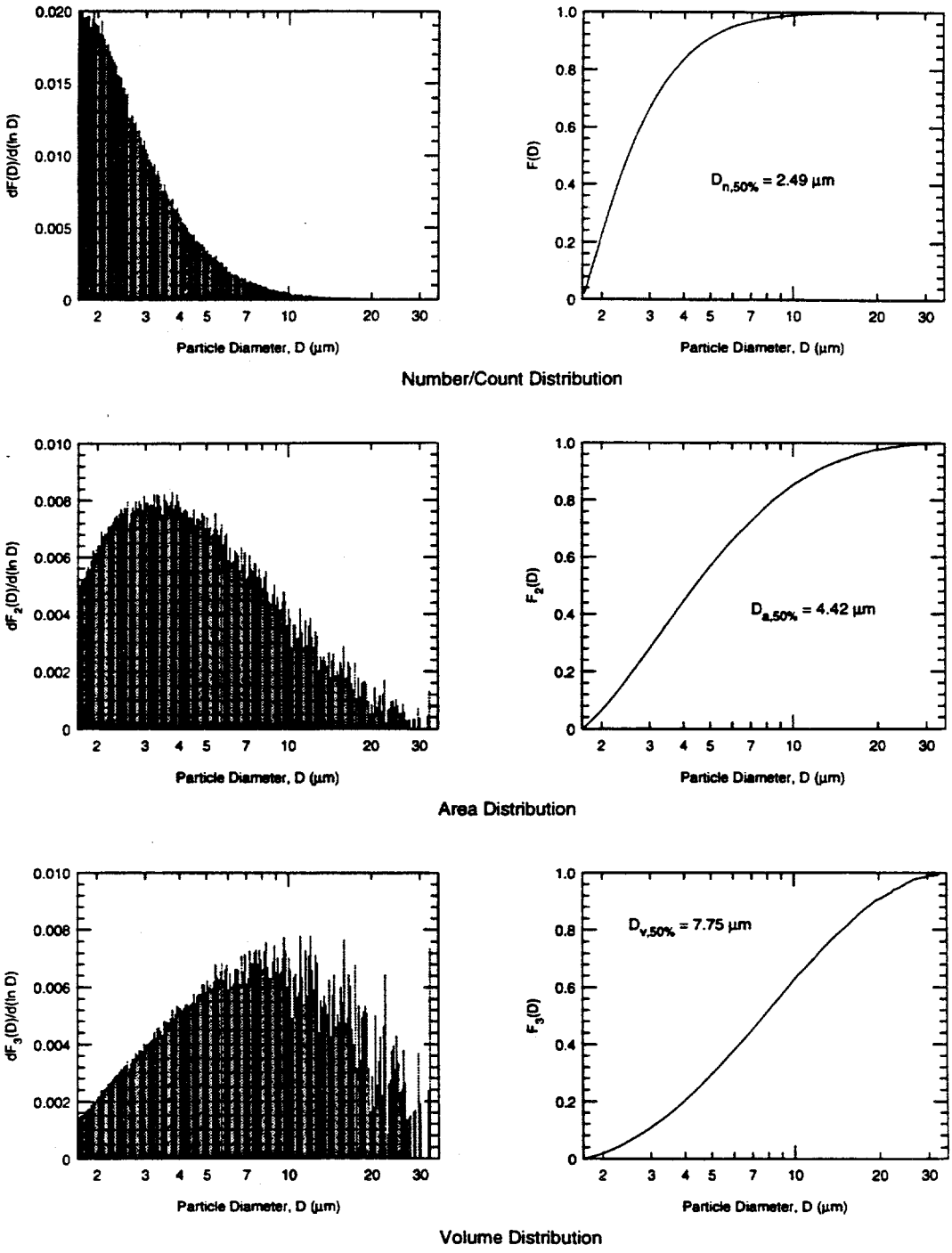

Figure D.11: Differential and cumulative size distributions of Upper Freeport baghouse ash (density > 2.2 g/cc) on the basis of number (count), area, and volume. Multisizer orifice = 50 μm. Total particle count = 197,375.

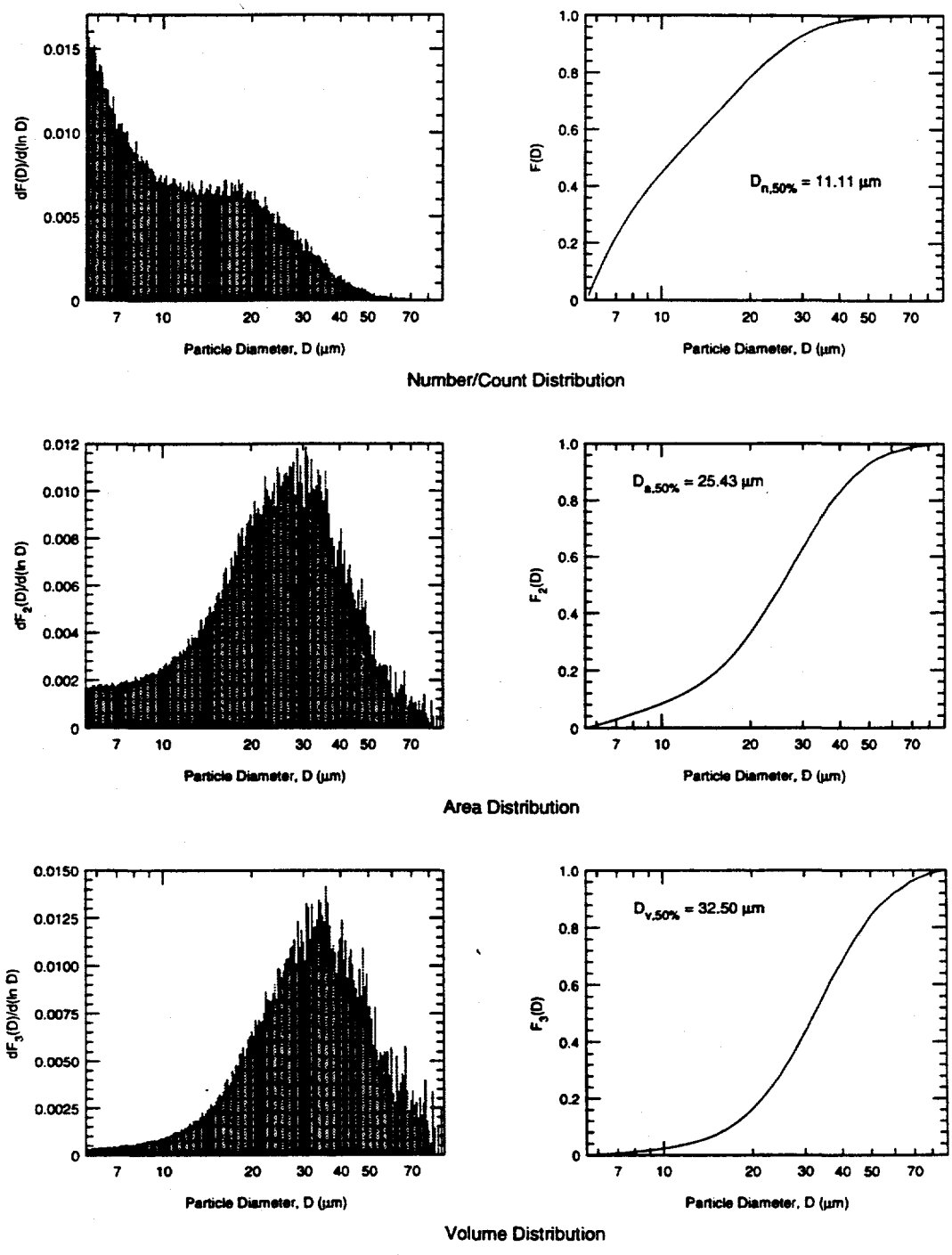

Figure D.12: Differential and cumulative size distributions of Illinois #6 baghouse ash (density < 2.2 g/cc) on the basis of number (count), area, and volume. Multisizer orifice = 140 μm. Total particle count = 103,730.

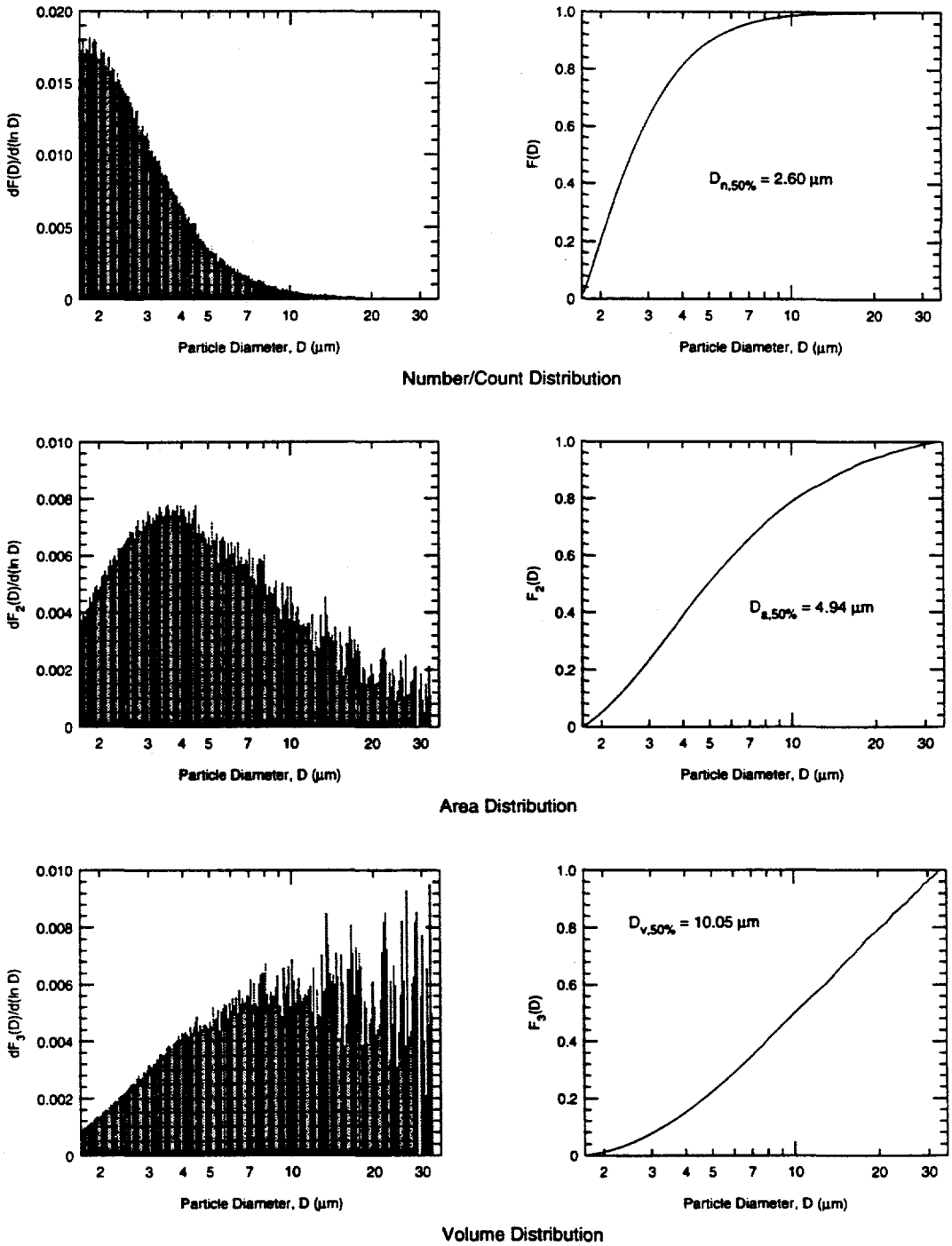

Figure D.13: Differential and cumulative size distributions of Illinois #6 baghouse ash (density > 2.2 g/cc) on the basis of number (count), area, and volume. Multisizer orifice = 50 μm. Total particle count = 141,540.

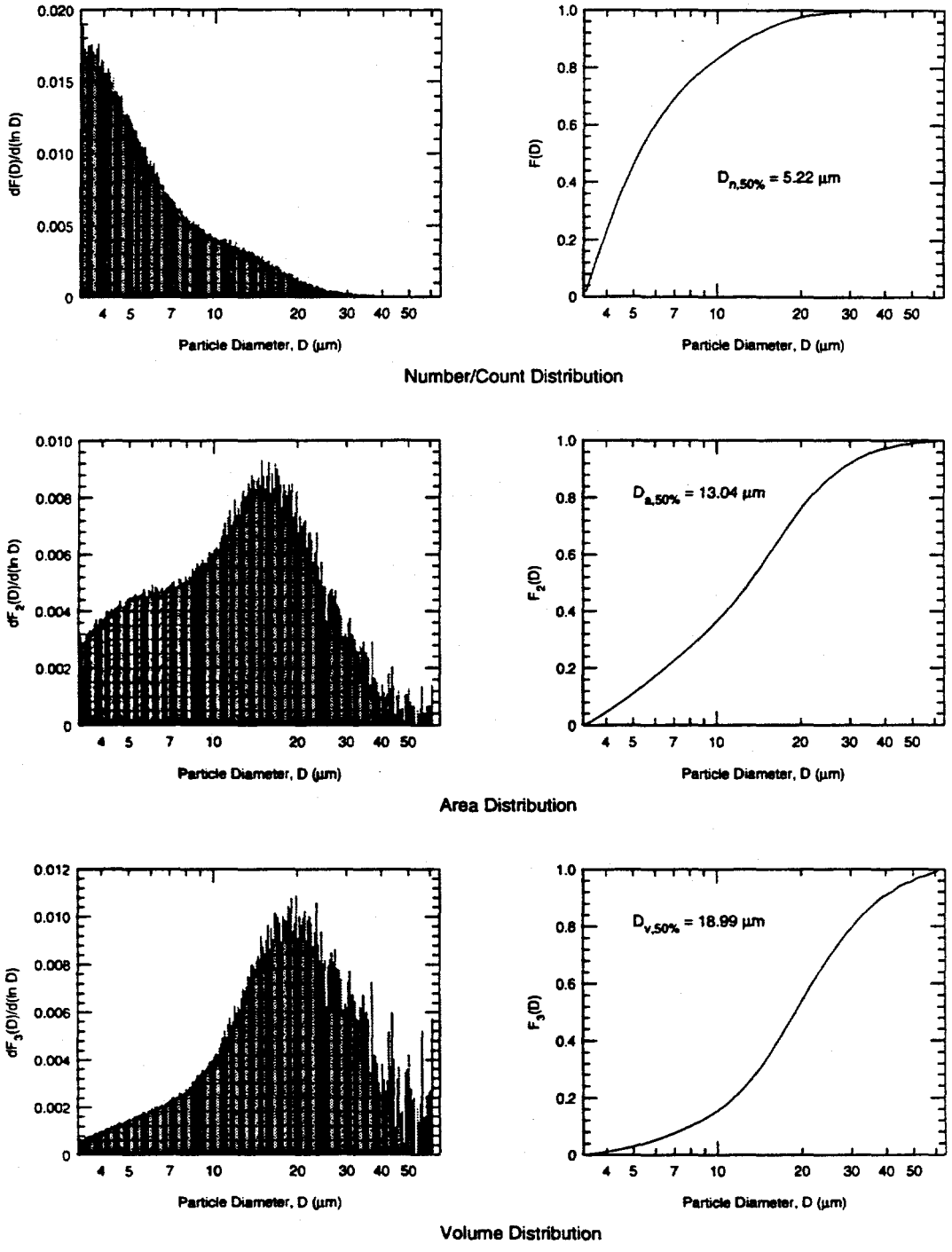

Figure D.14: Differential and cumulative size distributions of Kentucky #9 baghouse ash (density < 2.2 g/cc) on the basis of number (count), area, and volume. Multisizer orifice = 100 μm. Total particle count = 231,345.

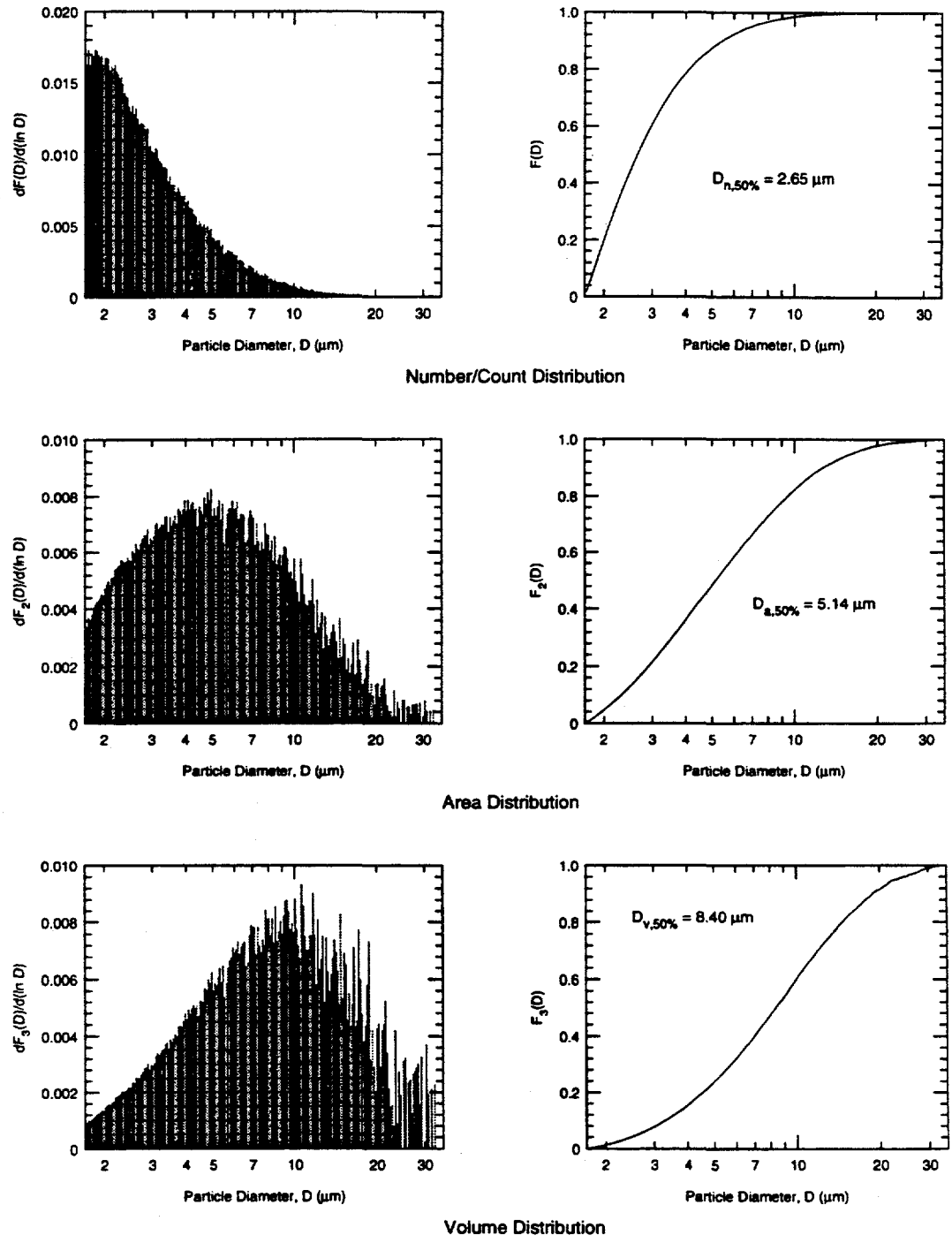

Figure D.15: Differential and cumulative size distributions of Kentucky #9 baghouse ash (density > 2.2 g/cc) on the basis of number (count), area, and volume. Multisizer orifice = 50 μm. Total particle count = 162,457.

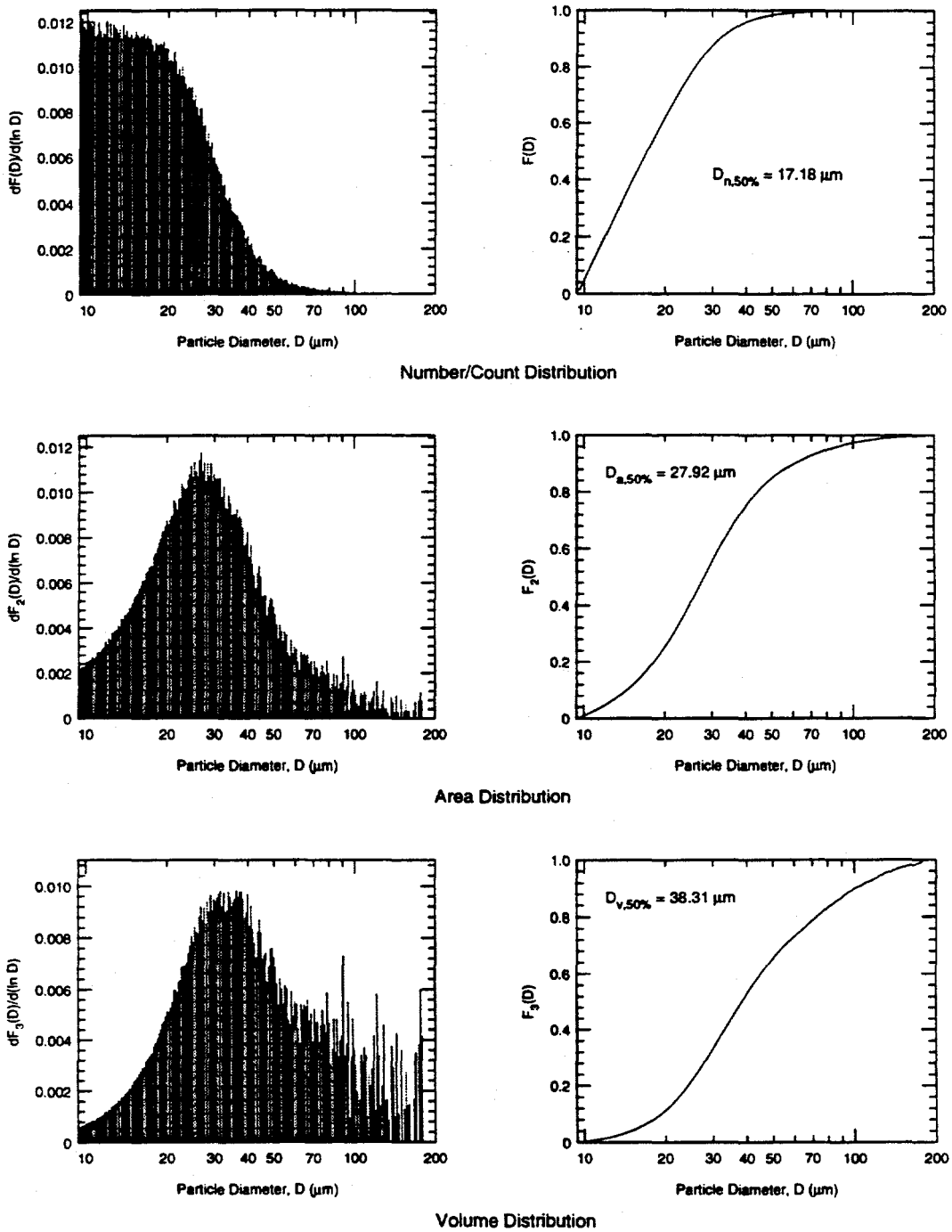

Figure D.16: Differential and cumulative size distributions of Eagle Butte ash (density < 2.2 g/cc) on the basis of number (count) area, and volume. Multisizer orifice = 280 μm. Total particle count = 163,007.

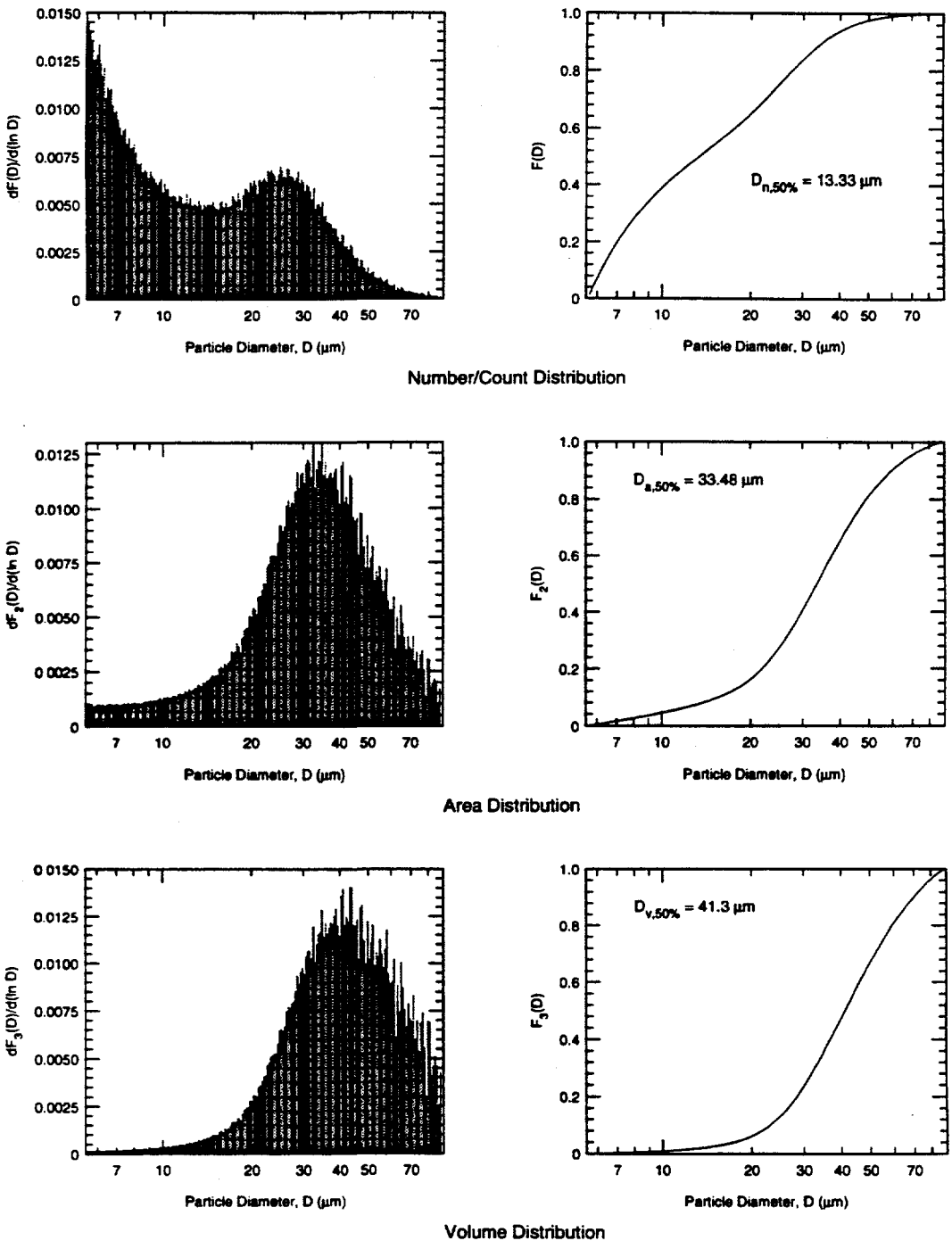

Figure D.17: Differential and cumulative size distributions of Beulah baghouse ash (density < 2.2 g/cc) on the basis of number (count) area, and volume. Multisizer orifice = 140 μm. Total particle count = 105,145.

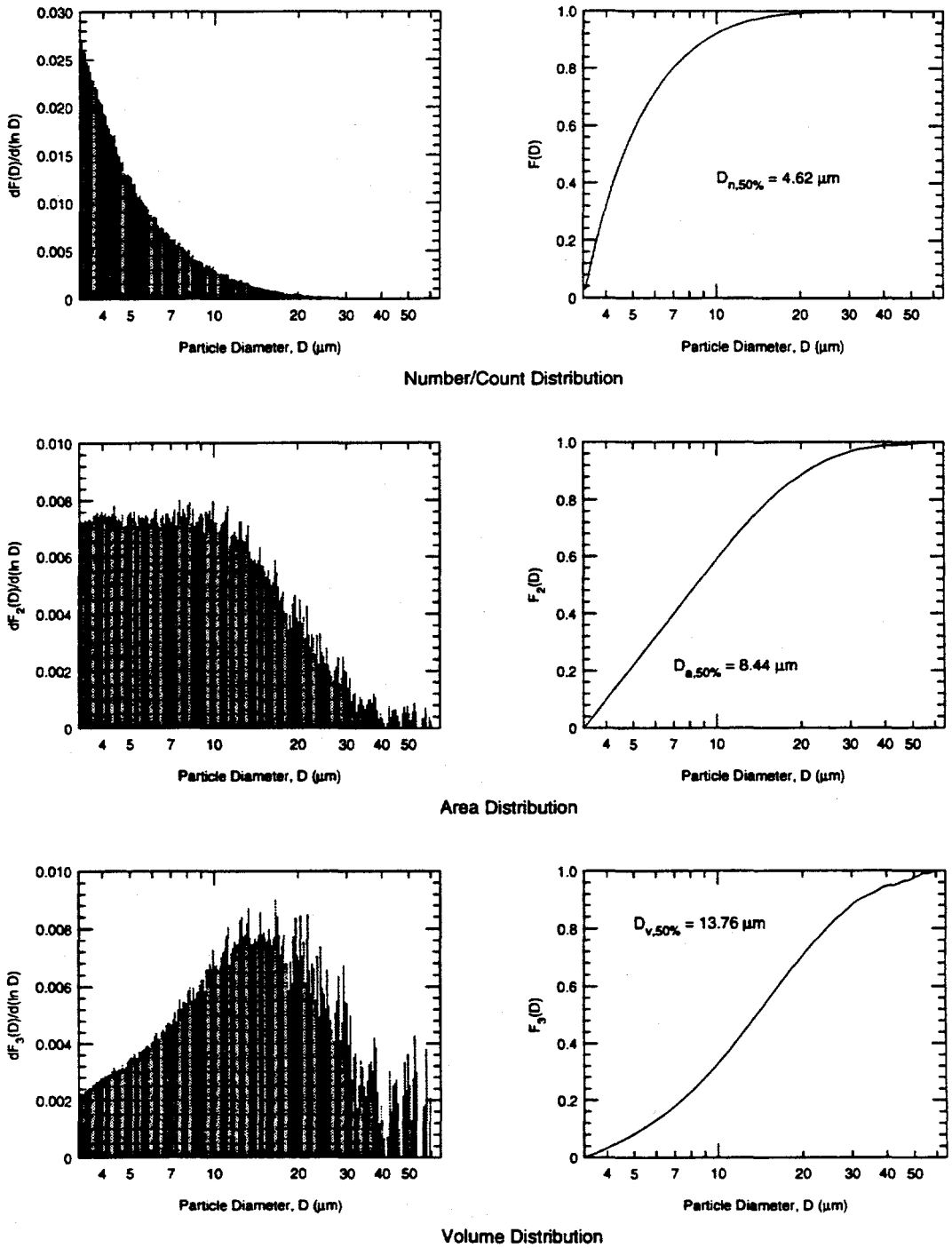

Figure D.18: Differential and cumulative size distributions of Beulah baghouse ash (density > 2.2 g/cc) on the basis of number (count) area, and volume. Multisizer orifice = 100 μm. Total particle count = 220,000.

Appendix E

EDS of Individual Particles

This Appendix describes possible errors arising in quantitative microanalysis of particulates and the various methods proposed for corrections.

A smooth, flat sample surface is needed for quantitative microanalysis using electron beams. The specimen surface is oriented at known angles to the electron beam and to the X-ray detector. The X-ray counts from the specimen and from a standard of known composition differ only because of compositional differences. By using established techniques like the ZAF correction procedure or the Bence-Albee method, the composition of the sample can be determined accurately relative to the composition of the standard (Goldstein, *et al*, 1984). However, when the specimen consists of particles (or for that matter, a rough surface), the two X-ray intensities may differ for additional reasons which are grouped under so-called 'geometrical effects'.

Geometrical Effects in Particle Analysis:

Three types of geometrical effects are identified: (a) mass effect, (b) absorption effect and (c) fluorescence effect (Small, 1979). They can be explained conveniently with the help of Figure E.1 (Armstrong, 1978).

(a) It is clear that when the volume of the particle is smaller than the electron interaction volume (for a bulk solid), some of the incident electrons will escape from both the side and the bottom of the particle. The loss of electrons leads to fewer X-rays being generated and consequently a decrease in the detected X-ray intensity. This phenomenon is called the mass effect and can become significant for small particles (e.g., for spherical particles of diameter $< 5\ \mu m$), or when the accelerating voltage is 20 kV or more (Goldstein, *et al*,

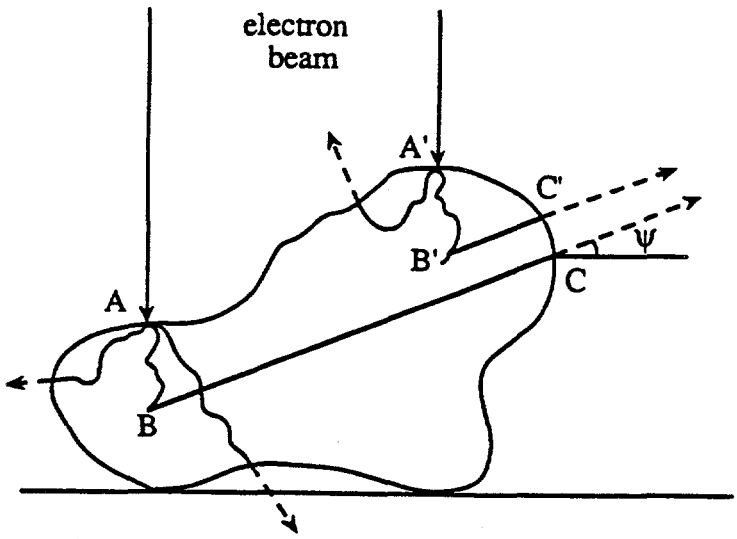

Figure E.1: Electron scattering and X-ray paths in an irregularly shaped particle (Armstrong, 1978).

1984). Additionally, as pointed out by Small (1979), there will also be a decrease in the X-ray count due to the electrons scattering from the sides of a particle. This is similar to the increase in scattering from a thick polished specimen when it is inclined rather than normal to the electron beam.

(b) For a smooth, flat bulk sample, the X-ray photons originating from different points at the same depth have to travel the same distance through the sample before emerging in the direction of the detector. The situation is quite different for particles, as can be seen in Figure E.1. Although the electron paths AB and A′B′ are equal (hence, the probabilities of X-ray production are equal), the corresponding X-ray paths in the direction of the spectrometer (at a take-off angle, ψ) are quite different. Thus, the photon originating at B has a greater probability of being absorbed on its way out than that originating at B′. Since absorption is exponentially dependent on path length, the particle geometry influences the detected X-ray intensity in the following two ways:

(i) **Beam Placement:** Figure E.2 (Goldstein, *et al*, 1984) shows that, for particles of size larger than the interaction volume, the location of the beam impact point on the particle in relation to the location of the detector can significantly affect the measured X-ray intensity. The characteristic X-rays, especially the low energy ones, produced by beam 3, will be considerably attenuated. One way to reduce this problem is to have the particle 'bracketed'

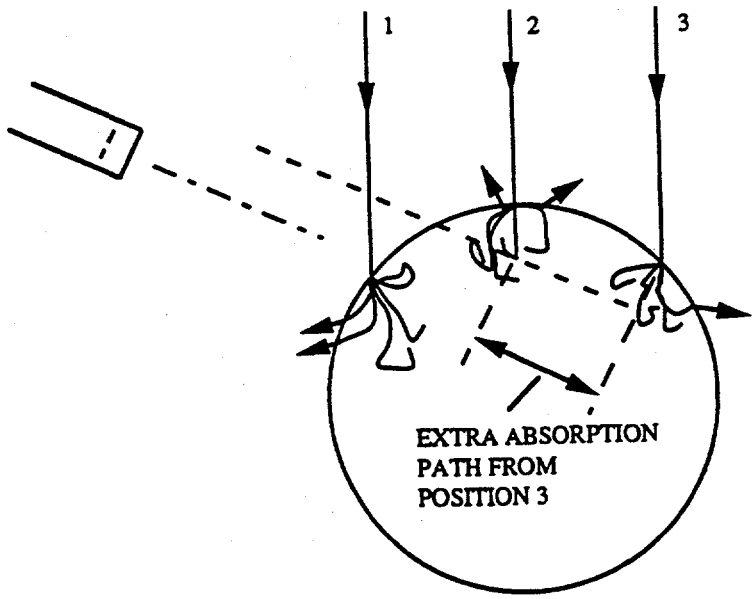

Figure E.2: Schematic to illustrate the significant difference in absorption paths when the beam is located (1) on the front, facing the X-ray detector, (2) on the top, and (3) on the back face of a particle (Goldstein *et al*, 1984).

(i.e., to use a partial field) by a rapidly scanning raster to ensure that all locations are excited.

In some analyses, for near-spherical particles, the electron beam is assumed to impact at the center of the particle. However, for particles of diameter $>5\ \mu m$, this itself can cause another problem in the form of increased absorption as illustrated in Figure E.3 (Goldstein, *et al*, 1984). In a SEM, the detector is usually placed at right angles to the beam axis. The tilt of the specimen holder provides an adequate take-off angle for the substrate. However, for an X-ray originating in the particle, the take-off angle is still zero; as a result of which it has to traverse a larger absorption path. This problem can be minimized for larger particles either by using a bracketed raster or by impinging the beam on the side of the particle facing the detector.

(ii) Particle size: In microprobe analysis, it is conventional to express the results in terms of k_A (or k-ratio), which is the ratio of the observed X-ray intensity of an element A in the sample to that in the standard. Absorption effects can influence the measured k-ratios differently for particles of different diameter. The electron interaction volume for a large size

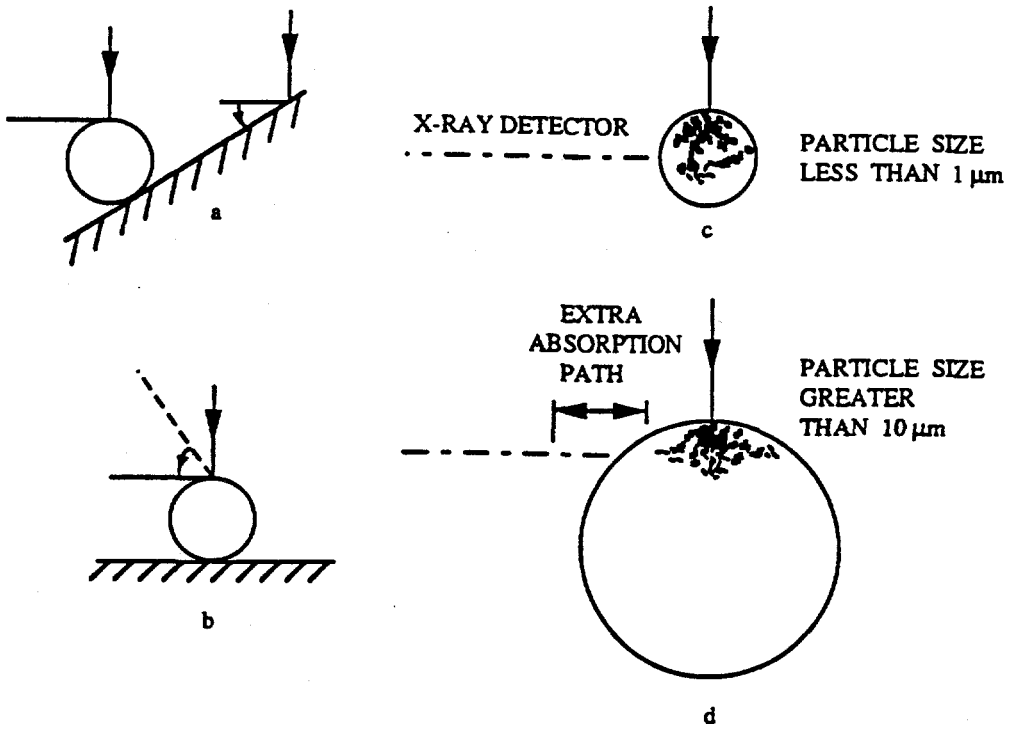

Figure E.3: Schematic illustrating the effect of particle size and detector position on X-ray path length. (a) Low take-off angle: beam set symmetrically on particle. (b) High take-off angle: beam located symmetrically on particle. (c) Low take-off angle: particle fully excited. (d) Low take-off angle: interaction volume significantly smaller than particle (Goldstein *et al*, 1984).

range of particles can be nearly the same as the corresponding volume in the bulk standard. However, the absorption path length can be significantly reduced for the particle due to its surface curvature compared to the flat standard. If the characteristic X-ray of an element of interest has low energy, this difference in the path lengths can cause the k-ratio to exceed unity. For particles of size smaller than the lower limit of this range (i.e.,$< 5\ \mu m$), the mass effect dominates. For particles larger than the upper limit of this range ($> 100\ \mu m$), the absorption paths in the sample and the standard become comparable in length. The k-ratios outside this interval are ≤ 1.

(c) Fluorescence of characteristic X-rays is induced by other higher energy characteristic X-rays or continuum X-rays (or both) produced by the primary electrons. From Figure E.4

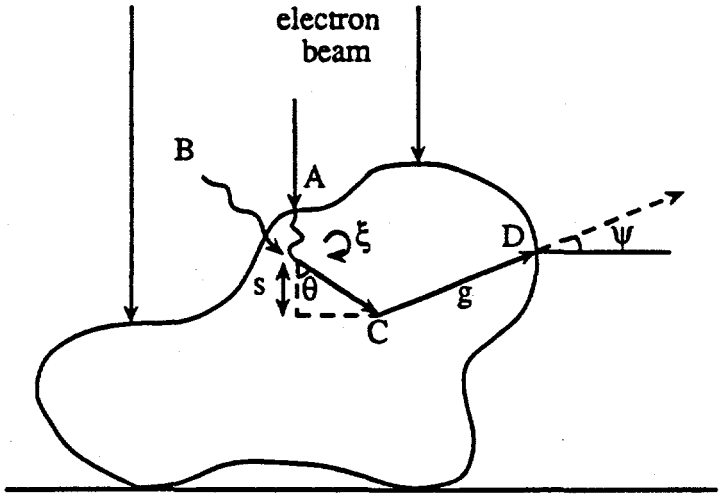

Figure E.4: Paths of fluorescing and fluoresced X-rays in a particle (Armstrong, 1978).

it is clear that the amount of detected secondary fluorescence radiation depends on the lengths of path BC and CD which vary considerably depending on particle size and shape (Armstrong, 1978).

Fluorescence occurs in a volume much larger than the electron interaction volume. A bulk target is large enough to absorb the fluorescence excitation while a particle (depending on its size) may not. Since the observed X-ray intensity is the sum of the primary X-radiation and the fluorescence radiation, the k-ratio for the particle will be reduced due to decreased secondary fluorescence as compared to the bulk specimen. However, the fluorescence effect is significant only when the specimen contains an element with characteristic X-ray lines that lie very close to the absorption edges of other elements. Fluorescence produced by the X-ray continuum is important when the sample contains a heavy element in a matrix of light elements. If a heavy element is not being analyzed, corrections for the continuum induced fluorescence can be ignored (Armstrong, 1978).

Correction Techniques for Geometrical Effects

Various techniques have been proposed for dealing with these geometric complications involved in EDS of particulate matter. They are described briefly here.

A rigorous correction scheme based on geometry (i.e., particle shape and size) is presented in (Armstrong, 1978). Particle shapes are approximated to standard geometrical solids such as a sphere, a prism, a square pyramid, etc. These models are used to perform

numerical integrations on previously published correction expressions, and the variable absorption path lengths for the X-ray photons are accounted for. The analysis yields results considerably more accurate compared to previous studies but involved lengthy computations which took large amounts of computer time at the time the paper was written. The author refers to his method as the analytic method.

In a later publication, the same investigator presents a faster, semi-empirical correction method without much sacrifice in accuracy (Armstrong, 1983). When the analysis is intended to place the particles in broad compositional categories in terms of the major elements, this correction method provides quite good results. Another semi-empirical method is presented by Aden and Buseck (1983). These two techniques are similar in their semi-empirical approach to the Bence-Albee method for bulk samples.

Some investigators have used a simple normalization of their results because the geometrical effects result in the sum of the concentrations being different from unity. Although this leads to small errors for small particles ($\leq 1\ \mu m$), it can cause serious errors in larger particles, when the absorption effects are dominant (Goldstein *et al*, 1984; Armstrong, 1978). In the latter case, a larger fraction of the low energy X-rays are absorbed.

A very different approach is the use of particle standards of known shape and composition (Goldstein *et al*, 1984). Multi-element glass standards in fibrous or spherical form are available, as are homogeneous mineral crystals that have been initially analyzed and then ground into fine particles. However, no literature dealing with the accuracy of this method appears to be available.

Finally, the peak-to-background method makes use of the fact that both the characteristic and the bremsstrahlung X-rays are produced in volumes which are nearly coincident (Small, 1979). Although the k-ratio for the peaks or the background varies with the particle size, the ratio of the k-ratios of the peak to the background is nearly independent of the particle size, except for very small particles. It has been pointed out by Aden and Buseck (1983) that the correction method based on this observation is simple to apply but can lead to substantial errors due to contribution to the background count by the substrate. Errors also occur when the thickness of the particle is less than the electron penetration range in the sample material.

It is important that the particles should not be located too close to each other on the substrate. Otherwise, scattered electrons from the particle under analysis can cause characteristic X-ray emission from an adjacent particle which may reach the detector and

increase the k-ratio. Similarly, secondary fluorescence may be induced in a neighboring particle by the emitted X-rays of the analyzed particle and subsequently detected. While the minimum separation distance depends on the relative sizes of the particles, a spacing of several times the median diameter of the particles is desirable.

Quantitative microanalysis of particulates has undergone rapid development in the past decade. New detector window materials now allow for accurate estimation of low-atomic number elements such as sodium. Increased computing power is used in analyzing larger samples and for more complex correction schemes for better accuracy. Unfortunately, the system used by UNDEERC for CCSEM studies performed for this project was not able to provide error estimates (e.g., in the form of error-bars). All published CCSEM studies on mineral matter in coal (e.g., Barta, *et al*, 1990; Moza and Austin, 1984; Huggins, *et al*, 1980), to this author's knowledge, also do not present error estimates. Often the specific correction scheme is the manufacturer's proprietary information. However, estimates of error-bounds on the composition of a particle are difficult to make without a knowledge of what form of correction, if any, has been applied to the k-ratios.

Appendix F

Statistical Analysis of CCSEM Data

The CCSEM/EDS data yield semi-quantitative estimates of chemical composition of single ash particles for sample sizes of 1000—2000 particles. For purposes of optical characterization, it is sufficient to form broad compositional classes using the data. Grouping particles by composition 'washes out' some of the EDS-related inaccuracies discussed in Appendix E. The second source of uncertainty is statistical and relates to the sample size. A measure of the uncertainity is obtained from the confidence intervals for the compositions of groups of particles that are presented in this Appendix. The effect of varying sample sizes on the mean composition is also discussed by randomly choosing samples of a hundred particles from the original sample of $\geq$ 1000 particles. The following analysis is performed on CCSEM data for Kentucky #9 and San Miguel ashes.

F.1 Background

It is necessary to define the relevant statistical terms used in the rest of this Appendix. Detailed discussions may be found in any elementary textbook of statistical analysis, e.g., Huntsberger and Billingsley (1977). The sample (size N) of fly ash particles, is picked at random from the population (i.e., all particles on the SEM stub) whose size is effectively infinite. The mean, $\bar{X}$, and standard deviation, s, of each of the twelve elements (or their oxides) are the point estimators of the true mean, μ, and standard deviation, σ, of the

population. A statistic is a quantity that is computed from the sampled data (e.g., $\bar{X}$ and s) while μ and σ are called the parameters. The sample variance, s^2, is an estimator of the population variance, σ^2. In contrast to point estimation, an interval estimation consists of two numbers between which the parameter being estimated will lie with some specified probability. This probability is called the confidence coefficient while the interval is called the confidence interval.

The estimates of the population parameters for the j^{th} element (or its oxide) are calculated as follows:

$$\bar{X}_j = \frac{\sum_{i=1}^{N} C_{i,j}}{N}$$

$$s_j = \sqrt{\frac{\sum_{i=1}^{N} (X_j - C_{i,j})^2}{N-1}}$$

Here $C_{i,j}$ is the fractional concentration of element j in the i^{th} particle.

Because the population parameters (μ and σ) are unknown, the confidence intervals ($\bar{X}$ and s) and the resulting limits have to be calculated using the t-statistic obtained from the above two estimators. The t-statistic is defined as

$$t = \frac{\bar{X} - \mu}{s/\sqrt{N}}$$

The distribution of this variable t, called the t-distribution (or Student's t-distribution) is a symmetric distribution with a zero mean value. Although it depends on N (the distribution is said to have a degree of freedom of $N-1$), it is independent of μ or σ. It is similar to the standard normal distribution but there is more area in the tails of the t-distribution, while the standard normal distribution is higher in the middle. As $N \rightarrow \infty, s \rightarrow \sigma$, and the t-distribution approaches the standard normal distribution. In essence, this is one form of the central limit theorem which states that when N is large, $\bar{X}$ has a normal distribution with mean μ and standard deviation, $\sigma/\sqrt{N}$. However, when N is small the distribution of $\bar{X}$ is given by the t-distribution with $N-1$ degrees of freedom. The t-distribution is tabulated for various values of t and $N-1$ in mathematical handbooks, or can be computed using the incomplete beta function (see Press *et al*, 1986). The importance of this distribution is that it allows one to create confidence intervals for the estimated population parameters from a single sample of size N regardless of the form of the population (in this case, the distribution of individual elements), as described next.

We define a value of $t = t_{\xi,\nu}$ such that

$$P(t < -t_{\xi,\nu}) = P(t > t_{\xi,\nu}) = \xi$$

Table F.1: Volume mean compositions and standard deviations for San Miguel and Kentucky #9 ashes.

	San Miguel		Kentucky #9	
	$\bar{X}$ (%)	s (%)	$\bar{X}$ (%)	s (%)
SiO_2	68.92±0.84	16.96	65.83±1.68	26.46
Al_2O_3	22.66±0.54	10.79	18.79±0.71	11.13
Fe_2O_3	0.51±0.34	6.93	4.78±1.02	16.07
CaO	2.95±0.52	10.38	3.38±0.88	13.91
Na_2O	2.41±0.09	1.82	0.32±0.06	0.96
K_2O	1.19±0.04	0.90	2.95±0.14	2.28
BaO	0.46±0.06	1.13	0.62±0.10	1.56
TiO_2	0.42±0.09	1.78	0.78±0.15	2.34
MgO	0.06±0.09	1.86	0.04±0.04	0.62
P_2O_5	0.02±0.03	0.58	0.03±0.11	1.79
SO_3	0.28±0.11	2.20	2.22±0.82	12.94
Cl	0.12±0.02	0.48	0.25±0.23	3.58

where ξ is the probability level and ν is the degree of freedom (usually $N-1$). Hence, the probability of t falling in the wings ($t < -t_{\xi,\nu}$ or $t > t_{\xi,\nu}$) is 2ξ. In other words, if the confidence coefficient is $1-\alpha$, (i.e., the probability that the statistic t lies in the central part of the distribution curve) then

$$P(-t_{\alpha/2,\nu} \geq t \leq t_{\alpha/2,\nu}) = 1-\alpha$$

By substituting for t and after a little algebra, one can write

$$P(L \geq \mu \leq R) = 1-\alpha$$

The $100(1-\alpha)\%$ confidence interval is bounded by L and R where

$$L = \bar{X} - t_{\alpha/2,N-1}\frac{s}{\sqrt{N}}$$

$$R = \bar{X} + t_{\alpha/2,N-1}\frac{s}{\sqrt{N}}$$

As $N \rightarrow \infty$, for a confidence coefficient of 0.95 ($\alpha = 0.05$), $t_{0.025,N-1} \rightarrow 1.96$. In practice its value is 1.96 when $N > 500$ ($t_{0.025,500} = 1.965$ and $t_{0.025,1000} = 1.963$).

The remaining statistical terms are introduced in course of the discussion.

Table F.2: Number mean compositions and standard deviations for San Miguel and Kentucky #9 ashes.

	San Miguel		Kentucky #9	
	$\bar{X}$ (%)	s (%)	$\bar{X}$ (%)	s (%)
SiO_2	61.36±0.75	15.18	54.11±1.51	23.72
Al_2O_3	25.09±0.52	10.52	17.93±0.71	11.10
Fe_2O_3	1.21±0.34	6.90	6.85±1.01	15.94
CaO	6.22±0.49	9.86	8.02±0.83	13.12
Na_2O	2.60±0.09	1.81	0.36±0.06	0.96
K_2O	0.79±0.04	0.81	2.72±0.14	2.26
BaO	0.54±0.06	1.13	0.88±0.10	1.54
TiO_2	0.84±0.09	1.73	1.36±0.14	2.26
MgO	0.27±0.09	1.85	0.19±0.04	0.60
P_2O_5	0.12±0.03	0.57	0.33±0.11	1.76
SO_3	0.77±0.11	2.14	6.67±0.77	12.15
Cl	0.20±0.02	0.47	0.59±0.23	3.56

F.2 Results

Table F.1 shows the volume mean compositions with confidence intervals, and the associated standard deviations, for Kentucky #9 and San Miguel ashes. The mean composition was calculated by weighting the particle composition with its volume. Strictly speaking, the confidence limits should be calculated using the deviation of individual particle composition from the number mean composition. However, as shown later, the difference is negligible.

The mean composition shown in Table F.2 is averaged on the basis of number. The most prolific oxide, silica, has the highest standard deviation since there are very few particles that are free of silica. Iron oxide in the Kentucky ash is present in a wider range of proportions than alumina. The two major constituents, SiO_2 and Al_2O_3, have uncertainity ranges that are <10% of $\bar{X}$. However, the contribution of the minor constituents such as CaO and Fe_2O_3 to the bulk composition can be predicted with far less accuracy. The confidence intervals in these cases are <40% of $\bar{X}$.

It is seen that SO_3 (and to a lesser extent, CaO) are present in higher percentages in the number mean of Table F.2 compared to Table F.1 indicating that smaller particles contain significantly higher amounts of these two oxides. It is also evident that larger particles

contain slightly higher proportions of silica. However, the values for Al_2O_3 are quite close in the two tables, which indicates that the presence of alumina is not correlated with particle size. These trends were noted earlier in Chapter 3. It is also clear from the two tables that confidence limits based on the number mean composition (Table F.2) are quite close to the volume based ones (Table F.1), even in cases where $\bar{X}$ is moderately correlated with the particle diameter.

Except for the major species, silica and alumina, the standard deviations are in many cases greater than the mean values, illustrating the large variations in composition from particle-to-particle. For smaller sample sizes ($N < 100$), it is possible to determine confidence limits for the standard deviations in a similar way, using the chi-square distribution instead of Student's t-distribution. However, the method does not appear to be applicable when the number of degrees of freedom of the chi-square distribution (i.e., $N - 1$) is large, under which condition the chi-square distribution is identical to the standard normal distribution.

Based on this data, it is possible to estimate the sample size needed for determining the presence of minor components with greater accuracy. Let n_w be the sample size which will yield a confidence interval of w%. Then we can write

$$w = 2t_{\alpha/2,n_w-1}\frac{s}{\sqrt{n_w}}$$

For instance, the iron oxide content of the Kentucky ash has a confidence interval of 2.04%. If the desired confidence interval is $w = 0.5\%$, then, using $s = 16.07\%$ and $t_{\alpha/2,n_{0.5}-1} = 1.96$, one obtains a sample size of $n_{0.5\%} = 15,873$. With current technology, CCSEM for such large sample sizes is not economically viable.

To compare the parameter estimates ($\bar{X}_i$ and s_i) obtained with samples smaller in size than those used above, the ash particles were randomly assigned to ten bins of approximately equal size. The composition means (by volume) for each group with appropriate confidence limits are shown in Tables F.3–F.6, for the two ashes. The sample size per bin (for the first nine bins) and the t-statistic value for 95% confidence are respectively 160 and 1.966 for San Miguel ash and 100 and 1.975 for Kentucky #9 ash. The final bin in each case contains the remaining ash particles. These tables, along with Table F.1, can be used to compare the composition information obtained with samples whose sizes differ by an order of magnitude. The ratio of the average confidence intervals for the larger sample to the smaller is approximately $\sqrt{N/n}$ (≈ 3). The numbers in these tables are measures of the

Table F.3: $\bar{X}(\%)$ and $s(\%)$ for ten groups of San Miguel ash particles, Groups 1–5.

	1	2	3	4	5
SiO_2	71.68±2.90,18.57	78.87±3.49,22.33	70.53±3.21,20.57	70.80±2.91,18.61	66.21±2.44,15.64
Al_2O_3	18.75±2.01,12.90	15.3 ±2.29,14.64	19.74±1.78,11.37	18.12±1.91,12.21	22.89±1.56,10.00
Fe_2O_3	2.17±1.77,11.34	0.10 ±0.86, 5.52	1.73±1.90,12.14	0.88±0.19, 1.21	0.43±0.91, 5.86
CaO	2.07±1.27, 8.13	1.40 ±1.59,10.17	2.48±1.94,12.40	3.87±2.02,12.97	4.79±1.60,10.23
Na_2O	2.36±0.28, 1.81	1.90 ±0.31, 1.99	2.42±0.30, 1.91	2.65±0.27, 1.71	2.23±0.32, 2.03
K_2O	0.88±0.13, 0.83	2.03 ±0.23, 1.50	1.22±0.14, 0.90	1.08±0.15, 0.94	0.59±0.13, 0.84
BaO	0.47±0.14, 0.90	0.07 ±0.11, 0.68	0.59±0.11, 0.70	0.84±0.23, 1.50	1.03±0.16, 1.03
TiO_2	0.31±0.18, 1.17	0.09 ±0.19, 1.20	0.50±0.21, 1.33	1.11±0.33, 2.11	0.96±0.21, 1.38
MgO	0.07±0.40, 2.57	0.02 ±0.21, 1.33	0.14±0.43, 2.75	0.03±0.18, 1.18	0.23±0.09, 0.58
P_2O_5	0.12±0.06, 0.40	0.00 ±0.07, 0.47	0.03±0.13, 0.81	0.03±0.09, 0.60	0.03±0.09, 0.60
SO_3	0.83±0.20, 1.28	0.15 ±0.77, 4.96	0.29±0.31, 2.00	0.43±0.27, 1.75	0.45±0.26, 1.64
Cl	0.28±0.11, 0.68	0.07 ±0.07, 0.43	0.33±0.07, 0.45	0.18±0.06, 0.40	0.17±0.06, 0.36

Table F.4: $\bar{X}(\%)$ and $s(\%)$ for ten groups of San Miguel ash particles, Groups 6–10.

	6	7	8	9	10
SiO_2	62.88±2.37,15.21	64.12±2.46,15.76	68.43±2.39,15.32	70.59±2.46,15.76	67.67±2.20,14.07
Al_2O_3	28.85±1.79,11.49	25.88±1.59,10.18	21.62±1.70,10.87	20.94±1.80,11.54	23.78±1.44, 9.21
Fe_2O_3	0.23±0.19, 1.24	0.81±1.46, 9.33	0.35±0.15, 0.97	0.50±0.84, 5.36	0.35±0.33, 2.13
CaO	3.56±1.50, 9.60	2.33±1.63,10.42	3.84±1.41, 9.06	3.92±1.35, 8.66	3.58±1.52, 9.74
Na_2O	2.63±0.26, 1.64	1.41±0.15, 1.80	0.81±0.13, 2.00	0.44±0.12, 1.74	0.54±0.10, 1.51
K_2O	1.01±0.15, 0.97	1.41±0.15, 0.99	0.81±0.13, 0.85	0.44±0.12, 0.76	0.54±0.10, 0.65
BaO	0.57±0.38, 2.42	0.72±0.12, 0.75	0.30±0.10, 0.65	0.18±0.12, 0.78	0.31±0.11, 0.72
TiO_2	0.14±0.61, 3.90	1.54±0.22, 1.43	0.84±0.18, 1.13	0.38±0.17, 1.09	0.38±0.14, 0.88
MgO	0.01±0.20, 1.28	0.04±0.15, 0.94	0.06±0.52, 3.36	0.30±0.12, 0.76	0.12±0.21, 1.32
P_2O_5	0.00±0.08, 0.54	0.01±0.08, 0.53	0.04±0.08, 0.53	0.00±0.02, 0.15	0.02±0.13, 0.83
SO_3	0.11±0.23, 1.49	0.41±0.24, 1.53	0.43±0.25, 1.58	0.31±0.18, 1.16	0.72±0.25, 1.57
Cl	0.01±0.06, 0.38	0.17±0.12, 0.77	0.21±0.06, 0.39	0.09±0.05, 0.29	0.26±0.06, 0.38

Table F.5: $\bar{X}(\%)$ and $s(\%)$ for ten groups of Kentucky #9 ash particles, Groups 1–5.

	1	2	3	4	5
SiO_2	71.06±5.83,29.36	62.69±5.08,25.63	66.63±4.76,23.98	68.74±5.35,26.96	61.21±4.94,24.90
Al_2O_3	13.05±2.28,11.52	18.13±2.29,11.55	20.76±2.48,12.51	16.08±2.02,10.19	23.11±2.25,11.32
Fe_2O_3	4.93±3.42,17.23	7.30±3.56,17.97	1.67±2.52,12.70	1.91±2.58,13.01	1.70±3.31,16.70
CaO	3.50±2.52,12.71	5.00±2.78,14.01	3.01±2.57,12.97	7.42±2.50,12.60	3.68±2.60,13.11
Na_2O	0.44±0.10, 0.48	0.14±0.12, 0.60	0.12±0.11, 0.54	0.18±0.15, 0.76	0.23±0.37, 1.88
K_2O	3.04±0.54, 2.74	2.67±0.36, 1.81	3.30±0.45, 2.28	1.74±0.58, 2.92	3.23±0.40, 2.03
BaO	0.54±0.24, 1.23	0.58±0.27, 1.38	0.88±0.34, 1.72	0.44±0.30, 1.53	1.23±0.32, 1.64
TiO_2	0.42±0.40, 2.03	1.00±0.39, 1.95	1.11±0.51, 2.56	0.99±0.48, 2.42	1.39±0.50, 2.53
MgO	0.07±0.11, 0.54	0.01±0.11, 0.57	0.01±0.07, 0.37	0.08±0.14, 0.70	0.08±0.11, 0.58
P_2O_5	0.02±0.94, 4.73	0.03±0.24, 1.21	0.05±0.19, 0.94	0.10±0.07, 0.34	0.00±0.14, 0.72
SO_3	2.72±2.64,13.33	2.16±2.53,12.74	2.38±1.97, 9.92	1.61±2.54,12.81	3.94±3.27,16.48
Cl	0.20±0.09, 0.46	0.30±1.13, 5.69	0.08±0.13, 0.64	0.70±0.17, 0.85	0.20±1.4, 7.39

Table F.6: $\bar{X}(\%)$ and $s(\%)$ for ten groups of Kentucky #9 ash particles, Groups 6–10.

	6	7	8	9	10
SiO_2	60.16±5.48,27.62	71.39±5.22,26.30	64.56±5.46,27.53	71.99±6.25,31.51	65.67±3.11,15.67
Al_2O_3	21.82±2.47,12.44	15.87±2.20,11.10	17.78±2.37,11.93	17.94±2.18,10.98	15.84±1.49,7.52
Fe_2O_3	10.11±4.05,20.42	3.23±3.31,16.67	6.66±3.25,16.41	1.97±3.04,15.31	4.24±1.91,9.61
CaO	1.98±3.17,15.96	2.44±2.56,12.92	2.33±3.31,16.67	2.45±3.05,15.38	8.03±1.70,8.55
Na_2O	0.59±0.21, 1.06	0.21±0.10, 0.51	0.43±0.29, 1.47	0.26±0.09, 0.46	0.34±0.07,0.37
K_2O	3.18±0.43, 2.16	4.00±0.50, 2.53	2.84±0.50, 2.51	2.01±0.42, 2.12	1.85±0.33,1.64
BaO	0.20±0.38, 1.90	0.42±0.30, 1.53	0.93±0.44, 2.24	0.73±0.21, 1.07	0.51±0.14,0.69
TiO_2	0.34±0.59, 2.98	0.62±0.49, 2.47	0.89±0.48, 2.40	0.63±0.38, 1.91	0.68±0.22,1.11
MgO	0.01±0.14, 0.72	0.07±0.12, 0.60	0.06±0.15, 0.74	0.02±0.11, 0.55	0.07±0.12,0.61
P_2O_5	0.01±0.18, 0.91	0.02±0.11, 0.57	0.05±0.32, 1.63	0.04±0.21, 1.04	0.09±0.12,0.61
SO_3	1.44±2.82,14.22	1.53±2.01,10.15	3.17±2.14,10.77	1.81±3.16,15.91	1.62±1.45,7.32
Cl	0.17±0.16, 0.82	0.20±0.12, 0.62	0.30±1.12, 5.63	0.15±0.13, 0.63	1.07±0.21,1.07

increased statistical accuracy of the current CCSEM data compared to previous studies in which only 50–100 particles were analyzed (e.g., Kaufherr and Lichtman, 1984).

The particles in the bins were picked at random from a larger sample, which in turn was randomly selected from the population (i.e., all the particles on the SEM stub). The two random selections are independent. Hence, each bin can be considered to be a random sample of the population. One may ask with what confidence can one assert that the ash sample in each bin was drawn from the same population. Populations whose values are divided into two or more classes (i.e., composition in terms of K elements) are called multinomial populations and any hypothesis on the association of the data can be tested using the χ^2 (chi-square) distribution, as described below. The hypothesis to be tested is that the compositions of bins are identical.

Two samples of ash particles, each of size n, yield a χ^2-statistic that is defined as

$$\chi^2 = \sum_{i=1}^{K} \frac{n(C_i^1 - C_i^2)^2}{C_i^1 + C_i^2}$$

where, in this case, C_i^1 and C_i^2 are the average concentrations of the i^{th} element in the first and second samples, respectively. The χ^2-statistic follows a distribution that depends on the degree of freedom $(K-1)$ and is skewed towards small values of χ^2. As K increases, the skewness decreases and as $K \rightarrow \infty$, the χ^2-distribution approaches the normal distribution shifted in the positive x-direction (since only non-negative values of χ^2 are possible). The distributions, for different values of χ^2 and $K-1$, can either be interpolated from tables, or computed using the incomplete gamma function (see Press *et al*, 1986).

Percentage points of the χ^2-distributions are defined by

$$P(\chi_\nu^2 \geq \chi_{\alpha,\nu}^2) = \alpha$$

i.e., $\chi_{\alpha,\nu}^2$ is that value for the χ^2-distribution with ν degrees of freedom such that the area to the right, i.e., the probability of a larger value, is α. Perfect agreement between the two data sets would give a χ^2 value of zero, and

$$P(\chi_{K-1}^2 \geq 0.0) = 0.0$$

For convenience we can define

$$Q(\chi_\nu^2 \geq \chi_{\alpha,\nu}^2) = 1 - P(\chi_\nu^2 \geq \chi_{\alpha,\nu}^2) = \alpha$$

Thus, $Q(\chi_\nu^2 \geq \chi_{\alpha,\nu}^2)$ is the probability that the observed chi-square, χ_ν^2, will exceed the value $\chi_{\alpha,\nu}^2$ even if the samples are drawn from the same population.

Table F.7: Chi-square probability that all ten groups have the same composition (San Miguel ash).

	1	2	3	4	5	6	7	8	9	10
1	1.0000	0.7967	1.0000	0.9898	0.8735	0.6051	0.9008	0.9607	0.9643	0.9622
2	0.7967	1.0000	0.8351	0.7698	0.3683	0.3218	0.3957	0.7249	0.7949	0.6274
3	1.0000	0.8351	1.0000	0.9992	0.9711	0.8177	0.9826	0.9932	0.9913	0.9846
4	0.9898	0.7698	0.9992	1.0000	0.9981	0.7840	0.9808	0.9996	0.9945	0.9871
5	0.8735	0.3683	0.9711	0.9981	1.0000	0.9714	0.9903	0.9997	0.9984	0.9995
6	0.6051	0.3218	0.8177	0.7840	0.9714	1.0000	0.9768	0.9750	0.9540	0.9918
7	0.9008	0.3957	0.9826	0.9808	0.9903	0.9768	1.0000	0.9940	0.9327	0.9862
8	0.9607	0.7249	0.9932	0.9996	0.9997	0.9750	0.9940	1.0000	0.9999	1.0000
9	0.9643	0.7949	0.9913	0.9945	0.9984	0.9540	0.9327	0.9999	1.0000	0.9999
10	0.9622	0.6274	0.9846	0.9871	0.9995	0.9918	0.9862	1.0000	0.9999	1.0000

Table F.8: Chi-square probability that all ten groups have the same composition (Kentucky #9 ash).

	1	2	3	4	5	6	7	8	9	10
1	1.0000	0.9948	0.9614	0.9561	0.8592	0.8751	0.9997	0.9989	0.9933	0.9803
2	0.9948	1.0000	0.9488	0.9499	0.9161	0.9879	0.9768	0.9996	0.9361	0.9949
3	0.9614	0.9488	1.0000	0.9737	0.9999	0.7061	0.9983	0.9738	0.9999	0.8843
4	0.9561	0.9499	0.9737	1.0000	0.9211	0.3849	0.9628	0.8200	0.9864	0.9999
5	0.8592	0.9161	0.9999	0.9211	1.0000	0.5922	0.9451	0.9562	0.9854	0.8156
6	0.8751	0.9879	0.7061	0.3849	0.5922	1.0000	0.8727	0.9928	0.7271	0.6490
7	0.9997	0.9768	0.9983	0.9628	0.9451	0.8727	1.0000	0.9935	0.9998	0.9387
8	0.9989	0.9996	0.9738	0.8200	0.9562	0.9928	0.9935	1.0000	0.9791	0.9259
9	0.9933	0.9361	0.9999	0.9864	0.9854	0.7271	0.9998	0.9791	1.0000	0.9300
10	0.9803	0.9949	0.8843	0.9999	0.8156	0.6490	0.9387	0.9259	0.9300	1.0000

Table F.9: Precision of CCSEM elemental results (Casuccio *et al*, 1983).

Elemental concentration (wt. %)	Average relative error (%)	95% confidence interval (%)
<1	35	0.65–1.35
2.5	32	1.94–3.06
5	16	4.36–5.64
10	8	8.8–11.2
>15	5	14.3–15.7

For the ten groups of data (i.e., $K = 10$) for each ash, Tables F.7 and F.8 show the values of $\chi^2_{\alpha,\nu}$ for any two groups. The numbers can be interpreted as $100P\%$ probability that the two samples are statistically the same. For example, for the San Miguel ash, the probability that the particles in Group 7 have the same average composition as those in Group 9 is 93.27%. Except for a few groups like Group 2 of San Miguel, (which contains a few large high-silica-low-alumina particles), all the other groups for both ashes have a high probability of having the same composition.

In conclusion, it can be said that *average* ash compositions obtained with sample sizes of 1000–2000 are of sufficient statistical accuracy for the major constituents of the ash (i.e., elements that constitute $\gtrsim$ 20% by mass). In contrast, the accuracy of composition measurement of an individual ash particle is limited by geometry related uncertainties as discussed in Appendix 7. As expected, the population parameters, μ and σ can be predicted with increasing accuracy (i.e., with increasingly narrow uncertainty intervals) as the sample size grows larger. Still, it is not possible to determine the concentrations of minor elements in the ash with sufficient accuracy using current CCSEM sample sizes.

There are fewer characteristic X-ray photons of elements present in small concentrations which introduces statistical uncertainity. Casuccio *et al* (1983) made precision estimates that are reproduced in Table F.9. As can be expected, the relative error decreases as the elemental concentration rises.

Appendix G

Detailed Chemical Composition Data

Data related to several aspects of chemical characterization of all six ashes are included here and are listed below.

- Ternary plots.
- CCSEM compositions averaged over micron-size bins.
- Distribution of the four dominant oxides (SiO_2, Al_2O_3, Fe_2O_3, and CaO) in the ashes.
- Distribution of Al_2O_3/SiO_2 and SiO_2/Fe_2O_3 ratios (from CCSEM).
- Comparison of bulk chemical composition of ashes.
- Comparison of Multisizer size distributions with those obtained from CCSEM data.
- Distribution of glass former/glass intermediate, and glass former/glass modifier ratios in the ashes.

The related discussions are in Chapter 4.

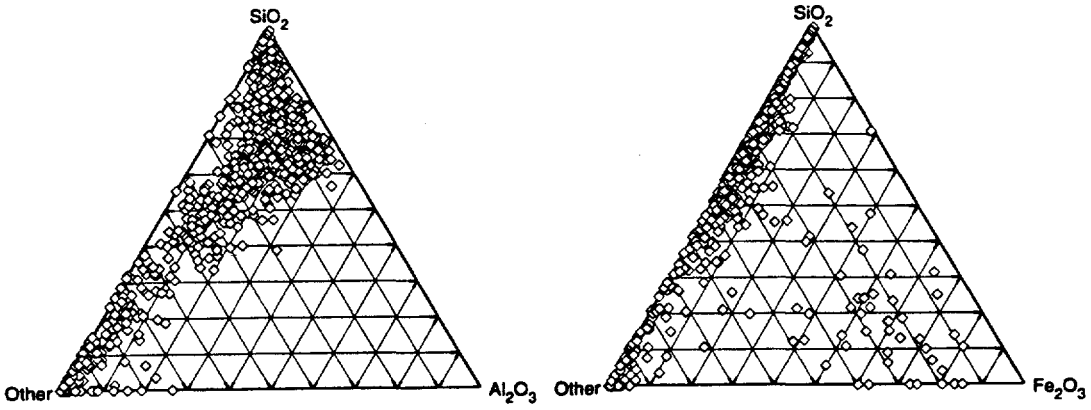

Figure G.1: Ternary plots for molar composition distribution of Kentucky #9 fly ash. Each point represents a particle.

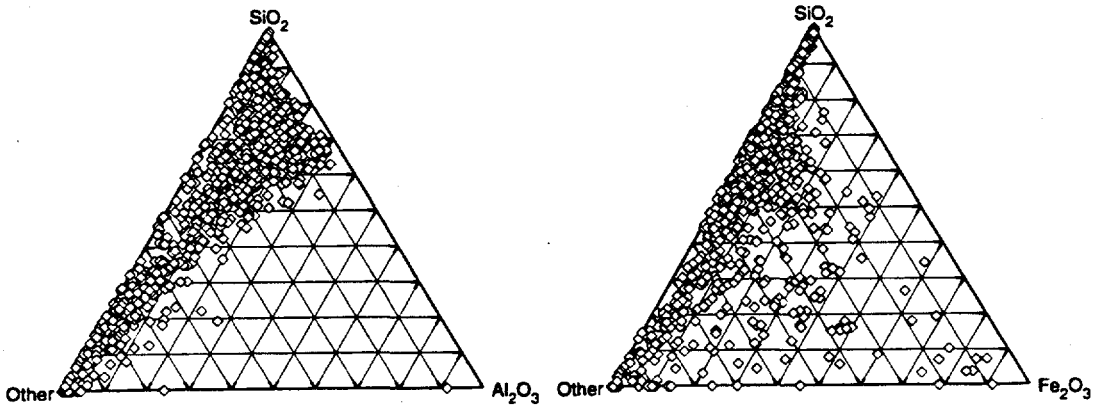

Figure G.2: Ternary plots for molar composition distribution of Illinois #6 fly ash. Each point represents a particle.

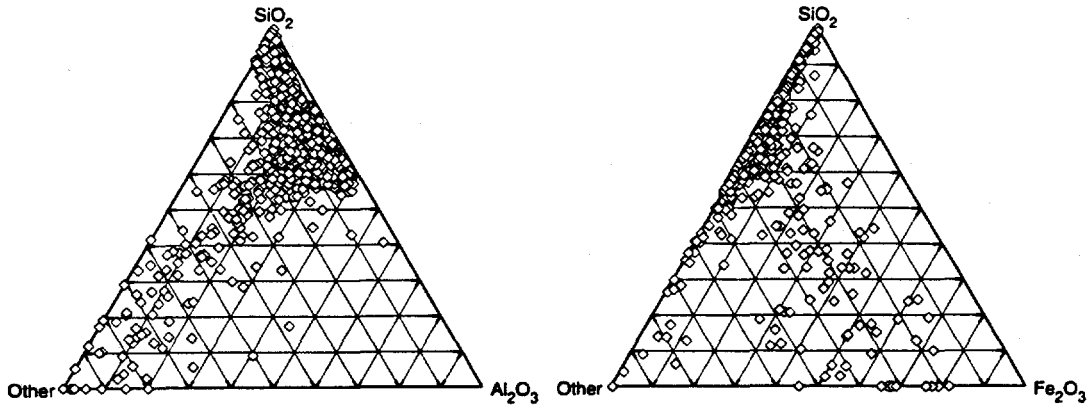

Figure G.3: Ternary plots for molar composition distribution of Upper Freeport fly ash. Each point represents a particle.

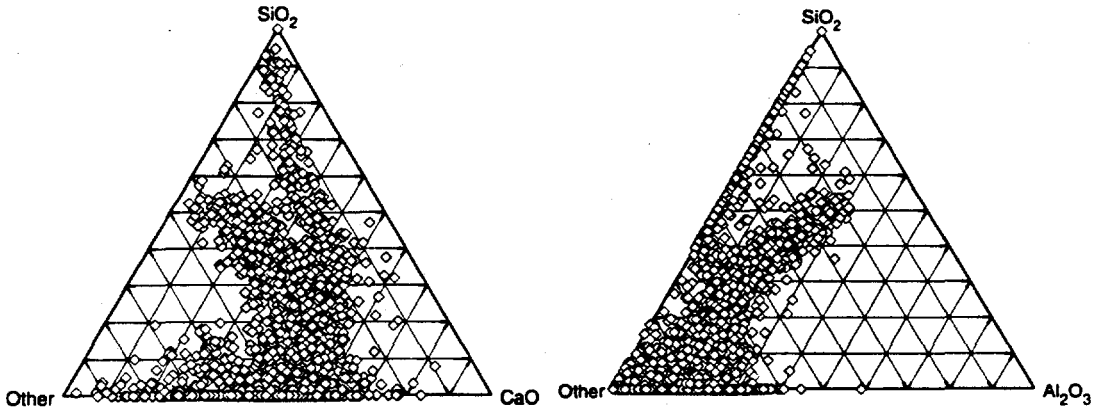

Figure G.4: Ternary plots for molar composition distribution of Eagle Butte fly ash. Each point represents a particle.

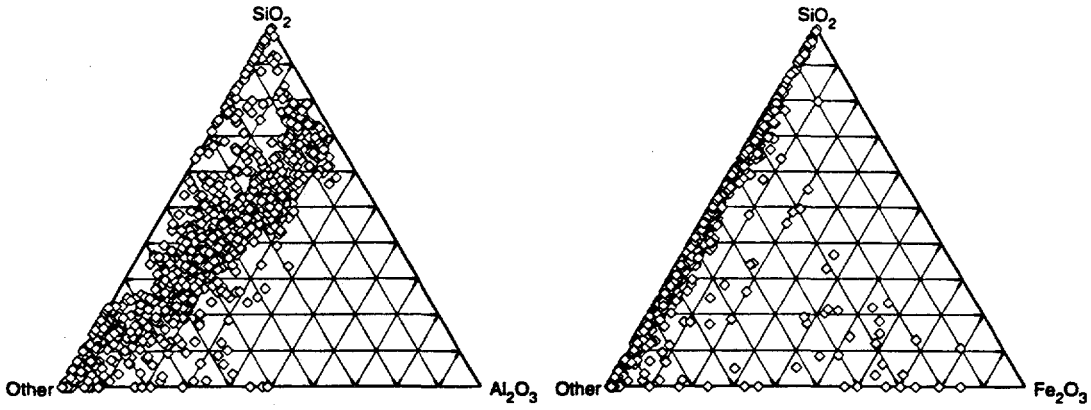

Figure G.5: Ternary plots for molar composition distribution of Beulah fly ash. Each point represents a particle.

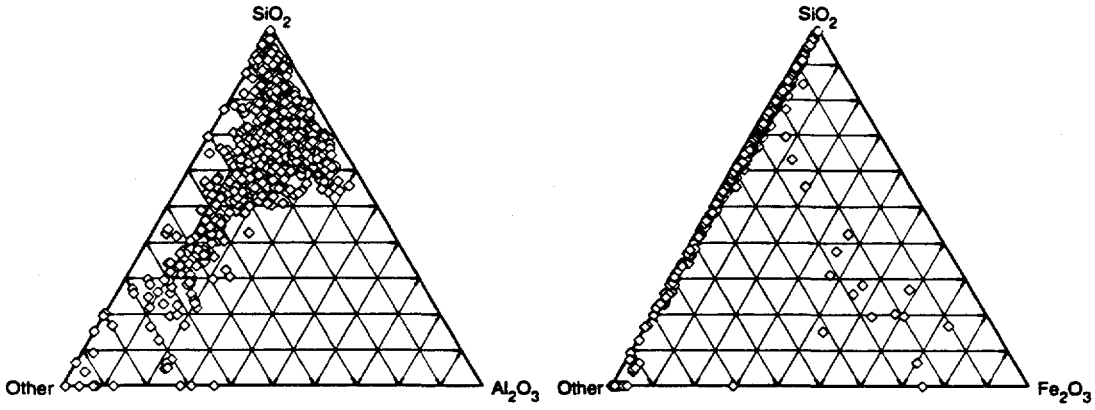

Figure G.6: Ternary plots for molar composition distribution of San Miguel fly ash. Each point represents a particle.

Table G.1: Oxide composition of Upper Freeport fly ash as a function of particle diameter (in μm). The number of particles detected in each size class is shown in the second column.

D (μm)	No.	Si	Al	Fe	Ca	Na	K	Ba	Ti	Mg	P	S	Cl
1	384	55.2	31.4	5.2	1.3	0.5	2.3	0.6	1.0	0.4	0.4	1.3	0.3
2	750	57.1	30.5	5.0	1.2	0.4	2.3	0.5	0.9	0.3	0.3	1.1	0.2
3	364	59.0	29.8	4.0	1.0	0.4	2.4	0.6	0.8	0.4	0.3	1.0	0.3
4	141	58.7	29.5	5.7	0.8	0.4	2.4	0.4	0.7	0.2	0.1	0.8	0.2
5	45	60.4	29.3	3.3	0.8	0.3	2.4	0.4	0.6	0.7	0.1	1.6	0.1
6	32	64.1	27.8	1.6	1.4	0.3	2.7	0.4	0.6	0.4	0.1	0.5	0.2

Table G.2: Oxide composition of Kentucky #9 fly ash as a function of particle diameter (in μm). The number of particles detected in each size class is shown in the second column.

D (μm)	No.	Si	Al	Fe	Ca	Na	K	Ba	Ti	Mg	P	S	Cl
1	204	43.4	16.5	9.3	10.2	0.6	2.6	0.8	1.5	0.3	0.9	13.0	0.8
2	151	50.1	19.3	5.1	10.7	0.5	2.7	1.1	1.6	0.3	0.3	7.3	0.9
3	132	50.8	18.8	6.5	9.6	0.2	2.7	1.1	1.4	0.2	0.3	7.5	0.8
4	104	52.2	18.7	10.3	7.6	0.2	2.6	1.0	1.7	0.2	0.3	4.8	0.4
5	83	61.3	17.3	6.2	6.2	0.3	3.1	0.7	1.1	0.0	0.1	3.4	0.3
6	52	61.7	17.9	4.5	7.4	0.3	2.5	0.9	1.6	0.1	0.1	2.9	0.3
7	39	60.0	21.4	4.5	4.6	0.3	2.7	0.6	1.0	0.0	0.1	4.5	0.3
8	32	67.0	19.3	1.9	4.1	0.3	2.9	0.6	0.7	0.1	0.0	2.9	0.1
9	33	58.3	17.5	6.8	9.2	0.1	2.2	0.7	0.8	0.1	0.1	3.7	0.5

Table G.3: Oxide composition of Eagle Butte fly ash as a function of particle diameter (in μm). The number of particles detected in each size class is shown in the second column.

D (μm)	No.	Si	Al	Fe	Ca	Na	K	Ba	Ti	Mg	P	S	Cl
1	672	19.2	24.7	3.0	35.0	0.4	0.3	1.0	1.6	9.1	0.8	4.5	0.3
2	782	19.8	25.3	3.2	33.6	0.6	0.3	0.9	1.5	10.2	0.7	3.6	0.3
3	245	18.3	25.1	3.5	35.3	0.9	0.3	0.8	1.3	10.2	0.7	3.5	0.3
4	91	23.8	23.5	2.7	32.7	1.6	0.3	0.6	1.2	9.5	0.6	3.2	0.4
5	40	16.6	25.0	2.8	34.6	1.3	0.4	0.7	1.3	13.8	0.5	2.8	0.2

Table G.4: Oxide composition of Beulah fly ash as a function of particle diameter (in μm). The number of particles detected in each size class is shown in the second column.

D (μm)	No.	Si	Al	Fe	Ca	Na	K	Ba	Ti	Mg	P	S	Cl
1	357	33.4	23.4	4.6	17.2	4.5	0.8	1.0	1.4	6.5	0.5	5.9	0.9
2	535	37.3	23.1	4.6	14.7	5.5	0.9	1.0	1.5	4.7	0.4	5.0	1.2
3	134	38.9	24.0	4.9	14.2	4.8	1.2	0.7	1.0	3.9	0.4	5.5	0.6
4	47	41.6	22.3	2.1	10.4	7.4	1.5	1.1	1.5	2.4	0.2	6.0	3.6

Table G.5: Oxide composition of San Miguel fly ash as a function of particle diameter (in μm). The number of particles detected in each size class is shown in the second column.

D (μm)	No.	Si	Al	Fe	Ca	Na	K	Ba	Ti	Mg	P	S	Cl
1	186	58.3	26.0	1.3	7.3	2.7	0.8	0.7	1.0	0.4	0.3	0.9	0.3
2	519	60.0	26.1	1.4	6.0	2.7	0.8	0.6	0.9	0.3	0.1	0.8	0.2
3	356	59.9	25.0	1.4	7.6	2.4	0.7	0.5	0.7	0.4	0.1	1.1	0.2
4	197	63.3	24.8	0.7	5.7	2.6	0.7	0.4	0.8	0.1	0.1	0.5	0.2
5	106	64.6	23.2	0.4	6.6	2.6	0.8	0.4	0.6	0.1	0.1	0.4	0.2
6	68	65.9	23.8	0.3	5.0	2.5	0.8	0.4	0.5	0.1	0.0	0.5	0.1
7	39	59.9	27.0	2.3	4.6	2.6	0.8	0.8	1.2	0.0	0.1	0.5	0.3

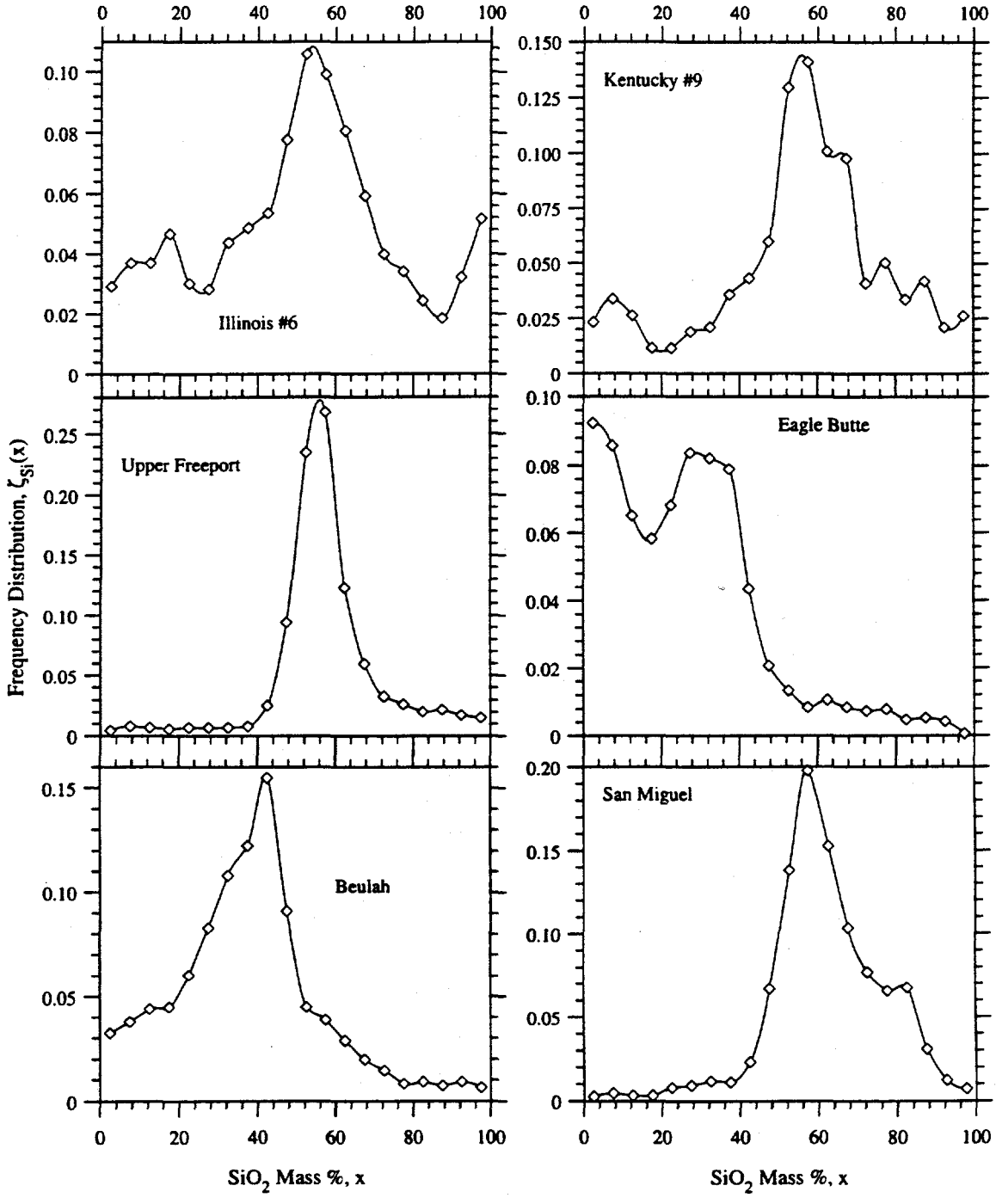

Figure G.7: SiO_2 distributions in the six ashes expressed as number fraction with oxide mass percentage x, the data being averaged over increments of 5%. Note different ordinate scales.

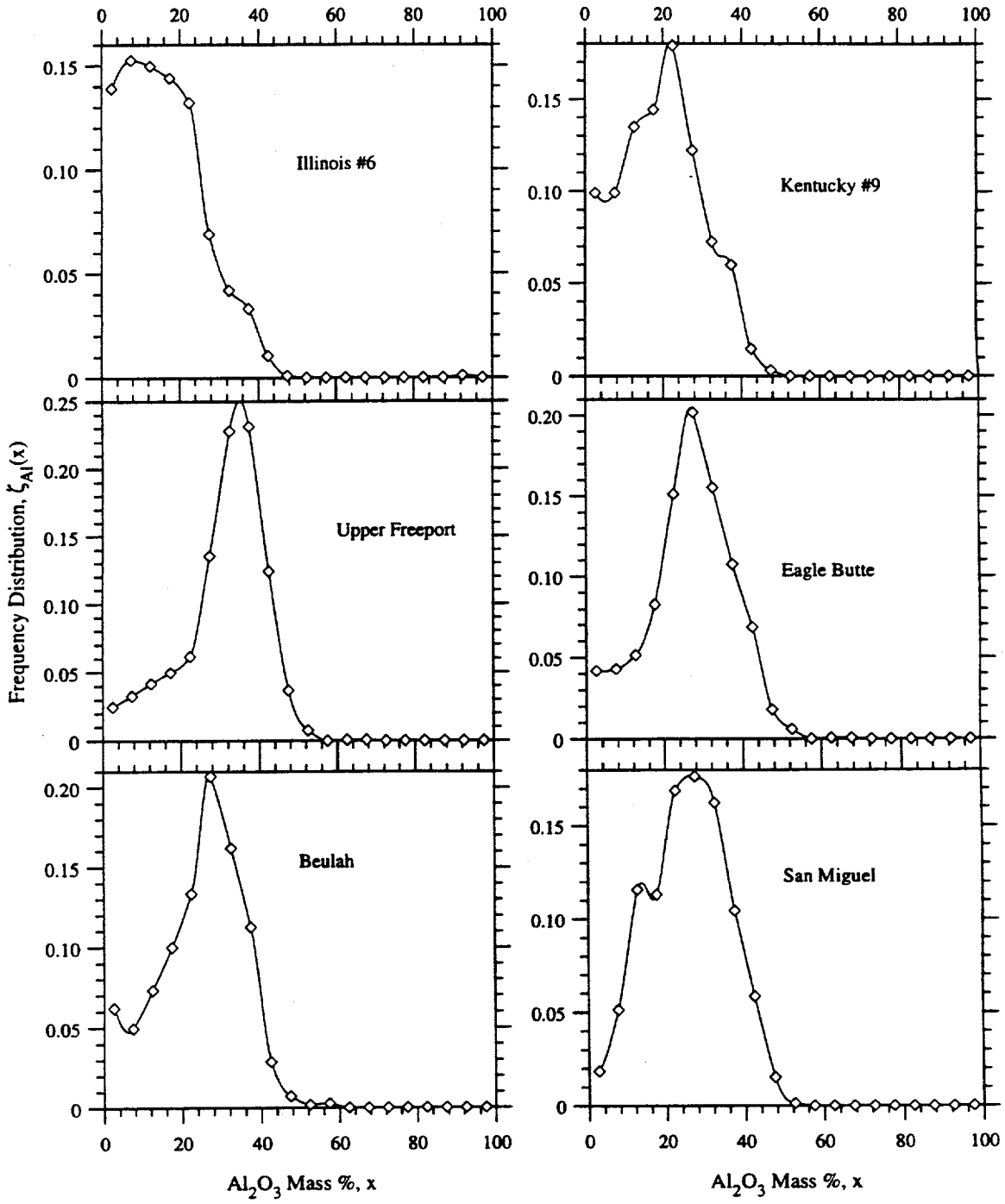

Figure G.8: Al_2O_3 distributions in the six ashes expressed as number fraction with oxide mass percentage x, the data being averaged over increments of 5%. Note different ordinate scales.

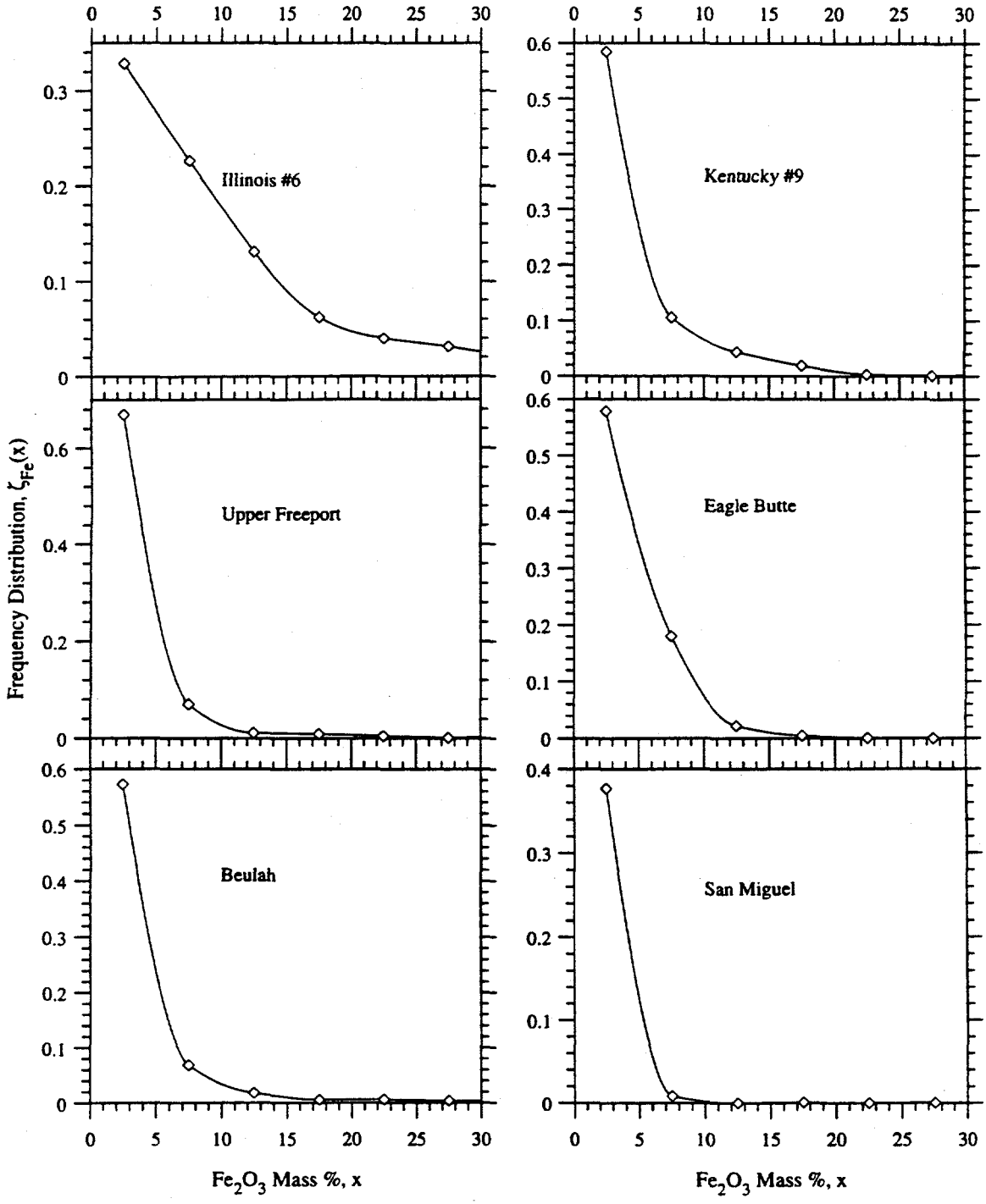

Figure G.9: Fe_2O_3 distributions in the six ashes expressed as number fraction with oxide mass percentage x, the data being averaged over increments of 5%. Note different ordinate scales.

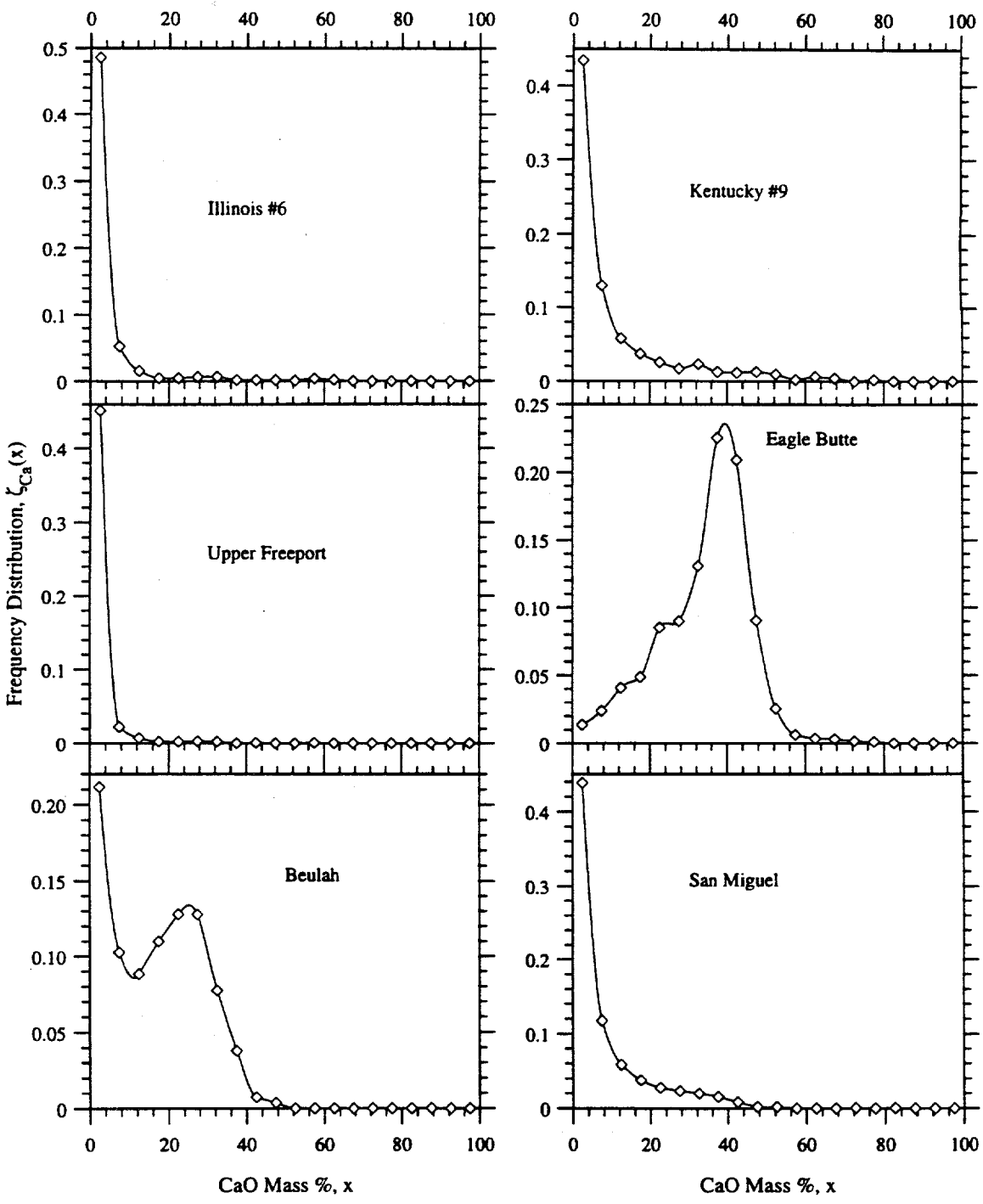

Figure G.10: CaO distributions in the six ashes expressed as number fraction with oxide mass percentage x, the data being averaged over increments of 5%. Note different ordinate scales.

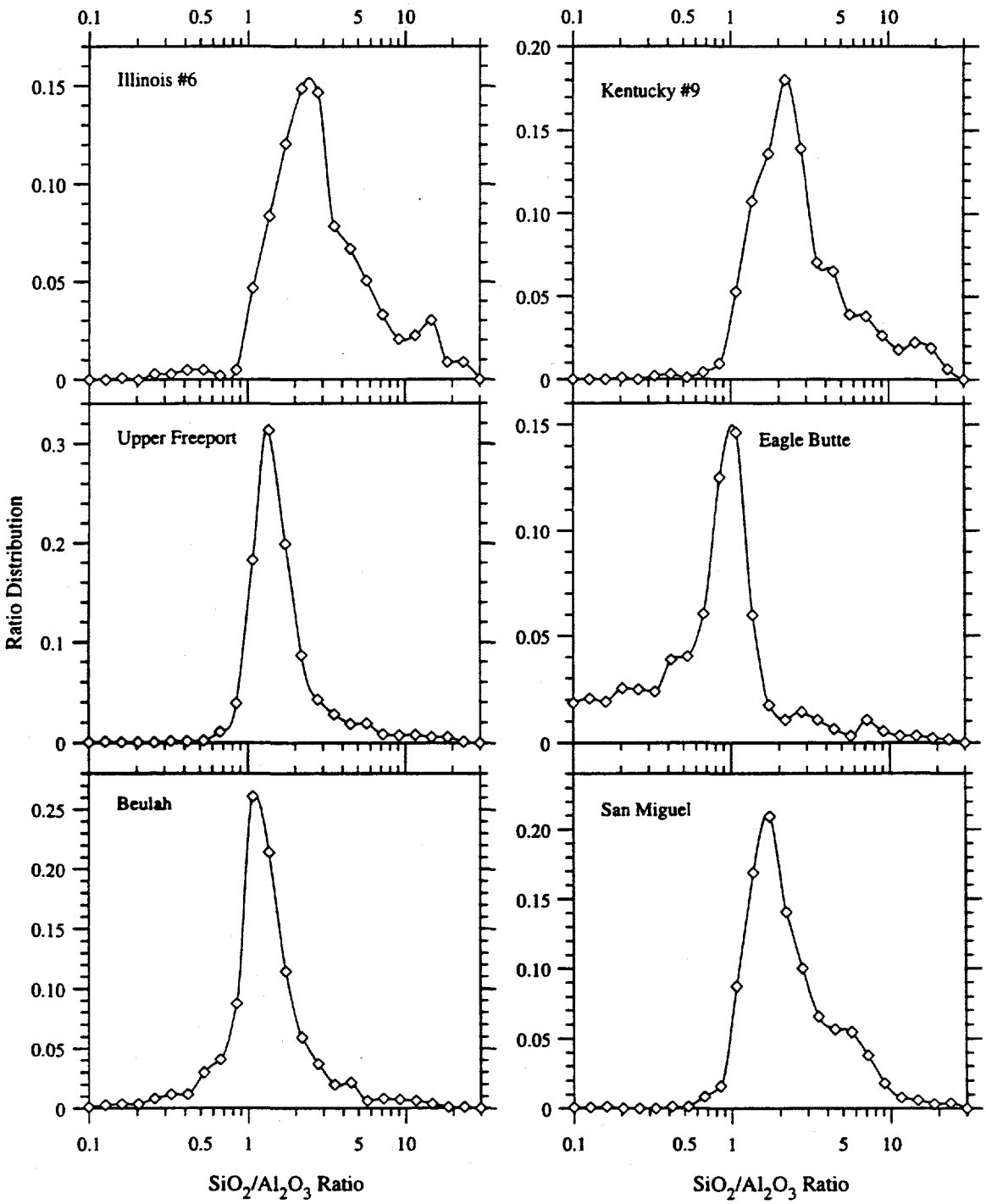

Figure G.11: Distributions of SiO_2/Al_2O_3 ratios for the six ashes expressed as number fraction with oxide ratio, x. The data has been averaged over increments of 5%. Note different ordinate scales.

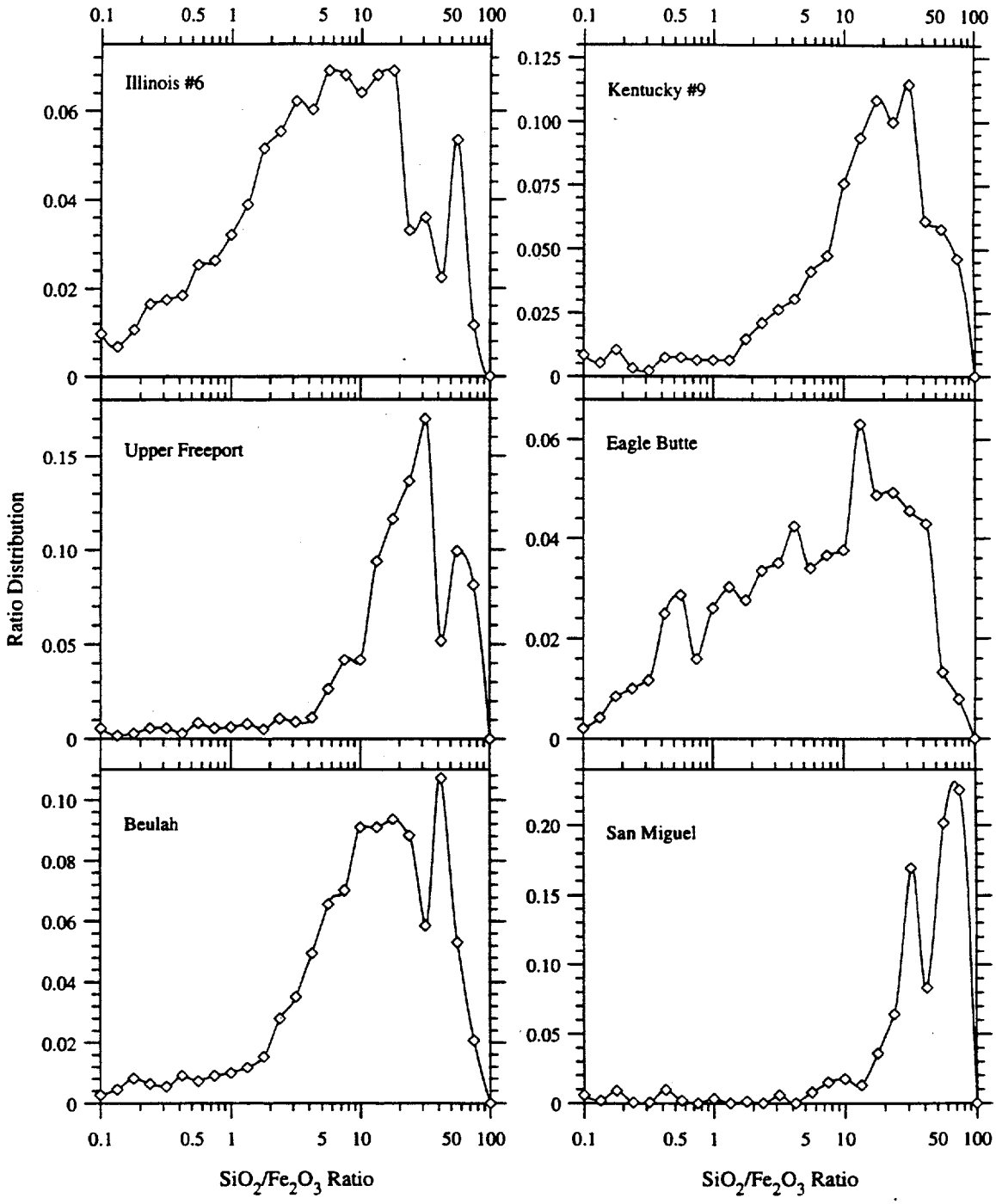

Figure G.12: Distributions of SiO_2/Fe_2O_3 ratios for the six ashes expressed as number fraction with oxide ratio, x. The data has been averaged over increments of 5%. Note different ordinate scales.

Table G.6: Comparison of bulk compositions of Illinois #6 ash. All figures are percentages, CCSEM data for 1029 particles. Column 3 and 4 show data obtained at PSI and Foster-Wheeler, respectively, after neglecting SO_3. In Column 5, ϑ_o is a bulk ash composition obtained using CCSEM and Multisizer size data (see Chapter 4). Column 6 shows the bulk composition after accounting for the Fe_2O_3 and SO_3 deficits.

	1	2	3	4	5	6
	Microprobe	**PSI**	**PSI/SO_3**	**Foster**	ϑ_o	ϑ_o/Fe_2O_3
SiO_2	49.39	46.4	48.6	50.3	57.7	58.0
Al_2O_3	21.09	18.1	19.0	18.1	14.6	14.7
Fe_2O_3	18.96	20.7	21.6	18.3	10.0	19.0
CaO	2.94	5.4	5.6	4.0	2.4	2.4
MgO	0.90	0.6	0.6	1.2	0.1	0.1
Na_2O	1.44	1.3	1.4	1.4	0.2	0.2
K_2O	2.17	2.1	2.2	2.3	2.8	2.8
Cl	0.64	N.A.	N.A.	0.0	0.3	0.3
TiO_2	0.68	0.9	0.9	0.9	1.4	1.4
SO_3	0.02	4.4	0.0	3.2	9.4	0.0
P_2O_5	0.19	0.1	0.1	0.3	0.3	0.3
BaO	1.58	N.A.	N.A.	0.0	0.8	0.8

Table G.7: Comparison of bulk compositions of Kentucky #9 ash. All figures are percentages, CCSEM data for 1029 particles. Column 3 and 4 show data obtained at PSI and Foster-Wheeler, respectively, after neglecting SO_3. In Column 5, ϑ_o is a bulk ash composition obtained using CCSEM and Multisizer size data (see Chapter 4). Column 6 shows the bulk composition after accounting for the Fe_2O_3 deficit.

	1	2	3	4	5	6
	Microprobe	**PSI**	**PSI/SO_3**	**Foster**	ϑ_o	ϑ_o/Fe_2O_3
SiO_2	47.19	44.1	46.3	44.5	61.6	57.1
Al_2O_3	28.95	20.3	21.4	18.3	18.1	16.8
Fe_2O_3	12.59	22.1	23.2	22.8	5.8	12.6
CaO	5.17	3.1	3.2	8.7	5.3	4.9
MgO	0.15	1.1	1.1	1.2	0.1	0.1
Na_2O	2.27	0.9	0.9	0.9	0.3	0.3
K_2O	2.24	2.6	2.7	2.6	2.8	2.6
Cl	0.00	N.A.	N.A.	0.0	0.4	0.3
TiO_2	1.06	1.1	1.1	0.9	1.0	1.0
SO_3	0.00	4.6	0.0	0.0	3.8	3.5
P_2O_5	0.25	0.1	0.1	0.1	0.1	0.1
BaO	0.12	N.A.	N.A.	0.0	0.7	0.7

Table G.8: Comparison of bulk compositions of Eagle Butte ash. All figures are percentages, CCSEM data for 1887 particles. Column 3 and 4 show data obtained at PSI and AMAX Coal Co., respectively, after neglecting SO_3. In Column 5, ϑ_o is a bulk ash composition obtained using CCSEM and Multisizer size data (see Chapter 4). Column 6 shows the bulk composition after accounting for the Fe_2O_3 deficit.

	1	2	3	4	5	6
	Microprobe	**PSI**	**PSI/SO_3**	**AMAX**	ϑ_o	ϑ_o/Fe_2O_3
SiO_2	28.53	28.3	32.8	35.35	25.6	25.6
Al_2O_3	17.44	15.5	18.0	14.88	20.7	20.8
Fe_2O_3	6.88	6.1	7.1	6.96	2.8	6.9
CaO	33.00	26.4	30.6	28.31	34.2	34.3
MgO	7.47	6.2	7.2	9.48	7.5	7.6
Na_2O	1.74	2.0	2.3	2.00	1.2	1.2
K_2O	0.00	0.2	0.2	0.29	0.3	0.3
Cl	1.05	N.A.	N.A.	N.A.	0.5	0.5
TiO_2	1.11	0.9	1.0	1.43	1.6	1.6
SO_3	0.01	13.7	0.0	0.0	4.4	0.0
P_2O_5	0.27	0.7	0.8	0.82	0.4	0.4
BaO	2.50	N.A.	N.A.	N.A.	0.8	0.8
Unknown	—	—	—	0.48	—	—

Table G.9: Comparison of bulk compositions of Beulah ash. All figures are percentages, CCSEM data for 1111 particles. Column 3 shows the PSI data after neglecting SO_3. In Column 4, ϑ_o is a bulk ash composition obtained using CCSEM and Multisizer size data (see Chapter 4). Column 5 shows the bulk composition after accounting for the Fe_2O_3 and SO_3 deficits.

	1	2	3	4	5
	Microprobe	**PSI**	**PSI/SO_3**	ϑ_o	ϑ_o/Fe_2O_3
SiO_2	31.70	22.2	28.4	38.1	36.5
Al_2O_3	33.51	14.9	19.1	26.2	25.1
Fe_2O_3	16.88	12.6	16.0	3.1	16.9
CaO	7.56	17.6	22.5	10.7	10.3
MgO	3.37	4.3	5.5	3.4	3.2
Na_2O	6.68	6.4	8.1	3.4	3.3
K_2O	1.49	0.3	0.4	1.8	1.7
Cl	0.02	N.A.	N.A.	1.4	1.3
TiO_2	0.67	0.0	0.0	0.9	0.9
SO_3	0.01	21.7	0.0	10.2	0.0
P_2O_5	0.39	0.0	0.0	0.2	0.2
BaO	0.62	N.A.	N.A.	0.6	0.6

Table G.10: Comparison of bulk compositions of San Miguel ash. All figures are percentages, CCSEM data for 1774 particles. Column 3 shows the PSI data after neglecting SO_3. In Column 4, ϑ_o is a bulk ash composition obtained using CCSEM and Multisizer size data (see Chapter 4). Column 5 shows the bulk composition after accounting for the Fe_2O_3 deficit.

	1	2	3	4	5
	Microprobe	**PSI**	**PSI/SO_3**	ϑ_o	ϑ_o/**Fe_2O_3**
SiO_2	64.66	65.9	67.7	69.1	67.7
Al_2O_3	21.51	20.5	21.1	21.7	21.3
Fe_2O_3	2.75	1.9	2.0	0.8	2.8
CaO	4.85	3.2	3.3	3.0	2.9
MgO	0.10	0.5	0.5	0.0	0.0
Na_2O	3.34	2.5	2.6	2.4	2.4
K_2O	1.80	1.8	1.9	1.0	1.0
Cl	0.01	N.A.	N.A.	0.2	0.2
TiO_2	0.91	0.9	0.9	0.8	0.7
SO_3	0.00	2.7	0.0	0.5	0.5
P_2O_5	0.03	<0.1	<0.1	0.0	0.0
BaO	0.12	N.A.	N.A.	0.5	0.5

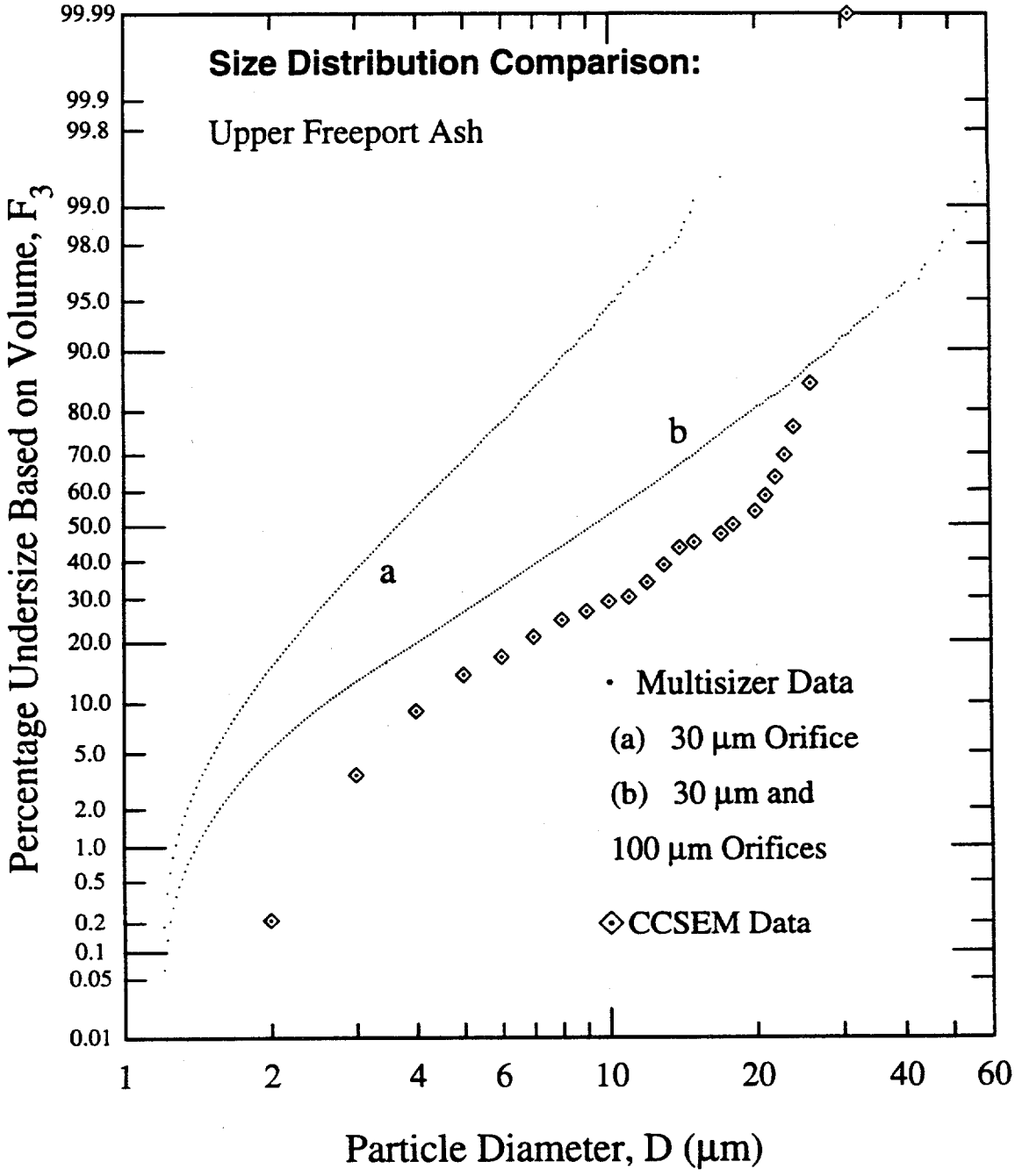

Figure G.13: Comparison of Upper Freeport ash size distribution obtained with Coulter Multisizer measurements (using three different sets of orifices) with CCSEM size data.

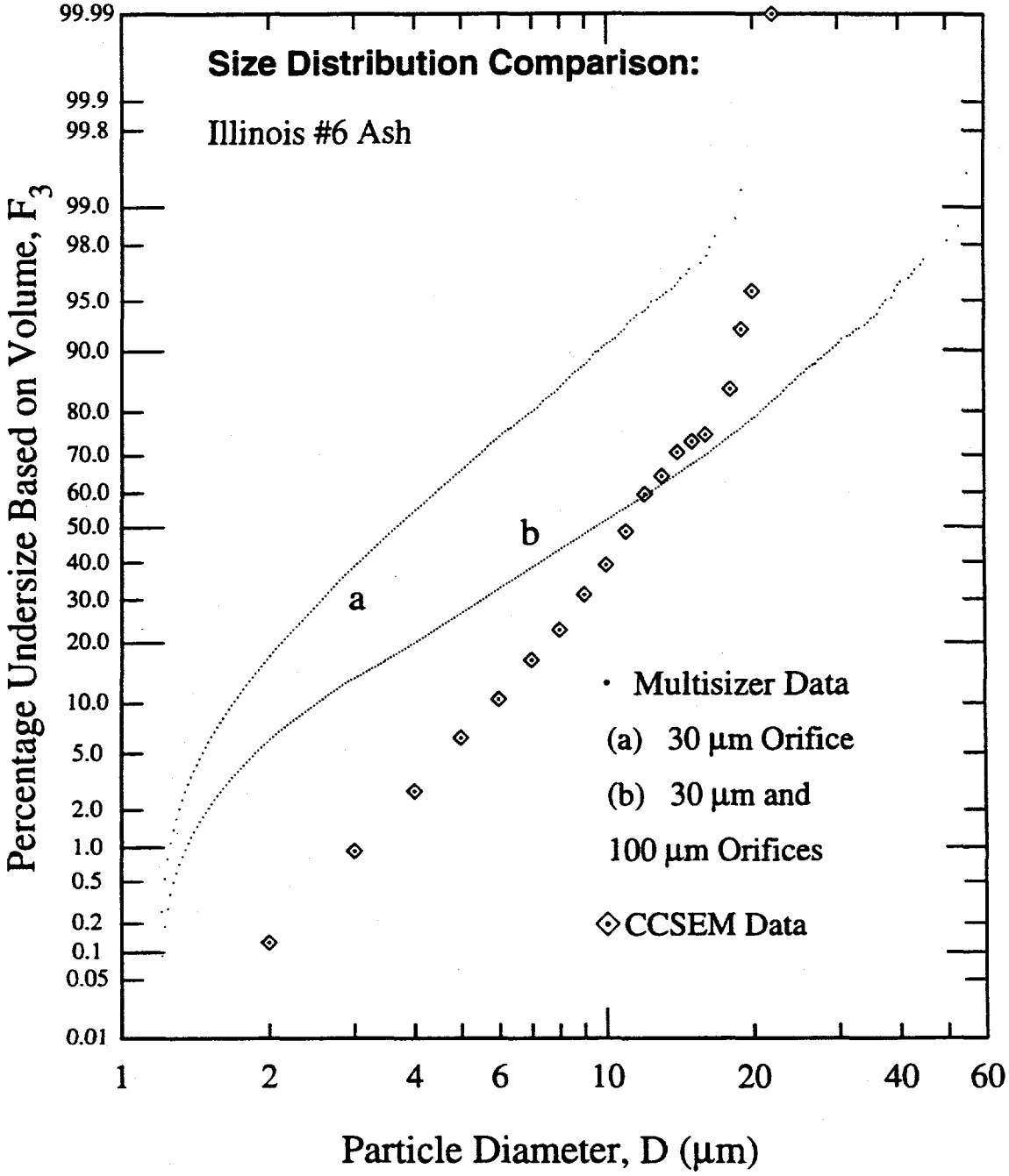

Figure G.14: Comparison of Illinois #6 ash size distribution obtained with Coulter Multisizer measurements (using three different sets of orifices) with CCSEM size data.

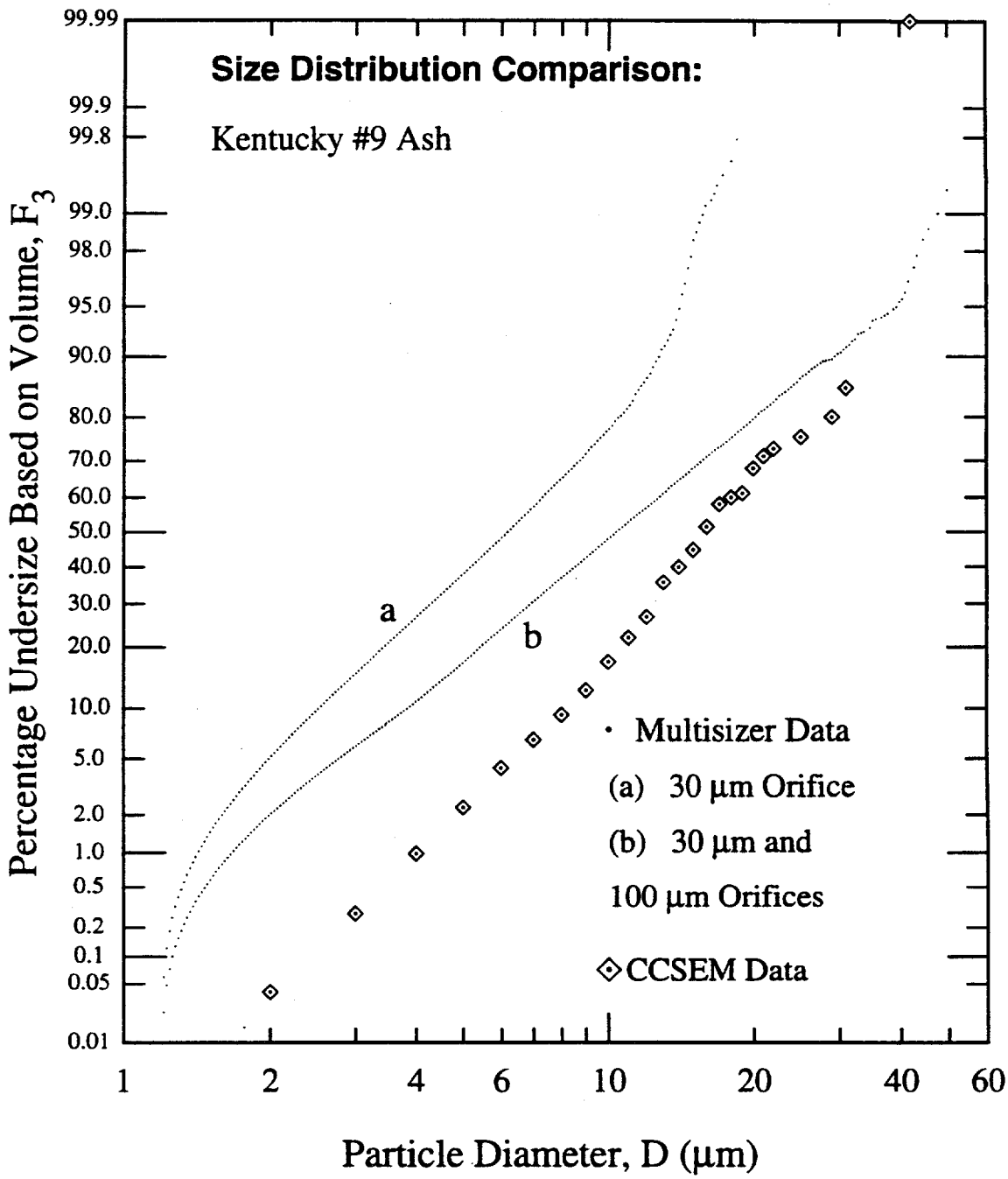

Figure G.15: Comparison of Kentucky #9 ash size distribution obtained with Coulter Multisizer measurements (using three different sets of orifices) with CCSEM size data.

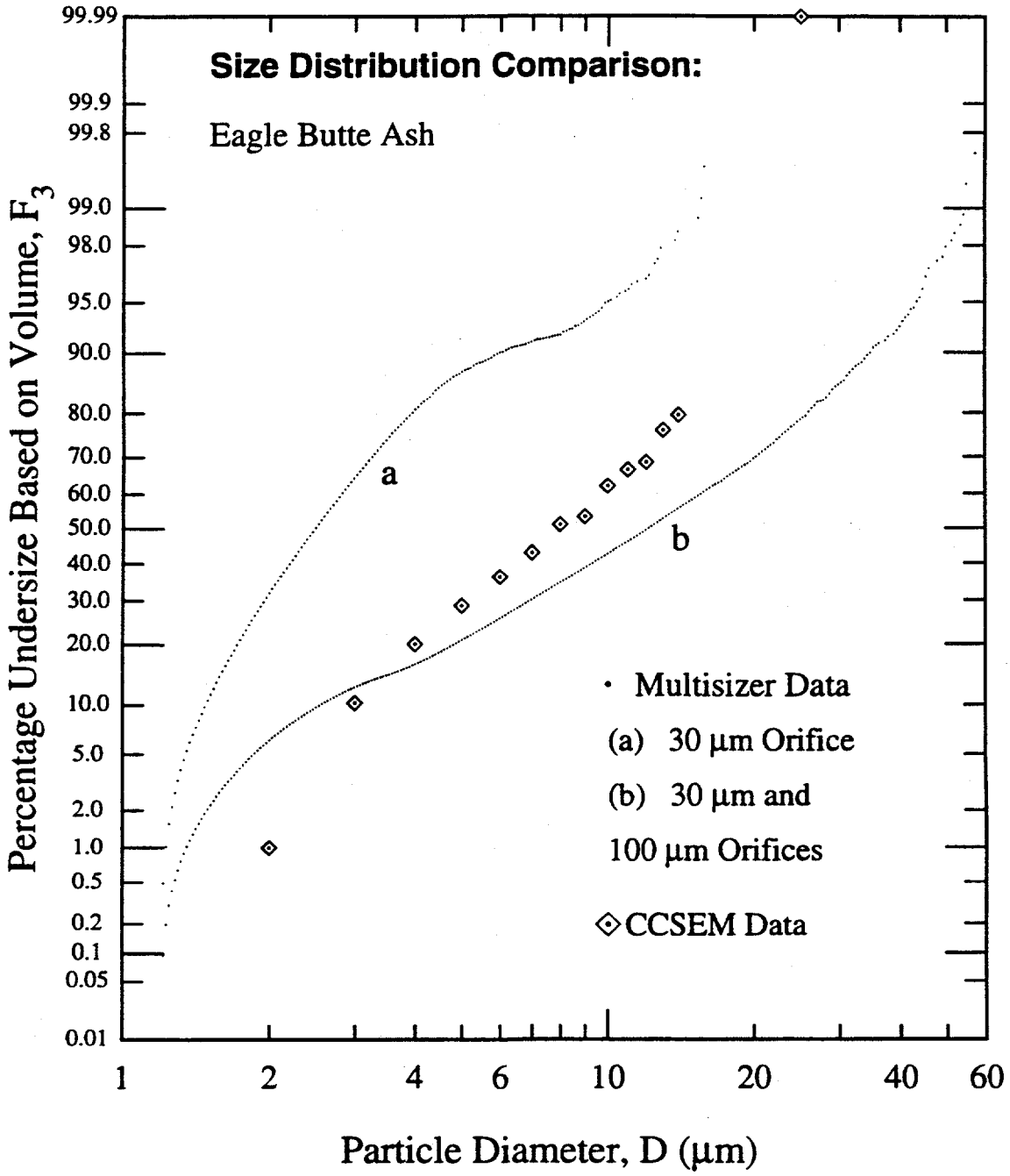

Figure G.16: Comparison of Eagle Butte ash size distribution obtained with Coulter Multisizer measurements (using three different sets of orifices) with CCSEM size data.

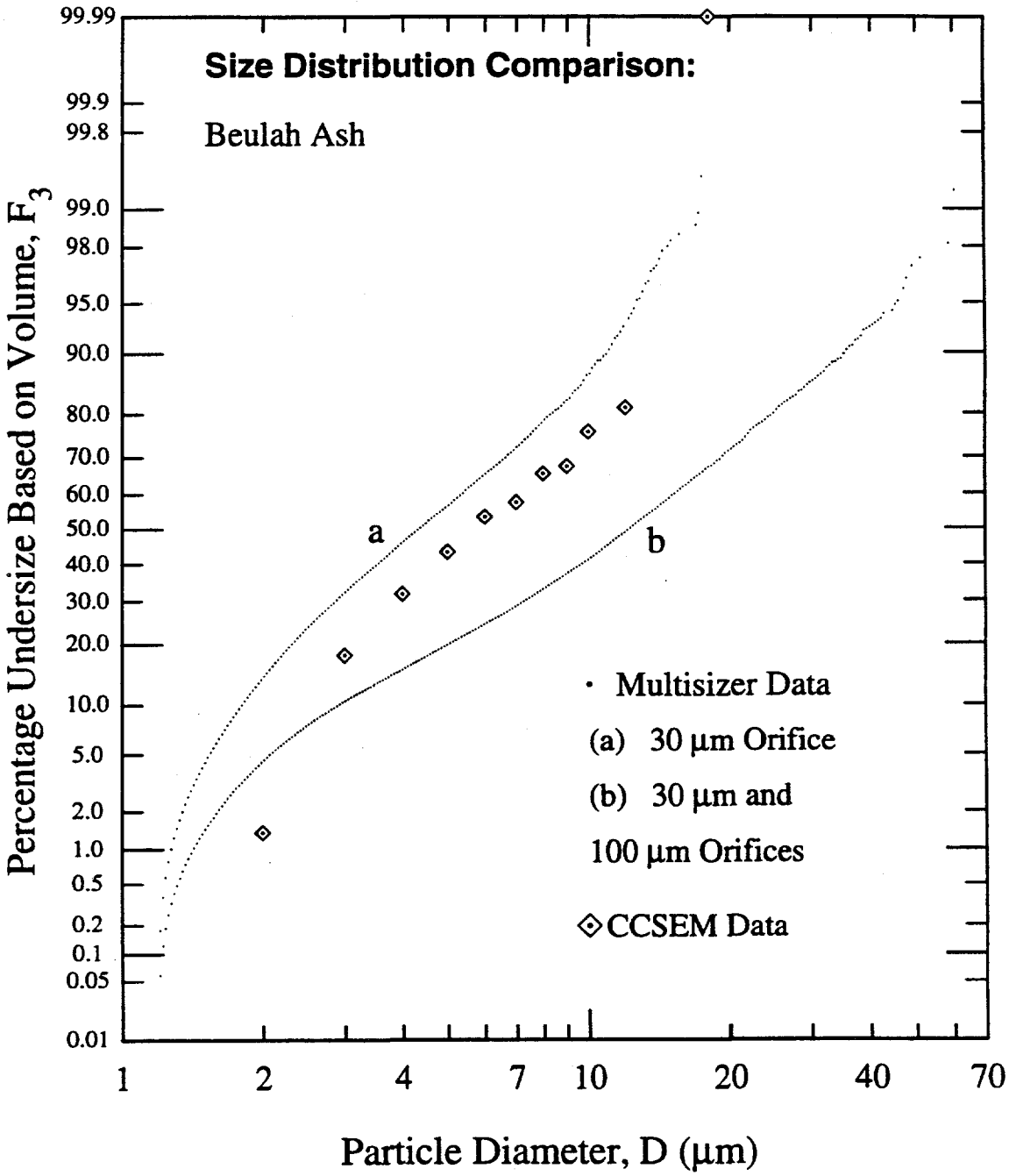

Figure G.17: Comparison of size distribution of the Beulah ash obtained with Coulter Multisizer measurements (using three different sets of orifices) with CCSEM size data.

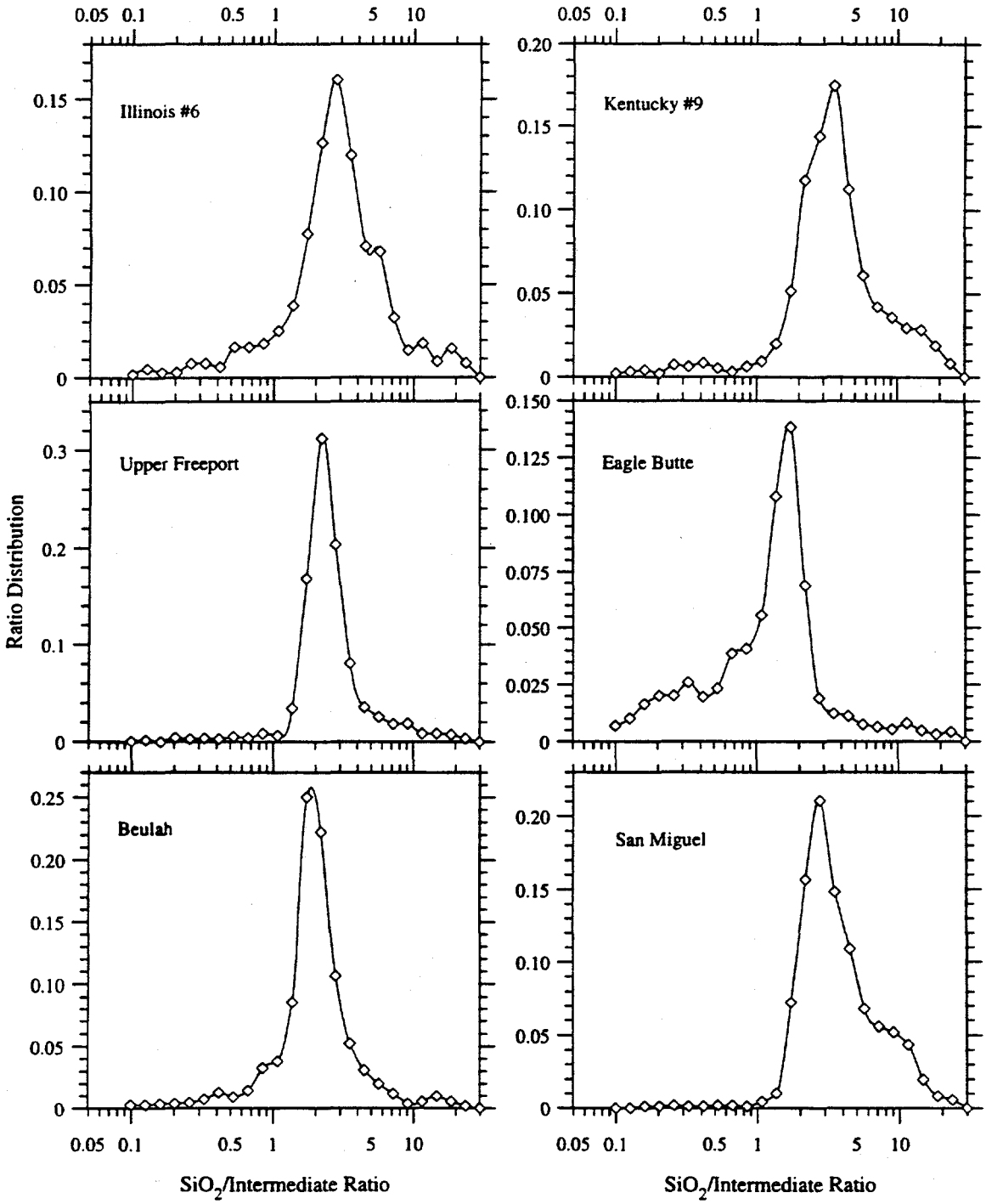

Figure G.18: Distributions of $SiO_2/(Al_2O_3+Fe_2O_3)$ ratios (glass former/glass intermediates) for the six ashes expressed as number fraction with oxide ratio, x. The data has been averaged over increments of 5%. Note different ordinate scales.

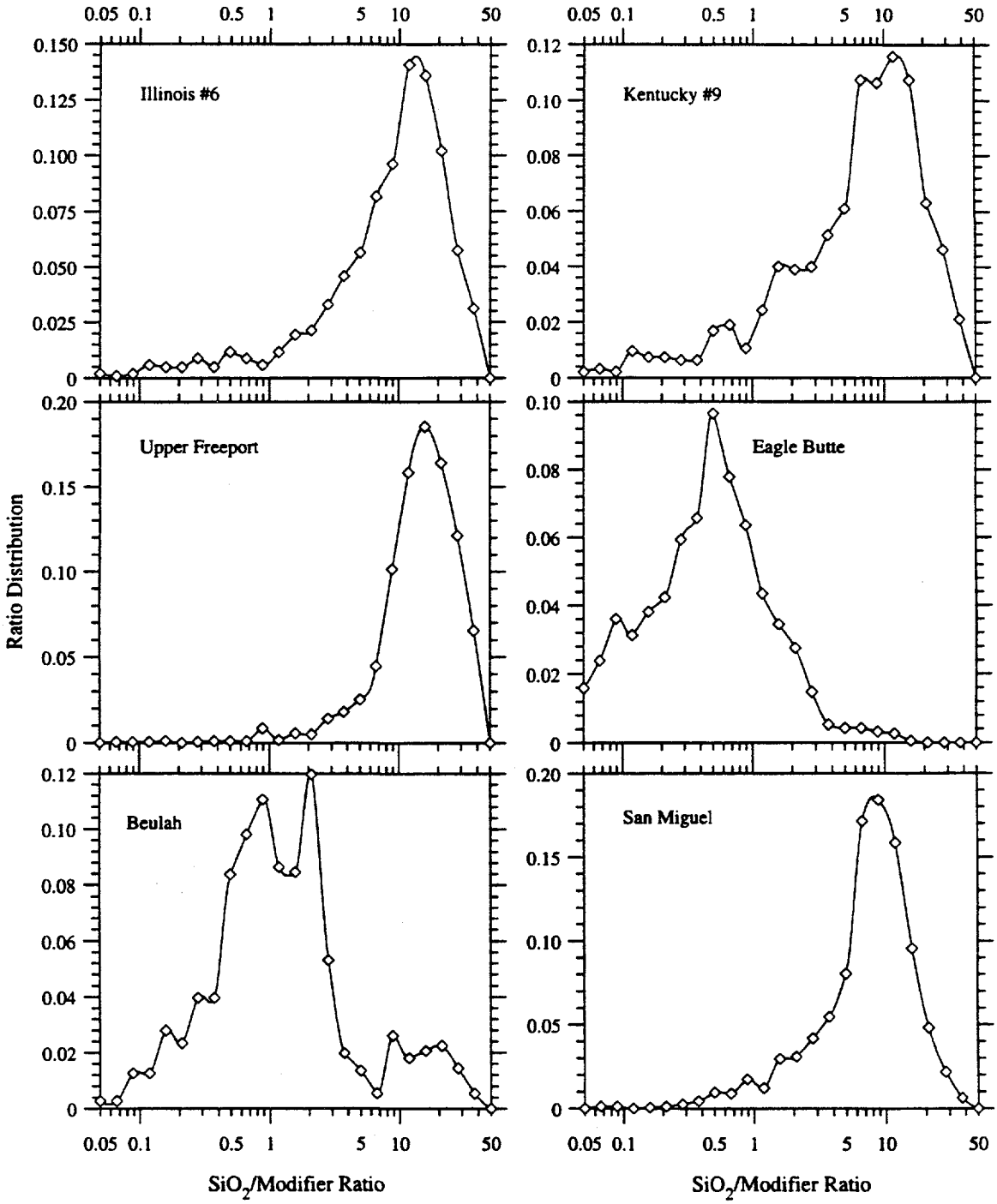

Figure G.19: Distributions of $SiO_2/(CaO+MgO+Na_2O+K_2O+BaO)$ ratios (i.e., ratios of glass former/glass modifiers) for the six ashes expressed as number fraction with oxide ratio, x. The data has been averaged over increments of 5%. Note different ordinate scales.

Appendix H

Tabulated refractive indices for CS_2, $CHBr_3$, and CCl_4

The spectral refractive indices of CS_2, $CHBr_3$, and CCl_4, measured using the near-normal reflectance technique at room temperature (see Chapter 5) are tabulated in this Appendix.

Table H.1: Spectral refractive index of CS_2.

$\lambda\,(\mu m)$	n	$\lambda\,(\mu m)$	n	$\lambda\,(\mu m)$	n
7.3	1.740	8.5	1.655	9.7	1.634
7.4	1.710	8.6	1.645	9.8	1.635
7.5	1.697	8.7	1.648	9.9	1.633
7.6	1.683	8.8	1.643	10.0	1.635
7.7	1.680	8.9	1.645	10.2	1.628
7.8	1.674	9.0	1.644	10.3	1.624
7.9	1.671	9.1	1.640	10.4	1.626
8.0	1.663	9.2	1.641	10.5	1.621
8.1	1.667	9.3	1.638	10.6	1.629
8.2	1.657	9.4	1.636	10.7	1.622
8.3	1.660	9.5	1.636	10.8	1.630
8.4	1.651	9.6	1.636	11.0	1.630

Table H.2: Spectral refractive index of $CHBr_3$.

λ (μm)	n	λ (μm)	n	λ (μm)	n	λ (μm)	n
1.0	1.584	3.6	1.572	7.7	1.557	10.0	1.565
1.1	1.583	3.7	1.573	7.8	1.558	10.1	1.565
1.2	1.581	3.8	1.572	7.9	1.556	10.2	1.563
1.3	1.582	3.9	1.573	8.0	1.553	10.3	1.562
1.4	1.581	4.0	1.572	8.1	1.551	10.4	1.560
1.5	1.579	4.1	1.570	8.2	1.548	10.5	1.559
1.6	1.580	4.4	1.569	8.3	1.546	10.6	1.559
1.7	1.576	4.5	1.571	8.4	1.540	10.7	1.557
1.8	1.577	4.6	1.571	8.45	1.536	10.75	1.556
1.9	1.573	4.7	1.569	8.5	1.528	10.8	1.558
2.0	1.578	4.8	1.569	8.55	1.520	10.85	1.554
2.1	1.578	5.0	1.568	8.6	1.505	10.9	1.554
2.2	1.577	5.2	1.564	8.65	1.478	11.0	1.556
2.3	1.576	5.4	1.566	8.7	1.434	11.1	1.550
2.4	1.572	5.5	1.566	8.75	1.458	11.15	1.548
2.5	1.573	5.6	1.565	8.76	1.488	11.2	1.549
2.6	1.571	5.7	1.564	8.78	1.567	11.3	1.544
2.7	1.573	5.8	1.564	8.8	1.649	11.4	1.544
2.8	1.573	6.0	1.565	8.82	1.703	11.5	1.543
3.0	1.573	6.2	1.564	8.84	1.720	11.6	1.543
3.1	1.575	6.25	1.567	8.85	1.719	11.7	1.542
3.2	1.574	6.3	1.565	8.86	1.710	11.8	1.542
3.25	1.572	6.4	1.563	8.9	1.668	11.9	1.540
3.27	1.569	6.45	1.568	8.95	1.635	12.0	1.539
3.275	1.567	6.6	1.564	9.0	1.617	12.1	1.537
3.29	1.566	6.7	1.564	9.1	1.592	12.2	1.532
3.3	1.565	6.9	1.558	9.2	1.584	12.3	1.530
3.31	1.560	7.0	1.564	9.3	1.577	12.4	1.527
3.32	1.571	7.1	1.557	9.4	1.573	12.5	1.526
3.325	1.583	7.2	1.560	9.5	1.569	12.6	1.524
3.33	1.587	7.3	1.562	9.6	1.568	12.7	1.526
3.35	1.582	7.4	1.559	9.7	1.565	12.8	1.522
3.4	1.573	7.5	1.557	9.8	1.564	12.9	1.516
3.5	1.572	7.6	1.559	9.9	1.561	13.0	1.509

Table H.3: Spectral refractive index of CCl_4 (Ebert *et al*, 1991).

$\lambda\ (\mu m)$	n	$\lambda\ (\mu m)$	n	$\lambda\ (\mu m)$	n
1.0	1.457	3.6	1.449	6.5	1.436
1.1	1.455	3.7	1.447	6.6	1.435
1.2	1.455	3.8	1.446	6.7	1.430
1.3	1.454	3.9	1.446	6.8	1.435
1.4	1.454	4.0	1.444	6.9	1.427
1.5	1.452	4.1	1.446	7.0	1.430
1.6	1.454	4.2	1.449	7.1	1.429
1.7	1.453	4.4	1.445	7.2	1.431
1.8	1.454	4.5	1.446	7.3	1.429
1.9	1.453	4.6	1.445	7.4	1.429
2.0	1.453	4.7	1.444	7.5	1.427
2.1	1.453	4.8	1.444	7.6	1.426
2.2	1.453	4.9	1.442	7.7	1.426
2.3	1.453	5.0	1.444	7.8	1.424
2.4	1.453	5.1	1.441	7.9	1.423
2.5	1.451	5.2	1.441	8.0	1.420
2.6	1.454	5.3	1.442	8.1	1.423
2.7	1.450	5.4	1.440	8.2	1.420
2.8	1.451	5.5	1.440	8.3	1.421
2.9	1.449	5.6	1.440	8.4	1.420
3.0	1.451	5.8	1.439	8.5	1.419
3.1	1.449	5.9	1.433	8.6	1.416
3.2	1.450	6.0	1.440	8.7	1.416
3.3	1.448	6.2	1.436	8.8	1.413
3.4	1.450	6.3	1.430	8.9	1.414
3.5	1.447	6.4	1.432	9.0	1.410

Appendix I

Composition and Refractive Index Classes

This section tabulates the composition classes developed in Chapter 4 for five of the six characterized ashes (the classes for the Illinois #6 ash were given in Section 4.4.3). The refractive index classes have been obtained from this information using correlations developed by Ebert (1993), and are given graphically.

Table I.1: Composition classes for Upper Freeport ash. All oxide numbers are mass percentages.

Class	SiO_2	Al_2O_3	Fe_2O_3	CaO	MgO	TiO_2	Others	Vol. %
1	57.1	34.6	2.1	0.8	0.2	0.7	4.4	36.1
2	65.2	26.8	1.8	0.6	0.3	0.6	4.6	18.2
3	84.5	9.5	1.1	0.5	0.1	0.4	3.9	13.9
4	50.0	38.6	3.4	1.5	0.5	1.1	5.0	25.5
5	20.2	17.3	41.6	5.3	1.3	2.6	11.7	6.3

Table I.2: Composition classes Kentucky #9 ash. All oxide numbers are mass percentages.

Class	SiO_2	Al_2O_3	Fe_2O_3	CaO	MgO	TiO_2	Others	Vol. %
1	54.7	26.9	3.2	5.1	0.1	1.4	8.6	30.0
2	67.2	20.3	2.4	2.5	0.1	0.8	6.6	33.5
3	87.4	6.0	0.7	1.4	0.0	0.6	3.9	19.8
4	41.0	20.4	7.6	12.8	0.4	2.7	15.2	7.8
5	10.7	6.3	26.2	25.1	0.5	1.7	29.5	9.6

Table I.3: Composition classes Eagle Butte ash. All oxide numbers are mass percentages.

Class	SiO_2	Al_2O_3	Fe_2O_3	CaO	MgO	TiO_2	Others	Vol. %
1	18.1	24.7	3.0	34.6	10.7	1.6	7.2	15.5
2	10.7	27.6	3.6	41.1	8.3	1.6	7.1	33.3
3	6.8	23.3	4.6	50.8	6.1	1.8	6.6	16.9
4	25.4	22.2	2.6	27.1	14.7	1.6	6.3	12.5
5	45.0	21.9	1.7	14.8	9.5	1.1	6.0	21.8

Table I.4: Composition classes Beulah ash. All oxide numbers are mass percentages.

Class	SiO_2	Al_2O_3	Fe_2O_3	CaO	MgO	TiO_2	Others	Vol. %
1	36.6	26.8	2.4	19.2	4.8	1.3	8.9	24.2
2	46.6	30.2	1.4	7.9	1.5	0.8	11.6	28.4
3	70.9	15.7	1.7	3.1	0.9	0.4	7.3	13.8
4	25.2	22.8	4.0	25.5	9.6	1.6	11.3	18.0
5	7.1	13.2	15.8	17.4	8.8	2.8	35.0	15.5

Table I.5: Composition classes San Miguel ash. All oxide numbers are mass percentages.

Class	SiO_2	Al_2O_3	Fe_2O_3	CaO	MgO	TiO_2	Others	Vol. %
1	61.0	28.2	0.5	4.5	0.1	0.8	4.9	24.2
2	70.2	20.4	0.5	3.1	0.1	0.6	5.1	20.2
3	83.5	10.2	0.3	1.3	0.1	0.3	4.4	21.1
4	53.2	34.1	0.6	6.2	0.1	0.8	4.9	29.1
5	30.7	23.7	8.2	26.3	2.1	2.4	6.6	7.4

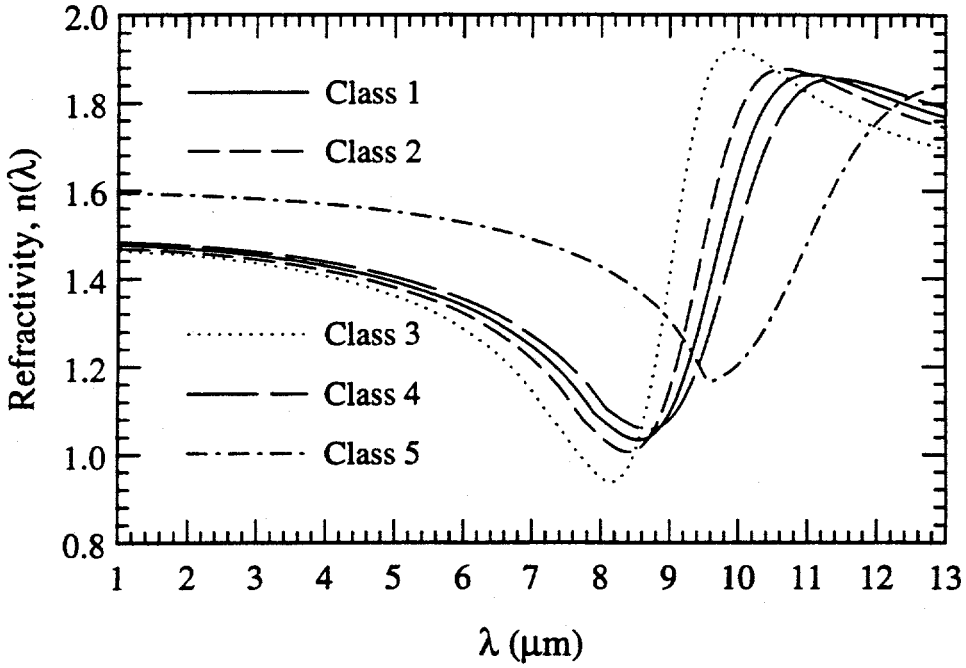

Figure I.1: The real part of the refractive index, $n(\lambda)$, of the five classes of Upper Freeport ash.

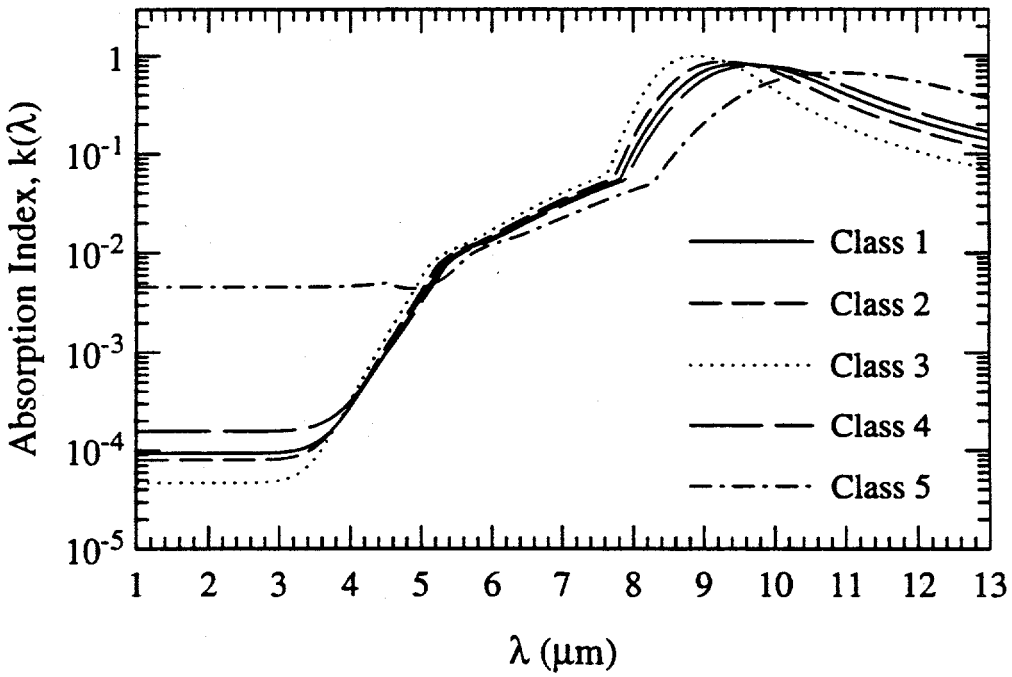

Figure I.2: The imaginary part of the refractive index, $k(\lambda)$, of the five classes of Upper Freeport ash.

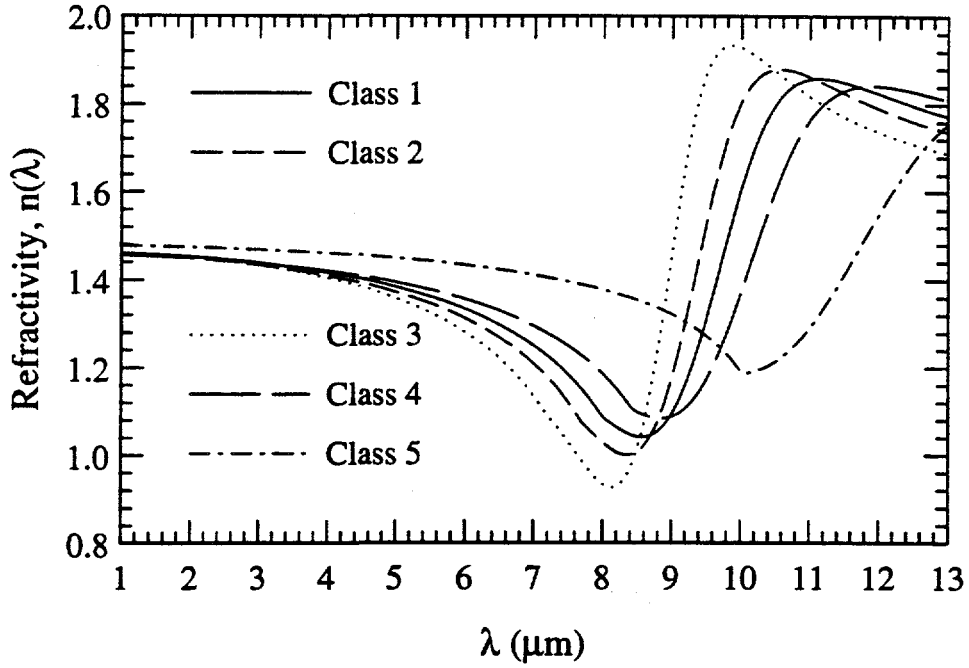

Figure I.3: The real part of the refractive index, $n(\lambda)$, of the five classes of Kentucky #9 ash.

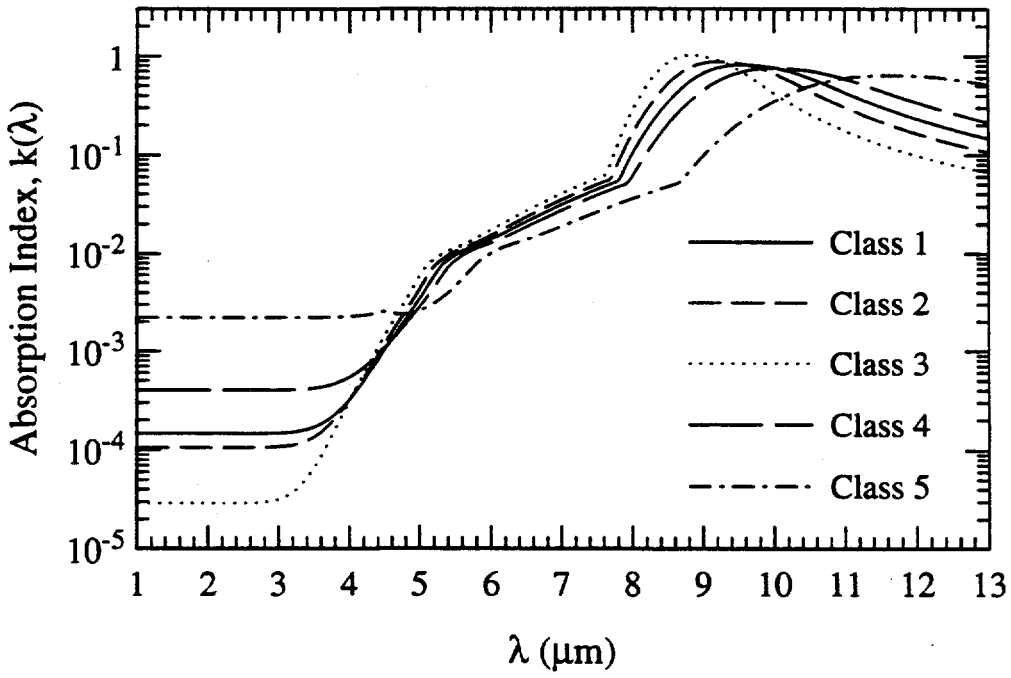

Figure I.4: The imaginary part of the refractive index, $k(\lambda)$, of the five classes of Kentucky #9 ash.

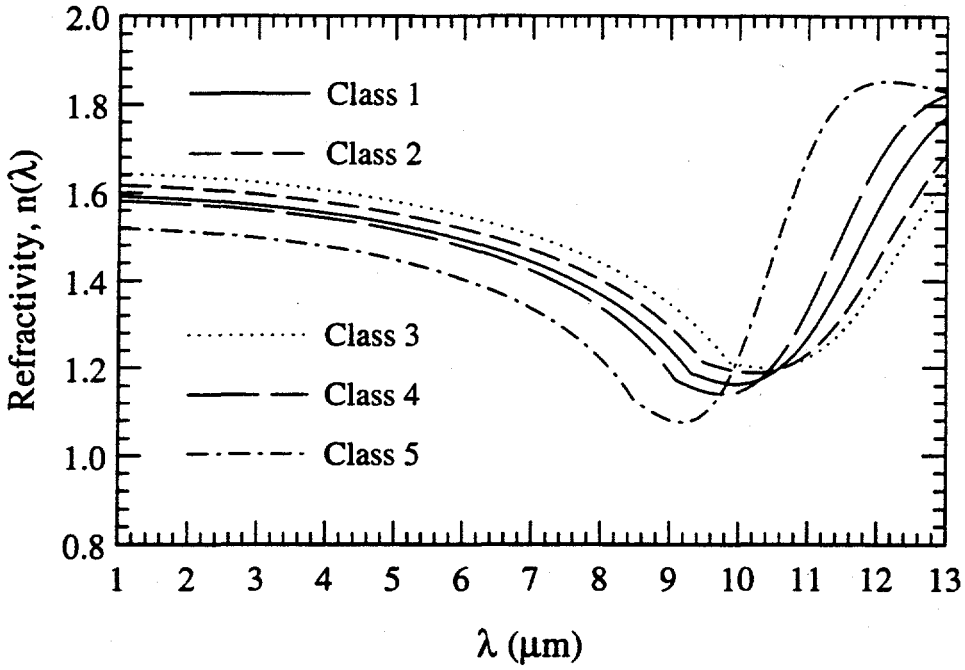

Figure I.5: The real part of the refractive index, $n(\lambda)$, of the five classes of Eagle Butte ash.

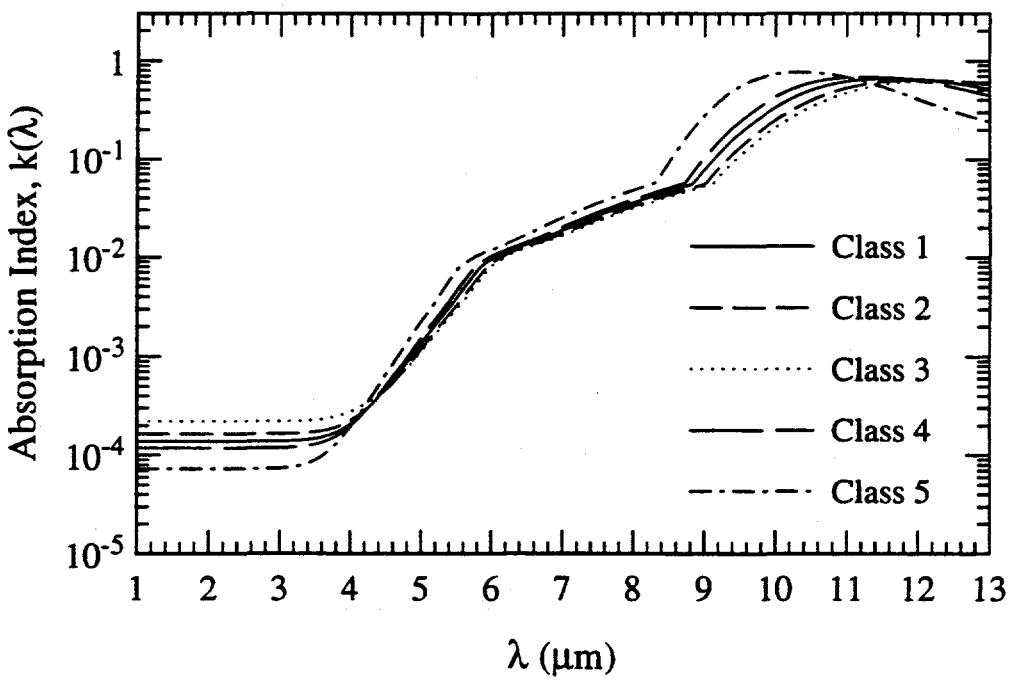

Figure I.6: The imaginary part of the refractive index, $k(\lambda)$, of the five classes of Eagle Butte ash.

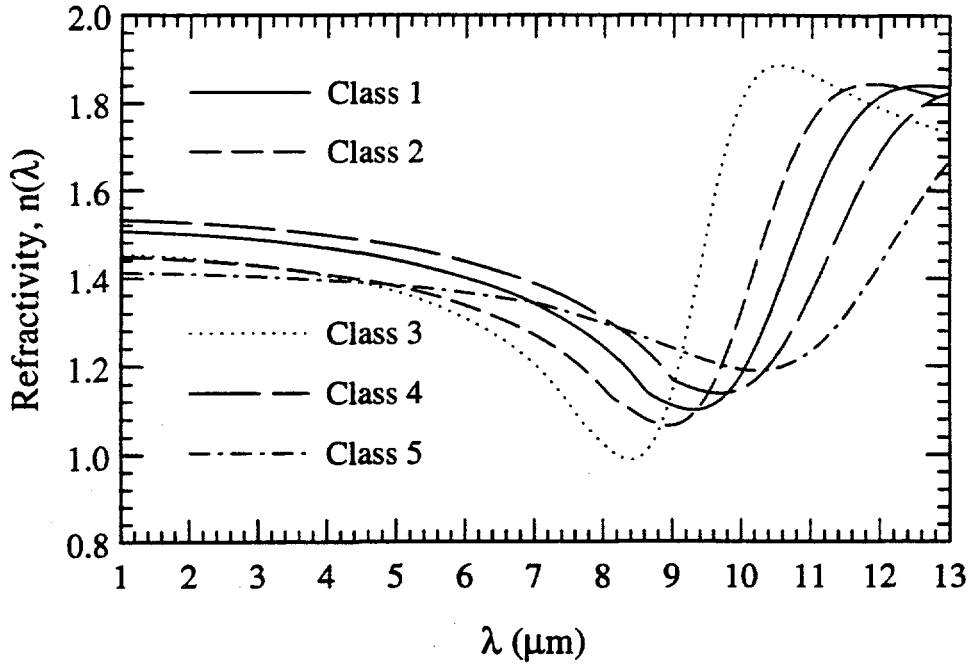

Figure I.7: The real part of the refractive index, $n(\lambda)$, of the five classes of Beulah ash.

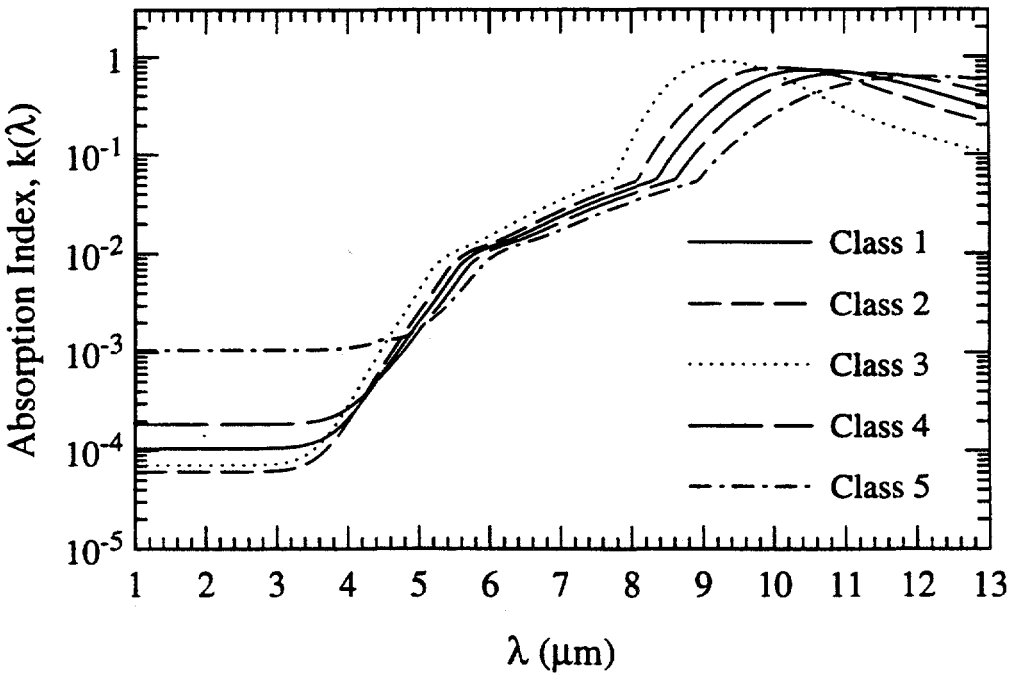

Figure I.8: The imaginary part of the refractive index, $k(\lambda)$, of the five classes of Beulah ash.

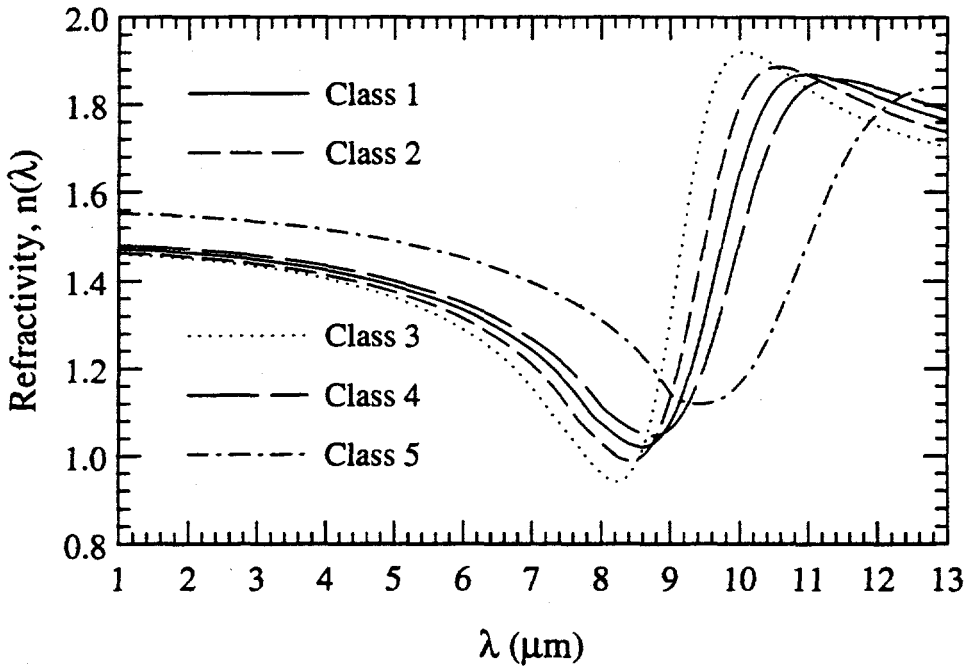

Figure I.9: The real part of the refractive index, $n(\lambda)$, of the five classes of San Miguel ash.

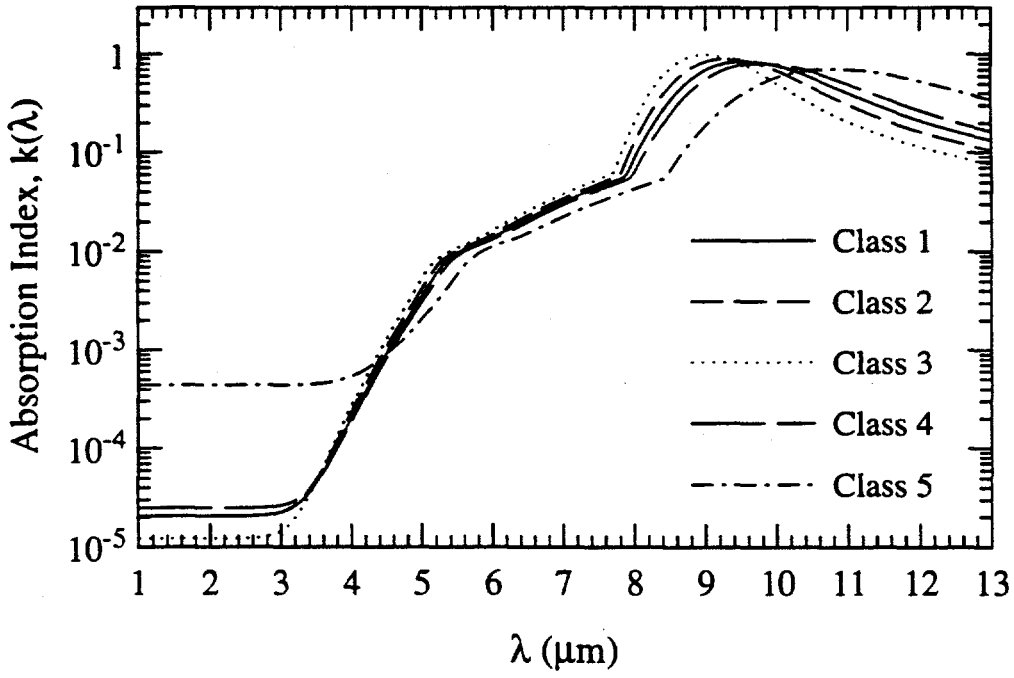

Figure I.10: The imaginary part of the refractive index, $k(\lambda)$, of the five classes of San Miguel ash.

Bibliography

[1] Aden G. D., and P. R. Buseck (1983). A Minicomputer Procedure for Quantitative EDS Analysis of Small Particles. *Microbeam Analysis*, 195.

[2] Aitchison, J., and J. A. C. Brown (1957). The Lognormal Distribution. Cambridge University Press, Cambridge, U.K.

[3] Allen, T. (1981). Particle Size Measurement. Chapman and Hall, London.

[4] Appen, A. A. (1970). The Chemistry of Glass, (in Russian), Izd. Chimia, Leningrad. Translated Data in: M .B. Volf. (1988). *Mathematical Approach to Glass*, Elsevier.

[5] Armstrong, J. T. (1978). Methods of Quantitative Analyses of Individual Microparticles with Electron Beam Instruments. *Scanning Electron Microscopy*, **1**, SEM Inc., AMF O'Hara, IL 60666, USA.

[6] Armstrong, J. T. (1983) Rapid Quantitative Analysis of Individual Microparticles Using the α-Factor Approach. *Microbeam Analysis*, 193.

[7] Barta L. E., G. Vamos, M. A. Toqan, J. D. Teare, J. M. Beer, A. F. Sarofim (1990). A Statistical Investigation on Particle to Particle Variation of Fly Ash Using SEM-AIA-EDAX Technique, *Material Research Society Symposium Proceedings*, **178**, 67–82.

[8] Bates, L. (1962). Ligand Field Theory and Absorption Spectra of Transition Metal-Ions in Glasses. In *Modern Aspects of the Vitreous State. Volume 2*, ed. J. D. Mackenzie. Butterworths, Washington.

[9] Bendow, B. (1978). Multiphonon Infrared Absorption in the Highly Transparent Frequency Regime of Solids. *Solid State Physics*, **33**, Academic Press, New York.

[10] Benson, S. (1989). Personal communication. Energy and Environmental Research Center. Grand Forks, ND 58202.

[11] Bohren, C. F., and D. R. Huffman (1983). *Absorption and Scattering of Light by Small Particles*, John Wiley & Sons.

[12] Boothroyd, S. A., and A. R. Jones (1984). Radiative Transfer Scattering Data Relevant to Fly Ash. *Journal of Physics D: Applied Physics*, **17**, 1107–1114.

[13] Boothroyd, S. A., and A. R. Jones (1986). A Comparison of Radiative Characteristics for Fly Ash and Coal. *International Journal of Heat and Mass Transfer*, **29**:11, 1649–1654.

[14] Born, M., and E. Wolf (1980). Principles of Optics. Sixth Edition, Pergamon Press, Oxford.

[15] Brown, J. A., and A. Teetsov (1976). Some Techniques for Handling Particles in SEM Studies. *Scanning Electron Microscopy. Proceedings of the Workshop on Techniques for Particulate Matter Studies in SEM (Part III)*, IIT Research Institute, Chicago.

[16] Browning, J. S. (1961). Heavy Liquids and Procedures for Laboratory Separation of Minerals. U.S. Department of the Interior, Bureau of Mines Information Circular No.8007, Washington D.C.

[17] Casuccio, G. S., P. B. Janocko, R. J. Lee, J. F. Kelly, S. L. Dattner, and J. S. Mgebroff (1983). The Use of Computer Controlled Scanning Electron Microscopy in Environmental Studies. *Journal of Air Pollution Control Association*, **33**:10, 937–943.

[18] Cardona, M. (1969). Optical Constants of Insulators: Dispersion Relations. In *Optical Properties of Solids*, ed. S. Nudelman and S. S. Mitra, Plenum Press, New York. 137–151.

[19] Carpenter, R. L., R. D. Clark, and Y. F. Su (1980). Fly Ash from Electrostatic Precipitators: Characterization of Large Spheres. *Journal of Air Pollution Control Association*, **30**:6, 679–681.

[20] Chandrasekhar, S. (1960). Radiative Transfer. Dover Publications, Inc., New York.

[21] Coulter Electronics Limited (1986). *Fine Particle Application Notes for Coulter Counters*. Luton, U.K.

[22] CRC Press (1985). CRC Handbook of Chemistry and Physics. 66th Edition, ed. R. C. Weast, CRC Press, West Palm Beach, Florida.

[23] Crow, E. L., and K. Shimizu (1988). Lognormal Distributions. Marcel Dekker Inc., New York.

[24] Daeschner, H. W. (1968/69). Wet Sieving with Precision Electroformed Sieves. *Powder Technology*, **2**, 349–355.

[25] Dave, J. V. (1970). Coefficients of the Legendre and Fourier Series for the Scattering Functions of Spherical Particles. *Applied Optics*, **9**:8, 1888–1898.

[26] Davison, R. L., D. F. S. Natusch, J. R. Wallace, and C. A. Evans, Jr. (1974). Trace Elements in Fly Ash. *Environmental Science and Technology*, **8**:13, 1107–1113.

[27] Del Monte, M. and C. Sabbioni (1984). Morphology and Mineralogy of Fly Ash from a Coal Fueled Power Plant. *Archives for Meteorology, Geophysics, and Bioclimatology*, **35**, 93–104.

[28] DeNee, P. B. (1978). Collecting, Handling and Mounting of Particles for SEM. *Scanning Electron Microscopy*, **1**, SEM Inc., AMF O'Hara, IL 60666, USA.

[29] Diamond, S. (1988). Rapid Particle Size Analysis of Fly Ash with a Commercial Laser Diffraction Instrument. *Material Research Society Symposium Proceedings*, **113**, 119–127.

[30] Ebert, J. L. (1993). Optical Properties of Molten Coal Slag. PhD Thesis, Department of Mechanical Engineering, Stanford University, Stanford, CA 94305.

[31] Ebert, J. L. (1992). Private communication.

[32] Ebert, J. L., S. A. Self, and S. Ghosal (1991). Optical Properties of Fly Ash. Quarterly Report No.13, Submitted to Pittsburgh Energy Technology Center, HTGL, Stanford University.

[33] Edwards, D. K. (1976). Molecular Gas Band Transfer. In *Advances in Heat Transfer*, Academic Press, New York.

[34] Engelhardt, G., M. Nofz, K. Forkel, F. G. Wihsmann, M. Magi, A. Samoson, E. Lippmaa (1985). Structural Studies of Calcium Aluminosilicate Glasses by High

Resolution Solid State ^{29}Si and ^{27}Al Magic Angle Spinning NMR. *Physics and Chemistry of Glasses*, **26**:5, 157–165.

[35] Field, M. A., D. W. Gill, B. B. Morgan, and P. G. W. Hawksley (1967). Combustion of Pulverized Coal. The British Coal Utilization and Research Association, Leatherhead, U. K.

[36] Fisher, G. L., B. A. Prentice, D. Silberman, J. M. Ondov, A. H. Biermann, R. C. Ragaini, and A. R. McFarland (1978). Physical and Morphological Studies of Size-Classified Coal Fly Ash. *Environmental Science and Technology*, **12**:4, 447–451.

[37] Flagan, R. C., and S. K. Friedlander (1978). Particle Formation in Pulverized Coal Combustion — a Review. In *Recent Developments in Aerosol Science*, ed. D. T. Shaw. Wiley, New York. 25–59.

[38] Flagan, R. C., and J. H. Seinfeld (1988). Fundamentals of Air Pollution Engineering. Prentice Hall, Englewood Cliffs, New Jersey.

[39] Furuya, K., Y. Miyajima, T. Chiba, and T. Kikuchi (1987). Elemental Characterization of Particle Size-Density Separated Coal Fly Ash by Spectrophotometry, ICP Emission Spectrometry, and SEM-EDAX. *Environmental Science and Technology*, **21**:9, 898–903.

[40] Ghosal, S., J. L. Ebert, and S. A. Self (1993a). The Infrared Refractive Indices of $CHBr_3$, CCl_4, and CS_2. *Infrared Physics*, in press.

[41] Ghosal, S., J. L. Ebert, and S. A. Self (1993b). Size Distributions of Fly Ashes by Coulter Multisizer: Use of Multiple Orifices and Fitting to Truncated Lognormal Function. *Particle and Particle Systems Characterization*, **10**, 11–18.

[42] Ghosal, S., and S. A. Self (1993a). Infrared Extinction Measurements on Fly Ash Dispersions. Presented at the American Society of Mechanical Engineers' Winter Annual Meeting, New Orleans, LA.

[43] Ghosal, S., and S. A. Self (1993b). Chemical Composition and Size Distribution Functions for Representative Coal Fly Ashes. Presented at the *Symposium on Ash Chemistry in Fossil Fuel Processes* at the American Chemical Society National Meeting at Chicago, IL.

[44] Ghosal, S., and S. A. Self (1993c). Optical Characterization of Coal Fly Ash", *Radiative Transfer — Theory and Applications*, ed. A. M. Smith and S. H. Chan, American Society of Mechanical Engineers, HTD, **244**, 105–115.

[45] Goldstein, J. I., D. E. Newbury, P. Echlin, D. C. Joy, C. Fiori, and E. Lifshin (1984). Scanning Electron Microscopy and X-Ray Microanalysis. Plenum Press, NY & London.

[46] Goodwin, D. G. (1986). Infrared Optical Constants of Coal Slags, PhD Thesis, HTGL Topical Report No. T-255, Stanford University, Stanford, CA 94305.

[47] Goodwin, D. G., and M. Mitchner (1989a). Infrared Optical Constants of Coal Slag: Dependence on Chemical Composition. *AIAA Journal of Thermophysics and Heat Transfer*, **3**:1, 53–60.

[48] Goodwin, D. G., and M. Mitchner (1989b). Flyash Radiative Properties and Effects on Radiative Heat Transfer in Coal-Fired Systems. *International Journal of Heat and Mass Transfer*. **32**:4, 627–638.

[49] Gupta, R. P., T. F. Wall, and J. S. Truelove (1983). Radiative Scatter by Fly Ash in Pulverized Coal-Fired Furnaces: Application of the Monte Carlo Method to Anisotropic Scatter. *International Journal of Heat and Mass Transfer*, **26**, 1649–1660.

[50] Gupta, R. P., and T. F. Wall (1985). The Optical Properties of Fly Ash in Coal Fired Furnaces. *Combustion and Flame*, **61**, 145–151.

[51] Hale, G. M., and M. R. Querry (1973). Optical Constants of Water in the 200 nm to 200 μm Wavelength Region. *Applied Optics*, **12**:3, 555–563.

[52] Hemmings, R. T., and E. E. Berry (1986). Speciation in Size and Density Fractionated Fly Ash. *Material Research Society Symposium Proceedings*, **65**, 91–104.

[53] Hemmings, R. T., E. E. Berry, B. J. Cornelius, and B. E. Scheetz (1987). Speciation in Size and Density Fractionated Fly Ash II. Characterization of Low–Calcium, High–Iron Fly Ash. *Material Research Society Symposium Proceedings*, **86**, 81–98.

[54] Hemmings, R. T., and E. E. Berry (1988). On the Glass in Coal Fly Ashes: Recent Advances. *Material Research Society Symposium Proceedings*, **113**, 3–38.

[55] Herdan, G. (1960). Small Particle Statistics. Butterworth, London 1960.

[56] Hodkinson, J. R. (1966). The Optical Measurement of Aerosols. In *Aerosol Science*, ed. C. N. Davies, Academic Press, New York.

[57] Holloway, D. J. (1972). The Physical Properties of Glass. Wykeham Publications Ltd., London and Winchester.

[58] Huntsberger, D. V., and P. Billingsley (1977). Elements of Statistical Inference, Allyn and Bacon, Inc.

[59] Huggins F. E., D. A. Kosmack, G. P. Huffman, and R. J. Lee (1980). Coal Mineralogies by SEM Automatic Image Analysis. *Scanning Electron Microscopy*, **1**, 531–540. SEM Inc., AMF O'Hara, IL 60666, USA.

[60] Huffman, G. P., F. E. Huggins, and G. R. Dunmyre (1981). Investigation of the High-Temperature Behaviour of Coal Ash in Reducing and Oxidizing Atmospheres. *Fuel*, **60**, 585–597.

[61] Im, K. H., and R. K. Ahluwalia (1990). Radiation Properties of Coal Combustion Products. Argonne National Laboratory, Chicago, Il. Report Prepared for US DOE under Contract W–31–109–Eng–38.

[62] Irvine, W. M., and J. B. Pollack (1968). Infrared Optical Properties of Water and Ice Spheres. *Icarus*, **8**, 324–360.

[63] Jackson, J. D. (1975). Classical Electrodynamics. Second Edition, Wiley, New York.

[64] Jenkins, F. A., and H. E. White (1981). Fundamentals of Optics. Fourth Edition, McGraw-Hill Book Company.

[65] Kang, S. G., A. R. Kerstein, J. J. Helble, and A. F. Sarofim (1990). Pulverized Coal Combustion: Bimodal Ash Particle Size Distribution. *Aerosol Science and Technology*, **13**, 401–412.

[66] Kang, S. G., J. J. Helble, A. F. Sarofim, and J. M. Beer (1988). *Proceedings of the Twenty-Second Symposium (International) on Combustion.* The Combustion Institute, Pittsburgh, PA. 231–238.

[67] Kaufherr, N. and D. Lichtman (1984). Comparison of Micron and Submicron Fly Ash Particles Using Scanning Electron Microscopy and X-ray Elemental Analysis. *Environmental Science and Technology*, **18**:7, 544–547.

[68] Kevex Corporation (1988). Energy-Dispersive X-Ray Microanalysis. Kevex Corporation, San Carlos, CA.

[69] Koch, R. (1989). Personal communication. Center for Materials Research, Stanford University, Stanford, CA 94305.

[70] Lee, R. J., F. E. Huggins, and G. P. Huffman (1978). Correlated Mossbauer-SEM Studies of Coal Mineralogy. *Scanning Electron Microscopy*, **1**, 561–568. SEM Inc., AMF O'Hara, IL 60666, USA.

[71] Lichtman, D., and S. Mroczkowski (1985). Scanning Electron Microscopy and Energy-Dispersive X-ray Spectroscopy Analysis of Submicrometer Coal Fly Ash Particles. *Environmental Science and Technology*, **19**:3, 274–277.

[72] Lovell, J., and S. Diamond (1986). A Simple Technique for Fly Ash Specimen Preparation for Scanning Electron Microscopy, *Material Research Society Symposium Proceedings*, **65**, 131–136.

[73] Lowe, A., I. M. Stewart, and T. F. Wall (1979). The Measurement and Interpretation of Radiation from Fly Ash Particles in Large Pulverized Coal Flames. *Proceedings of the Seventeenth Symposium (International) on Combustion.* The Combustion Institute, Pittsburgh, PA. 105–113.

[74] Lynch, D. W., and W. R. Hunter (1985). Optical Constants of Metals. In *Handbook of Optical Constants of Solids*, ed. E. D. Palik, 286–295, Academic Press, New York.

[75] Macek, A. (1979). Coal Combustion in Boilers: a Mature Technology Facing New Constraints. *Proceedings of the Seventeenth Symposium (International) on Combustion.* The Combustion Institute, Pittsburgh, PA. 65–74.

[76] Malitson, I. H. (1964). Refractive Properties of Barium Fluoride. *Journal of Optical Society of America*, **54**:5, 628–632.

[77] Mamane, Y., J. L. Miller, and T. G. Dzubay (1986). Characterization of Individual Fly Ash Particles Emitted from Coal and Oil-Fired Power Plants. *Atmospheric Environment*, **20**:11, 2125–2135.

[78] Marx, E. (1983). Data Analysis for Size and Refractive Index from Light Scattering by Small Spheres. *Aerosol Science and Technology*, **2**, 190.

[79] McCarthy, G. J. (1988). X-Ray Powder Diffraction for Studying the Mineralogy of Fly Ash. *Material Research Society Symposium Proceedings*, **113**, 75–86.

[80] Moza, A. K., and L. G. Austin (1983). Analysis of Pulverized Coal Particles (10–100 μm) for Fe, S, Ca, Si and Al on a Particle-to-Particle Basis. *Fuel*, **62**, 1468.

[81] Mysen, B. O., D. Virgo, and F. A. Seifert (1982). The Structure of Silicate Melts: Implications for Chemical and Physical Properties of Natural Magma. *Reviews of Geophysics and Space Physics*, **20**:3, 353–383.

[82] Mysen, B. O., D. Virgo, and F. A. Seifert (1985). Relationships Between Properties and Structure of Aluminosilicate Melts. *American Mineralogist*, **70**, 88–105.

[83] Mysen, B. O., D. Virgo, E. Neumann, and F. A. Seifert (1985). Redox Equilibria and the Structural States of Ferrous and Ferric Iron in Melts in the System CaO–MgO–Al_2O_3–SiO_2–FeO: Relationships Between Redox Equilibria, Melt Structure and Liquidus Phase Equilibria. *American Mineralogist*, **70**, 317–331.

[84] Nelder, J. A., and R. Mead (1965). A Simplex Method for Function Minimization. *Computer Journal*, **7**, 308–313.

[85] Newton, G. J., O. G. Raabe, and B. V. Mokler (1977). Cascade Impactor Design and Performance. *Journal of Aerosol Science*, **8**, 339–347.

[86] Norton, G. A., R. Markuszewski, and H. R. Shanks (1986). Morphological and Chemical Characterization of Iron-Rich Fly Ash Fractions. *Environmental Science and Technology*, **20**:4, 409–413.

[87] Pfund, A. H. (1935). The Dispersion of CS_2 and CCl_4 in the Infrared. *Journal of Optical Society of America*, **25**:11.

[88] Press, W. H., S. A. Teukolsky, W. T. Vetterling, and B. P. Flannery (1986). Numerical Recipes: The Art of Scientific Computing. Cambridge University Press.

[89] PSI Technology Company (1990). Transformation of Inorganic Coal Constituents in Combustion Systems", (Two Volumes.) Phase 1, Final Report Submitted to Pittsburgh Energy Technology Research Center, US DOE, Pittsburgh, PA.

[90] Pouchert, C. J. (1985). *The Aldrich Library of FT-IR Spectra*, Volume 1, First Edition, Aldrich Chemical Company.

[91] Qian, J. C., E. E. Lachowski, and F. P. Glasser (1989). The Microstructure of National Bureau of Standards Reference Fly Ash. *Material Research Society Symposium Proceedings*, **136**, 77–85.

[92] Ramsden, A. R., and M. Shibaoka (1982). Characterization and Analysis of Individual Fly Ash Particles from Coal-fired Power Stations by a Combination of Optical Microscopy, Electron Microscopy and Quantitative Electron Microprobe Analysis. *Atmospheric Environment*, **16**:9, 2191–2206.

[93] Raask, E. (1968). Cenospheres in Pulverized-Fuel Ash. *Journal of the Institute of Fuel*, **43**, 339–344.

[94] Ralajczak, H. (1967). In *Handbook of Spectroscopy, Volume II*, ed. J. W. Robinson, CRC Press, 20–21.

[95] Rothenberg, S. J., P. Denee, and P. Holloway (1980). Coal Combustion Fly Ash Characterization: Electron Spectroscopy for Chemical Analysis, Energy Dispersive X-ray Analysis, and Scanning Electron Microscopy. *Applied Spectroscopy*, **34**:5, 549–555.

[96] Schrader, B. (1989). Raman/Infrared Atlas of Organic Compounds. Second Edition, VCH Publishers, FRG.

[97] Seifert, F., M. O. Mysen, and D. Virgo (1982). Three-Dimensional Network Structure of Quenched Melts (Glass) in the Systems SiO_2–$NaAlO_2$, SiO_2–$CaAl_2O_4$ and SiO_2–$MgAl_2O_4$. *American Mineralogist*, **67**, 696–717.

[98] Self, S. A. (1989, 1990, 1991). Personal communications. Mechanical Engineering Department, Stanford University, Stanford, CA 94305.

[99] Siegel, R., and Howell J. R. (1992). Thermal Radiation Heat Transfer. Third Edition, Hemisphere Publishing Corporation.

[100] Simon, I. (1960). Infra-red Studies of Glass. In *Modern Aspects of the Vitreous State. Volume 1.* Ed. J. D. Mackenzie. Butterworths, Washington.

[101] Sirois, A. (1991). The Relationship between Mean and Standard Deviation in Precipitation Chemistry Measurements across Eastern North America. *Atmospheric Environment*, **25A**:2, 329–340.

[102] Small, J. A., K. F. J. Heinrich, D. E. Newbury, and R. L. Myklebust (1979). *Scanning Electron Microscopy*, **2**, 807–816. SEM Inc., AMF O'Hara, IL 60666, USA.

[103] Sweet, J. R., and W. B. White (1969). Study of Sodium Silicate Glasses and Liquids by Infrared Spectroscopy *Physics and Chemistry of Glasses*, **10**, 246–251.

[104] Tarpley, W., and C. Vitiello (1952). Infrared Spectra of Steroids: New Solvents for Steroids Difficultly Soluble in Carbon Disulfide, *Analytical Chemistry*, **24**:2, 315–318.

[105] Uhlmann, D. R., and H. Yinnon (1983). The Formation of Glasses. In *Glass: Science and Technology. Volume 1*, ed. D. R. Uhlmann and N. J. Kreidl. Academic Press, New York.

[106] van de Hulst, H. C. (1957). Light Scattering by Small Particles. Dover Publications.

[107] Veale, C. R. (1972). Fine Powders: Preparation, Properties and Uses. Applied Science Publishers Limited, London.

[108] Viskanta, R., A. Ungan, and M. P. Mengüc (1981). Predictions of Radiative Properties of Pulverized Coal and Fly-ash Polydispersions. ASME Paper 81-HT-24. Presented at 20th Joint ASME/AIChE National Heat Transfer Conference.

[109] Volz, F. E. (1973). Infrared Optical Constants of Ammonium Sulfate, Sahara Dust, Volcanic Pumice, and Fly Ash. *Applied Optics*, **12**, 564–568.

[110] Vorres, K. S. (1979). Effect of Composition on Melting Behaviour of Coal Ash. *Journal of Engineering for Power*. **101**, 497–499.

[111] Wall, T. F., A. Lowe, L. J. Wibberly, T. Mai-viet, and R. P. Gupta. (1981). Fly Ash Characteristics and Radiative Heat Transfer in Pulverized-Coal-Fired Furnaces. *Combustion Science and Technology*, **26**, 107–121.

[112] Wilhelmi, B. (1967). In *Handbook of Spectroscopy, Volume II*, ed. J. W. Robinson, CRC Press, 20.

[113] Wiscombe, W. (1987). Fast, Modern Mie Scattering Algorithms for Single Particles and Polydispersions, NASA Reference Publication.

[114] White, H. J. (1963). Industrial Electrostatic Precipitation. Addison-Wesley, Reading, Massachusetts.

[115] Wyatt, P. J. (1980). Some Chemical, Physical, and Optical Properties of Fly Ash Particles. *Applied Optics*, **19**, 975–983.

[116] Zallen, R. (1983). The Physics of Amorphous Solids. Second Edition, John Wiley and Sons, New York.

[117] Zachariasen, R. (1932). The Atomic Arrangement in Glass. *Journal of the American Chemical Society*, **54**, 3841.

[118] Zarzycki, J. (1982). Glasses and the Vitreous State. Cambridge University Press (Translation published in 1991).